
Frustrated magnetism, quench dynamics, and out-of-equilibrium criticality in quantum many-body lattices

Jad Camille Halimeh



München 2016

Frustrated magnetism, quench dynamics, and out-of-equilibrium criticality in quantum many-body lattices

Jad Camille Halimeh

Dissertation
an der Fakultät für Physik
der Ludwig–Maximilians–Universität
München

vorgelegt von
Jad Camille Halimeh
aus Aley, Libanon

München, den 21.12.2016

Erstgutachter: Ulrich Schollwöck

Zweitgutachter: Matthias Punk

Tag der mündlichen Prüfung: 16.01.2017

Contents

Zusammenfassung	vii
Abstract	ix
Publications	x
1 Introduction	1
1.1 Time-dependent density matrix renormalization group	2
1.1.1 Krylov subspace approximation	3
1.1.2 Suzuki-Trotter decomposition	3
1.2 Outline of this dissertation	4
1.3 Quantum spin liquids	6
1.3.1 Free energy for the $(\mathcal{A}, \mathcal{B})$ -ansätze	8
1.3.2 Free energy for the Q -ansätze	15
1.4 Quench dynamics	18
1.4.1 Integrable models	20
1.4.2 Nonintegrable models	21
1.4.3 Prethermalization	21
1.5 Dynamical phase transitions	23
1.5.1 Overview of equilibrium phase transitions	23
1.5.2 Landau-type dynamical phase transition (DPT-I)	31
1.5.3 Return-rate dynamical phase transition (DPT-II)	34
2 Spin structure factors of chiral quantum spin liquids on the kagome lattice	45
3 Prethermalization and persistent order in the absence of a thermal phase transition	55
4 Enriching the dynamical phase diagram of spin chains with long-range interactions	65
5 Chebyshev matrix product state approach for time evolution	75

6	Domain-wall melting in ultracold-boson systems with hole and spin-flip defects	89
7	Fractional excitations in cold atomic gases	105
8	Conclusion	111
	Acknowledgments	113
	Curriculum Vitae	114

Zusammenfassung

Die vorliegende Dissertation liefert einen Beitrag zum Verständnis von stark korrelierten Quantenvielteilchensystemen innerhalb und außerhalb des Gleichgewichtszustands, insbesondere die dynamischen Spinstrukturfaktoren von chiralen GAPPED Spin Flüssigkeiten auf dem Kagome Gitter mit antiferromagnetischer Heisenberg-Spinkopplung und nichtgleichgewichts Kritikalität in Systemen nach einem Quench.

Der dynamische Spinstrukturfaktor wird für chirale Schwinger-Boson Molekularfeldansätze hergeleitet und berechnet, wobei die Brechung der Zeitumkehrsymmetrie zum Vorschein kommt, ausgedrückt durch die Verringerung der üblichen sechsfachen Rotationsymmetrie des dynamischen Strukturfaktors auf eine dreifache Symmetrie. Andere interessante Eigenschaften werden hervorgehoben, wie der flache Beginn des Spinon-Kontinuums für den chiralen *cuboc1* Ansatz. Diese Arbeit bietet eine hilfreiche Verbindung zu inelastischen Neutronenstreuungsexperimenten, welche versuchen die Beschaffenheit möglicher spinflüssiger Grundzustände von Kandidatenmaterialien, wie etwa Herbertsmithite, aufzudecken.

Bezüglich Nichtgleichgewichtsdynamik bietet diese Dissertation eine numerische Untersuchung der zwei Hauptarten dynamischer Phasenübergänge: Einen Landau-artigen, welcher auf die Relaxation zu einem stationären Zustand angewiesen ist, von welchem ein Ordnungsparameter als Funktion des Quenchkontrollparameters (DPT-I) extrahiert werden kann und eine zweite Art, welche als Nichtanalytizität in der Loschmidt-Echo Rückgaberate als Funktion der Entwicklungszeit (DPT-II) entsteht. Mit dem paradigmatischen langreichweitigen Ising-Modell mit transversalem Feld arbeitend, stellen wir einen nicht trivialen Zusammenhang zwischen beiden Übergängen her, zeigen, dass DPT-I qualitativ und grundlegend verschieden von dem zugrundeliegenden Gleichgewichtsphasenübergang ist und entdecken eine neue *anormale* dynamische Phase, welche in Beziehung steht zu DPT-II für hinreichend langreichweitige Wechselwirkungen.

Zusätzlich zur dynamischen Kritikalität bietet diese Dissertation Ergebnisse der zeitabhängigen Dichtematrixrenormalisierungsgruppe (*t*-DMRG) für globale Quenche in dem Bose-Hubbard-Modell mit ein oder zwei Arten von Teilchen im eindimensionalen Raum für zwei Hauptzwecke; zum einen um Auswirkungen von Defekten im anfänglichen (präparierten) Zustand zu untersuchen und zu charakterisieren, zum anderen als Versuch die Erreichbarkeit längerer Entwicklungszeiten in *t*-DMRG zu verbessern durch Ausdruck der Zeitentwicklungsoperatoren mittels Chebyshev Polynomen.

Die in dieser Dissertation dargestellten Ergebnisse sind experimentell überprüfbar, erweitern das Verständnis für die beteiligten Phänomene und öffnen die Tür für weiter-

führende Forschung und Untersuchung der entsprechenden neuen Entdeckungen.

Abstract

The present dissertation contributes to the understanding of strongly-correlated quantum many-body systems in and out of equilibrium, in particular the dynamical structure factors of chiral gapped spin liquids on the kagome lattice with antiferromagnetic Heisenberg spin couplings and out-of-equilibrium criticality in systems that have undergone a quench.

The dynamical spin structure factor for chiral Schwinger-boson mean-field ansätze is derived and calculated, revealing time-reversal-symmetry breaking manifested in the reduction of the usual six-fold rotational symmetry of the dynamical structure factor into a three-fold rotational symmetry. Other interesting features are highlighted such as a flat onset of the spinon continuum for the *cuboc1* chiral ansatz. This work provides a useful connection to inelastic neutron scattering experiments that aim to unravel the nature of possible spin-liquid groundstates in candidate materials such as Herbertsmithite.

In out-of-equilibrium dynamics, this dissertation provides the numerical study of two main types of dynamical phase transitions: a Landau-type that relies on relaxation into a stationary state from which an order parameter can be extracted as a function of quench control parameter (DPT-I), and a second type arising as a nonanalyticity in the Loschmidt-echo return rate as a function of evolution time (DPT-II). Working with the paradigmatic long-range transverse-field Ising model, we establish a nontrivial connection between both transitions, show that DPT-I is qualitatively and fundamentally different from the corresponding equilibrium phase transition, and discover a new *anomalous* dynamical phase related to DPT-II for sufficiently long-range interactions.

In addition to dynamical criticality, this dissertation also provides time-dependent density matrix renormalization group (*t*-DMRG) results on global quenches in the one- and two-species Bose-Hubbard model in one-dimensional space for two main purposes with the first being the study and characterization of the effects of defects in the initial (prepared) state of the system on subsequent dynamics following a quench, and the second being an attempt to improve the accessibility of longer evolution times in *t*-DMRG through expanding the time-evolution operator in terms of Chebyshev polynomials.

The results provided in this dissertation are experimentally feasible for verification, expand on the understanding of the phenomena involved, and open the door for further research and investigation of the corresponding new findings.

Publications

This dissertation is based on the following journal articles listed in inverse submission chronological order.

- *Enriching the dynamical phase diagram of spin chains with long-range interactions*
Jad C. Halimeh and Valentin Zauner-Stauber
arXiv:1610.02019
- *Prethermalization and persistent order in the absence of a thermal phase transition*
Jad C. Halimeh, Valentin Zauner-Stauber, Ian P. McCulloch, Inés de Vega, Ulrich Schollwöck, and Michael Kastner
Phys. Rev. B **95**, 024302 (2017)
- *Spin structure factors of chiral quantum spin liquids on the kagome lattice*
Jad C. Halimeh and Matthias Punk
Phys. Rev. B **94**, 104413 (2016)
- *Chebyshev matrix product state approach for time evolution*
Jad C. Halimeh, Fabian Kolley, and Ian P. McCulloch
Phys. Rev. B **92**, 115130 (2015)
- *Domain-wall melting in ultracold-boson systems with hole and spin-flip defects*
Jad C. Halimeh, Anton Wöllert, Ian P. McCulloch, Ulrich Schollwöck, and Thomas Barthel
Phys. Rev. A **89**, 063603 (2014)
- *Fractional excitations in cold atomic gases*
Jens Honer, **Jad C. Halimeh**, Ian P. McCulloch, Ulrich Schollwöck, and Hans Peter Büchler
Phys. Rev. A **86**, 051606(R) (2012)

Chapter 1

Introduction

This dissertation deals with an eclectic mix of results that converge under one banner described by the title of this work. The subfield of physics involved is quantum many-body theory, and one can further restrict the scope of this dissertation under the umbrella of quantum many-body phenomena usually involving strong correlations either at equilibrium or in some (quasi-)steady state at some evolution time after a quench – a physical mechanism where a control parameter is suddenly and abruptly changed from some initial value to some final value at an initial time which we shall denote $t = 0/J$, with J some energy scale, for example the exchange coupling constant in the Ising model with ferromagnetic interactions. In this Introduction, we shall aim, in the following order, to (i) motivate the topics of this dissertation and (ii) briefly go over the numerical methods used in achieving a lot of its results, before (iii) drawing an outline of the presentation of the rest of the dissertation. Then we will (iv) offer an intuitive outlook on the main physical concepts included in this work, namely quantum spin liquids and dynamical criticality, and (v) also provide further in-depth details on some of the calculations involved in the main analytical results.

Before proceeding with this, however, it is proper to note that here we will be discussing two main topics of currently great research interest and effort. The first is (geometrically-)frustrated magnetism in the two-dimensional kagome lattice with antiferromagnetic spin couplings. Here, the lattice geometrical structure leads to conflicting spin-coupling configurations each favoring a different geometry, leading to very strong quantum fluctuations and a huge degeneracy in the groundstate – thermal ordering may not exist as quantum fluctuations are still too strong even at low temperatures. Therefore, it is always very useful to study such groundstates, or proposals thereof, and we do so in this dissertation by deriving and calculating the dynamical structure factor [1] of chiral gapped spin liquids on the Heisenberg antiferromagnetic kagome lattice within the framework of Schwinger-boson mean-field theory and projective symmetry group [2, 3, 4, 5].

The second main topic we consider is quantum quenches in general, and dynamical criticality in particular. Quantum quenches [6] are processes in which a system is prepared in some initial state and subsequently subjected to a sudden change in a control parameter in the Hamiltonian of this system. This leads to nontrivial dynamics and out-

of-equilibrium behavior that cannot be handled within the framework of linear-response theory or the fluctuation-dissipation theorem, but that is nevertheless intriguing in the sense that so-called *dynamical phase transitions* arise that do have a lot in common with the corresponding equilibrium phase transitions that physicists have studied extensively and understand more or less thoroughly. Here a vast world of new physics is accessed, where one tries to study, for example, the existence of dynamical universality classes, their classifying properties, their relationship (or lack thereof) to their equilibrium counterparts, and so on. In this dissertation, we provide results on quench dynamics [7, 8, 9, 10, 11] in one-dimensional quantum many-body lattices, study the effects of defects [7, 8] on this dynamics, investigate the possibility of better numerical methods to allow access to longer evolution times in it [9], and detect signatures of dynamical criticality [10, 11] arising due to it.

1.1 Time-dependent density matrix renormalization group

This section is adapted in full from Ref. [9], which constitutes Chapter 5 of this dissertation, and we choose to carry out this repetition because the time-dependent density matrix renormalization group (*t*-DMRG) is used heavily in obtaining the results in Chapters 3, 5, 6, and 7, and therefore, its presence here in the Introduction shall serve as an important go-to reference for those interested in a brief overview of the details of *t*-DMRG and its time-evolution engines: the Krylov subspace approximation and the Suzuki-Trotter decomposition. Indeed, it is not too extravagant to say that *t*-DMRG is perhaps irreplaceable in terms of efficiency and precision when it comes to the quench dynamics we simulate in this dissertation for usually strongly-correlated nonintegrable models with no known analytical solutions. In fact, *t*-DMRG is, in the subjective opinion of the author, the closest numerical tool to an actual laboratory experiment allowing us to study, with extreme and controlled precision, strongly-correlated many-body models that we may otherwise not be able to faithfully study.

A large part of the results of this dissertation has been calculated using *t*-DMRG [12, 13, 14, 15, 16, 17], an extremely useful method based on the description of the quantum state in terms of matrix product states (MPS) [18, 19, 20, 21, 22, 23, 24]

$$|\psi\rangle = \sum_{\{\sigma\}} c_{\sigma} |\sigma\rangle = \sum_{\{\sigma\}} A^{\sigma_1} \dots A^{\sigma_N} |\sigma\rangle, \quad (1.1)$$

where $\sigma = \{\sigma_1 \dots \sigma_N\}$ is the computational basis, A^{σ_1} and A^{σ_N} are D -dimensional row and column vectors, respectively, and A^{σ_i} ($i = 2, \dots, N - 1$) is a $D \times D$ matrix. Theoretically, every quantum state can be represented by an MPS if infinite matrix dimensions are allowed [25]. The practical relevance of such a state description lies in the fact that one can approximate the exact quantum state by an MPS with finite matrix dimension. From this perspective, MPS presents a class of states that compress exact many-body quantum

states such that the number of coefficients needed to describe the state scales linearly in the number of constituents as opposed to the exponential scaling in the exact representation. Furthermore, the approximation made in the compression step is well understood [20] and can be controlled by the matrix dimension D .

With the help of MPS, several methods have been developed to calculate the time evolution of one-dimensional many-body quantum systems [21]. The earliest methods utilized the Trotter [26, 27] decomposition of the time-evolution operator. Later approaches approximated the matrix exponential in the Krylov [28] subspace. Both methods have been successfully applied to a series of different physical problems [7, 8, 23, 24, 29].

Nevertheless, the times reachable with current methods are still very limited making the development of new methods still a very important and germane endeavor. The limitation of evolution times accessible with MPS-based methods is closely related to the amount of entanglement in the quantum state. The maximal entanglement between two subsystems described by an MPS is roughly given by the logarithm of the matrix dimension D . On the other hand, it has been shown that the entanglement after a quantum quench grows typically linearly in time [30] leading to an exponentially-growing matrix dimension, which is required in order to keep the error fixed.

1.1.1 Krylov subspace approximation

Instead of treating Schrödinger's equation as a differential equation, it is prudent to consider for time-independent Hamiltonians the time-evolution operator $\exp(-i\hat{H}t)$. Though this precludes the caveats of integration, it does not obviate the nontrivial task of evaluating an exponential of matrices [17, 31]. One of the most efficient methods is the so-called Krylov subspace approximation [17, 21, 28], where one realizes that our interest lies in $\exp(-i\hat{H}t)|\psi\rangle$ rather than $\exp(-i\hat{H}t)$. In DMRG $\hat{H}|\psi\rangle$ is available efficiently, and this can be utilized through forming the Krylov subspace by successive Gram-Schmidt orthonormalization of the set $\{|\psi\rangle, -i\hat{H}t|\psi\rangle, (-i\hat{H})^2t|\psi\rangle, \dots\}$, where $|\psi\rangle$ is assumed to be normalized here. Similarly to the related Lanczos method, where one calculates an $n \times n$ tridiagonal matrix $T = VAV^\dagger$ from a given matrix A using the transformation matrix V , one obtains n Krylov vectors that form the orthonormal columns of V . Here, $-i\hat{H}t$ is approximated regarding its extreme eigenvalues by VTV^\dagger to very good precision even for relatively small [17] n . The exponential is then given by the first column of $V \exp T$, where the latter exponential is now much easier to calculate.

1.1.2 Suzuki-Trotter decomposition

Another prominent and very proficient method for evaluating the above matrix exponential is the Suzuki-Trotter decomposition [17, 21, 26, 27], commonly referred to as simply Trotter. This method is mainly useful for Hamiltonians with nearest-neighbor interactions. In the case of a one-dimensional chain, the Hamiltonian $\hat{H} = \hat{H}_1 + \hat{H}_2$ is divided into odd- and even-bond terms, \hat{H}_1 and \hat{H}_2 , respectively, where $\hat{H}_1 = \sum_{i=1}^{N/2} \hat{h}_{2i-1}$ and $\hat{H}_2 = \sum_{i=1}^{N/2} \hat{h}_{2i}$. Here, \hat{h}_i is the local Hamiltonian linking sites i and $i+1$, and N is the total number of sites

on the lattice. $[\hat{H}_1, \hat{H}_2] \neq 0$ as neighboring local Hamiltonians do not commute in general, but all the terms in \hat{H}_1 and \hat{H}_2 commute. As such, the first-order Trotter decomposition of the infinitesimal time-evolution operator is

$$e^{-i\hat{H}\Delta t} = e^{-i\hat{H}_1\Delta t}e^{-i\hat{H}_2\Delta t} + \mathcal{O}(\Delta t^2). \quad (1.2)$$

Moreover, the second-order Trotter decomposition reads

$$e^{-i\hat{H}\Delta t} = e^{-i\hat{H}_1\Delta t/2}e^{-i\hat{H}_2\Delta t}e^{-i\hat{H}_1\Delta t/2} + \mathcal{O}(\Delta t^3). \quad (1.3)$$

One can go for yet higher orders and conclude that an n^{th} -order Trotter decomposition will yield over a time-step Δt an error of the order of $(\Delta t)^{n+1}$. As one requires $t/\Delta t$ time-steps in order to reach an evolution time t , the error grows at worst linearly [17] in time t , and therefore, the resulting error is bound by an expression of the order of $(\Delta t)^n t$. For the purposes of this study, it turns out that second-order Trotter is optimal.

Time-dependent DMRG (t -DMRG) uses adaptive Hilbert spaces that follow the state $|\psi(t)\rangle$ being optimally approximated, and was first proposed independently in the works of Daley, Kollath, Schollwöck, and Vidal [32] and White and Figuin [14]. Both these approaches are efficient implementations of the time-evolving block-decimation (TEBD) algorithm invented by Vidal [25, 33] for the classical simulation of the time evolution of weakly-entangled quantum states. As it turns out, there is a very strong connection between adaptive t -DMRG and the original TEBD algorithm, as discussed by Daley *et al.* [32] whereby DMRG naturally attaches good quantum numbers to state spaces utilized by the TEBD algorithm. This allows for drastic improvement in performance due to the use of such good quantum numbers.

1.2 Outline of this dissertation

Now that we have given a brief overview of the main numerical tool used in this dissertation, we can pause to outline what the rest of the latter entails. In the remainder of this Introduction, we shall focus on two aspects: (a) intuitive concepts and theory behind the physics involved, and (b) derivations that were omitted from the main Chapters of the dissertation, and that we believe would be of good use to students working on similar problems. As such, in Sec. 1.3, we discuss quantum spin liquids in general, and in particular gapped chiral spin liquids, before proceeding with applying the Schwinger-boson mean-field theory (SBMFT) on the antiferromagnetic Heisenberg model on the kagome lattice (AFKM), and carrying out the mean-field decoupling that allows us to eventually calculate the dynamical structure factors of several SBMFT ansätze, including chiral ones. Sec. 1.3 will thus serve as a prelude to Chapter 2 [1], as well as a place where the details of the results of Chapter 2 [1] can be found.

We then leave the world of two-dimensional physics, where basically integrable genuinely-interacting models are absent, to that of one-dimensional physics in Sec. 1.4 where the latter abound. Here we provide a brief overview of the theory of integrable and nonintegrable

one-dimensional many-body systems, and, correspondingly, the resulting steady states such systems are expected to relax to after a quench, which is not found in any of the Chapters of the dissertation as in the rigor presented in Sec. 1.4. In addition to the importance of understanding the differences between integrable and nonintegrable systems and what is to be expected in each when thrown out of equilibrium in the intermediate- and long-time limits due to (pre)thermalization, this serves as a good introduction to the richness of dynamical phase transitions and their presence even in the absence of their equilibrium counterparts.

Crucially, therefore, the overview in Sec. 1.5 of the equilibrium properties of the paradigmatic long-range power-law-interacting ($\sim 1/r^\alpha$ with r inter-spin distance) transverse field Ising model (LR-TFIM) would be in order. The LR-TFIM is nonintegrable, and thus not solvable exactly, for finite $\alpha > 0$, and we leave that task to t -DMRG in Chapter 3 and the infinite matrix product state (iMPS) technique based on the time-dependent variational principle (TDVP) in Chapter 4. Nevertheless, we consider the exactly-solvable limits of the fully-connected transverse-field Ising model (FC-TFIM) for $\alpha = 0$, which is exactly solved using mean-field theory, and the nearest-neighbor transverse-field Ising model (NN-TFIM) for $\alpha \rightarrow \infty$, which is exactly solved using a Jordan-Wigner transformation. We construct the phase diagrams of these two models, discuss what is known from perturbative renormalization group for the nonintegrable LR-TFIM, and motivate our subsequent work on dynamical phase transitions. In Sec. 1.5 we focus on two main types of dynamical phase transition (DPT) that one attempts to observe in a many-body system after a quench. The first is DPT-I, which is a Landau-type DPT where a proper order parameter is extracted when the system has settled into some sort of a (quasi-)steady state due to (pre)thermalization as a function of quench parameter. We show in Chapter 3 [10] how the DPT-I is related to relaxation properties of the system in addition to its corresponding equilibrium phase diagram, where prethermalization conspires to bring about dynamical order even in the absence of equilibrium finite-temperature order. The second is the DPT-II, which manifests as nonanalytic cusps in the Loschmidt-echo return rate as a function of time. We show in Chapter 4 [11] the existence of a new *anomalous* phase of the DPT-II that had not been found previously.

In Chapter 2 [1] we derive and calculate the dynamical structure factors for several SBMFT ansätze for chiral gapped spin liquids, where we show how time-reversal symmetry is broken due to chirality where the usual six-fold rotational symmetry of the dynamical structure factor reduces to three-fold.

In Chapter 3 [10] we discuss the Landau-type dynamical phase transition in the one-dimensional long-range power-law-interacting transverse-field Ising model, where we show that it qualitatively differs from its equilibrium counterpart, especially in that it persists with short-range interactions when there is no corresponding equilibrium thermal phase transition. We argue this is due to prethermalization giving way to a long-lived quasi-steady state for small quenches that would take extremely long to thermalize.

In Chapter 4 [11] we focus on the Loschmidt-echo dynamical phase transition in the one-dimensional long-range power-law-interacting transverse-field Ising model, where we show that even though it behaves qualitatively similarly to the nearest-neighbor case, for

sufficiently long-range interactions an anomalous phase arises characterized by anomalous nonanalytic cusps that behave differently to the regular cusps already established and discussed in the literature.

In Chapter 5 [9] we take a small detour and try our luck at a Chebyshev-based numerical improvement of time-evolution simulations in t -DMRG. Due to entanglement build-up, t -DMRG cannot realistically go beyond a certain evolution time, and so any attempt in kind of swerving around this limitation is worth the effort. We perform a Chebyshev expansion in the time domain, hoping for a more efficient distribution of the wavefunction entanglement over many Chebyshev vectors that may facilitate access to longer evolution times. We arrive at the conclusion that the Krylov approximation and Suzuki-Trotter decomposition still fare better, with the latter particularly powerful for systems with nearest-neighbor couplings.

In Chapter 6 [8] we turn our attention to the effect of defects on domain-wall melting in the one-dimensional two-species Bose-Hubbard model, which in the large-interaction limit maps onto the XXZ model. We find that the effect of hole defects (i.e. missing bosons) in the initial domain wall on the spatially-resolved magnetization can be removed by a linear combination of spatially-shifted observables. Moreover, for large interactions, the effect of holes can be neglected. However, spin-flip defects (equivalently, presence of a boson of the wrong species one either side of the domain wall) have adverse effects on the domain-wall melting since their dynamics occur on the same time scale as the melting itself, hence suggesting that experimental preparation schemes based on spin flips are best avoided.

In Chapter 7 [7] we study excitations in the tilted one-dimensional Bose-Hubbard model, which in the symmetry-broken phase manifest as domain walls with fractional statistics. An analytic approach is derived that shows the existence of a repulsively-bound state of fractional excitations above a critical center-of-mass momentum, and numerical simulations using t -DMRG support this finding.

We finally conclude with a summary of the main results of this dissertation and the underlying physical concepts in Chapter 8.

1.3 Quantum spin liquids

The overview part of this section is adapted in full from Ref. [1], which we nevertheless decided is important to place here again for the good flow of reading.

The potential to realize interesting quantum spin liquid states with fractionalized excitations and topological order has driven research on frustrated magnets in the last decades [34, 35, 36, 37]. One of the most promising candidate models is the spin-1/2 Heisenberg antiferromagnet on the two-dimensional kagome lattice. Many theoretical attempts have been made to unravel its groundstate properties, which are still not fully understood. While early approaches supported a symmetry broken valence bond solid state [38, 39], various different groundstates have been proposed since. Recent numerical works based on the density matrix renormalization group (DMRG) method provide strong evidence for a gapped \mathbb{Z}_2 spin liquid state [40, 41, 42, 43], whereas projected wavefunction studies favor

a gapless $U(1)$ -Dirac spin liquid groundstate [44, 45, 46], but this issue is not settled yet [47]. Both of these states do not break lattice symmetries and lack conventional long-range magnetic order due to strong quantum fluctuations associated with the frustrated spin-exchange interactions.

The interest in chiral spin liquids, which break time-reversal and parity symmetries, was triggered by Kalmeyer and Laughlin, who proposed that bosonic analogues of fractional quantum Hall states could be realized in frustrated magnets [48]. Within a slave-fermion approach these chiral states are stable phases of matter, because gauge fluctuations are gapped by a Chern-Simons term [49]. More recently, various theoretical works showed that such chiral spin liquids can be stabilized on the kagome lattice either by including further-neighbor interactions or additional terms that explicitly break time-reversal symmetry [50, 51, 52, 53, 54, 55, 56, 57, 58, 59].

As far as experiments are concerned, the mineral Herbertsmithite as well as organic charge transfer salts are the most promising candidate materials to host a spin liquid groundstate [60, 61, 62, 63]. While measurements on the triangular lattice organic salts are consistent with a gapless spin liquid, the kagome lattice compound Herbertsmithite likely has a gapped spin liquid groundstate. Inelastic neutron scattering experiments are compatible with a continuum of fractionalized spinon excitations [64], and recent NMR measurements indicate that the groundstate is gapped [65]. The fact that no sharp onset of the two-spinon continuum was observed in neutron scattering has been attributed to the presence of a flat band of topological vison excitations in gapped \mathbb{Z}_2 spin liquids [66], as well as to the contribution from impurities at low energies [67].

Various different spin liquid states have been proposed as potential groundstates of kagome Heisenberg antiferromagnets. In order to relate theoretical results to inelastic neutron scattering experiments, a better characterization of dynamical structure factors in kagome systems is clearly beneficial. In Chapter 2 we take a step in this direction by computing dynamical spin structure factors of simple chiral spin liquids using Schwinger-boson mean-field theory [2, 3]. Our approach is based on an earlier projective symmetry group classification of time-reversal symmetry breaking mean-field ansätze by Messio, Lhuillier, and Misguich [5]. We show that the dynamical spin structure factor $S(\mathbf{k}, \omega)$ shows clear signatures of time-reversal symmetry breaking, in contrast to static (equal-time) structure factors. In particular, momentum inversion symmetry $\mathbf{k} \rightarrow -\mathbf{k}$ is lost and consequently the six-fold rotation symmetry of $S(\mathbf{k}, \omega)$ around the Γ -point is reduced to three-fold rotations. Moreover, we show that the onset of the two-spinon continuum is rather flat for the *cuboc1* state, which has been argued to minimize the groundstate energy of the kagome Heisenberg antiferromagnet within the Schwinger-boson approach [4]. This particular chiral spin liquid state is a quantum disordered version of the magnetically ordered *cuboc1* state, which is a possible non-coplanar state of the classical AFKM model [68, 69].

It is important to note that this Schwinger-boson construction does not lead to chiral spin liquids of the Kalmeyer-Laughlin type. This is due to the fact that the condensation of boson bilinears reduces the gauge symmetry from $U(1)$ to \mathbb{Z}_2 . Consequently, the effective low energy theory is a Chern-Simons-Higgs theory with a condensed charge-2 Higgs field, the topological properties of which are typically equivalent to \mathbb{Z}_2 gauge theory [70, 71].

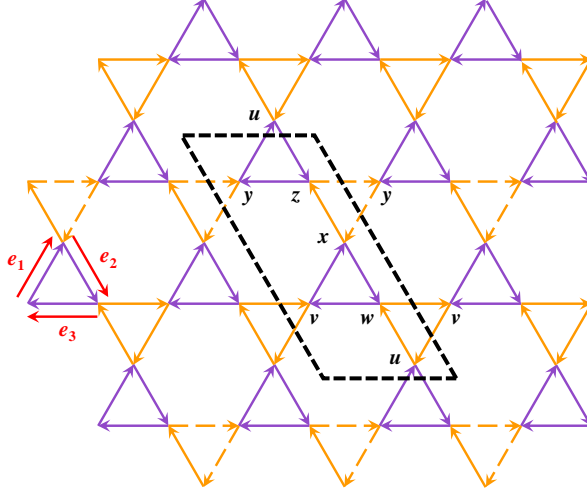


Figure 1.1: (Color online) The six-site unit cell of the general chiral SBMFT ansatz as discussed in Refs. [4] and [5]. The bond operators $\langle \hat{\mathcal{A}}_{lj} \rangle = |\hat{\mathcal{A}}_{lj}| e^{i\theta_{\mathcal{A}}}$ and $\langle \hat{\mathcal{B}}_{lj} \rangle = |\hat{\mathcal{B}}_{lj}| e^{i\theta_{\mathcal{B}}}$ between two neighboring sites l and j are such that at every bond one has $|\hat{\mathcal{A}}_{lj}| = \mathcal{A}$ and $|\hat{\mathcal{B}}_{lj}| = \mathcal{B}$. On purple (dark) bonds $\theta_{\mathcal{A}} = 0$ and $\theta_{\mathcal{B}} = \phi_{\mathcal{B}}$, while on orange (bright) bonds the phases are $\theta_{\mathcal{A}} = \phi_{\mathcal{A}'} + \varphi$ and $\theta_{\mathcal{B}} = \phi_{\mathcal{B}'} + \varphi$ with $\varphi = 0$ on undashed bonds and $\varphi = p_1\pi$ on dashed bonds, where $p_1 \in \{0, 1\}$ depending on the ansatz. Finally, the red arrows indicate the real-space vectors $\mathbf{e}_1 = a(1/2, \sqrt{3}/2)$, $\mathbf{e}_2 = a(1/2, -\sqrt{3}/2)$, and $\mathbf{e}_3 = a(-1, 0)$, with a the spacing between two neighboring sites, and $k_j = \mathbf{k} \cdot \mathbf{e}_j$. Figure adapted from Ref. [1].

In the remainder of this section we include the detailed derivation of the mean-field decoupling of the antiferromagnetic Heisenberg Hamiltonian on the kagome lattice within the framework of SBMFT, and calculate the free energy for several mean-field ansätze, including chiral ones. We believe this would be of use to students working on similar problems especially that a rigorous presentation of this derivation is hard to find in the literature.

1.3.1 Free energy for the $(\mathcal{A}, \mathcal{B})$ -ansätze

The antiferromagnetic Heisenberg model is described by the Hamiltonian

$$\hat{H} = J \sum_{\langle lj \rangle} \hat{\mathbf{S}}_l \cdot \hat{\mathbf{S}}_j, \quad (1.4)$$

where $J > 0$ (antiferromagnetic) and $\hat{\mathbf{S}}_l$ is the spin operator on site l . The Schwinger-boson representation of $\hat{\mathbf{S}}_l$ is given by

$$\hat{\mathbf{S}}_l = \frac{1}{2} \hat{b}_{l\alpha}^\dagger \hat{\sigma}_{\alpha\beta} \hat{b}_{l\beta}, \quad (1.5)$$

where we employ the summation convention over Greek letters, and $\hat{b}_{l\alpha}$ is a bosonic annihilation operator of spin α on site l , and hence these operators satisfy the commutation algebra

$$\left[\hat{b}_{l\alpha}, \hat{b}_{j\beta}^\dagger \right] = \delta_{lj} \delta_{\alpha\beta}, \quad (1.6)$$

$$\left[\hat{b}_{l\alpha}, \hat{b}_{j\beta} \right] = 0. \quad (1.7)$$

Moreover, the number of particles on a site is restricted to $2S$, with S being the length of the spin:

$$\hat{n}_l = \hat{b}_{l\alpha}^\dagger \hat{b}_{l\alpha} = 2S. \quad (1.8)$$

Here we see a very strong advantage of employing the Schwinger-boson mean-field theory (SBMFT), where the spin length S is treated as a continuous variable. In the large-spin-length limit $S \rightarrow \infty$, the system can be treated purely classically and long-range order is expected. On the other hand, in the small-spin-length limit ($S \leq 1/2$), we arrive at a spin-liquid phase where quantum fluctuations are prominent. This renders our Hamiltonian in the form

$$\begin{aligned} \hat{H} &= \frac{J}{4} \sum_{\langle lj \rangle} \hat{b}_{l\alpha}^\dagger \hat{\sigma}_{\alpha\beta} \hat{b}_{l\beta} \cdot \hat{b}_{j\gamma}^\dagger \hat{\sigma}_{\gamma\mu} \hat{b}_{j\mu} + \lambda \sum_j (\hat{n}_j - 2S) \\ &= \frac{J}{4} \sum_{\langle lj \rangle} (2\delta_{\alpha\mu} \delta_{\beta\gamma} - \delta_{\alpha\beta} \delta_{\gamma\mu}) \hat{b}_{l\alpha}^\dagger \hat{b}_{l\beta} \hat{b}_{j\gamma}^\dagger \hat{b}_{j\mu} + \lambda \sum_j (\hat{n}_j - 2S), \end{aligned} \quad (1.9)$$

where λ denotes the Lagrange multiplier that restricts the total number of Schwinger bosons per site to $2S$. We now introduce the bond operators

$$\hat{\mathcal{A}}_{lj} = \frac{1}{2} \epsilon^{\alpha\beta} \hat{b}_{l\alpha} \hat{b}_{j\beta}, \quad (1.10)$$

$$\hat{\mathcal{B}}_{lj} = \frac{1}{2} \hat{b}_{l\alpha}^\dagger \hat{b}_{j\alpha}, \quad (1.11)$$

where again we adopt a summation convention over Greek symbols, and $\epsilon^{\alpha\beta}$ is the fully antisymmetric tensor of $SU(2)$. One can show that $\hat{\mathbf{S}}_l \cdot \hat{\mathbf{S}}_j = \left(\hat{\mathcal{B}}_{lj}^\dagger \hat{\mathcal{B}}_{lj} - \hat{\mathcal{A}}_{lj}^\dagger \hat{\mathcal{A}}_{lj} \right) - \hat{n}_j/4$. Neglecting the constant terms $-\hat{n}_j/4$, we can rewrite our Hamiltonian as

$$\hat{H} = J \sum_{\langle lj \rangle} \left(\hat{\mathcal{B}}_{lj}^\dagger \hat{\mathcal{B}}_{lj} - \hat{\mathcal{A}}_{lj}^\dagger \hat{\mathcal{A}}_{lj} \right) + \lambda \sum_j (\hat{n}_j - 2S). \quad (1.12)$$

We now apply a mean-field theory in the bond operators such that

$$\left(\hat{\mathcal{A}}_{lj}^\dagger - \langle \hat{\mathcal{A}}_{lj}^\dagger \rangle\right) \left(\hat{\mathcal{A}}_{lj} - \langle \hat{\mathcal{A}}_{lj} \rangle\right) \approx 0, \quad (1.13)$$

$$\left(\hat{\mathcal{B}}_{lj}^\dagger - \langle \hat{\mathcal{B}}_{lj}^\dagger \rangle\right) \left(\hat{\mathcal{B}}_{lj} - \langle \hat{\mathcal{B}}_{lj} \rangle\right) \approx 0, \quad (1.14)$$

resulting in the mean-field Hamiltonian

$$\begin{aligned} \hat{H}_{\text{MF}} = & J \sum_{\langle lj \rangle} \left(\langle \hat{\mathcal{B}}_{lj} \rangle \hat{\mathcal{B}}_{lj}^\dagger + \langle \hat{\mathcal{B}}_{lj}^\dagger \rangle \hat{\mathcal{B}}_{lj} - \langle \hat{\mathcal{A}}_{lj} \rangle \hat{\mathcal{A}}_{lj}^\dagger - \langle \hat{\mathcal{A}}_{lj}^\dagger \rangle \hat{\mathcal{A}}_{lj} \right) \\ & + J \sum_{\langle lj \rangle} \left(\langle \hat{\mathcal{A}}_{lj}^\dagger \rangle \langle \hat{\mathcal{A}}_{lj} \rangle - \langle \hat{\mathcal{B}}_{lj}^\dagger \rangle \langle \hat{\mathcal{B}}_{lj} \rangle \right) + \lambda \sum_j (\hat{n}_j - 2S). \end{aligned} \quad (1.15)$$

We now seek to diagonalize this Hamiltonian, but first let us settle on definitions. The Fourier transform of a ladder operator is given by

$$\hat{b}_{l\alpha}^s = \frac{1}{\sqrt{N_{\mathbf{q}}}} \sum_{\mathbf{q}} \hat{b}_{\mathbf{q}\alpha}^s e^{i\mathbf{q}\cdot\mathbf{r}_l}, \quad (1.16)$$

$$\hat{b}_{l\alpha}^{s\dagger} = \frac{1}{\sqrt{N_{\mathbf{q}}}} \sum_{\mathbf{q}} \hat{b}_{\mathbf{q}\alpha}^{s\dagger} e^{-i\mathbf{q}\cdot\mathbf{r}_l}, \quad (1.17)$$

where the symbol s makes explicit what the band is on site l , and $N_{\mathbf{q}}$ is what is often referred to as a volume, but is in fact the number of \mathbf{q} -points summed over in the Fourier transforms above. Furthermore, we will switch from a summation over sites $\langle lj \rangle$, to a summation over unit cells $\langle mn \rangle$, while explicitly expressing all the bond terms within one unit cell. Before we do that, we remind ourselves of the mean-field parameters

$$\langle \hat{\mathcal{B}}_{lj} \rangle = \langle \hat{\mathcal{B}}_{lj}^\dagger \rangle^* = |\hat{\mathcal{B}}_{lj}| e^{i\theta_{\mathcal{B}}}, \quad (1.18)$$

$$\langle \hat{\mathcal{A}}_{lj} \rangle = \langle \hat{\mathcal{A}}_{lj}^\dagger \rangle^* = |\hat{\mathcal{A}}_{lj}| e^{i\theta_{\mathcal{A}}}, \quad (1.19)$$

where $|\hat{\mathcal{B}}_{lj}| = \mathcal{B}$ and $|\hat{\mathcal{A}}_{lj}| = \mathcal{A}$ are the same for each bond, but the phases $\theta_{\mathcal{B}}$ and $\theta_{\mathcal{A}}$ are bond-dependent. Following a chiral ansatz, and following Messio's notation, the Hamiltonian, when summing over unit cells, reads:

$$\begin{aligned}
\hat{H}_{\text{MF}} &= J \sum_{\langle lj \rangle} \left(\langle \hat{\mathcal{B}}_{lj} \rangle \hat{\mathcal{B}}_{lj}^\dagger - \langle \hat{\mathcal{A}}_{lj} \rangle \hat{\mathcal{A}}_{lj}^\dagger + \text{H.c.} \right) \\
&\quad + J \sum_{\langle lj \rangle} \left(\langle \hat{\mathcal{A}}_{lj}^\dagger \rangle \langle \hat{\mathcal{A}}_{lj} \rangle - \langle \hat{\mathcal{B}}_{lj}^\dagger \rangle \langle \hat{\mathcal{B}}_{lj} \rangle \right) + \lambda \sum_j (\hat{n}_j - 2S) \\
&= J \sum_{\langle mn \rangle} \left\{ \mathcal{B} e^{i\phi_{\mathcal{B}}} \left[\hat{\mathcal{B}}_{uv}^\dagger + \hat{\mathcal{B}}_{vw}^\dagger + \hat{\mathcal{B}}_{wu}^\dagger + \hat{\mathcal{B}}_{zx}^\dagger + \left(\hat{\mathcal{B}}_{xy}^\dagger + \hat{\mathcal{B}}_{yz}^\dagger \right) e^{ip_1\pi} \right]_{(m,n),\text{red}} \right. \\
&\quad + \mathcal{B} e^{i\phi_{\mathcal{B}}} \left[\hat{\mathcal{B}}_{xv}^\dagger + \hat{\mathcal{B}}_{vw}^\dagger + \hat{\mathcal{B}}_{wx}^\dagger + \hat{\mathcal{B}}_{zu}^\dagger + \hat{\mathcal{B}}_{uy}^\dagger + \hat{\mathcal{B}}_{yz}^\dagger \right]_{(m,n),\text{blue}} \\
&\quad - \mathcal{A} e^{i\phi_{\mathcal{A}}} \left[\hat{\mathcal{A}}_{uv}^\dagger + \hat{\mathcal{A}}_{vw}^\dagger + \hat{\mathcal{A}}_{wu}^\dagger + \hat{\mathcal{A}}_{zx}^\dagger + \left(\hat{\mathcal{A}}_{xy}^\dagger + \hat{\mathcal{A}}_{yz}^\dagger \right) e^{ip_1\pi} \right]_{(m,n),\text{red}} \\
&\quad \left. - \mathcal{A} \left[\hat{\mathcal{A}}_{xv}^\dagger + \hat{\mathcal{A}}_{vw}^\dagger + \hat{\mathcal{A}}_{wx}^\dagger + \hat{\mathcal{A}}_{zu}^\dagger + \hat{\mathcal{A}}_{uy}^\dagger + \hat{\mathcal{A}}_{yz}^\dagger \right]_{(m,n),\text{blue}} + \text{H.c.} \right\} \\
&\quad + \lambda \sum_{\langle mn \rangle} (\hat{n}_u + \hat{n}_v + \hat{n}_w + \hat{n}_x + \hat{n}_y + \hat{n}_z)_{(m,n)} \\
&\quad + 2JN_s (|\mathcal{A}|^2 - |\mathcal{B}|^2) - \lambda N_s 2S, \tag{1.20}
\end{aligned}$$

with N_s being the total number of sites on the Kagome lattice. Note that here even though we represent bond operators in \hat{H}_{MF} with no explicit dependence on the unit cell position (m, n) , they are in fact very much dependent on the unit cell position, otherwise, we would be miscounting bonds. As such, for ease of notation, we introduce the subscript (m, n) after every term that depends on the unit cell position in \hat{H}_{MF} .

Now if we recall $N_{\mathbf{q}}$ from our definitions of the Fourier transforms, it would be useful to relate it to N_s , as this is convenient when we proceed with the free energy minimization (self-consistent determination of the mean-field parameters). Here, each site on the unit-cell has the same periodicity as the unit cell itself on the Kagome lattice. This means, that the (first) Brillouin zone (or the Wigner-Seitz primitive cell containing $\mathbf{q} = \mathbf{0}$ in reciprocal space - the other Wigner-Seitz unit cells are not Brillouin zones) will contain the same number of momenta points as there are unit cells in the Kagome lattice, and, as such, we now know that if we choose to integrate over the first Brillouin zone, then we have $N_s = 6N_{\mathbf{q}}$, as we have six independent sites per unit cell and $N_{\mathbf{q}}$ is the number of unit cells in this case.

We now proceed with expressing H_{MF} in momentum space:

$$\begin{aligned}
\hat{H}_{\text{MF}} &= \frac{J}{2} \sum_{\langle mn \rangle} \left\{ \mathcal{B} e^{i\phi_{\mathcal{B}}} \left[\hat{b}_{u\alpha} \hat{b}_{v\alpha}^\dagger + \hat{b}_{v\alpha} \hat{b}_{w\alpha}^\dagger + \hat{b}_{w\alpha} \hat{b}_{u\alpha}^\dagger + \hat{b}_{z\alpha} \hat{b}_{x\alpha}^\dagger + \left(\hat{b}_{x\alpha} \hat{b}_{y\alpha}^\dagger + \hat{b}_{y\alpha} \hat{b}_{z\alpha}^\dagger \right) e^{ip_1\pi} \right]_{(m,n),\text{red}} \right. \\
&\quad + \mathcal{B} e^{i\phi_{\mathcal{B}}} \left[\hat{b}_{x\alpha} \hat{b}_{v\alpha}^\dagger + \hat{b}_{v\alpha} \hat{b}_{w\alpha}^\dagger + \hat{b}_{w\alpha} \hat{b}_{x\alpha}^\dagger + \hat{b}_{z\alpha} \hat{b}_{u\alpha}^\dagger + \hat{b}_{u\alpha} \hat{b}_{y\alpha}^\dagger + \hat{b}_{y\alpha} \hat{b}_{z\alpha}^\dagger \right]_{(m,n),\text{blue}} \\
&\quad - \mathcal{A} e^{i\phi_{\mathcal{A}}} \varepsilon^{\alpha\beta} \left[\hat{b}_{u\alpha}^\dagger \hat{b}_{v\beta}^\dagger + \hat{b}_{v\alpha}^\dagger \hat{b}_{w\beta}^\dagger + \hat{b}_{w\alpha}^\dagger \hat{b}_{u\beta}^\dagger + \hat{b}_{z\alpha}^\dagger \hat{b}_{x\beta}^\dagger + \left(\hat{b}_{x\alpha}^\dagger \hat{b}_{y\beta}^\dagger + \hat{b}_{y\alpha}^\dagger \hat{b}_{z\beta}^\dagger \right) e^{ip_1\pi} \right]_{(m,n),\text{red}} \\
&\quad - \mathcal{A} \varepsilon^{\alpha\beta} \left[\hat{b}_{x\alpha}^\dagger \hat{b}_{v\beta}^\dagger + \hat{b}_{v\alpha}^\dagger \hat{b}_{w\beta}^\dagger + \hat{b}_{w\alpha}^\dagger \hat{b}_{x\beta}^\dagger + \hat{b}_{z\alpha}^\dagger \hat{b}_{u\beta}^\dagger + \hat{b}_{u\alpha}^\dagger \hat{b}_{y\beta}^\dagger + \hat{b}_{y\alpha}^\dagger \hat{b}_{z\beta}^\dagger \right]_{(m,n),\text{blue}} + \text{H.c.} \left. \right\} \\
&\quad + \lambda \sum_{\langle mn \rangle} \left(\hat{b}_{u\alpha}^\dagger \hat{b}_{u\alpha} + \hat{b}_{v\alpha}^\dagger \hat{b}_{v\alpha} + \hat{b}_{w\alpha}^\dagger \hat{b}_{w\alpha} + \hat{b}_{x\alpha}^\dagger \hat{b}_{x\alpha} + \hat{b}_{y\alpha}^\dagger \hat{b}_{y\alpha} + \hat{b}_{z\alpha}^\dagger \hat{b}_{z\alpha} \right)_{(m,n)} \\
&\quad + 2JN_s (|\mathcal{A}|^2 - |\mathcal{B}|^2) - \lambda N_s 2S \\
&= \frac{JN_s}{12N_{\mathbf{k}}} \sum_{\mathbf{k}} \left\{ \mathcal{B} e^{i\phi_{\mathcal{B}}} \left[\hat{b}_{\mathbf{k}\alpha}^u \hat{b}_{\mathbf{k}\alpha}^{v\dagger} e^{-ik_1} + \hat{b}_{\mathbf{k}\alpha}^v \hat{b}_{\mathbf{k}\alpha}^{w\dagger} e^{-ik_3} + \hat{b}_{\mathbf{k}\alpha}^w \hat{b}_{\mathbf{k}\alpha}^{u\dagger} e^{-ik_2} + \hat{b}_{\mathbf{k}\alpha}^z \hat{b}_{\mathbf{k}\alpha}^{x\dagger} e^{-ik_2} \right. \right. \\
&\quad + \left. \left(\hat{b}_{\mathbf{k}\alpha}^x \hat{b}_{\mathbf{k}\alpha}^{y\dagger} e^{-ik_1} + \hat{b}_{\mathbf{k}\alpha}^y \hat{b}_{\mathbf{k}\alpha}^{z\dagger} e^{-ik_3} \right) e^{ip_1\pi} \right] \\
&\quad + \mathcal{B} e^{i\phi_{\mathcal{B}}} \left[\hat{b}_{\mathbf{k}\alpha}^x \hat{b}_{\mathbf{k}\alpha}^{v\dagger} e^{ik_1} + \hat{b}_{\mathbf{k}\alpha}^v \hat{b}_{\mathbf{k}\alpha}^{w\dagger} e^{ik_3} + \hat{b}_{\mathbf{k}\alpha}^w \hat{b}_{\mathbf{k}\alpha}^{x\dagger} e^{ik_2} + \hat{b}_{\mathbf{k}\alpha}^z \hat{b}_{\mathbf{k}\alpha}^{u\dagger} e^{ik_2} + \hat{b}_{\mathbf{k}\alpha}^u \hat{b}_{\mathbf{k}\alpha}^{y\dagger} e^{ik_1} + \hat{b}_{\mathbf{k}\alpha}^y \hat{b}_{\mathbf{k}\alpha}^{z\dagger} e^{ik_3} \right] \\
&\quad - \mathcal{A} e^{i\phi_{\mathcal{A}}} \varepsilon^{\alpha\beta} \left[\hat{b}_{\mathbf{k}\alpha}^{u\dagger} \hat{b}_{-\mathbf{k}\beta}^{v\dagger} e^{ik_1} + \hat{b}_{\mathbf{k}\alpha}^{v\dagger} \hat{b}_{-\mathbf{k}\beta}^{w\dagger} e^{ik_3} + \hat{b}_{\mathbf{k}\alpha}^{w\dagger} \hat{b}_{-\mathbf{k}\beta}^{u\dagger} e^{ik_2} + \hat{b}_{\mathbf{k}\alpha}^{z\dagger} \hat{b}_{-\mathbf{k}\beta}^{x\dagger} e^{ik_2} \right. \\
&\quad + \left. \left(\hat{b}_{\mathbf{k}\alpha}^{x\dagger} \hat{b}_{-\mathbf{k}\beta}^{y\dagger} e^{ik_1} + \hat{b}_{\mathbf{k}\alpha}^{y\dagger} \hat{b}_{-\mathbf{k}\beta}^{z\dagger} e^{ik_3} \right) e^{ip_1\pi} \right] \\
&\quad - \mathcal{A} \varepsilon^{\alpha\beta} \left[\hat{b}_{\mathbf{k}\alpha}^{x\dagger} \hat{b}_{-\mathbf{k}\beta}^{v\dagger} e^{-ik_1} + \hat{b}_{\mathbf{k}\alpha}^{v\dagger} \hat{b}_{-\mathbf{k}\beta}^{w\dagger} e^{-ik_3} + \hat{b}_{\mathbf{k}\alpha}^{w\dagger} \hat{b}_{-\mathbf{k}\beta}^{x\dagger} e^{-ik_2} + \hat{b}_{\mathbf{k}\alpha}^{z\dagger} \hat{b}_{-\mathbf{k}\beta}^{u\dagger} e^{-ik_2} \right. \\
&\quad + \left. \hat{b}_{\mathbf{k}\alpha}^{u\dagger} \hat{b}_{-\mathbf{k}\beta}^{y\dagger} e^{-ik_1} + \hat{b}_{\mathbf{k}\alpha}^{y\dagger} \hat{b}_{-\mathbf{k}\beta}^{z\dagger} e^{-ik_3} \right] + \text{H.c.} \left. \right\} \\
&\quad + \frac{\lambda N_s}{6N_{\mathbf{k}}} \sum_{\mathbf{k}} \left(\hat{b}_{\mathbf{k}\alpha}^{u\dagger} \hat{b}_{\mathbf{k}\alpha}^u + \hat{b}_{\mathbf{k}\alpha}^{v\dagger} \hat{b}_{\mathbf{k}\alpha}^v + \hat{b}_{\mathbf{k}\alpha}^{w\dagger} \hat{b}_{\mathbf{k}\alpha}^w + \hat{b}_{\mathbf{k}\alpha}^{x\dagger} \hat{b}_{\mathbf{k}\alpha}^x + \hat{b}_{\mathbf{k}\alpha}^{y\dagger} \hat{b}_{\mathbf{k}\alpha}^y + \hat{b}_{\mathbf{k}\alpha}^{z\dagger} \hat{b}_{\mathbf{k}\alpha}^z \right) \\
&\quad + 2JN_s (|\mathcal{A}|^2 - |\mathcal{B}|^2) - \lambda N_s 2S, \tag{1.21}
\end{aligned}$$

where we made use of the relation $\sum_{\langle mn \rangle} e^{\pm i(\mathbf{k} \pm \mathbf{q}) \cdot (m\mathbf{R}_1 + n\mathbf{R}_2)} = (N_s/6) \delta_{\mathbf{k}, \mp \mathbf{q}}$, and we denote $k_j = \mathbf{k} \cdot \mathbf{e}_j$, with $j = 1, 2, 3$ and $\mathbf{e}_1 = a(1/2, \sqrt{3}/2)^\top$, $\mathbf{e}_2 = a(1/2, -\sqrt{3}/2)^\top$, and $\mathbf{e}_3 = a(-1, 0)^\top$ with a the spacing between two adjacent sites. Note that here the prefactor to the Kronecker delta function is the number of unit cells $N_s/6$ and not the number of the sites N_s , and this is because if we set $\mathbf{k} \pm \mathbf{q} = 0$, the series is simply a count of the number of unit cells in position space on the Kagome lattice. This makes sense as the periodicity of each band coincides with that of the unit cells in position space, rather than with the sites. We now rearrange terms:

$$\begin{aligned}
& \frac{\lambda N_s}{6N_{\mathbf{k}}} \sum_{\mathbf{k}} \left(\hat{b}_{\mathbf{k}\alpha}^{u\dagger} \hat{b}_{\mathbf{k}\alpha}^u + \hat{b}_{\mathbf{k}\alpha}^{v\dagger} \hat{b}_{\mathbf{k}\alpha}^v + \hat{b}_{\mathbf{k}\alpha}^{w\dagger} \hat{b}_{\mathbf{k}\alpha}^w + \hat{b}_{\mathbf{k}\alpha}^{x\dagger} \hat{b}_{\mathbf{k}\alpha}^x + \hat{b}_{\mathbf{k}\alpha}^{y\dagger} \hat{b}_{\mathbf{k}\alpha}^y + \hat{b}_{\mathbf{k}\alpha}^{z\dagger} \hat{b}_{\mathbf{k}\alpha}^z \right) \\
&= \frac{\lambda N_s}{6N_{\mathbf{k}}} \sum_{\mathbf{k}} \left(\hat{b}_{\mathbf{k}\uparrow}^{u\dagger} \hat{b}_{\mathbf{k}\uparrow}^u + \hat{b}_{\mathbf{k}\uparrow}^{v\dagger} \hat{b}_{\mathbf{k}\uparrow}^v + \hat{b}_{\mathbf{k}\uparrow}^{w\dagger} \hat{b}_{\mathbf{k}\uparrow}^w + \hat{b}_{\mathbf{k}\uparrow}^{x\dagger} \hat{b}_{\mathbf{k}\uparrow}^x + \hat{b}_{\mathbf{k}\uparrow}^{y\dagger} \hat{b}_{\mathbf{k}\uparrow}^y + \hat{b}_{\mathbf{k}\uparrow}^{z\dagger} \hat{b}_{\mathbf{k}\uparrow}^z + \right. \\
&\quad \left. + \hat{b}_{-\mathbf{k}\downarrow}^{u\dagger} \hat{b}_{-\mathbf{k}\downarrow}^u + \hat{b}_{-\mathbf{k}\downarrow}^{v\dagger} \hat{b}_{-\mathbf{k}\downarrow}^v + \hat{b}_{-\mathbf{k}\downarrow}^{w\dagger} \hat{b}_{-\mathbf{k}\downarrow}^w + \hat{b}_{-\mathbf{k}\downarrow}^{x\dagger} \hat{b}_{-\mathbf{k}\downarrow}^x + \hat{b}_{-\mathbf{k}\downarrow}^{y\dagger} \hat{b}_{-\mathbf{k}\downarrow}^y + \hat{b}_{-\mathbf{k}\downarrow}^{z\dagger} \hat{b}_{-\mathbf{k}\downarrow}^z \right) \\
&= \frac{\lambda N_s}{6N_{\mathbf{k}}} \sum_{\mathbf{k}} \left(\hat{b}_{\mathbf{k}\uparrow}^{u\dagger} \hat{b}_{\mathbf{k}\uparrow}^u + \hat{b}_{\mathbf{k}\uparrow}^{v\dagger} \hat{b}_{\mathbf{k}\uparrow}^v + \hat{b}_{\mathbf{k}\uparrow}^{w\dagger} \hat{b}_{\mathbf{k}\uparrow}^w + \hat{b}_{\mathbf{k}\uparrow}^{x\dagger} \hat{b}_{\mathbf{k}\uparrow}^x + \hat{b}_{\mathbf{k}\uparrow}^{y\dagger} \hat{b}_{\mathbf{k}\uparrow}^y + \hat{b}_{\mathbf{k}\uparrow}^{z\dagger} \hat{b}_{\mathbf{k}\uparrow}^z + \right. \\
&\quad \left. + \hat{b}_{-\mathbf{k}\downarrow}^u \hat{b}_{-\mathbf{k}\downarrow}^{u\dagger} + \hat{b}_{-\mathbf{k}\downarrow}^v \hat{b}_{-\mathbf{k}\downarrow}^{v\dagger} + \hat{b}_{-\mathbf{k}\downarrow}^w \hat{b}_{-\mathbf{k}\downarrow}^{w\dagger} + \hat{b}_{-\mathbf{k}\downarrow}^x \hat{b}_{-\mathbf{k}\downarrow}^{x\dagger} + \hat{b}_{-\mathbf{k}\downarrow}^y \hat{b}_{-\mathbf{k}\downarrow}^{y\dagger} + \hat{b}_{-\mathbf{k}\downarrow}^z \hat{b}_{-\mathbf{k}\downarrow}^{z\dagger} - 6 \right) \\
&= \frac{\lambda N_s}{6N_{\mathbf{k}}} \sum_{\mathbf{k}} \left(\hat{b}_{\mathbf{k}\uparrow}^{u\dagger} \hat{b}_{\mathbf{k}\uparrow}^u + \hat{b}_{\mathbf{k}\uparrow}^{v\dagger} \hat{b}_{\mathbf{k}\uparrow}^v + \hat{b}_{\mathbf{k}\uparrow}^{w\dagger} \hat{b}_{\mathbf{k}\uparrow}^w + \hat{b}_{\mathbf{k}\uparrow}^{x\dagger} \hat{b}_{\mathbf{k}\uparrow}^x + \hat{b}_{\mathbf{k}\uparrow}^{y\dagger} \hat{b}_{\mathbf{k}\uparrow}^y + \hat{b}_{\mathbf{k}\uparrow}^{z\dagger} \hat{b}_{\mathbf{k}\uparrow}^z + \right. \\
&\quad \left. + \hat{b}_{-\mathbf{k}\downarrow}^u \hat{b}_{-\mathbf{k}\downarrow}^{u\dagger} + \hat{b}_{-\mathbf{k}\downarrow}^v \hat{b}_{-\mathbf{k}\downarrow}^{v\dagger} + \hat{b}_{-\mathbf{k}\downarrow}^w \hat{b}_{-\mathbf{k}\downarrow}^{w\dagger} + \hat{b}_{-\mathbf{k}\downarrow}^x \hat{b}_{-\mathbf{k}\downarrow}^{x\dagger} + \hat{b}_{-\mathbf{k}\downarrow}^y \hat{b}_{-\mathbf{k}\downarrow}^{y\dagger} + \hat{b}_{-\mathbf{k}\downarrow}^z \hat{b}_{-\mathbf{k}\downarrow}^{z\dagger} \right) - \lambda N_s. \quad (1.22)
\end{aligned}$$

As such, our per-site mean-field Hamiltonian is

$$\frac{\hat{H}_{\text{MF}}}{N_s} = \frac{1}{6N_{\mathbf{k}}} \sum_{\mathbf{k}} \Psi_{\mathbf{k}}^\dagger \hat{\mathbf{D}}_{\mathbf{k}} \Psi_{\mathbf{k}} + 2J (|\mathcal{A}|^2 - |\mathcal{B}|^2) - \lambda(1 + 2S), \quad (1.23)$$

where we have introduced the spinor

$$\Psi = \begin{pmatrix} \hat{b}_{\mathbf{k}\uparrow}^u \\ \hat{b}_{\mathbf{k}\uparrow}^v \\ \hat{b}_{\mathbf{k}\uparrow}^w \\ \hat{b}_{\mathbf{k}\uparrow}^x \\ \hat{b}_{\mathbf{k}\uparrow}^y \\ \hat{b}_{\mathbf{k}\uparrow}^z \\ \hat{b}_{-\mathbf{k}\downarrow}^{u\dagger} \\ \hat{b}_{-\mathbf{k}\downarrow}^{v\dagger} \\ \hat{b}_{-\mathbf{k}\downarrow}^{w\dagger} \\ \hat{b}_{-\mathbf{k}\downarrow}^{x\dagger} \\ \hat{b}_{-\mathbf{k}\downarrow}^{y\dagger} \\ \hat{b}_{-\mathbf{k}\downarrow}^{z\dagger} \end{pmatrix}, \quad (1.24)$$

and $\hat{\mathbf{D}}_{\mathbf{k}}$ is the Hermitian matrix

$$D_{\mathbf{k}} = \lambda \mathbb{1}_{12} + C_{\mathbf{k}}, \quad (1.25)$$

with $\mathbb{1}_d$ the $d \times d$ identity matrix, and

$$C_{\mathbf{k}} = \frac{J}{2} \begin{pmatrix} R_{\mathbf{k}}(\phi_{\mathcal{B}'}) & T_{\mathbf{k}} & P_{\mathbf{k}}(\phi_{\mathcal{A}'}) & Q_{\mathbf{k}} \\ T_{\mathbf{k}}^\dagger & R_{\mathbf{k}}(\phi_{\mathcal{B}'} + p_1\pi) & Q_{\mathbf{k}} & P_{\mathbf{k}}(\phi_{\mathcal{A}'} + p_1\pi) \\ P_{\mathbf{k}}^\dagger(\phi_{\mathcal{A}'}) & Q_{\mathbf{k}}^\dagger & R_{-\mathbf{k}}^*(\phi_{\mathcal{B}'}) & T_{-\mathbf{k}}^* \\ Q_{\mathbf{k}}^\dagger & P_{\mathbf{k}}^\dagger(\phi_{\mathcal{A}'} + p_1\pi) & T_{-\mathbf{k}}^\dagger & R_{-\mathbf{k}}^*(\phi_{\mathcal{B}'} + p_1\pi) \end{pmatrix}, \quad (1.26)$$

$$R_{\mathbf{k}}(\nu) = \mathcal{B} \begin{pmatrix} 0 & e^{-i(\nu-k_1)} & e^{i(\phi_{\mathcal{B}'}-k_2)} \\ e^{i(\nu-k_1)} & 0 & e^{-i(\nu-k_3)} + e^{-i(\phi_{\mathcal{B}}+k_3)} \\ e^{-i(\phi_{\mathcal{B}'}-k_2)} & e^{i(\nu-k_3)} + e^{i(\phi_{\mathcal{B}}+k_3)} & 0 \end{pmatrix}, \quad (1.27)$$

$$T_{\mathbf{k}} = \mathcal{B} \begin{pmatrix} 0 & e^{-i(\phi_{\mathcal{B}}+k_1)} & e^{i(\phi_{\mathcal{B}}+k_2)} \\ e^{i(\phi_{\mathcal{B}}+k_1)} & 0 & 0 \\ e^{-i(\phi_{\mathcal{B}}+k_2)} & 0 & 0 \end{pmatrix}, \quad (1.28)$$

$$P_{\mathbf{k}}(\nu) = \mathcal{A} \begin{pmatrix} 0 & -e^{i(\nu+k_1)} & e^{i(\phi_{\mathcal{A}'}-k_2)} \\ e^{i(\nu-k_1)} & 0 & -e^{i(\nu+k_3)} - e^{-ik_3} \\ -e^{i(\phi_{\mathcal{A}'}+k_2)} & e^{i(\nu-k_3)} + e^{ik_3} & 0 \end{pmatrix}, \quad (1.29)$$

$$Q_{\mathbf{k}} = \mathcal{A} \begin{pmatrix} 0 & -e^{-ik_1} & e^{ik_2} \\ e^{ik_1} & 0 & 0 \\ -e^{-ik_2} & 0 & 0 \end{pmatrix}. \quad (1.30)$$

Upon a Bogoliubov transformation (see Ref. [1]), we obtain the eigenvalues $[\epsilon_{\mathbf{k}\uparrow}, -\epsilon_{-\mathbf{k}\downarrow}]$ of the matrix $\tau^6 \hat{\mathbf{D}}$, where

$$\tau^d = \begin{pmatrix} \mathbb{1}_d & 0_d \\ 0_d & -\mathbb{1}_d \end{pmatrix}, \quad (1.31)$$

and 0_d is the $d \times d$ zero matrix. The free energy per site is then

$$\frac{E_{\text{MF}}}{N_s} = \frac{1}{6N_{\mathbf{k}}} \sum_{\mathbf{k},s} \epsilon_{\mathbf{k}\uparrow}^s + 2J(|A|^2 - |B|^2) - \lambda(1 + 2S), \quad (1.32)$$

where here s denotes the band. Note that due to rotational symmetry, we have $\epsilon_{\mathbf{k}\uparrow}^s = \epsilon_{\mathbf{k}\downarrow}^s$, but there is no reflection symmetry due to the chirality, and this means that we no longer have $\epsilon_{\mathbf{k}\uparrow}^s = \epsilon_{-\mathbf{k}\downarrow}^s$.

1.3.2 Free energy for the Q -ansätze

We know that

$$\begin{aligned}
\hat{H} &= J \sum_{\langle lj \rangle} \hat{\mathbf{S}}_l \cdot \hat{\mathbf{S}}_j \\
&= \frac{J}{4} \sum_{\langle lj \rangle} \hat{b}_{l\alpha}^\dagger \hat{\sigma}_{\alpha\beta} \hat{b}_{l\beta} \cdot \hat{b}_{j\gamma}^\dagger \hat{\sigma}_{\gamma\mu} \hat{b}_{j\mu} \\
&= \frac{J}{4} \sum_{\langle lj \rangle} (2\delta_{\alpha\mu}\delta_{\beta\gamma} - \delta_{\alpha\beta}\delta_{\gamma\mu}) \hat{b}_{l\alpha}^\dagger \hat{b}_{l\beta} \hat{b}_{j\gamma}^\dagger \hat{b}_{j\mu}.
\end{aligned} \tag{1.33}$$

We introduce the Schwinger-boson bond operator

$$\hat{Q}_{lj} = \frac{1}{2} \varepsilon^{\alpha\beta} \hat{b}_{l\alpha} \hat{b}_{j\beta}, \tag{1.34}$$

and evaluate

$$\begin{aligned}
-2J \sum_{\langle lj \rangle} \hat{Q}_{lj}^\dagger \hat{Q}_{lj} &= \frac{J}{4} \sum_{\langle lj \rangle} (-2) \varepsilon^{\alpha\gamma} \varepsilon^{\beta\mu} \hat{b}_{l\alpha}^\dagger \hat{b}_{j\gamma}^\dagger \hat{b}_{l\beta} \hat{b}_{j\mu} \\
&= \frac{J}{4} \sum_{\langle lj \rangle} (2\delta_{\alpha\mu}\delta_{\beta\gamma} - 2\delta_{\alpha\beta}\delta_{\gamma\mu}) \hat{b}_{l\alpha}^\dagger \hat{b}_{l\beta} \hat{b}_{j\gamma}^\dagger \hat{b}_{j\mu} \\
&= \frac{J}{4} \sum_{\langle lj \rangle} (2\delta_{\alpha\mu}\delta_{\beta\gamma} - \delta_{\alpha\beta}\delta_{\gamma\mu}) \hat{b}_{l\alpha}^\dagger \hat{b}_{l\beta} \hat{b}_{j\gamma}^\dagger \hat{b}_{j\mu} - \frac{J}{4} \sum_{\langle lj \rangle} \hat{b}_{l\alpha}^\dagger \hat{b}_{l\alpha} \hat{b}_{j\gamma}^\dagger \hat{b}_{j\gamma} \\
&= J \sum_{\langle lj \rangle} \hat{\mathbf{S}}_l \cdot \hat{\mathbf{S}}_j - \frac{J}{4} \sum_{\langle lj \rangle} \hat{n}_j \hat{n}_l.
\end{aligned} \tag{1.35}$$

As such, we see that by dropping the constant term $-J/4 \sum_{\langle lj \rangle} \hat{n}_j \hat{n}_l$, we can rewrite our Hamiltonian as

$$\hat{H} = -2J \sum_{\langle lj \rangle} \hat{Q}_{lj}^\dagger \hat{Q}_{lj}. \tag{1.36}$$

We now apply a mean-field approximation

$$\left(\hat{Q}_{lj}^\dagger - \langle \hat{Q}_{lj} \rangle^* \right) \left(\hat{Q}_{lj} - \langle \hat{Q}_{lj} \rangle \right) \approx 0 \tag{1.37}$$

$$\Leftrightarrow \hat{Q}_{lj}^\dagger \hat{Q}_{lj} \approx \langle \hat{Q}_{lj} \rangle \hat{Q}_{lj}^\dagger + \langle \hat{Q}_{lj} \rangle^* \hat{Q}_{lj} - |\langle \hat{Q}_{lj} \rangle|^2, \tag{1.38}$$

and constrain, through the Lagrange multiplier λ , the number of bosons per site to $2S$. This leads to

$$\hat{H}_{\text{MF}} = -2J \sum_{\langle lj \rangle} \left(\langle \hat{Q}_{lj} \rangle \hat{Q}_{lj}^\dagger + \text{H.c.} \right) + 2J \sum_{\langle lj \rangle} |\langle \hat{Q}_{lj} \rangle|^2 + \lambda \sum_j (\hat{n}_j - 2S). \quad (1.39)$$

Let us now switch from a summation over sites to one over unit cells, where a unit cell has the position $m\mathbf{R}_1 + n\mathbf{R}_2$, where \mathbf{R}_1 and \mathbf{R}_2 are primitive vectors on the lattice. Our Hamiltonian now evaluates (see Ref. [2] for unit cell):

$$\begin{aligned} \hat{H}_{\text{MF}} &= -J \sum_{\langle mn \rangle} \varepsilon^{\alpha\beta} \left[Q_1 \left(\hat{b}_{u\alpha}^\dagger \hat{b}_{v\beta}^\dagger + \hat{b}_{v\alpha}^\dagger \hat{b}_{w\beta}^\dagger + \hat{b}_{w\alpha}^\dagger \hat{b}_{u\beta}^\dagger \right)_{(m,n),>} \right. \\ &\quad \left. + Q_2 \left(\hat{b}_{u\alpha}^\dagger \hat{b}_{v\beta}^\dagger + \hat{b}_{v\alpha}^\dagger \hat{b}_{w\beta}^\dagger + \hat{b}_{w\alpha}^\dagger \hat{b}_{u\beta}^\dagger \right)_{(m,n),>>} + \text{H.c.} \right] \\ &\quad + \lambda \sum_{\langle mn \rangle} \left(\hat{n}_u + \hat{n}_v + \hat{n}_w \right) + 2J \sum_{\langle mn \rangle} (3|Q_1|^2 + 3|Q_2|^2) - \lambda N_s 2S \\ &= -J \sum_{\langle mn \rangle} \varepsilon^{\alpha\beta} \left[Q_1 \left(\hat{b}_{u\alpha}^\dagger \hat{b}_{v\beta}^\dagger + \hat{b}_{v\alpha}^\dagger \hat{b}_{w\beta}^\dagger + \hat{b}_{w\alpha}^\dagger \hat{b}_{u\beta}^\dagger \right)_{(m,n),>} \right. \\ &\quad \left. + Q_2 \left(\hat{b}_{u\alpha}^\dagger \hat{b}_{v\beta}^\dagger + \hat{b}_{v\alpha}^\dagger \hat{b}_{w\beta}^\dagger + \hat{b}_{w\alpha}^\dagger \hat{b}_{u\beta}^\dagger \right)_{(m,n),>>} + \text{H.c.} \right] \\ &\quad + \lambda \sum_{\langle mn \rangle} \left(\hat{n}_u + \hat{n}_v + \hat{n}_w \right) + 2J N_s (|Q_1|^2 + |Q_2|^2) - \lambda N_s 2S \\ &= -\frac{J N_s}{3N_k} \varepsilon^{\alpha\beta} \sum_{\mathbf{k}} \left[Q_1 \left(\hat{b}_{\mathbf{k}\alpha}^{u\dagger} \hat{b}_{-\mathbf{k}\beta}^{v\dagger} e^{ik_1} + \hat{b}_{\mathbf{k}\alpha}^{v\dagger} \hat{b}_{-\mathbf{k}\beta}^{w\dagger} e^{ik_2} + \hat{b}_{\mathbf{k}\alpha}^{w\dagger} \hat{b}_{-\mathbf{k}\beta}^{u\dagger} e^{ik_3} \right) \right. \\ &\quad \left. + Q_2 \left(\hat{b}_{\mathbf{k}\alpha}^{u\dagger} \hat{b}_{-\mathbf{k}\beta}^{v\dagger} e^{-ik_1} + \hat{b}_{\mathbf{k}\alpha}^{v\dagger} \hat{b}_{-\mathbf{k}\beta}^{w\dagger} e^{-ik_2} + \hat{b}_{\mathbf{k}\alpha}^{w\dagger} \hat{b}_{-\mathbf{k}\beta}^{u\dagger} e^{-ik_3} \right) + \text{H.c.} \right] \\ &\quad + \frac{\lambda N_s}{3N_k} \sum_{\mathbf{k}} \left(\hat{b}_{\mathbf{k}\alpha}^{u\dagger} \hat{b}_{\mathbf{k}\alpha}^u + \hat{b}_{\mathbf{k}\alpha}^{v\dagger} \hat{b}_{\mathbf{k}\alpha}^v + \hat{b}_{\mathbf{k}\alpha}^{w\dagger} \hat{b}_{\mathbf{k}\alpha}^w \right) + 2J N_s (|Q_1|^2 + |Q_2|^2) - \lambda N_s 2S \\ &= -\frac{J N_s}{3N_k} \varepsilon^{\alpha\beta} \sum_{\mathbf{k}} \left[\left(Q_1 e^{ik_1} + Q_2 e^{-ik_1} \right) \hat{b}_{\mathbf{k}\alpha}^{u\dagger} \hat{b}_{-\mathbf{k}\beta}^{v\dagger} + \left(Q_1 e^{ik_2} + Q_2 e^{-ik_2} \right) \hat{b}_{\mathbf{k}\alpha}^{v\dagger} \hat{b}_{-\mathbf{k}\beta}^{w\dagger} \right. \\ &\quad \left. + \left(Q_1 e^{ik_3} + Q_2 e^{-ik_3} \right) \hat{b}_{\mathbf{k}\alpha}^{w\dagger} \hat{b}_{-\mathbf{k}\beta}^{u\dagger} + \text{H.c.} \right] \\ &\quad + \frac{\lambda N_s}{3N_k} \sum_{\mathbf{k}} \left(\hat{b}_{\mathbf{k}\uparrow}^{u\dagger} \hat{b}_{\mathbf{k}\uparrow}^u + \hat{b}_{\mathbf{k}\uparrow}^{v\dagger} \hat{b}_{\mathbf{k}\uparrow}^v + \hat{b}_{\mathbf{k}\uparrow}^{w\dagger} \hat{b}_{\mathbf{k}\uparrow}^w + \hat{b}_{-\mathbf{k}\downarrow}^u \hat{b}_{-\mathbf{k}\downarrow}^{u\dagger} + \hat{b}_{-\mathbf{k}\downarrow}^v \hat{b}_{-\mathbf{k}\downarrow}^{v\dagger} + \hat{b}_{-\mathbf{k}\downarrow}^w \hat{b}_{-\mathbf{k}\downarrow}^{w\dagger} \right) \\ &\quad + 2J N_s (|Q_1|^2 + |Q_2|^2) - \lambda N_s (1 + 2S), \end{aligned} \quad (1.40)$$

which leads to the per-site mean-field Hamiltonian

$$\frac{\hat{H}_{MF}}{N_s} = \frac{1}{3N_k} \sum_{\mathbf{k}} \Psi_{\mathbf{k}}^\dagger \hat{\mathbf{D}}_{\mathbf{k}} \Psi_{\mathbf{k}} + 2J(|Q_1|^2 + |Q_2|^2) - \lambda(1 + 2S), \quad (1.41)$$

where

$$\Psi = \begin{pmatrix} \hat{b}_{\mathbf{k}\uparrow}^u \\ \hat{b}_{\mathbf{k}\uparrow}^v \\ \hat{b}_{\mathbf{k}\uparrow}^w \\ \hat{b}_{-\mathbf{k}\downarrow}^{u\dagger} \\ \hat{b}_{-\mathbf{k}\downarrow}^{v\dagger} \\ \hat{b}_{-\mathbf{k}\downarrow}^{w\dagger} \end{pmatrix}, \quad (1.42)$$

and $\hat{\mathbf{D}}_{\mathbf{k}}$ is the Hermitian matrix

$$\hat{\mathbf{D}}_{\mathbf{k}} = \begin{pmatrix} \hat{\mathbf{R}}_{\mathbf{k}} & \hat{\mathbf{P}}_{\mathbf{k}} \\ \hat{\mathbf{P}}_{\mathbf{k}}^\dagger & \hat{\mathbf{R}}_{-\mathbf{k}}^* \end{pmatrix} = \begin{pmatrix} \hat{\mathbf{R}}_{\mathbf{k}} & \hat{\mathbf{P}}_{\mathbf{k}} \\ \hat{\mathbf{P}}_{\mathbf{k}}^\dagger & \hat{\mathbf{R}}_{-\mathbf{k}}^\top \end{pmatrix}, \quad (1.43)$$

with $\hat{\mathbf{R}}_{\mathbf{k}} = \lambda \mathbf{1}_3$ and

$$\hat{\mathbf{P}}_{\mathbf{k}} = -J \begin{pmatrix} 0 & Q_1 e^{ik_1} + Q_2 e^{-ik_1} & -Q_1 e^{-ik_3} - Q_2 e^{ik_3} \\ -Q_1 e^{-ik_1} - Q_2 e^{ik_1} & 0 & Q_1 e^{ik_2} + Q_2 e^{-ik_2} \\ Q_1 e^{ik_3} + Q_2 e^{-ik_3} & -Q_1 e^{-ik_2} - Q_2 e^{ik_2} & 0 \end{pmatrix}, \quad (1.44)$$

where one can directly see that $\hat{\mathbf{P}}_{\mathbf{k}} = -\hat{\mathbf{P}}_{-\mathbf{k}}^\top$.

Upon a Bogoliubov transformation (see Refs. [1] and [2]), we obtain the eigenvalues $[\epsilon_{\mathbf{k}\uparrow}, -\epsilon_{-\mathbf{k}\downarrow}]$ of $\tau^3 \hat{\mathbf{D}}$. The free energy per site is then

$$\frac{E_{MF}}{N_s} = \frac{1}{3N_k} \sum_{\mathbf{k},s} \epsilon_{\mathbf{k}\uparrow}^s + 2J(|Q_1|^2 + |Q_2|^2) - \lambda(1 + 2S), \quad (1.45)$$

where here s denotes the band. Note that due to rotational symmetry, we have $\epsilon_{\mathbf{k}\uparrow}^s = \epsilon_{\mathbf{k}\downarrow}^s$, and due to reflection symmetry this means that we also have $\epsilon_{\mathbf{k}\uparrow}^s = \epsilon_{-\mathbf{k}\downarrow}^s$.

Free energy of the $Q_1 = Q_2$ ansatz

Let us now consider the $Q_1 = Q_2 = Q$ ansatz [2] and get an analytical expression of the free energy. We start off by simplifying $\hat{\mathbf{P}}_{\mathbf{k}}$:

$$\begin{aligned}
\hat{\mathbf{P}}_{\mathbf{k}} &= -JQ \begin{pmatrix} 0 & e^{ik_1} + e^{-ik_1} & -e^{-ik_3} - e^{ik_3} \\ -e^{-ik_1} - e^{ik_1} & 0 & e^{ik_2} + e^{-ik_2} \\ e^{ik_3} + e^{-ik_3} & -e^{-ik_2} - e^{ik_2} & 0 \end{pmatrix} \\
&= -2JQ \begin{pmatrix} 0 & \cos k_1 & -\cos k_3 \\ -\cos k_1 & 0 & \cos k_2 \\ \cos k_3 & -\cos k_2 & 0 \end{pmatrix}.
\end{aligned} \tag{1.46}$$

This leads to

$$\hat{\mathbf{P}}_{\mathbf{k}}^\dagger \hat{\mathbf{P}}_{\mathbf{k}} = 4J^2Q^2 \begin{pmatrix} \cos^2 k_1 + \cos^2 k_3 & -\cos k_3 \cos k_2 & -\cos k_1 \cos k_2 \\ -\cos k_2 \cos k_3 & \cos^2 k_1 + \cos^2 k_2 & -\cos k_1 \cos k_3 \\ -\cos k_2 \cos k_1 & -\cos k_3 \cos k_1 & \cos^2 k_3 + \cos^2 k_2 \end{pmatrix}, \tag{1.47}$$

and this matrix has a zero eigenvalue and one doubly-degenerate eigenvalue

$$\mathbf{p}^2 = 4J^2Q^2 (\cos^2 k_1 + \cos^2 k_2 + \cos^2 k_3). \tag{1.48}$$

As such, the $\epsilon_{\mathbf{k}\uparrow}$ -values are λ (non-degenerate) and $\sqrt{\lambda^2 - \mathbf{p}^2}$ (doubly-degenerate). This leads to

$$\frac{E_{MF}}{N_s} = \frac{1}{3N_k} \sum_{\mathbf{k}} [\lambda + 2\sqrt{\lambda^2 - \mathbf{p}^2}] + 4JQ^2 - \lambda(1 + 2S). \tag{1.49}$$

1.4 Quench dynamics

Consider the Hamiltonian $\hat{H}(\lambda)$ where λ is some control parameter, such as external-magnetic-field strength in the transverse-field Ising model or interaction strength in the Hubbard model. Let us prepare our system in the groundstate $|\psi_0\rangle$ (at temperature $T = 0$, for simplicity) of the Hamiltonian $\hat{H}(\lambda_i)$. Then at time $t = 0$, we abruptly and suddenly change λ from its initial value λ_i to its final value of λ_f . This is a so-called *global quantum quench*, which leads to violent dynamics at short time scales and usually to some kind of steady state at long times. The nature of the latter strongly depends on the nature of the Hamiltonian itself, and whether or not it is integrable. This is discussed in the following.

We are interested in the description of the dynamics of *local finite operators* on the chain of L sites in the thermodynamic limit $L \rightarrow \infty$. Very succinctly, a local finite operator is one whose range does not scale with system size. In other words, a local finite operator acts on a finite number of sites in the system such that these sites are separated by a finite distance [72]. Let us call such an operator \hat{O} , and now we can express its time evolution

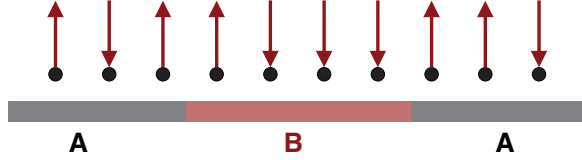


Figure 1.2: (Color online) Figure adapted from Ref. [72]. Here, an arbitrarily-chosen local finite subsystem B and its complement A partition the total quantum system. If, in the thermodynamic limit, the expectation values of all nontrivial operators acting on B relax in the long-time limit, then the system is said to have relaxed.

$$\begin{aligned} \langle \psi(t) | \hat{O} | \psi(t) \rangle &= \sum_{mn} \langle \psi_0 | e^{i\hat{H}t} | m \rangle \langle m | \hat{O} | n \rangle \langle n | e^{-i\hat{H}t} | \psi_0 \rangle \\ &= \sum_{mn} \langle \psi_0 | m \rangle \langle m | \hat{O} | n \rangle \langle n | \psi_0 \rangle e^{i(E_m - E_n)t}, \end{aligned} \quad (1.50)$$

where $\{|n\rangle\}$ are the eigenstates of \hat{H} with $\{E_n\}$ their corresponding eigenenergies. The exponential term in (1.50) is the beacon of quantum interference effects in the dynamics of this system after the quench. We note here that if the initial state $|\psi_0\rangle$ is not an eigenstate of \hat{H} (if it were, this would not be a quench and the dynamics would be quite boring), then (1.50) shows that the excited states of \hat{H} have gotten occupied after the quench. Thus, through quenching, we explore a region of the Hilbert space that is distinct from that containing the groundstate and low-lying excitations [72].

Relaxation of the whole quantum system is clearly impossible from (1.50), but local relaxation, i.e. relaxation of a local operator is indeed possible if one considers the corresponding finite subsystem B on which this local operator is defined. The subsystem B is described over time by the density matrix $\hat{\rho}_B(t)$, and local relaxation is achieved only if [72]

$$\lim_{t \rightarrow \infty} \lim_{L \rightarrow \infty} \hat{\rho}_B(t) = \hat{\rho}_B(\infty) \quad (1.51)$$

for any finite subsystem B . Consequently, a stationary state is defined as a time-independent density matrix $\hat{\rho}^{\text{SS}}$ describing the full system where for any subsystem B one has

$$\lim_{L \rightarrow \infty} \text{Tr}_A(\hat{\rho}^{\text{SS}}) = \hat{\rho}_B(\infty), \quad (1.52)$$

where A is the complement of B in the full system. The next step is to investigate what $\hat{\rho}^{\text{SS}}$ can be. One thing for sure is that $\hat{\rho}^{\text{SS}}$, being a stationary (or steady) state of the whole quantum system, is a fictitious, albeit very convenient, construct. Its fictitiousness is due to the fact that the full quantum system will not really relax as we have constantly ongoing quantum interference effects as seen in (1.50).

1.4.1 Integrable models

A closed quantum system is said to be integrable when it is described by a Hamiltonian that has *local* conservation laws $\hat{\mathcal{I}}_n$ [72, 73, 74], also known as *local* integrals of motion, such that

$$\left[\hat{H}, \hat{\mathcal{I}}_n \right] = \left[\hat{\mathcal{I}}_n, \hat{\mathcal{I}}_m \right] = 0. \quad (1.53)$$

These integrals of motion will naturally constrain the dynamics of the system through

$$\langle \psi(t) | \hat{\mathcal{I}}_n | \psi(t) \rangle = \langle \psi_0 | e^{i\hat{H}t} \hat{\mathcal{I}}_n e^{-i\hat{H}t} | \psi_0 \rangle = \langle \psi_0 | \hat{\mathcal{I}}_n | \psi_0 \rangle, \quad (1.54)$$

which is clearly a constant for all evolution times t . In lattice models, which are of interest to this dissertation, integrable systems are found in non-interacting fermionic and bosonic systems [75, 76, 77], models mappable to free fermionic systems such as the transverse-field Ising model [78, 79, 80, 81, 82, 83, 84, 85, 86, 87, 88, 89, 90, 91, 92, 93, 94, 95, 96] and XY chains [97, 98, 99, 100, 101, 102, 103, 104, 105], the Heisenberg chain (solvable through Bethe ansatz) [106, 107, 108, 109, 110, 111, 112, 113, 114, 115, 116, 117, 118, 119, 120, 121, 122, 123, 124, 125], and the Hubbard model [126, 127, 128, 129, 130].

The constraint (1.54) forbids the system from thermalizing, but rather leads to it relaxing to a generalized Gibbs ensemble (GGE)

$$\hat{\rho}^{\text{GGE}} = \frac{e^{-\sum_n \lambda_n \hat{\mathcal{I}}_n}}{\text{Tr} \left[e^{-\sum_n \lambda_n \hat{\mathcal{I}}_n} \right]}, \quad (1.55)$$

where λ_n are Lagrange multipliers fixed by the initial conditions of the system [72]. Thus, for an integrable system, the steady state is a GGE ($\hat{\rho}^{\text{SS}} = \hat{\rho}^{\text{GGE}}$). As one can see from (1.52), a system is said to relax into a GGE, therefore, if

$$\lim_{L \rightarrow \infty} \text{Tr}_A(\hat{\rho}^{\text{GGE}}) = \hat{\rho}_B(\infty), \quad (1.56)$$

for any subsystem B . Theoretically, one can solve for $\hat{\rho}^{\text{GGE}}$ by assuming one has full knowledge of all the integrals of motion, and recognizing that

$$\langle \psi_0 | \hat{\mathcal{I}}_n | \psi_0 \rangle = \text{Tr} \left[\hat{\rho}^{\text{GGE}} \hat{\mathcal{I}}_n \right], \quad (1.57)$$

which leads to n equations with n unknowns, the latter being the Lagrange multipliers λ_n . Then, one can experimentally, for example, look for relaxation with respect to a finite subsystem B and determine $\hat{\rho}_B(\infty)$, and check if (1.56) is satisfied, in which case one can be certain of the system having relaxed into a GGE.

1.4.2 Nonintegrable models

Alternatively, our quantum system may not be integrable, and this type of system is said to be nonintegrable. In such a case, according to the Eigenstate Thermalization Hypothesis (ETH) [131, 132], the system is expected to thermalize to a Gibbs (thermal) ensemble

$$\hat{\rho}^{\text{th}} = \frac{e^{-\hat{H}/T}}{\text{Tr} \left[e^{-\hat{H}/T} \right]}, \quad (1.58)$$

where the temperature T can be determined by assuming full knowledge of \hat{H} and recognizing that

$$\langle \psi_0 | \hat{H} | \psi_0 \rangle = \text{Tr} \left[\hat{\rho}^{\text{th}} \hat{H} \right]. \quad (1.59)$$

Consequently, the relation

$$\lim_{L \rightarrow \infty} \text{Tr}_A(\hat{\rho}^{\text{th}}) = \hat{\rho}_B(\infty) \quad (1.60)$$

must be satisfied in order for the system to have thermalized.

1.4.3 Prethermalization

Clearly, in both cases (integrable or nonintegrable models) it would be extremely optimistic to expect that one would have full knowledge of the local integrals of motion or the Hamiltonian, unless the problem is extremely trivial. In particular, nonintegrable systems are in general not solvable analytically, which automatically means that one does not have *a priori* access to the full spectrum of the system, and numerical methods would be necessary to attempt to answer whether or not the system indeed thermalizes at long times. In the end, one has to realize that the ETH is in fact a hypothesis, and it is not known whether or not it can be proven for general interacting (nonintegrable) systems. Thus, even though it is expected, and very realistically so, that a nonintegrable system would eventually thermalize, this cannot be taken with absolute certainty. Naturally, one then turns to experiment, but the latter, whether a laboratory setup or a numerical simulation, is limited, mainly due to decoherence, in the accessible evolution times. For nonintegrable systems where integrability is only slightly broken, relaxation into a thermal stationary state would take incredibly long, or, as Pasquale Calabrese once aptly put it in a lecture, until after the Sun has died.

Indeed, employing a hand-waving argument one can consider an integrable Hamiltonian \hat{H} to which a small integrability breaking term $\delta h \cdot \hat{O}$ is added to give the (slightly-)nonintegrable Hamiltonian

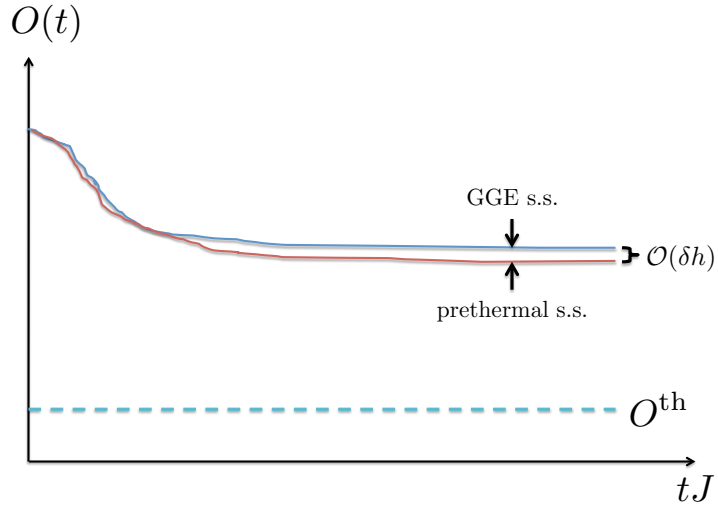


Figure 1.3: (Color online) An intuitive illustration of prethermalization in a system with weak breaking of integrability. When integrability is intact, the system relaxes to a generalized Gibbs ensemble (GGE), and a steady-state value O^{GGE} of the expectation value of \hat{O} is reached at late times. Once small integrability term is introduced [see (1.62)], the system prethermalizes on its way to the GGE, whereby in this prethermal quasi-steady state \hat{O} relaxes to $O^{\text{preth}} \sim O^{\text{GGE}} - \mathcal{O}(\delta h)$. This procedure is analogous to small quenches in a strongly nonintegrable model merely due to slow relaxation.

$$\hat{H}' = \hat{H} + \delta h \cdot \hat{O}, \quad (1.61)$$

with $\delta h \ll 1$. Consequently, and very roughly speaking, the new integrals of motion will be

$$\hat{\mathcal{I}}' = \hat{\mathcal{I}} + \delta h \cdot \hat{O}. \quad (1.62)$$

Straightforwardly one sees that

$$[\hat{H}', \hat{\mathcal{I}}'] \sim \mathcal{O}(\delta h), \quad (1.63)$$

which means that, even though conservation laws are broken, they are only very weakly so, and relaxation into a stationary state will take very long. This has already been shown, for example, in the Fermi-Hubbard model [133], and Fig. 1.3 presents an illustration of

prethermalization in a system with weak nonintegrability. As such, it is clear that there are quenches where it would make no sense to wait for thermalization to occur as it is simply numerically and experimentally unfeasible, but where relaxation to thermalization leads to a prethermal quasi-steady state from which one can extract an order parameter, for example, and quantify nonequilibrium properties. Note that prethermalization is not restricted only to integrable or slightly-nonintegrable systems, but rather are present in systems far from integrability. This can be quickly understood by considering a quench where the system is prepared in the groundstate of $\hat{H}(\lambda)$ and then time-evolved under $\hat{H}(\lambda+\delta\lambda)$ with $\delta\lambda \ll 1$. In general, this very tiny quench will lead to very weak dynamics, since it is not *violent* enough to induce quick relaxation into a thermal state [10], and instead, the system will relax very slowly to a thermal state, staying in a prethermal state for quite a long time on the way there.

1.5 Dynamical phase transitions

1.5.1 Overview of equilibrium phase transitions

Phase transitions are among the most intriguing phenomena in the natural world, from everyday phase transitions such as the vaporization (liquid to gas) of water to those carried out in specialized physics laboratories around the world such as the superfluid-Mott insulator transition [6] and the metal-superconductor transition [134]. A phase transition is a nonanalyticity in the Gibbs free energy, where, according to the Ehrenfest classification, an n^{th} -order phase transition is one in which the n^{th} derivative of the Gibbs free energy has a discontinuous jump at the critical point. As the name suggests, the phase transition denotes going from one phase to a second phase where, in general, some symmetry is broken, or alternatively, according to Noether's theorem, a certain physical quantity is no longer conserved. Continuous (second-order) equilibrium phase transitions are of great interest in condensed-matter research, and those emerge in universality classes that, in general, depend on

- number of spatial dimensions,
- number of components of the order parameter,
- and the symmetry of the model.

Phase transitions in different models belonging to the same universality class basically show identical nonanalytic properties in the behavior of their order parameter, specific heat, susceptibility, and other derivatives of the free energy in the immediate vicinity of the critical point. In other words, models with phase transitions in the same universality class possess the same equilibrium critical exponents. It is thus of great interest to see if this concept of universality would carry on to out-of-equilibrium criticality. Before diving any deeper into this issue, however, we shall seek in the following a more solid footing in the

equilibrium phase transitions of the transverse-field Ising model at various range-lengths of interactions, owing to the fact that this paradigmatic model will be crucial to our results in Chapters 3 and 4.

Fully-connected transverse-field Ising model

To put things in perspective, a very instructive example is the fully-connected Ising model [135]

$$\mathcal{H} = -\frac{J}{2N} \sum_{i,j=1}^N \sigma_i \sigma_j, \quad (1.64)$$

which is exactly solvable in mean-field theory. In order to ensure intensive scaling of energy density, we use the Kac normalization by dividing by the number of sites N . Using that $d\sigma_i = \sigma_i - \langle \sigma_j \rangle \ll 1$, where this approximation is the essence of mean-field theory, and that $\langle \sigma_i \rangle = \langle \sigma_j \rangle = M$ due to translational invariance ($N \rightarrow \infty$ or periodic boundary conditions), a mean-field decoupling of (1.64) reads

$$\begin{aligned} \mathcal{H} &= -\frac{J}{2N} \sum_{i,j=1}^N [(\sigma_i - \langle \sigma_i \rangle) + \langle \sigma_i \rangle][(\sigma_j - \langle \sigma_j \rangle) + \langle \sigma_j \rangle] \\ &\approx -\frac{J}{2N} \sum_{i,j=1}^N [(\sigma_i + \sigma_j) M - M^2] \\ &= -JM \sum_{i=1}^N \sigma_i + \frac{JNM^2}{2}. \end{aligned} \quad (1.65)$$

We now proceed with calculating the partition function at temperature T (with the Boltzmann constant set to unity):

$$\begin{aligned} \mathcal{Z} &= \text{Tr} \left[e^{-\frac{\mathcal{H}}{T}} \right] \\ &= \sum_{\{\sigma_i\}} e^{-\frac{\mathcal{H}(\{\sigma_i\})}{T}} \\ &= e^{-\frac{JNM^2}{2T}} \prod_{i=1}^N \sum_{\sigma_i=\pm 1} e^{\frac{JM\sigma_i}{T}} \\ &= e^{-\frac{JNM^2}{2T}} \left[2 \cosh \left(\frac{JM}{T} \right) \right]^N. \end{aligned}$$

The free energy is then

$$\begin{aligned}\mathcal{F} &= -T \ln \mathcal{Z} \\ &= \frac{JNM^2}{2} - NT \ln \left[2 \cosh \left(\frac{JM}{T} \right) \right].\end{aligned}\quad (1.66)$$

At equilibrium, the free energy is minimized with respect to the magnetization order parameter:

$$\frac{\partial \mathcal{F}}{\partial M} = JNM - JN \tanh \left(\frac{JM}{T} \right) \stackrel{!}{=} 0, \quad (1.67)$$

which leads to

$$M = \tanh \left(\frac{JM}{T} \right), \quad (1.68)$$

where we see that nonzero solutions of M occur only when $T < J$, while for $T > J$ the only solution is $M = 0$. Thus, we conclude that the critical temperature of the fully-connected Ising model is $T_c = J$.

We now consider the fully-connected Ising model with a transverse field (FC-TFIM)

$$\mathcal{H} = -\frac{J}{2N} \sum_{i,j=1}^N \sigma_i^z \sigma_j^z - h \sum_i \sigma_i^x, \quad (1.69)$$

which can be rewritten as

$$\frac{H}{N} = -\frac{J}{2} (S^z)^2 - h S^x, \quad (1.70)$$

where $S^a = \frac{1}{N} \sum_{i=1}^N \sigma_i^a$ with $a = x, y, z$. At zero temperature, the semiclassical energy density is given by

$$\mathcal{E} = -\frac{J}{2} \sin^2 \theta - h \cos \theta \cos \phi, \quad (1.71)$$

where on the Bloch sphere we have $(S^x, S^y, S^z) = (\cos \theta \cos \phi, \cos \theta \sin \phi, \sin \theta)$. Minimizing with respect to θ we find that for $h < J$ (ferromagnetic phase) the minima of \mathcal{E} occur at $\theta = \arccos(h/J)$, while for $h > J$ the minima of \mathcal{E} are at $\theta = \pi/2$. Thus we conclude that the quantum critical point of the FC-TFIM is $h_c = J$. Thus, we here see that the FC-TFIM has both a quantum (zero-temperature) phase transition and a thermal

(finite-temperature) phase transition. In fact, the critical line in the T - h plane is given by [135, 136]

$$\frac{h_c^{\text{th}}}{J} = \tanh\left(\frac{h_c^{\text{th}}}{T}\right), \quad (1.72)$$

giving an implicit relation between the critical field at a temperature T and the temperature T itself, thus delineating the boundary between the ordered ferromagnetic phase below this line and the disordered paramagnetic phase above it.

Nearest-neighbor transverse-field Ising model

Let us now turn our attention to the one-dimensional nearest-neighbor Ising model

$$\mathcal{H} = -J \sum_{i=1}^{N-1} \sigma_i \sigma_{i+1}, \quad (1.73)$$

where $J > 0$ is a coupling constant. In one-dimensional space with very short-range interactions, mean-field theory fails due to strong fluctuations. However, one can use a Peierls' argument to determine the critical temperature that goes about trying to assess what happens upon introducing a *droplet* of length L of spin-downs to the fully-polarized state of spin-ups. If one considers, in the thermodynamic limit $N \rightarrow \infty$, a site i , then there are L ways of introducing a droplet that contains this site, thereby leading to an entropy

$$S = \ln L, \quad (1.74)$$

where once again Boltzmann's constant is set to unity. Consequently, this leads to the free energy

$$\mathcal{F} = \mathcal{E} - TS = \mathcal{E}_0 + 4J - T \ln L, \quad (1.75)$$

where $\mathcal{E}_0 = -NJ$ is the energy of the fully-polarized state, and the term $4J$ comes from the couplings of spin-ups with the spin-downs of the droplet at its edges. Clearly, any finite temperature in (1.75) leads to a complete proliferation of the droplet, as it is energetically favorable then to have L as big as possible. Therefore, one can conclude that the critical temperature of the nearest-neighbor Ising model is $T_c = 0$, i.e. it has no thermal phase transition.

Let us now find the quantum critical point of the nearest-neighbor transverse-field Ising model (NN-TFIM) given by the Hamiltonian

$$\mathcal{H} = -J \sum_{i=1}^{N-1} \sigma_i^z \sigma_{i+1}^z - h \sum_{i=1}^N \sigma_i^x. \quad (1.76)$$

This model can be exactly mapped onto a spinless-fermion system using the Jordan-Wigner transformation [137]

$$\hat{\sigma}_i^x = 1 - 2\hat{c}_i^\dagger \hat{c}_i, \quad (1.77)$$

$$\hat{\sigma}_i^z = - \left[\prod_{j<i} (1 - 2\hat{c}_j^\dagger \hat{c}_j) \right] (\hat{c}_i + \hat{c}_i^\dagger), \quad (1.78)$$

where $\hat{c}_i^{(\dagger)}$ is a fermionic annihilation (creation) operator on site i , satisfying the fermionic canonical anticommutation relations

$$\{\hat{c}_i^\dagger, \hat{c}_j\} = \delta_{i,j}, \quad (1.79)$$

$$\{\hat{c}_i, \hat{c}_j\} = \{\hat{c}_i^\dagger, \hat{c}_j^\dagger\} = 0. \quad (1.80)$$

Plugging (1.77) and (1.78) into (1.76), we derive

$$\begin{aligned} \mathcal{H} &= -J \sum_{i=1}^{N-1} \sigma_i^z \sigma_{i+1}^z - h \sum_{i=1}^N \sigma_i^x \\ &= -J \sum_{i=1}^{N-1} \left[\prod_{j<i} (1 - 2\hat{c}_j^\dagger \hat{c}_j) \right] (\hat{c}_i + \hat{c}_i^\dagger) \left[\prod_{l<i+1} (1 - 2\hat{c}_l^\dagger \hat{c}_l) \right] (\hat{c}_{i+1} + \hat{c}_{i+1}^\dagger) - h \sum_{i=1}^N (1 - 2\hat{c}_i^\dagger \hat{c}_i) \\ &= -J \sum_{i=1}^{N-1} \left[\prod_{j<i} (1 - 2\hat{c}_j^\dagger \hat{c}_j) \right]^2 (\hat{c}_i + \hat{c}_i^\dagger) (1 - 2\hat{c}_i^\dagger \hat{c}_i) (\hat{c}_{i+1} + \hat{c}_{i+1}^\dagger) - h \sum_{i=1}^N (1 - 2\hat{c}_i^\dagger \hat{c}_i) \\ &= -J \sum_{i=1}^{N-1} (\hat{c}_i + \hat{c}_i^\dagger) (1 - 2\hat{c}_i^\dagger \hat{c}_i) (\hat{c}_{i+1} + \hat{c}_{i+1}^\dagger) - h \sum_{i=1}^N (1 - 2\hat{c}_i^\dagger \hat{c}_i) \\ &= -J \sum_{i=1}^{N-1} [\hat{c}_i + \hat{c}_i^\dagger - 2\hat{c}_i (1 - \hat{c}_i \hat{c}_i^\dagger) - 2\hat{c}_i^\dagger \hat{c}_i^\dagger \hat{c}_i] (\hat{c}_{i+1} + \hat{c}_{i+1}^\dagger) - h \sum_{i=1}^N (1 - 2\hat{c}_i^\dagger \hat{c}_i) \\ &= -J \sum_{i=1}^{N-1} (\hat{c}_i^\dagger - \hat{c}_i) (\hat{c}_{i+1} + \hat{c}_{i+1}^\dagger) - h \sum_{i=1}^N (1 - 2\hat{c}_i^\dagger \hat{c}_i) \\ &= -J \sum_{i=1}^N (\hat{c}_i^\dagger \hat{c}_{i+1} + \hat{c}_i^\dagger \hat{c}_{i+1}^\dagger - \hat{c}_i \hat{c}_{i+1} - \hat{c}_i \hat{c}_{i+1}^\dagger - 2g \hat{c}_i^\dagger \hat{c}_i + g), \end{aligned} \quad (1.81)$$

where we have denoted $g = h/J$ whilst keeping in mind periodic boundary conditions or the thermodynamic limit $N \rightarrow \infty$. We now carry out a Fourier transformation

$$\hat{c}_i = \frac{1}{\sqrt{N}} \sum_k^{\text{B.z.}} \hat{c}_k e^{iki} \Leftrightarrow \hat{c}_i^\dagger = \frac{1}{\sqrt{N}} \sum_k^{\text{B.z.}} \hat{c}_k^\dagger e^{-iki}. \quad (1.82)$$

This renders (1.81) in the form

$$\begin{aligned} \mathcal{H} &= -J \sum_{i=1} (\hat{c}_i^\dagger \hat{c}_{i+1} + \hat{c}_i^\dagger \hat{c}_{i+1}^\dagger - \hat{c}_i \hat{c}_{i+1} - \hat{c}_i \hat{c}_{i+1}^\dagger - 2g \hat{c}_i^\dagger \hat{c}_i + g) \\ &= -\frac{J}{N} \sum_{i=1} \sum_{k,q}^{\text{B.z.}} \left(\hat{c}_k^\dagger \hat{c}_q e^{-i(k-q)i} e^{iq} + \hat{c}_k^\dagger \hat{c}_q^\dagger e^{-i(k+q)i} e^{-iq} \right. \\ &\quad \left. - \hat{c}_k \hat{c}_q e^{i(k+q)i} e^{iq} - \hat{c}_k \hat{c}_q^\dagger e^{i(k-q)i} e^{-iq} - 2g \hat{c}_k^\dagger \hat{c}_q e^{-i(k-q)i} + g \right) \\ &= -J \sum_k^{\text{B.z.}} \left(\hat{c}_k^\dagger \hat{c}_k e^{ik} + \hat{c}_k^\dagger \hat{c}_{-k}^\dagger e^{ik} - \hat{c}_k \hat{c}_{-k} e^{-ik} - \hat{c}_k \hat{c}_k^\dagger e^{-ik} - 2g \hat{c}_k^\dagger \hat{c}_k + g \right) \\ &= J \sum_k^{\text{B.z.}} \left(2[g - \cos k] \hat{c}_k^\dagger \hat{c}_k - i \sin k \hat{c}_k^\dagger \hat{c}_{-k}^\dagger + i \sin k \hat{c}_{-k} \hat{c}_k - g \right) \\ &= J \sum_k^{\text{B.z.}} \left([g - \cos k] \hat{c}_k^\dagger \hat{c}_k + [g - \cos k] (1 - \hat{c}_{-k} \hat{c}_{-k}^\dagger) - i \sin k \hat{c}_k^\dagger \hat{c}_{-k}^\dagger + i \sin k \hat{c}_{-k} \hat{c}_k - g \right) \\ &= J \sum_k^{\text{B.z.}} \left([g - \cos k] \hat{c}_k^\dagger \hat{c}_k - [g - \cos k] \hat{c}_{-k} \hat{c}_{-k}^\dagger - i \sin k \hat{c}_k^\dagger \hat{c}_{-k}^\dagger + i \sin k \hat{c}_{-k} \hat{c}_k - \cos k \right) \\ &= J \sum_k^{\text{B.z.}} \left(\hat{\Psi}_k^\dagger D_k \hat{\Psi}_k - \cos k \right), \end{aligned} \quad (1.83)$$

with the fermionic spinor

$$\hat{\Psi} = \begin{pmatrix} \hat{c}_k \\ \hat{c}_{-k}^\dagger \end{pmatrix}, \quad (1.84)$$

and

$$D_k = \begin{pmatrix} g - \cos k & -i \sin k \\ i \sin k & -[g - \cos k] \end{pmatrix}. \quad (1.85)$$

We now diagonalize (1.83) by carrying out the Bogoliubov transformation

$$\hat{\Psi}_k = \mathcal{U}_k \hat{\Gamma}_k, \quad (1.86)$$

with the Bogoliubov fermionic spinor

$$\hat{\Gamma} = \begin{pmatrix} \hat{\gamma}_k \\ \hat{\gamma}_{-k}^\dagger \end{pmatrix}, \quad (1.87)$$

and the diagonalizing unitary matrix

$$\mathcal{U}_k = \begin{pmatrix} \cos(\theta_k/2) & i \sin(\theta_k/2) \\ i \sin(\theta_k/2) & \cos(\theta_k/2) \end{pmatrix}, \quad (1.88)$$

where

$$\theta_k = \arctan \left(\frac{\sin k}{g + \cos k} \right). \quad (1.89)$$

This leads, up to some energy offset that we ignore, to the diagonalized Hamiltonian

$$\mathcal{H} = J \sum_k^{\text{B.z.}} \hat{\Gamma}_k^\dagger M_k \hat{\Gamma}_k,$$

with

$$M_k = \mathcal{U}_k^\dagger D_k \mathcal{U}_k = \begin{pmatrix} \epsilon_k & 0 \\ 0 & -\epsilon_k \end{pmatrix}, \quad (1.90)$$

where

$$\epsilon_k = \sqrt{g^2 - 2 \cos kg + 1}. \quad (1.91)$$

We see here that at $k = 0$, the system has a Bogoliubov-quasiparticle gap

$$\Delta = \sqrt{g^2 - 2g + 1} = |g - 1|, \quad (1.92)$$

which vanishes at the quantum critical point $g_c = h_c/J = 1$, giving us the quantum critical point of the NN-TFIM in one-dimensional space as $h_c = J$.

Long-range transverse-field Ising model

As such, we see now that in one-dimensional space we have a quantum phase transition for both the FC-TFIM and the NN-TFIM, but only the FC-TFIM has a thermal phase transition. But what about the general long-range power-law-interacting transverse-field Ising model (LR-TFIM)? The latter is described by the Hamiltonian

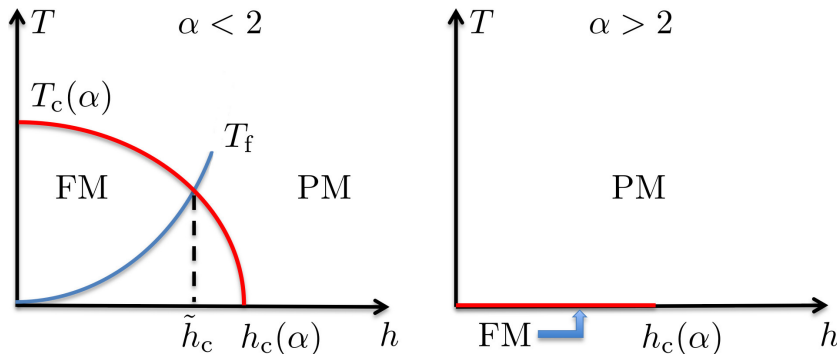


Figure 1.4: (Color online) Equilibrium phase diagram of the long-range power-law-interacting ($1/r^\alpha$ with r inter-spin distance) transverse-field Ising model (LR-TFIM). Using perturbative renormalization group [138], it can be shown that LR-TFIM has a quantum (zero-temperature) phase transition for all values of α . However, a finite-temperature (thermal) phase transition exists for this model only when $\alpha \leq 2$. For $\alpha = 2$ (not shown), the phase transition is a Kosterlitz-Thouless type. This equilibrium phase diagram can be reached, in a very convoluted manner, by quenching and waiting for the nonintegrable LR-TFIM ($0 < \alpha < \infty$) to thermalize. However, this would reveal no interesting dynamical properties. Figure adapted from Ref. [10].

$$\hat{H} = -J \sum_{i < j} \frac{\hat{\sigma}_i^z \hat{\sigma}_j^z}{|i - j|^\alpha} - h \sum_j \hat{\sigma}_j^x, \quad (1.93)$$

where $\alpha \geq 0$, with $\alpha = 0$ corresponding to the FC-TFIM and $\alpha \rightarrow \infty$ to the NN-TFIM. For a positive finite nonzero α , this model is nonintegrable and hence cannot be easily solved analytically. In Ref. [138], however, perturbative renormalization group is used to show that the LR-TFIM has a thermal phase transition only when $\alpha \leq 2$, and the α -dependent universality classes are derived for the general long-range case, where for $\alpha < 5/3$ mean-field analysis is exact and one obtains the long-range mean-field critical exponents

$$\gamma = 1, \quad \nu = \frac{1}{\alpha - 1}, \quad \eta = 3 - \alpha, \quad (1.94)$$

and for $\alpha > 3$ the phase transition is of the same universality class as in the nearest-neighbor transverse-field Ising model.

The result summarized in Fig. 1.4 is a very interesting one in that it naturally leads to the following correct, yet trivial, conclusion: *If the LR-TFIM is prepared in its ground-state ($T = 0$) and then subsequently undergoes a quench, since a quench injects energy density into the system, it effectively will lead the system to have a finite temperature upon thermalization, and therefore a finite order parameter may exist if and only if $\alpha \leq 2$, and therefore a dynamical phase transition (DPT) may exist in the LR-TFIM if and only if*

$\alpha \leq 2$. Indeed, this statement is not incorrect *per se*, in that it totally depends on what exactly one considers to be a *dynamical* phase transition. In the most stringent sense, a dynamical phase transition whose properties are gauged only upon thermalization does not really provide any information about dynamics in the system. In fact, such an analysis of post-thermalization dynamical phase transitions is nothing but a convoluted way of looking at the equilibrium phase diagram of the model under consideration. This is the topic we shall discuss next.

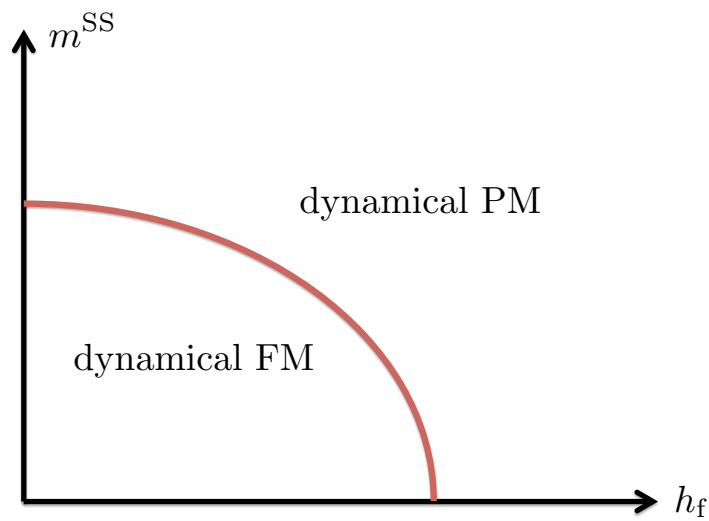


Figure 1.5: (Color online) Contrary to what may be naively drawn from Fig. 1.4, the Landau-type dynamical phase transition (DPT-I) exists for any α , even for values of $\alpha > 2$ where a corresponding finite temperature does not exist [138]. It turns out that prethermalization conspires in this model for $\alpha > 2$ to give rise to a quasi-steady state, namely the prethermal state, from which a stationary value m^{SS} of the order parameter (for quenches from $h_i < h_c(\alpha)$) can be extracted. For quenches to h_f not much different from h_i , the prethermal state carries a finite nonzero order parameter for the times accessible in our numerical simulations. For $\alpha < 2$ one sees the same behavior, albeit it is not so straightforward to judge whether the result is due to thermalization or prethermalization. This is a very interesting, and also challenging, point to further investigate.

1.5.2 Landau-type dynamical phase transition (DPT-I)

A Landau-type dynamical phase transition, which we shall denote by DPT-I, is a DPT where after quenching a system prepared in some initial state, we look for a Landau-type nonanalyticity in the free energy as a function of the quench control parameter, as per the

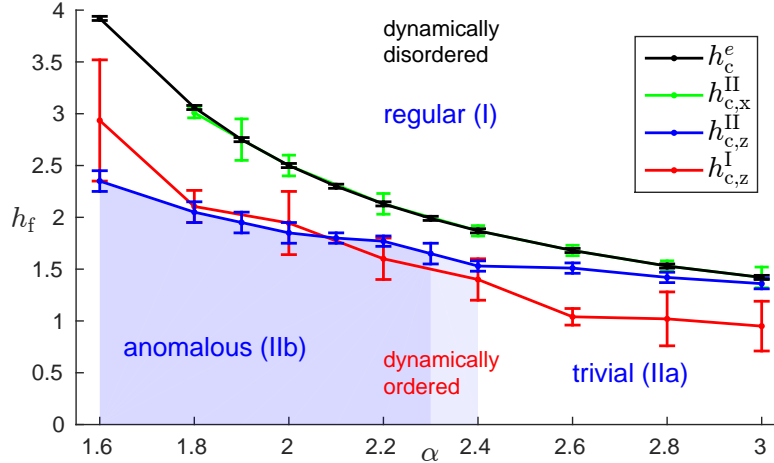


Figure 1.6: (Color online) Dynamical phase diagram of the LR-TFIM: h_c^e is the equilibrium critical line, $h_{c,z}^I$ is the DPT-I critical line, $h_{c,z(x)}^{II}$ is the DPT-II critical line for quenches from $h_i = 0$ ($h_i \rightarrow \infty$) which signifies the onset of *regular cusps* for quenches above (below) it. Note how the critical lines $h_{c,x}^{II}$ and h_c^e overlap very well within the precision of our numerical simulations. For quenches from $h_i = 0$ to below $h_{c,z}^{II}$, the system exhibits a trivial (cusp-free) phase for $\alpha \gtrsim 2.3$ and an anomalous phase for $\alpha \lesssim 2.3$. The dynamically ordered and disordered phases are related to DPT-I [10] and are separated by $h_{c,z}^I$. Figure adapted from Ref. [11].

Ehrenfest classification in equilibrium phase transitions. This could be, for example, a non-differentiable function of the order parameter as a function of the control parameter in case the system is prepared in the ordered phase. Starting from the disordered (\mathbb{Z}_2 -symmetric) phase means that the order parameter is always zero as quenching with a \mathbb{Z}_2 -symmetric Hamiltonian cannot break \mathbb{Z}_2 symmetry and yield a finite order parameter. This sort of DPT greatly resembles the Landau-type equilibrium phase transition (EPT). Assuming for the moment that we start from the equilibrium ordered phase, the only question here is how to extract the order parameter, and the answer is to find in a prethermal regime [139, 140, 141] a persistent (quasi-)steady state [133, 142, 143, 144, 145, 146, 147, 148, 149] where measuring such an order parameter makes sense. This steady state need not be an equilibrium state. As discussed in Sec. 1.4, even if our system is highly nonintegrable, small quenches can lead to long-lived prethermal quasi-steady states when thermalization may take too long to be observed experimentally or numerically.

Indeed, the DPT-I is a fascinating phenomenon to study as it can offer valuable insight into possible *dynamical* universality classes just as in the equilibrium case, where vastly different models exhibit the same equilibrium critical behavior, even though away from criticality they are quite dissimilar in their properties. In fact, it is this prospect of dynamical universality that makes dynamical phase transitions so interesting from a fundamental point of view, as universality classes in equilibrium are fascinating in them-

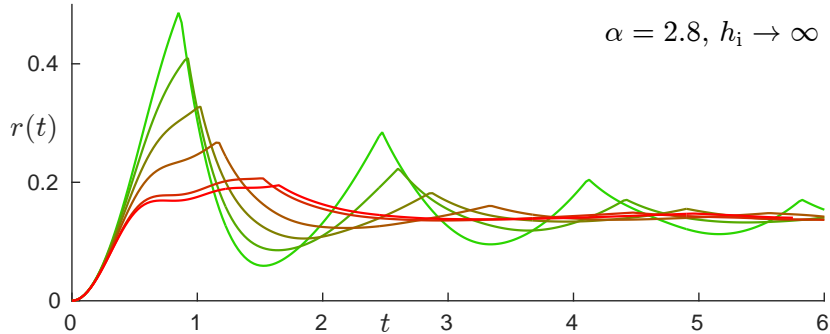


Figure 1.7: (Color online) Return-rate function $r(t)$ for $\alpha = 2.8$, quenches from $h_i \rightarrow \infty$ to $h_f \in [0.75, 1.40] < h_{c,x}^{\text{II}}(\alpha = 2.8)$ (from green to red). Figure adapted from Ref. [11].

selves and have been the topic of intense research. Moreover, it would be interesting to investigate the relationship between the dynamical universality class and its equilibrium counterpart. Are the critical exponents the same? Is there a certain relationship between them?

Considering again the LR-TFIM and its α -dependent phase diagram in Fig. 1.4, one wonders, given the prominent difference in the phase diagram from $\alpha < 2$ to $\alpha > 2$, whether or not the corresponding dynamical phase diagrams are also quite different. In fact, taking the trivial scenario of quantifying a DPT according to the steady-state value of the order parameter upon thermalization, one would expect the dynamical phase diagram to more or less mimic what one sees for equilibrium in Fig. 1.4. In fact, the corresponding dynamical phase diagram in such a case would be completely nonexistent for $\alpha > 2$, since any quench from, say $h_i = 0$ at $T = 0$, leads to populating the excited eigenstates of the quenching Hamiltonian, in turn leading to a finite temperature with respect to the quenching Hamiltonian, and thus automatically rendering the system in a disordered (paramagnetic) state. On the other hand, and as shown for $\alpha > 2$ in Fig. 1.4, this same effective quench temperature would lead to the dynamical critical field to shift to the left. This result is not surprising at all, and is in fact trivial inasmuch that it gives us no nontrivial information whatsoever about the actual dynamics.

Alternatively, one can classify dynamical phase transitions based on true nonequilibrium processes, such as prethermalization. The prethermal regime allows for a quasi-steady state that makes possible the measurement of an order parameter at intermediate evolution times as a function of the quenching parameter. This, in turn, leads to persistent dynamical order even when the corresponding thermal phase transition is absent, which gives rise to the DPT-I critical line h_c^{I} in Fig. 1.6 for quenches from $h_i = 0$. This is discussed in detail in Chapters 3 and 4, but it is interesting to note that this dynamical critical line h_c^{I} lies below the equilibrium critical line h_c^{e} . This is in agreement with our argument that quenches add energy density into the system, pushing the order parameter more towards a disordered phase (see Fig. 1.4).

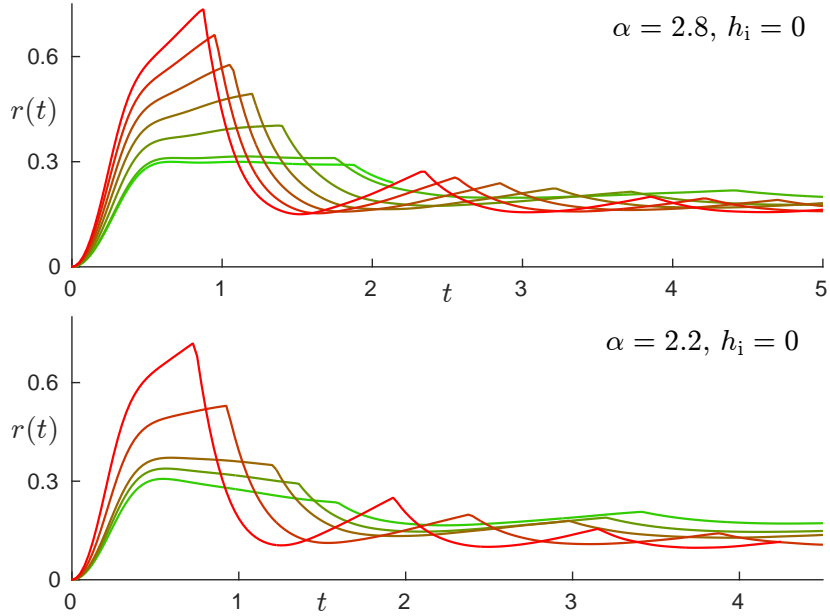


Figure 1.8: (Color online) Return-rate function $r(t)$ for quenches from $h_i = 0$ to $h_f \in [1.50, 2.30]$ (from green to red) for $\alpha = 2.8$ (top) and $h_f \in [1.80, 2.80]$ (from green to red) for $\alpha = 2.2$ (bottom). This behavior is qualitatively the same for all α . Figure adapted from Ref. [11].

1.5.3 Return-rate dynamical phase transition (DPT-II)

Consider a system in the groundstate $|\psi_0\rangle$ of Hamiltonian $\hat{H}(\lambda_i)$, where at $t = 0$ we quench this system with Hamiltonian $\hat{H}(\lambda_f)$, which for brevity we shall hereon denote as \hat{H} . The Loschmidt echo

$$G(t) = \langle \psi_0 | \psi(t) \rangle = \langle \psi_0 | e^{-i\hat{H}t} | \psi_0 \rangle \quad (1.95)$$

is the probability amplitude of the system returning to its initial state at some $t > 0$. A connection [95] was made between the Loschmidt echo (1.95) in a quantum system undergoing time evolution and the partition function of a system at thermal equilibrium at temperature T

$$\mathcal{Z} = \text{Tr}[e^{-\hat{H}/T}], \quad (1.96)$$

by considering the former as a boundary partition function with boundary condition $|\psi_0\rangle$ and complex temperature $1/z$

$$\mathcal{Z}_b = \langle \psi_0 | e^{-z\hat{H}} | \psi_0 \rangle, \quad (1.97)$$

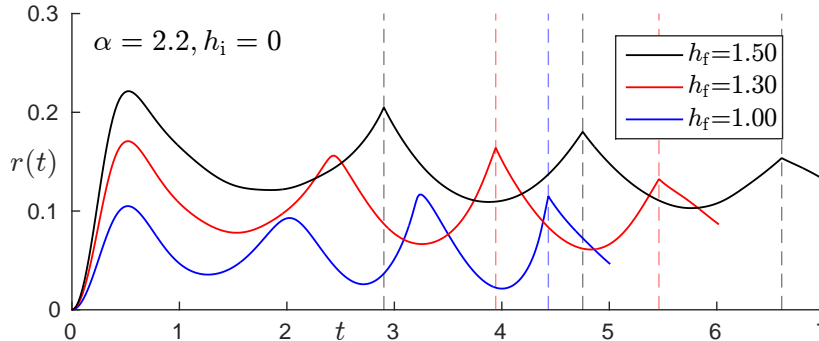


Figure 1.9: (Color online) Examples of anomalous cusps (marked by vertical dashed lines) for $h_f < h_{c,z}^{\text{II}}$. It is apparent that with increasing h_f more such cusps develop at smaller times, while their respective locations however move to higher times. Figure adapted from Ref. [11].

with the imaginary axis $z = it$. Subsequently, the return-rate function

$$r(t) = - \lim_{L \rightarrow \infty} \frac{1}{L} \ln |G(t)|^2 \quad (1.98)$$

can be seen as an analogue of the per-site free energy in which nonanalyticities signal the return-rate dynamical phase transition, which we shall hereon denote DPT-II. The DPT-II has been the subject of intense research recently, with analytical [95, 150, 151, 152, 153, 154] and numerical [11, 136, 155, 156] studies, and even recently experimental observations have been reported [157]. The nonanalyticity in the return rate that indicates the presence of a DPT-II arises in the form of nonanalytic cusps in this return rate that display interesting properties. In the seminal work of Ref. [95], it was shown that in the NN-TFIM, when one quenches from one equilibrium phase into the other at $T = 0$, the DPT-II occurs. Moreover, the stronger the inter-phase quench is (i.e. the greater $|h_i - h_f|$, roughly speaking), the sharper these cusps are, and the closer they are to one another in evolution time [95, 11]. Moreover, it was also reported that the general rule of inter-phase quenching to see a DPT-II in the NN-TFIM is not universal, and there are examples where intra-phase quenches lead to DPT-II, and inter-phase quenches that exhibit no DPT-II at all [158, 159].

In Chapter 4, we look at the DPT-II in the LR-TFIM for two types of quenches: those from $h_i \rightarrow \infty$ (X-quenches) and those from $h_i = 0$ (Z-quenches) using the infinite matrix product state method based on the time-dependent variational principle [160, 161]. Our results agree with those of Ref. [95] for X-quenches in the LR-TFIM in the large- α limit, as can be seen in Fig. 1.7. As can be seen in Fig. 1.6, the X-quench dynamical critical line $h_{c,x}^{\text{II}}$ for DPT-II coincides, within our numerical precision, with the equilibrium critical line h_c^e . Quenching from $h_i \rightarrow \infty$ to any $h_f > h_c^e$ leads to no cusps in the return rate regardless of the value of α , and hence no DPT-II appears. On the other hand, for all α one always finds a DPT-II when quenching from $h_i \rightarrow \infty$ to any $h_f < h_c^e$, i.e. by crossing the

equilibrium quantum critical point, as reported in Ref. [95] for the NN-TFIM. However, long-range interactions lead to very interesting behavior for the Z-quenches from $h_i = 0$. Firstly, much like the dynamical critical line for the DPT-I, we see that the Z-quench DPT-II critical line $h_{c,z}^{\text{II}} < h_c^e$. Moreover, there seems to be a nontrivial relation between the DPT-I and the DPT-II in the Z-quenches, albeit within our numerical precision, this is far from conclusive. For Z-quenches to $h_f > h_{c,z}^{\text{II}}$, we get regular cusps for all α , as shown in Fig. 1.8. More interestingly, we see that even though Z-quenches to $h_f < h_{c,z}^{\text{II}}$ show no cusps for larger α values, a new class of *anomalous* cusps appear for $\alpha \lesssim 2.3$ (see Fig. 1.9) that behave qualitatively differently from their regular counterparts that appear only when quenching from one dynamical phase to another in that the anomalous cusps get more temporally separated with increasing quench strength, and appear at later times in the return rate whereby they are preceded by analytic crests. This result greatly enriches the dynamical phase diagram of spin chains with long-range interactions.

Bibliography

- [1] J. C. Halimeh and M. Punk, Phys. Rev. B **94**, 104413 (2016).
- [2] S. Sachdev, Phys. Rev. B **45**, 12377 (1992).
- [3] F. Wang and A. Vishwanath, Phys. Rev. B **74**, 174423 (2006).
- [4] L. Messio, B. Bernu, and C. Lhuillier, Phys. Rev. Lett., **108**, 207204 (2012).
- [5] L. Messio, C. Lhuillier, and G. Misguich, Phys. Rev. B **87**, 125127 (2013).
- [6] M. Greiner, O. Mandel, T. Esslinger, T. W. Hänsch, and I. Bloch, Nature **415**, 39-44 (2002).
- [7] J. Honer, J. C. Halimeh, I. McCulloch, U. Schollwöck, and H. P. Büchler, Phys. Rev. A **86**, 051606(R) (2012).
- [8] J. C. Halimeh, A. Wöllert, I. P. McCulloch, U. Schollwöck, and T. Barthel, Phys. Rev. A **89**, 063603 (2014).
- [9] J. C. Halimeh, F. Kolley, and I. P. McCulloch, Phys. Rev. B **92**, 115130 (2015).
- [10] J. C. Halimeh, V. Zauner-Stauber, I. P. McCulloch, I. de Vega, U. Schollwöck, and M. Kastner, arXiv:1610.01468.
- [11] J. C. Halimeh and V. Zauner-Stauber, arXiv:1610.02019.
- [12] M. Cazalilla and B. Marston, Phys. Rev. Lett. **88** 256403 (2002).
- [13] H. G. Luo, T. Xiang, and X. Q. Wang, Phys. Rev. Lett. **91** 049701 (2003).
- [14] S.R. White and A. Feiguin, Phys. Rev. Lett. **93** 076401 (2004).
- [15] U. Schollwöck, Rev. Mod. Phys. **77**, 259 (2005).
- [16] S. R. White, Phys. Rev. Lett. **69**, 2863 (1992).
- [17] U. Schollwöck, J. Phys. Soc. Jpn. **74** (Suppl.), 246 (2005).
- [18] S. Östlund, and S. Rommer, Phys. Rev. Lett. **75** 3537 (1995).

-
- [19] J. Dukelsky, M. A. Martin-Delgado, T. Nishino and G. Sierra, *Europhys. Lett.* **43**, 457 (1997).
- [20] F. Verstraete, and J. I. Cirac, *Phys. Rev. Lett.* **73** 094423 (2006).
- [21] U. Schollwöck, *Ann. Phys. (NY)* **326**, 96 (2011).
- [22] F. Verstraete, J. J. García-Ripoll, and J. I. Cirac, *Phys. Rev. Lett.* **93**, 207204 (2004).
- [23] A. Feiguin and S. White, *Phys. Rev. B* **72**, 020404 (2005).
- [24] D. Gobert, C. Kollath, U. Schollwöck, and G. Schütz, *Phys. Rev. E* **71**, 036102 (2005).
- [25] G. Vidal, *Phys. Rev. Lett.* **91** 147902 (2003).
- [26] H. F. Trotter, *Proc. Am. Math. Soc.* **10** 545 (1959).
- [27] M. Suzuki, *Prog. Theor. Phys.* **56** 1454 (1976).
- [28] A. N. Krylov, *News of Academy of Sciences of USSR*, 1931, VII, Nr. 4, 491-539 (in Russian).
- [29] A. Flesch, M. Cramer, I. P. McCulloch, U. Schollwöck, and J. Eisert, *Phys. Rev. A* **78**, 033608 (2008).
- [30] P. Calabrese and J. Cardy, *J. Stat. Mech.* (2005) P04010.
- [31] C. Moler and Ch. van Loan, *SIAM Review* **45** 3 (2003).
- [32] A. J. Daley, C. Kollath, U. Schollwöck, and G. Vidal, *J. Stat. Mech.: Theory Exp.* (2004) P04005.
- [33] G. Vidal, *Phys. Rev. Lett.* **93** 040502 (2004).
- [34] L. Balents, *Nature* **464**, 199 (2010).
- [35] S. Sachdev, *Nature Physics* **4**, 173 (2008).
- [36] L. Savary and L. Balents, arXiv:1604.03048.
- [37] M.R. Norman, arXiv:1604.03048.
- [38] J. B. Marston and C. Zeng, *J. Appl. Phys.* **69**, 5962 (1991).
- [39] P. W. Leung and V. Elser, *Phys. Rev. B* **47**, 5459 (1993)
- [40] S. Yan, D. A. Huse, and S. R. White, *Science* **332**, 1173 (2011).
- [41] H.-C. Jiang, Z. Wang, and L. Balents, *Nature Physics* **8**, 902-905 (2012).

- [42] S. Depenbrock, I. P. McCulloch, and U. Schollwöck Phys. Rev. Lett. **109**, 067201 (2012).
- [43] F. Kolley, S. Depenbrock, I. P. McCulloch, U. Schollwöck, V. Alba, Phys. Rev. B **91**, 104418 (2015).
- [44] Y. Ran, M. Hermele, P.A. Lee, and X.-G. Wen, Phys. Rev. Lett. **98**, 117205 (2007).
- [45] Y. Iqbal, F. Becca, S. Sorella, and D. Poilblanc Phys. Rev. B **87**, 060405(R) (2013).
- [46] Y. Iqbal, D. Poilblanc, and F. Becca, Phys. Rev. B **91**, 020402(R) (2015).
- [47] T. Li, arXiv:1601.02165.
- [48] V. Kalmeyer and R. B. Laughlin, Phys. Rev. Lett. **59**, 2095 (1987); Phys. Rev. B **39**, 11879 (1989).
- [49] X.-G. Wen, F. Wilczek, and A. Zee, Phys. Rev. B **39**, 11413 (1989).
- [50] M. Greiter, D.F. Schroeter, and R. Thomale, Phys. Rev. B **89**, 165125 (2014).
- [51] Y.-C. He, D.N. Sheng, and Y. Chen, Phys. Rev. Lett. **112**, 137202 (2014).
- [52] S.-S. Gong, W. Zhu, and D.N. Sheng, Nature Scientific Reports **4**, 6317 (2014).
- [53] S.-S. Gong, W. Zhu, L. Balents, and D.N. Sheng, Physical Review B **91**, 075112 (2015).
- [54] B. Bauer, L. Cincio, B.P. Keller, M. Dolfi, G. Vidal, S. Trebst, and A.W.W. Ludwig, Nature Comm. **5**, 5137 (2014).
- [55] Y.-C. He and Y. Chen, Phys. Rev. Lett. **114**, 037201 (2015).
- [56] W.-J. Hu, W. Zhu, Y. Zhang, S. Gong, F. Becca, and D.N. Sheng, Phys. Rev. B **91**, 041124(R) (2015).
- [57] S. Bieri, L. Messio, B. Bernu, and C. Lhuillier, Phys. Rev. B **92**, 060407(R) (2015).
- [58] K. Kumar, K. Sun, and E. Fradkin, Phys. Rev. B **92**, 094433 (2015).
- [59] A. Wietek, A. Sterdyniak, and A.M. Läuchli, Phys. Rev. B **92**, 125122 (2015).
- [60] M. P. Shores, E. A. Nytko, B. M. Bartlett, and D. G. Nocera, J. Am. Chem. Soc. **127**, 13462 (2005).
- [61] M. A. de Vries, J. R. Stewart, P. P. Deen, J. O. Piatek, G. J. Nilsen, H. M. Rønnow, and A. Harrison, Phys. Rev. Lett. **103**, 237201 (2009).
- [62] J. S. Helton et al., Phys. Rev. Lett. **98**, 107204 (2007).

- [63] B.J. Powell and R.H. McKenzie, Rep. Prog. Phys. **74**, 056501 (2011).
- [64] T.-H. Han, J.S. Helton, S. Chu, D.G. Nocera, J. A. Rodriguez-Rivera, C. Broholm, and Y. S. Lee, Nature **492**, 406 (2012).
- [65] M. Fu, T. Imai, T.-H. Han, and Y. S. Lee, Science **350**, 655 (2015).
- [66] M. Punk, D. Chowdhury, and S. Sachdev, Nat. Phys. **10**, 289-293 (2014).
- [67] T.-H. Han, M.R. Norman, J.-J. Wen, J.A. Rodriguez-Rivera, J.S. Helton, C. Broholm, and Y.S. Lee, arXiv:1512.06807.
- [68] O. Janson, J. Richter, and H. Rosner, J. Phys.: Conf. Ser. **145**, 012008 (2009).
- [69] L. Messio, C. Lhuillier, and G. Misguich, Phys. Rev. B **83**, 184401 (2011).
- [70] R. Dijkgraaf and E. Witten, Commun. Math. Phys. **129**, 393 (1990).
- [71] M. Barkeshli, arXiv:1307.8194.
- [72] F. H. L. Essler and M. Fagotti, J. Stat. Mech. 064002 (2016).
- [73] V. E. Korepin, A. G. Izergin, and N. M. Bogoliubov, *Quantum Inverse Scattering Method, Correlation Functions, and Algebraic Bethe Ansatz*, (Cambridge University Press, 1993).
- [74] B. Davies and V. E. Korepin, arXiv:1109:6604.
- [75] A. C. Cassidy, C. W. Clark, and M. Rigol, Phys. Rev. Lett. **106** 140405 (2011).
- [76] C. Gramsch and M. Rigol, Phys. Rev. A **86** 053615 (2012).
- [77] T. M. Wright, M. Rigol, M. J. Davis, and K. V. Kheruntsyan, Phys. Rev. Lett. **113** 050601 (2014).
- [78] P. Calabrese, F. H. L. Essler, and M. Fagotti, Phys. Rev. Lett. **106** 227203 (2011).
- [79] P. Calabrese, F. H. L. Essler, and M. Fagotti, J. Stat. Mech. P07016 (2012).
- [80] P. Calabrese, F. H. L. Essler, and M. Fagotti, J. Stat. Mech. P07022 (2012).
- [81] M. Fagotti and F. H. L. Essler, Phys. Rev. B **87** 245107 (2013).
- [82] F. H. L. Essler, S. Evangelisti, and M. Fagotti, Phys. Rev. Lett. **109** 247206 (2012).
- [83] M. Fagotti, Phys. Rev. B **87** 165106 (2013).
- [84] M. Kormos, L. BucciAntini, and P. Calabrese, Europhys. Lett. **107** 40002 (2014).
- [85] L. BucciAntini, M. Kormos, P. Calabrese, J. Phys. A: Math. Theor. **47** 175002 (2014).

-
- [86] D. Rossini, A. Silva, G. Mussardo, and G. E. Santoro, Phys. Rev. Lett. **102** 127204 (2009); D. Rossini, S. Suzuki, G. Mussardo, G. E. Santoro, and A. Silva, Phys. Rev. B **82** 144302 (2010).
- [87] F. Iglói and H. Rieger, Phys. Rev. Lett. **85** 3233 (2000).
- [88] K. Sengupta, S. Powell, and S. Sachdev, Phys. Rev. A **69** 053616 (2004).
- [89] A. Silva, Phys. Rev. Lett. **101** 120603 (2008).
- [90] F. Iglói and H. Rieger, Phys. Rev. Lett. **106** 035701 (2011).
- [91] L. Foini, L. F. Cugliandolo, and A. Gambassi, Phys. Rev. B **84** 212404 (2011).
- [92] H. Rieger and F. Igli, Phys. Rev. B **84** 165117 (2011).
- [93] D. Schuricht and F. H. L. Essler, J. Stat. Mech. P04017 (2012).
- [94] L. Foini, L. F. Cugliandolo, and A. Gambassi, J. Stat. Mech. P09011 (2012).
- [95] M. Heyl, A. Polkovnikov, and S. Kehrein, Phys. Rev. Lett. **110** 135704 (2013).
- [96] T. Caneva, E. Canovi, D. Rossini, G. E. Santoro, and A. Silva, J. Stat. Mech. P07015 (2011).
- [97] T. Antal, Z. Racz, A. Rakos, and G. M. Schutz, Phys. Rev. E **59** 4912 (1999).
- [98] E. Barouch, B. McCoy, and M. Dresden, Phys. Rev. A **2** 1075 (1970).
- [99] E. Barouch and B. McCoy, Phys. Rev. A **3** 786 (1971).
- [100] E. Barouch and B. McCoy, Phys. Rev. A **3** 2137 (1971).
- [101] M. Fagotti and P. Calabrese, Phys. Rev. A **78** 010306 (2008).
- [102] M. A. Cazalilla, A. Iucci, and M.-C. Chung, Phys. Rev. E **85** 011133 (2012).
- [103] B. Blass, H. Rieger, and F. Iglói, Europhys. Lett. **99** 30004 (2012).
- [104] M. Fagotti, J. Stat. Mech. P03016 (2014).
- [105] M. Fagotti, J. Stat. Mech. 063105 (2016).
- [106] M. Collura, P. Calabrese, and F. H. L. Essler, Phys. Rev. B **92** 125131 (2015).
- [107] J. Lancaster and A. Mitra, Phys. Rev. E **81** 061134 (2010).
- [108] T. Sabetta and G. Misguich, Phys. Rev. B **88** 245114 (2013).
- [109] L. Bonnes, F. H. L. Essler, and A. Läuchli, Phys. Rev. Lett. **113** 187203 (2014).

-
- [110] E. Canovi, D. Rossini, R. Fazio, G. Santoro, and A. Silva, *New J. Phys.* **14** 095020 (2012).
- [111] M. Fagotti and F. H. L. Essler, *J. Stat. Mech.* P07012 (2013).
- [112] B. Pozsgay, *J. Stat. Mech.* P07003 (2013).
- [113] M. Fagotti, arXiv:1308.0277; B. Pozsgay, *J. Stat. Mech.* P10028.
- [114] W. Liu and N. Andrei, *Phys. Rev. Lett.* **112** 257204 (2014).
- [115] P. Barmettler, M. Punk, V. Gritsev, E. Demler, and E. Altman, *Phys. Rev. Lett.* **102** 130603 (2009); P. Barmettler, M. Punk, V. Gritsev, E. Demler, and E. Altman, *New J. Phys.* **12** 055017 (2010).
- [116] M. Fagotti, M. Collura, F. H. L. Essler, and P. Calabrese, *Phys. Rev. B* **89** 125101 (2014).
- [117] E. Ilievski, J. De Nardis, B. Wouters, J.-S. Caux, F. H. L. Essler, and T. Prosen, *Phys. Rev. Lett.* **115** 157201 (2015).
- [118] M. Brockmann, B. Wouters, D. Fioretto, J. De Nardis, R. Vlijm, and J.-S. Caux, *J. Stat. Mech.* P12009 (2014).
- [119] B. Wouters, J. De Nardis, M. Brockmann, D. Fioretto, M. Rigol, and J.-S. Caux, *Phys. Rev. Lett.* **113** 117202 (2014).
- [120] B. Pozsgay, *J. Stat. Mech.* P06011 (2014).
- [121] B. Pozsgay, M. Mestyán, M. A. Werner, M. Kormos, G. Zaránd, and G. Takács, *Phys. Rev. Lett.* **113** 117203 (2014).
- [122] M. Mestyán, B. Pozsgay, G. Takács, and M. A. Werner M A, *J. Stat. Mech.* P04001 (2015).
- [123] M. Rigol, *Phys. Rev. E* **90** 031301 (2014).
- [124] J. Mossel and J.-S. Caux, *New J. Phys.* **12** 055028 (2010).
- [125] V. Alba and P. Calabrese, arXiv:1512.02213 (2015).
- [126] M. Kollar and M. Eckstein, *Phys. Rev. A* **78** 013626 (2008).
- [127] T. Enss and J. Sirker, *New J. Phys.* **14** 023008 (2012).
- [128] D. Iyer, R. Mondaini, S. Will, and M. Rigol, *Phys. Rev. A* **90** 031602 (2014).
- [129] L. Riegger, G. Orso, and F. Heidrich-Meisner, *Phys. Rev. A* **91** 043623 (2015).

-
- [130] A. Bauer, F. Dorfner, and F. Heidrich-Meisner, *Phys. Rev. A* **91** 053628 (2015).
- [131] J. M. Deutsch, *Phys. Rev. A* **43** 2046 (1991).
- [132] M. Srednicki, *Phys. Rev. E* **50** 888 (1994).
- [133] M. Moeckel and S. Kehrein, *Phys. Rev. Lett.* **100**, 175702 (2008).
- [134] H. Onnes, *Comm. Phys. Lab. Univ. Leiden* **122**, 124 (1911).
- [135] A. Das, K. Sengupta, D. Sen, and B. K. Chakrabarti, *Phys. Rev. B* **74**, 144423 (2006).
- [136] B. Zunkovic, M. Heyl, M. Knap, and A. Silva, arXiv:1609.08482.
- [137] O. Derzhko and T. Krokhamalskii, *Phys. Stat. Sol. (b)* **208**, 221 (1998).
- [138] A. Dutta and J. K. Bhattacharjee, *Phys. Rev. B* **64**, 184106 (2001).
- [139] M. Eckstein and M. Kollar, *Phys Rev. Lett.* **100** 120404 (2008).
- [140] M. Eckstein, M. Kollar and P. Werner, *Phys Rev. Lett.* **103** 056403 (2009).
- [141] N. Tsuji, M. Eckstein, and P. Werner, *Phys. Rev. Lett.* **110** 136404 (2013).
- [142] M. Moeckel and S. Kehrein, *New J. Phys.* **12** 055016 (2010).
- [143] B. Sciolla and G. Biroli, *Phys. Rev. Lett.* **105** 220401 (2010).
- [144] B. Sciolla and G. Biroli, *J. Stat. Mech.* 2011, P11003.
- [145] A. Gambassi and P. Calabrese, *Europhys. Lett.* **95** 66007 (2011).
- [146] B. Sciolla and G. Biroli, *Phys. Rev. B* **88** 201110 (2013).
- [147] A. Chandran, A. Nanduri, S. S. Gubser, and S. L. Sondhi, *Phys. Rev. B* **88** 024306 (2013).
- [148] A. Maraga, A. Chiocchetta, A. Mitra, and A. Gambassi, *Phys. Rev. E* **92** 042151 (2015).
- [149] P. Smacchia, M. Knap, E. Demler, and A. Silva, *Phys. Rev. B* **91** 205136 (2015).
- [150] M. Heyl, *Phys. Rev. Lett.* **113** 205701 (2014).
- [151] M. Heyl, *Phys. Rev. Lett.* **115** 140602 (2015).
- [152] M. Heyl, arXiv:1608.06659.
- [153] S. Campbell, arXiv:1608.05325.

- [154] B. Zunkovic, A. Silva, and M. Fabrizio, *Phil. Trans. R. Soc. A* **374**, 20150160 (2016).
- [155] E. Canovi, P. Werner, and M. Eckstein, *Phys. Rev. Lett.* **113** 265702 (2014).
- [156] C. Karrasch and D. Schuricht, *Phys. Rev. B* **87** 195104 (2013).
- [157] N. Fläschner et al., arXiv1608:05616.
- [158] F. Andraschko and J. Stirker, *Phys. Rev. B* **89** 125120 (2014).
- [159] S. Vajna and B. Dóra, *Phys. Rev. B* **89** 161105(R) (2014).
- [160] M. Fannes, B. Nachtergaele, and R. Werner, *Comm. Math. Phys.* **144**, 443 (1992).
- [161] F. Verstraete, V. Murg, and J. I. Cirac, *Adv. Phys.* **57**, 143 (2008).

Chapter 2

Spin structure factors of chiral quantum spin liquids on the kagome lattice

The antiferromagnetic Heisenberg model on the kagome lattice (AFKM) is a paradigm of frustrated magnetism. The groundstate of the AFKM is still unsolved, and is the topic of intense research. Schwinger-boson mean-field theory (SBMFT) has proven to be a powerful tool in the study of possible groundstate candidates for the AFKM. On the other hand, inelastic neutron scattering experiments have been a crucial tool in studying materials that show promise as hosts of spin-liquid groundstates, such as Herbertsmithite and organic transfer salts. Therefore, dynamical structure factors of candidate groundstates would potentially offer an important connection to experiment, and as such a proper characterization of them is very useful. In this work, we derive and calculate the dynamical structure factor of various chiral ansätze within the framework of SBMFT.

- *Spin structure factors of chiral quantum spin liquids on the kagome lattice*
Jad C. Halimeh and Matthias Punk
Phys. Rev. B **94**, 104413 (2016)

Spin structure factors of chiral quantum spin liquids on the kagome latticeJad C. Halimeh¹ and Matthias Punk^{1,2}¹*Physics Department and Arnold Sommerfeld Center for Theoretical Physics, Ludwig-Maximilians-Universität München, D-80333 München, Germany*²*Center for NanoScience, Ludwig-Maximilians-Universität München, D-80333 München, Germany*

(Received 25 June 2016; published 13 September 2016)

We calculate dynamical spin structure factors for gapped chiral spin liquid states in the spin-1/2 Heisenberg antiferromagnet on the kagome lattice using Schwinger-boson mean-field theory. In contrast to static (equal-time) structure factors, the dynamical structure factor shows clear signatures of time-reversal symmetry breaking for chiral spin liquid states. In particular, momentum inversion $\mathbf{k} \rightarrow -\mathbf{k}$ symmetry as well as the sixfold rotation symmetry around the Γ point are lost. We highlight other interesting features, such as a relatively flat onset of the two-spinon continuum for the *cuboc1* state. Our work is based on the projective symmetry group classification of time-reversal symmetry breaking Schwinger-boson mean-field states by Messio, Lhuillier, and Misguich.

DOI: [10.1103/PhysRevB.94.104413](https://doi.org/10.1103/PhysRevB.94.104413)**I. INTRODUCTION**

The potential to realize interesting quantum spin liquid states with fractionalized excitations and topological order has driven research on frustrated magnets in the last decades [1–4]. One of the most promising candidate models is the spin-1/2 Heisenberg antiferromagnet on the two-dimensional kagome lattice. Many theoretical attempts have been made to unravel its ground-state properties, which are still not fully understood. While early approaches supported a symmetry broken valence bond solid state [5,6], various different ground states have been proposed since. Recent numerical works based on the density matrix renormalization group (DMRG) method provide strong evidence for a gapped \mathbb{Z}_2 spin liquid state [7–10], whereas projected wave-function studies favor a gapless U(1)-Dirac spin liquid ground state [11–13], but this issue is not settled yet [14]. Both of these states do not break lattice symmetries and lack conventional long-range magnetic order due to strong quantum fluctuations associated with the frustrated spin-exchange interactions.

The interest in chiral spin liquids, which break time-reversal and parity symmetries, was triggered by Kalmeyer and Laughlin, who proposed that bosonic analogues of fractional quantum Hall states could be realized in frustrated magnets [15]. Within a slave-fermion approach these chiral states are stable phases of matter, because gauge fluctuations are gapped by a Chern-Simons term [16]. More recently, various theoretical works showed that such chiral spin liquids can be stabilized on the kagome lattice either by including further-neighbor interactions or additional terms that explicitly break time-reversal symmetry [17–26].

As far as experiments are concerned, the mineral Herbertsmithite as well as organic charge transfer salts are the most promising candidate materials to host a spin liquid ground state [27–30]. While measurements on the triangular lattice organic salts are consistent with a gapless spin liquid, the kagome lattice compound Herbertsmithite likely has a gapped spin liquid ground state. Inelastic neutron scattering experiments are compatible with a continuum of fractionalized spinon excitations [31], and recent NMR measurements indicate that the ground state is gapped [32]. The fact that no sharp onset of the two-spinon continuum was observed in neutron scattering has been attributed to the presence of a flat band of topological

vison excitations in gapped \mathbb{Z}_2 spin liquids [33], as well as to the contribution from impurities at low energies [34].

Various different spin liquid states have been proposed as potential ground states of kagome Heisenberg antiferromagnets. In order to relate theoretical results to inelastic neutron scattering experiments, a better characterization of dynamical structure factors in kagome systems is clearly beneficial. In this work we take a step in this direction by computing dynamical spin structure factors of simple chiral spin liquids using Schwinger-boson mean-field theory [35,36]. Our approach is based on an earlier projective symmetry group classification of time-reversal symmetry breaking mean-field *Ansätze* by Messio, Lhuillier, and Misguich [37]. We show that the dynamical spin structure factor $S(\mathbf{k}, \omega)$ shows clear signatures of time-reversal symmetry breaking, in contrast to static (equal-time) structure factors. In particular, momentum inversion symmetry $\mathbf{k} \rightarrow -\mathbf{k}$ is lost and consequently the sixfold rotation symmetry of $S(\mathbf{k}, \omega)$ around the Γ point is reduced to threefold rotations. Moreover, we show that the onset of the two-spinon continuum is rather flat for the *cuboc1* state, which has been argued to minimize the ground-state energy of the kagome Heisenberg antiferromagnet within the Schwinger-boson approach [38]. This particular chiral spin liquid state is a quantum disordered version of the magnetically ordered *cuboc1* state, which is a possible noncoplanar state of the classical AFKM model [39,40].

It is important to note that this Schwinger-boson construction does not lead to chiral spin liquids of the Kalmeyer-Laughlin type. This is due to the fact that the condensation of boson bilinears reduces the gauge symmetry from U(1) to \mathbb{Z}_2 . Consequently, the effective low-energy theory is a Chern-Simons-Higgs theory with a condensed charge-2 Higgs field, the topological properties of which are typically equivalent to \mathbb{Z}_2 gauge theory [41,42].

The remainder of our paper is structured as follows. In Sec. II, we review the Schwinger-boson mean-field theory (SBMFT) for time-reversal symmetry breaking *Ansätze* and calculate the spinon dispersions. In Sec. III, we determine the mean-field parameters self-consistently for all SBMFT *Ansätze* considered in this work. In Sec. IV, the spin structure factor for a general chiral SBMFT *Ansatz* is derived. Lastly, in Sec. V, we present and discuss the numerically computed structure factors. We conclude with Sec. VI.

II. MODEL AND METHODS

The Hamiltonian of the antiferromagnetic Heisenberg model is given by

$$\hat{H} = J \sum_{\langle lj \rangle} \hat{\mathbf{S}}_l \cdot \hat{\mathbf{S}}_j, \quad (1)$$

where $J > 0$, $\hat{\mathbf{S}}_l$ is the spin operator on lattice site l and the sum runs over nearest-neighbor sites. In the following, we use the Schwinger-boson representation of spin operators

$$\hat{\mathbf{S}}_l = \frac{1}{2} \hat{b}_{l\alpha}^\dagger \hat{\sigma}_{\alpha\beta} \hat{b}_{l\beta}, \quad (2)$$

where here, and throughout this paper, we employ a summation convention over repeated Greek indices, and $\hat{b}_{l\alpha}$, $\hat{b}_{l\alpha}^\dagger$ are bosonic annihilation and creation operators, respectively, of spin α on site l . Consequently, the Hamiltonian can be written as

$$\hat{H} = \frac{J}{4} \sum_{\langle lj \rangle} (2\delta_{\alpha\mu}\delta_{\beta\gamma} - \delta_{\alpha\beta}\delta_{\gamma\mu}) \hat{b}_{l\alpha}^\dagger \hat{b}_{l\beta} \hat{b}_{j\gamma}^\dagger \hat{b}_{j\mu} + \lambda \sum_j (\hat{n}_j - 2S), \quad (3)$$

where the Lagrange multiplier λ constrains the number of bosons per site to $2S$, with S the length of the spin. Note that this length constraint is only imposed on average here and in the following mean-field approximation. It can be enforced exactly by allowing for a space- and imaginary time dependent Lagrange multiplier, which leads to a theory of bosonic spinons coupled to an emergent U(1) gauge field [35]. However, for the spin liquid states considered in this work, the condensation of bosonic bilinears gaps out gauge fluctuations and the mean-field approximation is justified.

A. Schwinger-boson mean-field theory

We now introduce the SU(2)-invariant bond operators

$$\hat{\mathcal{A}}_{lj} = \frac{1}{2} \varepsilon^{\alpha\beta} \hat{b}_{l\alpha} \hat{b}_{j\beta}, \quad (4)$$

$$\hat{\mathcal{B}}_{lj} = \frac{1}{2} \hat{b}_{l\alpha}^\dagger \hat{b}_{j\alpha}, \quad (5)$$

where $\varepsilon^{\alpha\beta}$ is the fully antisymmetric tensor of SU(2). One can show that $\hat{\mathbf{S}}_l \cdot \hat{\mathbf{S}}_j = (\hat{\mathcal{B}}_{lj}^\dagger \hat{\mathcal{B}}_{lj} - \hat{\mathcal{A}}_{lj}^\dagger \hat{\mathcal{A}}_{lj})$ for $l \neq j$ and the Hamiltonian can be rewritten as

$$\hat{H} = J \sum_{\langle lj \rangle} (\hat{\mathcal{B}}_{lj}^\dagger \hat{\mathcal{B}}_{lj} - \hat{\mathcal{A}}_{lj}^\dagger \hat{\mathcal{A}}_{lj}) + \lambda \sum_j (\hat{n}_j - 2S). \quad (6)$$

Next, we apply a mean-field decoupling of the bond operators resulting in the mean-field Hamiltonian

$$\begin{aligned} \hat{H}_{\text{MF}} = & J \sum_{\langle lj \rangle} ((\hat{\mathcal{B}}_{lj}^\dagger) \hat{\mathcal{B}}_{lj}^\dagger - \langle \hat{\mathcal{A}}_{lj} \rangle \hat{\mathcal{A}}_{lj}^\dagger + \text{H.c.}) \\ & + J \sum_{\langle lj \rangle} (\langle \hat{\mathcal{A}}_{lj}^\dagger \rangle \langle \hat{\mathcal{A}}_{lj} \rangle - \langle \hat{\mathcal{B}}_{lj}^\dagger \rangle \langle \hat{\mathcal{B}}_{lj} \rangle) + \lambda \sum_j (\hat{n}_j - 2S). \end{aligned} \quad (7)$$

$\langle \mathcal{A}_{lj} \rangle$ and $\langle \mathcal{B}_{lj} \rangle$ are free complex mean-field parameters that will be computed self-consistently by extremizing the free energy. Even though most SBMFT studies use one or the other, including both $\langle \mathcal{A}_{lj} \rangle$ and $\langle \mathcal{B}_{lj} \rangle$ has been proven to lead to a

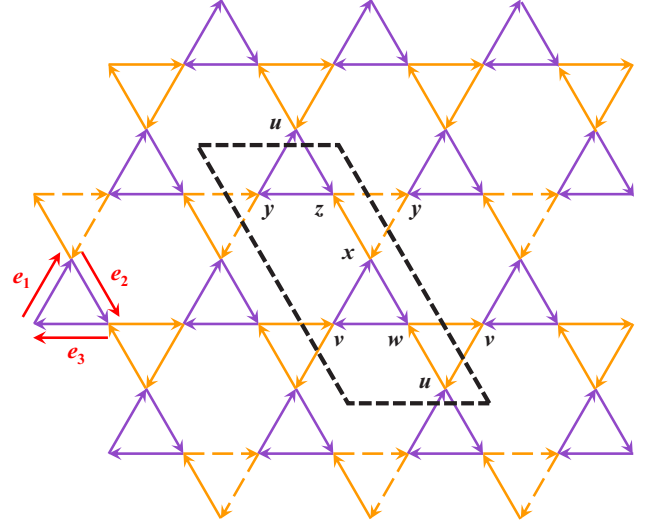


FIG. 1. The six-site unit cell of the general chiral SBMFT *Ansatz* as discussed in Refs. [38,37]. The bond operators $\langle \hat{\mathcal{A}}_{lj} \rangle = |\hat{\mathcal{A}}_{lj}| e^{i\theta_A}$ and $\langle \hat{\mathcal{B}}_{lj} \rangle = |\hat{\mathcal{B}}_{lj}| e^{i\theta_B}$ between two neighboring sites l and j are such that at every bond one has $|\hat{\mathcal{A}}_{lj}| = \mathcal{A}$ and $|\hat{\mathcal{B}}_{lj}| = \mathcal{B}$. On purple (dark) bonds $\theta_A = 0$ and $\theta_B = \phi_B$, while on orange (bright) bonds the phases are $\theta_A = \phi_A + \phi$ and $\theta_B = \phi_B + \phi$ with $\phi = 0$ on undashed bonds and $\phi = p_1\pi$ on dashed bonds, where $p_1 \in \{0,1\}$ depending on the *Ansatz*. Finally, the red arrows indicate the real-space vectors $\mathbf{e}_1 = a(1/2, \sqrt{3}/2)$, $\mathbf{e}_2 = a(1/2, -\sqrt{3}/2)$, and $\mathbf{e}_3 = a(-1, 0)$, with a the spacing between two neighboring sites, and $k_j = \mathbf{k} \cdot \mathbf{e}_j$.

better description of the spectrum of excitations in frustrated magnets [43,44], where $\langle \mathcal{A}_{lj} \rangle$ describes singlet amplitudes and $\langle \mathcal{B}_{lj} \rangle$ describes boson hopping amplitudes. A set $\{\langle \mathcal{A}_{lj} \rangle, \langle \mathcal{B}_{lj} \rangle\}$ specifies a mean-field *Ansatz*. For the symmetric, time-reversal breaking spin-liquids considered in Refs. [38], [37] the mean-field parameters take the form

$$\langle \hat{\mathcal{A}}_{lj} \rangle = \langle \hat{\mathcal{A}}_{lj}^\dagger \rangle^* = |\hat{\mathcal{A}}_{lj}| e^{i\theta_A}, \quad (8)$$

$$\langle \hat{\mathcal{B}}_{lj} \rangle = \langle \hat{\mathcal{B}}_{lj}^\dagger \rangle^* = |\hat{\mathcal{B}}_{lj}| e^{i\theta_B}, \quad (9)$$

where the moduli $|\hat{\mathcal{A}}_{lj}| = \mathcal{A}$ and $|\hat{\mathcal{B}}_{lj}| = \mathcal{B}$ are the same on each bond, but the phases θ_B and θ_A are bond-dependent. The detailed form of these *Ansätze* is shown in Fig. 1. Taking the Fourier transform of the Schwinger-boson operator as

$$\hat{b}_{l\alpha}^s = \frac{1}{\sqrt{N_q}} \sum_{\mathbf{q}} \hat{b}_{\mathbf{q}\alpha}^s e^{i\mathbf{q} \cdot \mathbf{r}_l}, \quad (10)$$

where s is a band index, \mathbf{r}_l is the position of site l , and N_q is the number of \mathbf{q} points summed over in the Fourier transform, and adopting a general chiral *Ansatz* following the notation of Ref. [37], the Hamiltonian in reciprocal space reads

$$\begin{aligned} \hat{H}_{\text{MF}} = & \sum_{\mathbf{k}} \hat{\Psi}_{\mathbf{k}}^\dagger D_{\mathbf{k}} \hat{\Psi}_{\mathbf{k}} + 2J N_s (|\mathcal{A}|^2 - |\mathcal{B}|^2) \\ & - \lambda N_s (1 + 2S), \end{aligned} \quad (11)$$

where we have introduced the spinor

$$\hat{\Psi}_k = \begin{pmatrix} \hat{b}_{k\uparrow}^u \\ \vdots \\ \hat{b}_{k\uparrow}^z \\ \hat{b}_{-k\downarrow}^{u\dagger} \\ \vdots \\ \hat{b}_{-k\downarrow}^{z\dagger} \end{pmatrix}, \quad (12)$$

with the superscript letters denoting one of the six bands $\{u, v, w, x, y, z\}$ of the six-site unit cell shown in Fig. 1, and D_k is the Hermitian block matrix

$$D_k = \lambda \mathbb{1}_{12} + C_k, \quad (13)$$

with $\mathbb{1}_d$ the $d \times d$ identity matrix, and

$$C_k = \frac{J}{2} \begin{pmatrix} R_k(\phi_{B'}) & T_k & P_k(\phi_{A'}) & Q_k \\ T_k^\dagger & R_k(\phi_{B'} + p_1\pi) & Q_k & P_k(\phi_{A'} + p_1\pi) \\ P_k^\dagger(\phi_{A'}) & Q_k^\dagger & R_{-k}^*(\phi_{B'}) & T_{-k}^* \\ Q_k^\dagger & P_k^\dagger(\phi_{A'} + p_1\pi) & T_{-k}^\dagger & R_{-k}^*(\phi_{B'} + p_1\pi) \end{pmatrix}, \quad (14)$$

$$R_k(v) = \mathcal{B} \begin{pmatrix} 0 & e^{-i(v-k_1)} & e^{i(\phi_{B'}-k_2)} \\ e^{i(v-k_1)} & 0 & e^{-i(v-k_3)} + e^{-i(\phi_B+k_3)} \\ e^{-i(\phi_{B'}-k_2)} & e^{i(v-k_3)} + e^{i(\phi_B+k_3)} & 0 \end{pmatrix}, \quad (15)$$

$$T_k = \mathcal{B} \begin{pmatrix} 0 & e^{-i(\phi_B+k_1)} & e^{i(\phi_B+k_2)} \\ e^{i(\phi_B+k_1)} & 0 & 0 \\ e^{-i(\phi_B+k_2)} & 0 & 0 \end{pmatrix}, \quad (16)$$

$$P_k(v) = \mathcal{A} \begin{pmatrix} 0 & -e^{i(v+k_1)} & e^{i(\phi_{A'}-k_2)} \\ e^{i(v-k_1)} & 0 & -e^{i(v+k_3)} - e^{-ik_3} \\ -e^{i(\phi_{A'}+k_2)} & e^{i(v-k_3)} + e^{ik_3} & 0 \end{pmatrix}, \quad (17)$$

$$Q_k = \mathcal{A} \begin{pmatrix} 0 & -e^{-ik_1} & e^{ik_2} \\ e^{ik_1} & 0 & 0 \\ -e^{-ik_2} & 0 & 0 \end{pmatrix}. \quad (18)$$

Here we denote the real-space vectors $\mathbf{e}_1 = a(1/2, \sqrt{3}/2)$, $\mathbf{e}_2 = a(1/2, -\sqrt{3}/2)$, and $\mathbf{e}_3 = a(-1, 0)$, and $k_j = \mathbf{k} \cdot \mathbf{e}_j$, as shown in Fig. 1, with $j \in \{1, 2, 3\}$ and a the intersite spacing, which we set to unity.

B. Bogoliubov transformation

Finally, we perform a Bogoliubov transformation by defining the bosonic operators

$$\hat{\Gamma}_k = \begin{pmatrix} \hat{\gamma}_{k\uparrow}^u \\ \vdots \\ \hat{\gamma}_{k\uparrow}^z \\ \hat{\gamma}_{-k\downarrow}^{u\dagger} \\ \vdots \\ \hat{\gamma}_{-k\downarrow}^{z\dagger} \end{pmatrix}, \quad (19)$$

which are related to the Schwinger-boson ladder operators by the linear transformation

$$\hat{\Psi}_k = M_k \hat{\Gamma}_k, \quad (20)$$

whereby $\hat{\Gamma}$ will satisfy the canonical commutation relations and diagonalize \hat{H}_{MF} if

$$M_k^\dagger \tau^6 M_k = \tau^6, \quad (21)$$

$$M_k^\dagger D_k M_k = \tilde{\epsilon}_k, \quad (22)$$

where the Bogoliubov rotation matrix takes the block form

$$M_k = \begin{pmatrix} U_k & X_k \\ V_k & Y_k \end{pmatrix}. \quad (23)$$

Furthermore,

$$\tau^6 = \begin{pmatrix} \mathbb{1}_6 & \mathbf{0} \\ \mathbf{0} & -\mathbb{1}_6 \end{pmatrix} \quad (24)$$

and

$$\tilde{\epsilon}_k = \begin{pmatrix} \mathcal{E}_{k\uparrow} & \mathbf{0} \\ \mathbf{0} & \mathcal{E}_{-k\downarrow} \end{pmatrix} \quad (25)$$

is a 12×12 diagonal matrix representing the bosonic eigenenergies for up-spins at momentum \mathbf{k} and down spins at momentum $-\mathbf{k}$, where the 6×6 diagonal matrix $\mathcal{E}_{p\alpha}$ carries

TABLE I. Self-consistent mean-field parameters and corresponding free energy per site $f_{\text{MF}} = \mathcal{F}_{\text{MF}}/N_s$ for the *cuboc1*, *cuboc2*, *octahedral*, $q = 0$, and $\sqrt{3} \times \sqrt{3}$ SBMFT *Ansätze* on the AFKM. The asterisk denotes a free mean-field parameter of the *Ansatz*, which is self-consistently determined in the gapped spin liquid phase for spin $S = 0.2$.

	<i>cuboc1</i>	<i>cuboc2</i>	<i>octahedral</i>	$q = 0$	$\sqrt{3} \times \sqrt{3}$
$p1$	1	1	1	0	0
\mathcal{A}	0.2616*	0.2624*	0.2617*	0.2626*	0.2637*
$\phi_{\mathcal{A}'}$	1.0143*	0	π	0	π
\mathcal{B}	0.0540*	0.0535*	0.0536*	0.0577*	0.0574*
$\phi_{\mathcal{B}}$	π	3.1417*	3.1416*	π	π
$\phi_{\mathcal{B}'}$	π	$-\phi_{\mathcal{B}}$	$\phi_{\mathcal{B}}$	π	π
λ	0.4086*	0.4137*	0.4096*	0.4125*	0.4182*
f_{MF}	-0.13127	-0.13200	-0.13134	-0.13148	-0.13266

the bosonic eigenenergies $\epsilon_{p\alpha}^s$ along its diagonal with s the band index whose values range in $\{u, v, w, x, y, z\}$, the six bands comprising our unit cell as illustrated in Fig. 1, while \mathbf{p} and α are the momentum and spin polarization, respectively, and $\mathbf{0}$ is the 6×6 zero matrix. It is to be noted here that $\tilde{\epsilon}_{\mathbf{k}}$ has this form due to SU(2) symmetry. Note, however, that for chiral *Ansätze* one has $\epsilon_{\mathbf{k}\uparrow}^s \neq \epsilon_{-\mathbf{k}\downarrow}^s$, because the $\mathbf{k} \rightarrow -\mathbf{k}$ symmetry is broken. Nevertheless, we still have $\epsilon_{\mathbf{k}\uparrow}^s = \epsilon_{\mathbf{k}\downarrow}^s$ due to SU(2) symmetry.

III. SELF-CONSISTENT MEAN-FIELD PARAMETERS

Before proceeding with the numerical computation of the spin structure factors we first determine the self-consistent mean-field parameters for each *Ansatz* that we consider by extremizing the free energy

$$\frac{\partial \mathcal{F}_{\text{MF}}}{\partial \mathcal{O}_j} = 0, \quad (26)$$

$$\frac{\partial \mathcal{F}_{\text{MF}}}{\partial \lambda} = 0, \quad (27)$$

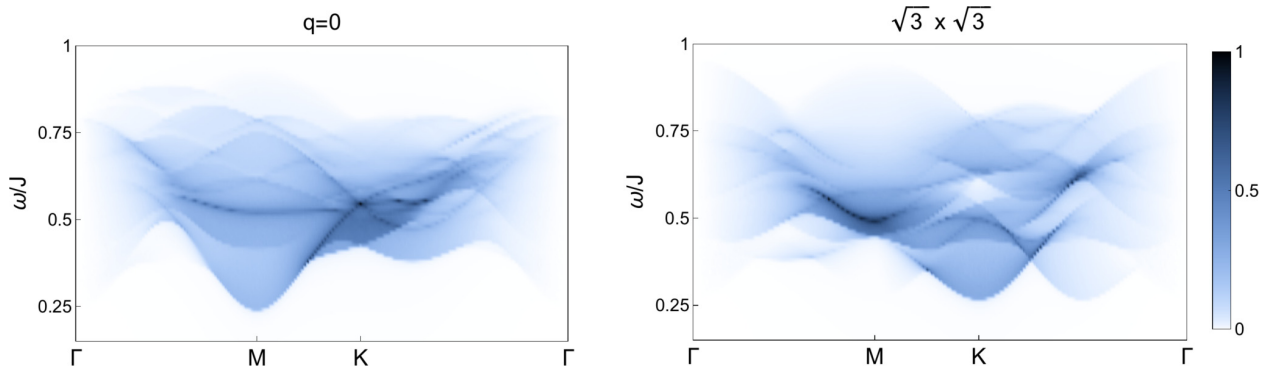


FIG. 2. The normalized dynamic structure factor along the Γ - M - K - Γ high-symmetry lines for the nonchiral SBMFT *Ansätze* $q = 0$ (left) and $\sqrt{3} \times \sqrt{3}$ (right) in the gapped spin liquid phase at $S = 0.2$.

where \mathcal{O}_j are the free mean-field parameters (denoted by an asterisk in Table I) of the given *Ansatz*, and \mathcal{F}_{MF} is the mean-field free energy derived from Eq. (11) to be

$$\mathcal{F}_{\text{MF}} = \sum_{\mathbf{k}} \sum_s^{\text{B.z.}} \epsilon_{\mathbf{k}\uparrow}^s + 2JN_s(|\mathcal{A}|^2 - |\mathcal{B}|^2) - \lambda N_s(1 + 2S), \quad (28)$$

where B.z. stands for the first Brillouin zone. In this work we consider two nonchiral *Ansätze* ($q = 0$ and $\sqrt{3} \times \sqrt{3}$) as well as three further *Ansätze* (*cuboc1*, *cuboc2*, and *octahedral*) that can break time reversal [37,38]. In the following, we set $J = 1$ and $S = 0.2$. With this artificially small value of the spin we ensure that all *Ansätze* describe a state deep in the spin-liquid phase, which is what we're interested in. We find the stationary point of \mathcal{F}_{MF} by an adaptive-grid method that seeks to minimize $\sum_j (\partial \mathcal{F}_{\text{MF}} / \partial \mathcal{O}_j)^2$, stopping only when this sum is of the order of 10^{-8} or better. The results of this extremization procedure for all *Ansätze* that we consider are shown in Table I. The self-consistent mean-field parameters for the different *Ansätze* turn out to be quite close to one another. In particular, all five *Ansätze* exhibit very similar values for \mathcal{A} , \mathcal{B} , and λ , the only parameters that are free in all *Ansätze*. The main difference is in the phases, some of which are fixed by the specific form of an *Ansatz*, while others are free.

It is important to note that the phase $\phi_{\mathcal{B}}$ for the *cuboc2* as well as the *octahedral Ansatz* turns out to be equal to π within numerical accuracy. Consequently, the saddle points of these two *Ansätze* describe nonchiral spin-liquid phases, where time-reversal and parity symmetries are restored. In our computation only the *cuboc1 Ansatz* turns out to be chiral. Note, however, that interactions beyond nearest neighbors can stabilize chiral saddle points of the *cuboc2* form, where the phase $\phi_{\mathcal{B}}$ takes a nontrivial value [38].

IV. SPIN STRUCTURE FACTORS

The dynamic spin structure factor is defined as

$$S(\mathbf{k}, \omega) = \frac{1}{N_s} \sum_{l,j} e^{i\mathbf{k} \cdot (\mathbf{r}_l - \mathbf{r}_j)} \int_{-\infty}^{\infty} dt e^{-i\omega t} \langle \hat{\mathbf{S}}_l(t) \cdot \hat{\mathbf{S}}_j \rangle, \quad (29)$$

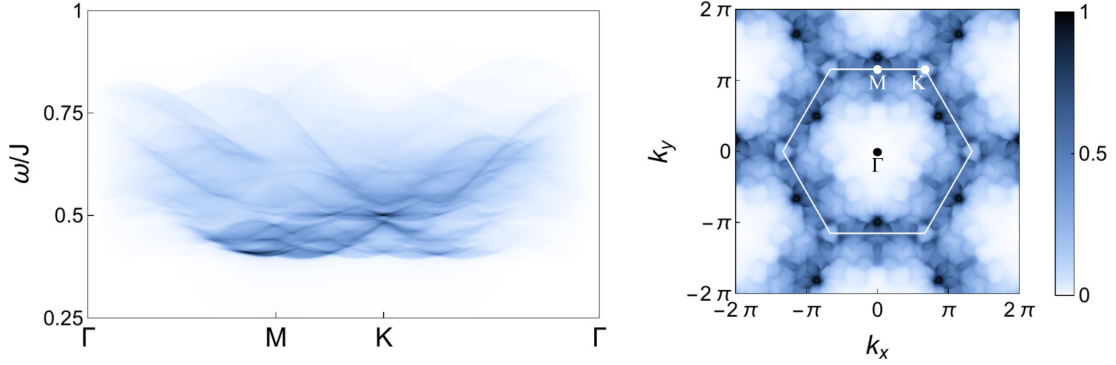


FIG. 3. The normalized dynamic structure factor for the chiral *cuboc1* Ansatz along the Γ - M - K - Γ high-symmetry lines (left) and in the \mathbf{k} plane at $\omega = 0.45J$ (right) in the gapped spin liquid phase at $S = 0.2$. The white hexagon in the right panel marks the extended Brillouin zone. Note that the dynamic structure factor at fixed frequency (right) is not symmetric under inversion and only has a threefold rotation symmetry due to time-reversal symmetry breaking (see main text).

which, using the Bogoliubov operators, can be expressed at $T = 0$ and in the absence of a spinon condensate as

$$\begin{aligned}
 S(\mathbf{k}, \omega) = & \frac{3}{2} \sum_{s,r,m,n} \frac{1}{N_q} \sum_q^{\text{B.z.}} \{ X_{sn}^*(-\mathbf{q}) U_{sm}(\mathbf{k}-\mathbf{q}) [U_{rm}^*(\mathbf{k}-\mathbf{q}) X_{rn}(-\mathbf{q}) - Y_{rn}(-\mathbf{q}) V_{rm}^*(\mathbf{k}-\mathbf{q})] \delta(\omega - \epsilon_{q\downarrow}^n - \epsilon_{\mathbf{k}-\mathbf{q}\uparrow}^m) \\
 & + 2X_{sn}^*(-\mathbf{q}) Y_{sm}^*(-\mathbf{k}+\mathbf{q}) [Y_{rm}(-\mathbf{k}+\mathbf{q}) X_{rn}(-\mathbf{q}) + Y_{rn}(-\mathbf{q}) X_{rm}(-\mathbf{k}+\mathbf{q})] \delta(\omega - \epsilon_{q\downarrow}^n - \epsilon_{\mathbf{k}-\mathbf{q}\downarrow}^m) \\
 & + 2V_{sn}(\mathbf{q}) U_{sm}(\mathbf{k}-\mathbf{q}) [U_{rm}^*(\mathbf{k}-\mathbf{q}) V_{rn}^*(\mathbf{q}) + U_{rn}^*(\mathbf{q}) V_{rm}^*(\mathbf{k}-\mathbf{q})] \delta(\omega - \epsilon_{q\uparrow}^n - \epsilon_{\mathbf{k}-\mathbf{q}\uparrow}^m) + V_{sn}(\mathbf{q}) Y_{sm}^*(-\mathbf{k}+\mathbf{q}) \\
 & \times [Y_{rm}(-\mathbf{k}+\mathbf{q}) V_{rn}^*(\mathbf{q}) - U_{rn}^*(\mathbf{q}) X_{rm}(-\mathbf{k}+\mathbf{q})] \delta(\omega - \epsilon_{q\uparrow}^n - \epsilon_{\mathbf{k}-\mathbf{q}\downarrow}^m) \}, \quad (30)
 \end{aligned}$$

where s, r, m , and n are band indices taking values in $\{u, v, w, x, y, z\}$. The static (equal-time) structure factor is obtained by integrating over frequencies $S(\mathbf{k}) = \int d\omega S(\mathbf{k}, \omega)$.

V. RESULTS AND DISCUSSION

We use the VEGAS [45] Monte Carlo integration routine to numerically evaluate the dynamic structure factors of the *Ansätze* shown in Table I, while approximating the Dirac δ functions in Eq. (30) as Lorentzian functions with a width 10^{-3} for numerical reasons. The nonchiral *Ansätze* $q = 0$ and $\sqrt{3} \times \sqrt{3}$ were first discussed in Ref. [35], and their dynamic structure factors were calculated in Ref. [33], although using an *Ansatz* with $\langle \mathcal{B}_{ij} \rangle = 0$. Similar dynamical structure factors for fermionic mean-field spin liquids have been computed in Ref. [46]. In Fig. 2, we show their dynamic structure factors along the Γ - M - K - Γ high-symmetry lines in the gapped spin liquid phase with $S = 0.2$, using the self-consistent mean-field parameters shown in Table I. Note that we've adopted a normalization where the maximum of the structure factors is set to unity for convenience. Our results are qualitatively very similar to those in Ref. [33]. The small differences come from the fact that the spinon dispersions are slightly altered when taking nonzero $\langle \mathcal{B}_{ij} \rangle$'s into account.

Figures 3–5 show the dynamic structure factors in the \mathbf{k} plane for fixed frequencies ω , as well as along the Γ - M - K - Γ high-symmetry lines for the *cuboc1*, *cuboc2*, and *octahedral* *Ansätze*, respectively, in the gapped spin liquid phase with spin $S = 0.2$. The dynamic structure factor at $\omega = 0.45J$ for *cuboc1* in Fig. 3 shows that inversion symmetry is lost with respect to the Γ point due to time-reversal symmetry breaking.

Consequently, the usual sixfold rotational symmetry is reduced to a threefold one. One would expect to see the same for the *cuboc2* (at $\omega = 0.45J$) and *octahedral* (at $\omega = 0.48J$) *Ansätze* in Figs. 4 and 5, respectively, as they allow for nontrivial Aharonov-Bohm phases when a spinon is taken around a plaquette. However, as shown in Table I, the saddle point value of ϕ_B at $S = 0.2$ is equal to π within numerical accuracy, which, along with the fixed phase $\phi_A = 0$ (*cuboc2*) or π (*octahedral*), leads to a time-reversal invariant *Ansatz*. The $\mathbf{k} \rightarrow -\mathbf{k}$ symmetry as well as the sixfold rotational symmetry is thus retained in the dynamical structure factor. On the other hand, for the *cuboc1* *Ansatz*, the free phase ϕ_A takes on a value other than $n\pi$ ($n \in \mathbb{Z}$), leading to a chiral spin liquid with broken time-reversal and parity symmetry. An interesting feature in the *cuboc1* dynamical structure factor along the Γ - M - K - Γ high-symmetry lines in Fig. 3 is the relatively flat onset of the two-spinon continuum compared to the $q = 0$ and $\sqrt{3} \times \sqrt{3}$ case.

The static structure factors for the *cuboc1*, *cuboc2*, and *octahedral* *Ansätze*, shown in Fig. 6, are qualitatively very similar. Note that the static structure factor for the chiral *cuboc1* state doesn't show signs of time-reversal or parity symmetry breaking. This can be understood by recognizing from Eq. (29) that one can write

$$\begin{aligned}
 S(-\mathbf{k}, \omega) &= \frac{1}{N_s} \sum_{l,j} e^{i\mathbf{k} \cdot (\mathbf{r}_l - \mathbf{r}_j)} \int_{-\infty}^{\infty} dt e^{-i\omega t} \langle \hat{\mathbf{S}}_l \cdot \hat{\mathbf{S}}_j(t) \rangle \\
 &= \frac{1}{N_s} \sum_{l,j} e^{i\mathbf{k} \cdot (\mathbf{r}_l - \mathbf{r}_j)} \int_{-\infty}^{\infty} dt e^{-i\omega t} \langle \hat{\mathbf{S}}_l(-t) \cdot \hat{\mathbf{S}}_j \rangle \quad (31)
 \end{aligned}$$

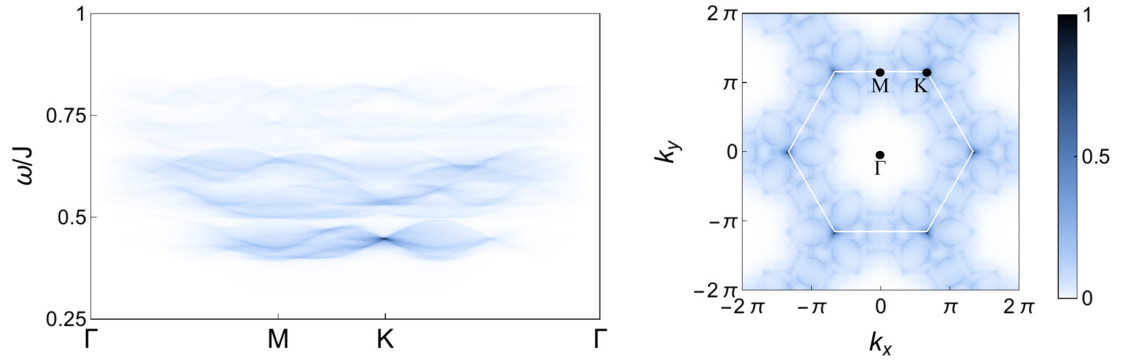


FIG. 4. The normalized dynamic structure factor for the *cuboc2* ansatz along the Γ -M-K- Γ high-symmetry lines (left) and in the k -plane at $\omega = 0.45J$ (right) in the gapped spin liquid phase at $S = 0.2$. Note that the saddle point values of the mean-field parameters for the *cuboc2* ansatz preserve time-reversal symmetry at $S = 0.2$, consequently this state is not chiral.

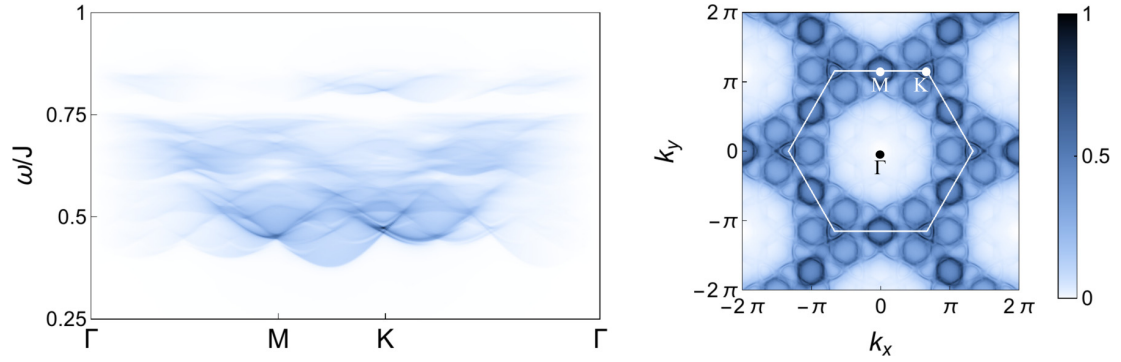


FIG. 5. The normalized dynamic structure factor for the *octahedral* ansatz along the Γ -M-K- Γ high-symmetry lines (left) and in the k -plane at $\omega = 0.48J$ (right) in the gapped spin liquid phase at $S = 0.2$. Note that the saddle point is non-chiral, as in the case of the *cuboc2* ansatz.

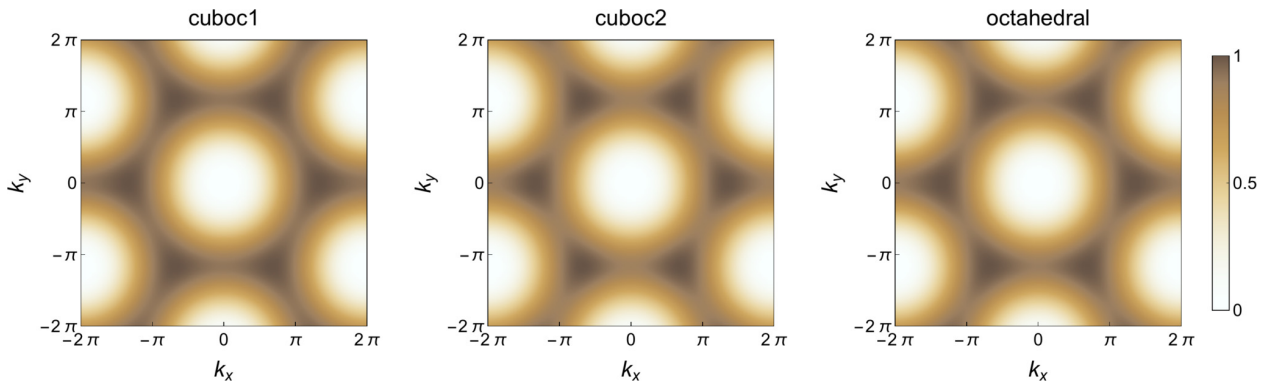


FIG. 6. Normalized static spin structure factors for the *cuboc1*, *cuboc2*, and *octahedral* Ansätze in the gapped spin liquid phase with spin $S = 0.2$. Note that the static structure factor of the chiral *cuboc1* state does not show signs of time-reversal symmetry breaking (see main text).

by a simple relabeling of the site indices. It is clear from Eqs. (31) and (29) that $S(-\mathbf{k}, \omega) = S(\mathbf{k}, \omega)$ only if $\langle \hat{\mathbf{S}}_i(-t) \cdot \hat{\mathbf{S}}_j \rangle = \langle \hat{\mathbf{S}}_i(t) \cdot \hat{\mathbf{S}}_j \rangle$ is time-reversal invariant. On the other hand, the static (equal-time) structure factor is always invariant under $\mathbf{k} \rightarrow -\mathbf{k}$.

Lastly, the variational ground-state energies of the five different *Ansätze* considered here are listed in the last line of Table I. We find that the nonchiral $\sqrt{3} \times \sqrt{3}$ *Ansatz* has the lowest energy at $S = 0.2$. Note that this is in contrast to Ref. [38], who find that the *cuboc1* state has the lowest energy. It is worth mentioning here that the SBMFT approach is not quantitatively reliable to find the true ground state of the kagome Heisenberg antiferromagnet, nor does it give variational upper bounds to the ground-state energy. This is due to the fact that the spin-length constraint is only imposed on average, and thus unphysical states are only approximately projected out. Consequently, the main purpose of our work is not to determine the true ground state of the kagome Heisenberg antiferromagnet, but to highlight features in dynamical correlation functions of different chiral spin liquid states.

VI. CONCLUSION

We computed static and dynamic spin structure factors of several chiral and nonchiral SBMFT *Ansätze* deep in the gapped spin liquid phase at spin $S = 0.2$. Even though the *cuboc1*, *cuboc2*, and *octahedral Ansätze* allow for time-reversal symmetry breaking, only the saddle-point of the *cuboc1 Ansatz* is chiral, which can be seen directly in the dynamic structure factor at fixed frequency, as seen in Fig. 3. Time-reversal symmetry breaking manifests itself by breaking the inversion symmetry with respect to the Γ point, as well as reducing the usual sixfold rotational symmetry present for nonchiral *Ansätze* to a threefold rotational symmetry.

ACKNOWLEDGMENTS

J.C.H. is grateful to Pavel Kos and Lode Pollet for fruitful discussions, as well as to Guy Almog for providing Fig. 1. This work is supported by the Nanosystems Initiative Munich (NIM).

-
- [1] L. Balents, *Nature (London)* **464**, 199 (2010).
 - [2] S. Sachdev, *Nat. Phys.* **4**, 173 (2008).
 - [3] L. Savary and L. Balents, [arXiv:1601.03742](https://arxiv.org/abs/1601.03742).
 - [4] M. R. Norman, [arXiv:1604.03048](https://arxiv.org/abs/1604.03048).
 - [5] J. B. Marston and C. Zeng, *J. Appl. Phys.* **69**, 5962 (1991).
 - [6] P. W. Leung and V. Elser, *Phys. Rev. B* **47**, 5459 (1993).
 - [7] S. Yan, D. A. Huse, and S. R. White, *Science* **332**, 1173 (2011).
 - [8] H.-C. Jiang, Z. Wang, and L. Balents, *Nat. Phys.* **8**, 902 (2012).
 - [9] S. Depenbrock, I. P. McCulloch, and U. Schollwöck, *Phys. Rev. Lett.* **109**, 067201 (2012).
 - [10] F. Kolley, S. Depenbrock, I. P. McCulloch, U. Schollwöck, and V. Alba, *Phys. Rev. B* **91**, 104418 (2015).
 - [11] Y. Ran, M. Hermele, P. A. Lee, and X.-G. Wen, *Phys. Rev. Lett.* **98**, 117205 (2007).
 - [12] Y. Iqbal, F. Becca, S. Sorella, and D. Poilblanc, *Phys. Rev. B* **87**, 060405(R) (2013).
 - [13] Y. Iqbal, D. Poilblanc, and F. Becca, *Phys. Rev. B* **91**, 020402(R) (2015).
 - [14] T. Li, [arXiv:1601.02165](https://arxiv.org/abs/1601.02165).
 - [15] V. Kalmeyer and R. B. Laughlin, *Phys. Rev. Lett.* **59**, 2095 (1987); *Phys. Rev. B* **39**, 11879 (1989).
 - [16] X.-G. Wen, F. Wilczek, and A. Zee, *Phys. Rev. B* **39**, 11413 (1989).
 - [17] M. Greiter, D. F. Schroeter, and R. Thomale, *Phys. Rev. B* **89**, 165125 (2014).
 - [18] Y.-C. He, D. N. Sheng, and Y. Chen, *Phys. Rev. Lett.* **112**, 137202 (2014).
 - [19] S.-S. Gong, W. Zhu, and D. N. Sheng, *Nat. Sci. Rep.* **4**, 6317 (2014).
 - [20] S.-S. Gong, W. Zhu, L. Balents, and D. N. Sheng, *Phys. Rev. B* **91**, 075112 (2015).
 - [21] B. Bauer, L. Cincio, B. P. Keller, M. Dolfi, G. Vidal, S. Trebst, and A. W. W. Ludwig, *Nat. Commun.* **5**, 5137 (2014).
 - [22] Y.-C. He and Y. Chen, *Phys. Rev. Lett.* **114**, 037201 (2015).
 - [23] W.-J. Hu, W. Zhu, Y. Zhang, S. Gong, F. Becca, and D. N. Sheng, *Phys. Rev. B* **91**, 041124(R) (2015).
 - [24] S. Bieri, L. Messio, B. Bernu, and C. Lhuillier, *Phys. Rev. B* **92**, 060407(R) (2015).
 - [25] K. Kumar, K. Sun, and E. Fradkin, *Phys. Rev. B* **92**, 094433 (2015).
 - [26] A. Wietek, A. Sterdyniak, and A. M. Läuchli, *Phys. Rev. B* **92**, 125122 (2015).
 - [27] M. P. Shores, E. A. Nytko, B. M. Bartlett, and D. G. Nocera, *J. Am. Chem. Soc.* **127**, 13462 (2005).
 - [28] M. A. de Vries, J. R. Stewart, P. P. Deen, J. O. Piatek, G. J. Nilsen, H. M. Rønnow, and A. Harrison, *Phys. Rev. Lett.* **103**, 237201 (2009).
 - [29] J. S. Helton *et al.*, *Phys. Rev. Lett.* **98**, 107204 (2007).
 - [30] B. J. Powell and R. H. McKenzie, *Rep. Prog. Phys.* **74**, 056501 (2011).
 - [31] T.-H. Han, J. S. Helton, S. Chu, D. G. Nocera, J. A. Rodriguez-Rivera, C. Broholm, and Y. S. Lee, *Nature (London)* **492**, 406 (2012).
 - [32] M. Fu, T. Imai, T.-H. Han, and Y. S. Lee, *Science* **350**, 655 (2015).
 - [33] M. Punk, D. Chowdhury, and S. Sachdev, *Nat. Phys.* **10**, 289 (2014).
 - [34] T.-H. Han, M. R. Norman, J.-J. Wen, J. A. Rodriguez-Rivera, J. S. Helton, C. Broholm, and Y. S. Lee, *Phys. Rev. B* **94**, 060409 (2016).
 - [35] S. Sachdev, *Phys. Rev. B* **45**, 12377 (1992).
 - [36] F. Wang and A. Vishwanath, *Phys. Rev. B* **74**, 174423 (2006).
 - [37] L. Messio, C. Lhuillier, and G. Misguich, *Phys. Rev. B* **87**, 125127 (2013).
 - [38] L. Messio, B. Bernu, and C. Lhuillier, *Phys. Rev. Lett.* **108**, 207204 (2012).
 - [39] O. Janson, J. Richter, and H. Rosner, *J. Phys.: Conf. Ser.* **145**, 012008 (2009).
 - [40] L. Messio, C. Lhuillier, and G. Misguich, *Phys. Rev. B* **83**, 184401 (2011).

- [41] R. Dijkgraaf and E. Witten, *Commun. Math. Phys.* **129**, 393 (1990).
- [42] M. Barkeshli, [arXiv:1307.8194](https://arxiv.org/abs/1307.8194).
- [43] A. Mezio, C. N. Sposetti, L. O. Manuel, and A. E. Trumper, *Europhys. Lett.* **94**, 47001 (2011).
- [44] R. Flint and P. Coleman, *Phys. Rev. B* **79**, 014424 (2009).
- [45] G. P. Lepage, *J. Comput. Phys.* **27**, 192 (1978).
- [46] T. Dodds, S. Bhattacharjee, and Y. B. Kim, *Phys. Rev. B* **88**, 224413 (2013).

Chapter 3

Prethermalization and persistent order in the absence of a thermal phase transition

Using mean-field theory, the fully-connected transverse-field Ising model (FC-TFIM) can be exactly solved to show the existence of a rich phase diagram at zero and finite temperature, with a quantum critical point $h_c = J$ and critical temperature $T_c = J$, with J the coupling constant (see Chapter 1 for the corresponding derivations). Moreover, using a Jordan-Wigner transformation to map the nearest-neighbor transverse-field Ising model (NN-TFIM), one can show that the latter has a quantum critical point $h_c = J$, and a simple Peierls' argument forbids the presence of a finite-temperature phase transition (see Chapter 1 for both derivations). From perturbative renormalization group one can determine that the long-range power-law-interacting ($\sim 1/r^\alpha$ with r inter-spin distance) transverse-field Ising model (LR-TFIM), for which the FC-TFIM and NN-TFIM are special (integrable) cases, has a quantum phase transition for all α , albeit a thermal phase transition for only $\alpha \leq 2$. One would expect that then this should mean that the dynamical phase transitions should behave qualitatively the same, since those arise after a quench in the system initially at zero temperature, which effectively injects energy density that upon thermalization should put the system in a higher(-than-zero) temperature leading to no dynamical criticality in systems in the short-range universality class. This picture is only hypothetically correct. Indeed, the Eigenstate Thermalization Hypothesis (ETH) suggests thermalization to occur in a nonintegrable system ($0 < \alpha \ll \infty$ in the case of the LR-TFIM) in the long-time limit. However, there are two problems here: (i) ETH is a hypothesis (which nevertheless may be absolutely true), and it is not straightforward to determine whether a steady state reached by the nonintegrable system is indeed a thermal state, as theoretically, this would require knowledge of the whole spectrum of the nonintegrable Hamiltonian (see Chapter 1 for the theory), and (ii) for small quenches, the system may take incredibly long to relax into a steady state, and for all intents and purposes, it is impossible to tell, whether numerically or experimentally, what this steady state is since we would not have access to such long evolution times. Nevertheless, such small

quenches lead to a prethermal quasi-steady state from which a steady-state value of the order parameter can be extracted as a function of quench parameter. In this work we show how prethermalization conspires to give rise to dynamical order even in the absence of a corresponding equilibrium thermal phase transition. We argue that this dynamical order is due to a Landau-type dynamical phase transition, which we term DPT-I.

- *Prethermalization and persistent order in the absence of a thermal phase transition*
Jad C. Halimeh, Valentin Zauner-Stauber, Ian P. McCulloch, Inés de Vega, Ulrich Schollwöck, and Michael Kastner
Phys. Rev. B **95**, 024302 (2017)

Prethermalization and persistent order in the absence of a thermal phase transitionJad C. Halimeh,¹ Valentin Zauner-Stauber,² Ian P. McCulloch,³ Inés de Vega,¹ Ulrich Schollwöck,¹ and Michael Kastner^{4,5}¹*Physics Department and Arnold Sommerfeld Center for Theoretical Physics, Ludwig-Maximilians-Universität München, D-80333 München, Germany*²*Vienna Center for Quantum Technology, University of Vienna, Boltzmanngasse 5, 1090 Wien, Austria*³*ARC Centre for Engineered Quantum Systems, School of Mathematics and Physics, The University of Queensland, St Lucia, Queensland 4072, Australia*⁴*National Institute for Theoretical Physics, Stellenbosch 7600, South Africa*⁵*Institute of Theoretical Physics, Department of Physics, University of Stellenbosch, Stellenbosch 7600, South Africa*

(Received 7 October 2016; revised manuscript received 16 December 2016; published 6 January 2017)

We numerically study the dynamics after a parameter quench in the one-dimensional transverse-field Ising model with long-range interactions ($\propto 1/r^\alpha$ with distance r), for finite chains and also directly in the thermodynamic limit. In nonequilibrium, i.e., before the system settles into a thermal state, we find a long-lived regime that is characterized by a prethermal value of the magnetization, which in general differs from its thermal value. We find that the ferromagnetic phase is stabilized dynamically: as a function of the quench parameter, the prethermal magnetization shows a transition between a symmetry-broken and a symmetric phase, even for those values of α for which no finite-temperature transition occurs in equilibrium. The dynamical critical point is shifted with respect to the equilibrium one, and the shift is found to depend on α as well as on the quench parameters.

DOI: [10.1103/PhysRevB.95.024302](https://doi.org/10.1103/PhysRevB.95.024302)**I. INTRODUCTION**

In equilibrium, phase transitions and critical phenomena are well established and much studied, and implications like universality and scaling are well understood. Extending these concepts to nonequilibrium is a topic of active research. Fundamentally different notions of so-called dynamical quantum phase transitions have been proposed, but their mutual relations, and also the associated universality classes and scaling laws, are only poorly understood. In this paper we are concerned with a type of dynamical quantum phase transition that is based on the notion of an order parameter, similar to Landau's theory of phase transitions in equilibrium. The key idea is to identify a dynamical quantum phase transition on the basis of a suitable order parameter in a prethermal regime, i.e., a nonequilibrium regime in which the system may be found before relaxing to thermal equilibrium, and which persists sufficiently long such that a value can be assigned to the order parameter [1–14]. A prethermal state retains some memory of the initial state of the system, therefore the prethermal value of the order parameter will in general differ from its thermal equilibrium value, and it may or may not show symmetry breaking and other signatures associated with the occurrence of a phase transition [15].

A simple protocol for probing such a dynamical quantum phase transition is a quantum quench into the vicinity of an equilibrium quantum critical point. Consider a family of Hamiltonians $H(\lambda) = H_1 + \lambda H_2$, parametrized by $\lambda \in \mathbb{R}$. In equilibrium at zero temperature and some critical parameter value λ_c , a quantum phase transition will in many cases occur, i.e., an abrupt change of the ground-state properties of H . The idea of a quantum quench is to prepare the system in the ground state of $H(\lambda_0)$, and then, starting at time $t = 0$, time-evolve that state under $H(\lambda)$ with $\lambda \neq \lambda_0$. Depending on the quench parameters and the system under investigation, signatures similar to those of the equilibrium phase transition may or may not persist and be visible after the quench, critical properties may be modified, enhanced, or attenuated.

Questions of this sort have previously been addressed mostly in mean-field models [5,6] and field theories [7,9,10].

Dynamical quantum phase transitions are expected to be related in some way to their equilibrium counterparts, as they show a similar kind of symmetry breaking and are signalled by the same order parameter. Whether such a relation exists in all cases, and what its precise nature is, is a question that we want to address in this paper. A relation to equilibrium quantum phase transitions at $T = 0$ is supported by the fact that in previous work dynamical quantum phase transitions have been observed by quenching into the vicinity of a quantum critical point. Additionally, a relation to a finite- T phase transition may be conjectured by noticing that a quench populates excited states above the ground state of the postquench Hamiltonian, which generically, at least after sufficiently long times, are expected to approach a thermal distribution with $T > 0$.

II. LONG-RANGE TRANSVERSE-FIELD ISING MODEL

To probe the relation between equilibrium and dynamical quantum phase transitions, we study a model that has a quantum phase transition at zero temperature, and additionally, depending on a parameter, may or may not have a finite- T transition as well. A model that has these desired properties is the transverse-field Ising model (TFIM) with ferromagnetic power-law interactions,

$$H(h) = - \sum_{i>j=1}^L \frac{\sigma_i^z \sigma_j^z}{|i-j|^\alpha} - h \sum_{i=1}^L \sigma_i^x. \quad (1)$$

We consider one-dimensional lattices consisting of L lattice sites, and σ_i^a with $a \in \{x, y, z\}$ denote the components of Pauli spin-1/2 operators on lattice site i . The exponent α in (1) tunes the range of the spin-spin interaction, from all-to-all coupling at $\alpha = 0$ to nearest-neighbor coupling in the limit $\alpha \rightarrow \infty$. We restrict the discussion to exponents $\alpha > 1$, so that an N -dependent scaling factor to make the Hamiltonian (1) extensive is not needed. For all values of α , this model has

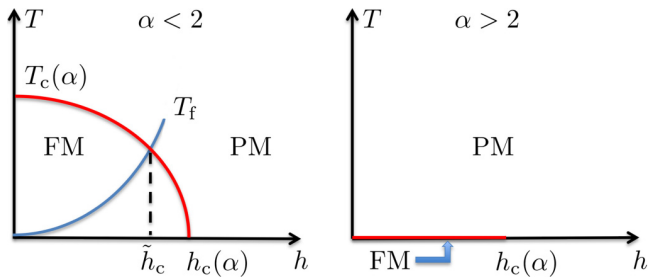


FIG. 1. Schematic phase diagram of the long-range TFIM (1). The model exhibits an equilibrium quantum phase transition at a critical point $h_c(\alpha)$ for all values of α . A finite- T phase transition occurs only for $\alpha < 2$ (left), but not for $\alpha > 2$ (right). Quenching from $h_i = 0$ to $h_f = h$ and letting the system thermalize, equilibrium states on a line $T_f(h)$ (blue line in the left plot) are reached at long times. The phase-transition line is crossed at a field $\tilde{h}_c < h_c(\alpha)$, which results in a shift of the critical field with respect to the quantum critical point.

a quantum phase transition at some critical magnetic field $h_c(\alpha)$, whereas a finite- T phase transition occurs only for $\alpha \leq 2$ [16,17] (see Fig. 1 for an illustration).

We use the magnetic field h as a quench parameter, starting in the ground state $|\psi_i\rangle$ of an initial Hamiltonian $H(h_i)$ at time $t = 0$, and then time-evolving that state under the evolution generated by a Hamiltonian $H(h_f)$ with a field h_f different from h_i . We will mainly consider quenches starting from $h_i = 0$, i.e., initial states from the degenerate ground space, where we pick the symmetry-broken, fully polarized state in the $+z$ direction. Our aim is to detect the occurrence of a dynamical quantum phase transition by monitoring the magnetization

$$m(t) = \frac{1}{L} \sum_{j=1}^L \langle \psi_i(t) | \sigma_j^z | \psi_i(t) \rangle, \quad (2)$$

where $|\psi_i(t)\rangle = \exp[-iH(h_f)t]|\psi_i\rangle$ is the time-evolved state after the quench.

Except for the extreme cases $\alpha = 0$ and $\alpha = \infty$, the model (1) is nonintegrable, and is expected to thermalize in the long-time limit. Hence, in that limit, the magnetization (2) will show order-parameter-like behavior for $\alpha < 2$, or be vanishing throughout for $\alpha > 2$, as predicted by the phase diagrams in Fig. 1. While thermalization will happen eventually, the corresponding time scale can be extremely long, so long in fact that it may become irrelevant for experimental observations.

III. DYNAMICAL QUANTUM PHASE TRANSITIONS

A dynamical quantum phase transition may be detected by studying the order parameter m as a function of the final quench parameter h_f in a nonequilibrium regime corresponding to intermediate time scales. To generate some intuition on what kind of behavior to expect, it is instructive to consider two limiting cases: (i) For small quenches from $h_i = 0$ to $h_f \gtrsim 0$, excitations above the ground state of $H(h_f)$ are only sparsely populated, the dynamics towards a finite- T thermal state of Hamiltonian will take place very slowly, and a memory of the nonvanishing magnetization of the ground state of $H(0)$ will be retained for a long time. (ii) For a large quench well beyond the

critical point, $h_f \gg h_c(\alpha)$, excitations are massively populated, no slow variables are expected to exist, and a rapid approach to $m = 0$ is expected. In between these two extreme cases (i) and (ii), one may expect a transition between a regime with nonvanishing magnetization at small h_f and a regime with vanishing m at large h_f . Such a dynamical quantum phase transition has previously been observed in the TFIM with all-to-all interactions ($\alpha = 0$) [12,18,19], but this case is special in more than one way and its behavior is not expected to be generic.

IV. NUMERICAL METHODS

In this paper we use two complementary numerical methods to study dynamical quantum phase transitions after a quench in the general (nonintegrable) TFIM with long-range interactions (1). The first is the time-dependent density matrix renormalization-group (t -DMRG) [20–27] method with Krylov [28] time evolution, which we apply to finite chains of up to 128 sites. The second is a method based on a time-dependent variational principle for matrix product states [22,29–31], tailored for simulating the dynamics of long-range lattice systems in the thermodynamic limit. Details on this numerical method, which we abbreviate by iMPS, are provided in the companion paper [32]. The combination of the two methods allows us to observe finite-size effects as would be visible in experimental realization on the one side, but also clean infinite-system idealizations as they are used in theoretical approaches. Both numerical methods are certified in the sense that they use well controlled approximations, tunable by an upper bound of the entanglement of the simulated states, which we set to achieve good simulation accuracies. During the simulation we monitor the order parameter m as a function of time (2), as illustrated in Fig. 2 for different quench parameters.

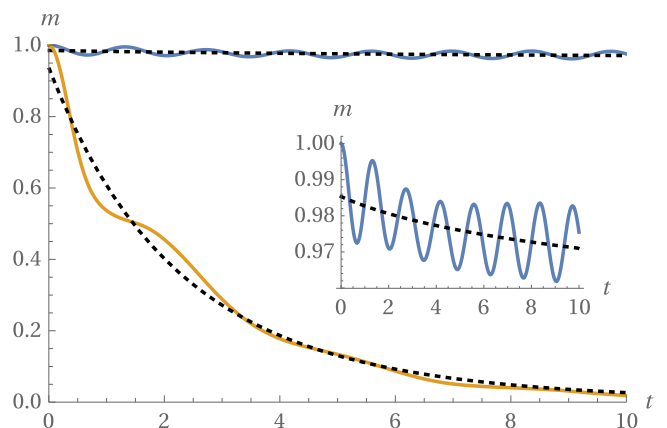


FIG. 2. Time evolution of the order parameter m as obtained from iMPS simulations for long-range exponent $\alpha = 3$. (Data from finite-size t -DMRG simulations look very similar.) For a strong quench from $h_i = 0$ to $h_f = 0.99$, the magnetization quickly decays towards zero (yellow line) and is well approximated by a power law (lower black line). For a small quench from $h_i = 0$ to $h_f = 0.28$, the magnetization shows an initial decay away from its initial value of 1 on a fast time scale (inset), and then saturates to a nonzero value for rather long times (blue line). Eventually, for the chosen parameter values and on a time scale not accessible in simulations, the system will thermalize to a state with zero magnetization.

The time scales that can be reached in the simulation depend on the lattice size L , but also on other system and quench parameters. The simulation methods used are considered the current state of the art for one-dimensional spin systems.

V. THERMAL BEHAVIOR AFTER A QUENCH

Before discussing dynamical quantum phase transitions at intermediate times, it is instructive to review the well-known equilibrium physics of the long-range TFIM [16,17] in the context of quantum quenches and long-time limits. Starting in the ground state corresponding to $h_i = 0$ and quenching to $h_f \neq 0$, the system will not be in the ground state of $H(h_f)$. A nonintegrable model like the one we are studying is then believed to thermalize after a sufficiently long time towards a finite-temperature Gibbs state. The temperature of that state depends on h_f , and this dependence can be described by some function $T_f(h_f)$. This implies that, by performing a quench and waiting sufficiently long for the system to thermalize, one explores the (T, h) equilibrium phase diagram along the line $(T_f(h_f), h_f)$ parametrized by h_f (blue line in Fig. 1). A phase transition will be observed for all $\alpha \leq 2$ as predicted by equilibrium thermodynamics, and it will occur at a critical field \tilde{h}_c [corresponding to the value at which $T_f(h)$ crosses the thermal equilibrium transition line] that is smaller than h_c of the quantum phase transition.

VI. DYNAMICAL QUANTUM PHASE TRANSITION OF THE LONG-RANGE TFIM

Quenching and waiting for thermalization to occur is therefore not a way of observing nonequilibrium physics. To probe dynamical features we have to look at shorter time scales. The inset of Fig. 2 indicates that it is indeed reasonable and beneficial to use equilibrium concepts for the description of nonequilibrium observations on intermediate time scales. The magnetization in that plot starts at 1, and quickly decays away from this value to reach a plateau of $\tilde{m} = 0.97$ around which it oscillates for the times reached in simulations. This prethermal value differs from thermal equilibrium, which is known to be $m = 0$ for the parameters used in Fig. 2. The existence of two separate time scales is a key ingredient for making dynamical quantum phase transitions a meaningful concept: a fast time scale, on which the system evolves away from its trivial initial state, is needed, and a much longer time scale on which thermal equilibrium is reached, such that a long-lived almost-constant nonequilibrium value \tilde{m} can be assigned at intermediate times. Our aim is to extract from the simulation data such prethermal magnetization values \tilde{m} , which are indicative of the nonequilibrium physics on intermediate time scales relevant in various experimental settings. For some parameter values, the quasistationary value \tilde{m} is clearly visible and easy to extract, while in other cases the limited simulation times require a fit and subsequent extrapolation to later times. These fitting and extrapolation procedures, which are described in more detail in the Appendix, are part of the “definition” we use to extract the prethermal magnetization \tilde{m} . While the bare simulation data are essentially free of errors, the fitting procedure introduces some uncertainty, and extrapolation of the fit function to later times can lead to a significant enhancement of these errors in \tilde{m} .

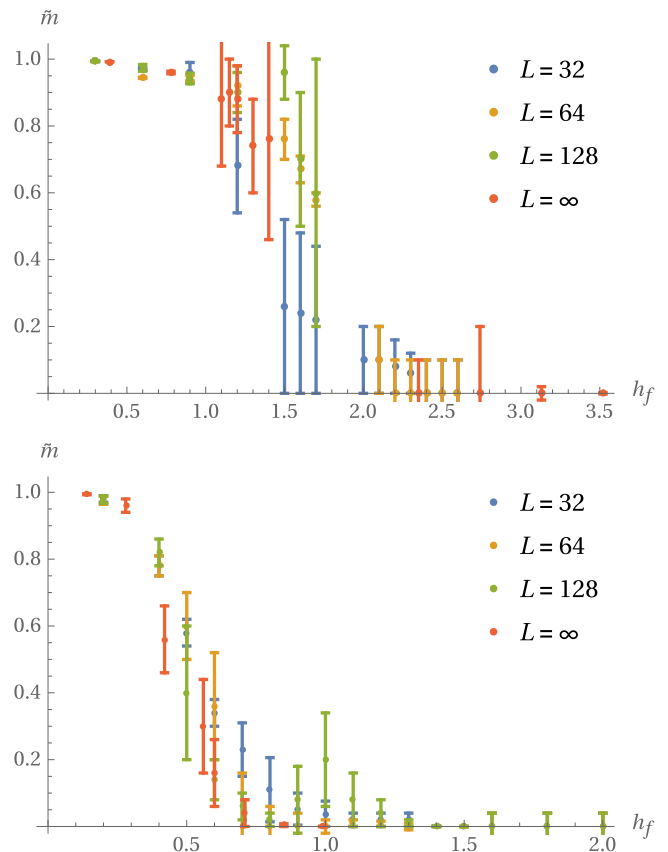


FIG. 3. Prethermal magnetization \tilde{m} plotted as a function of the final quench parameter h_f . Both plots are for quenches starting from $h_i = 0$, and for various system sizes as indicated in the legends. The existence of a magnetized phase for small h_f and an unmagnetized phase for large h_f is clearly visible for $\alpha = 1.6$ (top) and $\alpha = 3$ (bottom).

Plotting the thus obtained prethermal magnetization \tilde{m} as a function of the quench parameter h_f , we find a behavior that is reminiscent of an order parameter; see Fig. 3. Due to the error bars of \tilde{m} it is difficult to determine the precise transition point of this dynamical quantum phase transition on the basis of our numerical data, but we can confirm the existence of a magnetized phase for small quenches, and an unmagnetized phase for large quenches. Remarkably, the magnetized phase is clearly visible also for $\alpha = 3$, and hence the dynamical phase diagram in this case differs drastically from its equilibrium counterpart, which does not have a ferromagnetic phase for $\alpha > 2$. The comparison with iMPS data for infinite lattices confirms that this finding is not a finite-size artefact and indeed persists in the thermodynamic limit. Unfortunately, the (rather conservatively estimated) error bars in Fig. 3 do not allow us to clearly establish whether or not the transition from the magnetized to the unmagnetized phase is indeed a sharp one, or to even extract critical exponents of such a dynamical quantum phase transition. As is evident from Fig. 3, the critical field \tilde{h}_c at which the transition occurs becomes smaller for larger exponents α . This suggests that for such shorter-ranged interactions the prethermalized state can be dynamically stabilized only for smaller quenches, and in that

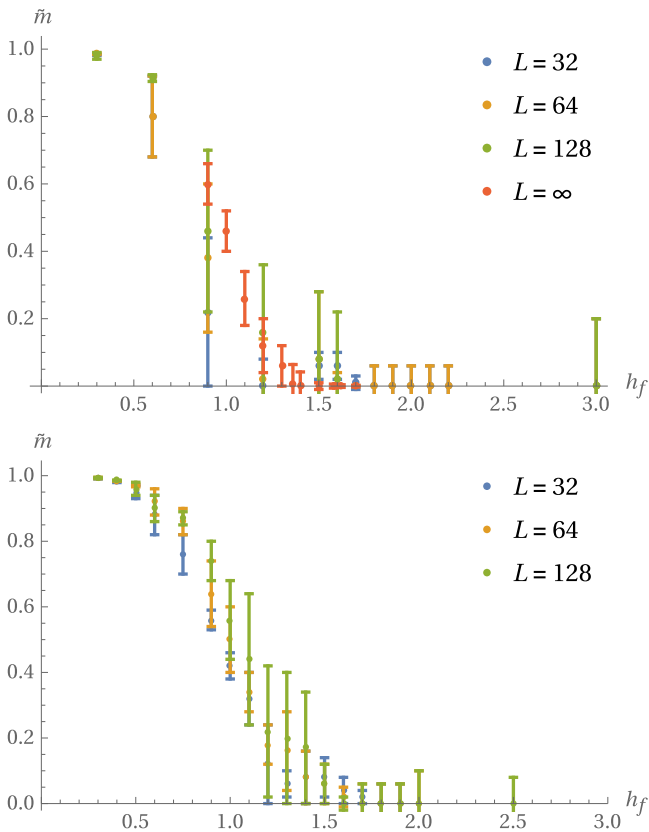


FIG. 4. Prethermal magnetization \tilde{m} plotted as a function of the final quench parameter h_f for $\alpha = 2.3$. Top: quenching from $h_i = 0$; bottom: quenching from $h_i = 0.2$. Both plots show qualitatively similar behavior. A slight dependence of the dynamical critical point on h_i , as expected for the thermal behavior in the long-time limit after the quench, might also be present in the prethermalized regime on intermediate time scales, but cannot be established beyond doubt.

sense the ferromagnetically ordered state is less robust. We expect that \tilde{h}_c approaches h_i in the limit $\alpha \rightarrow \infty$, in agreement with the observation that exponential decay to the (generalized Gibbs) equilibrium value sets in immediately in the TFIM with nearest-neighbor interactions.

VII. OTHER TYPES OF QUENCHES

As is usually the case in critical phenomena, the dynamical critical point is expected to be nonuniversal, but to depend on details of the Hamiltonian and, in our case, also on the quench protocol, in particular the initial quench parameter h_i . From the above discussion of the thermal equilibrium behavior after a quench, it appears plausible that also the dynamical critical point \tilde{h}_c should be shifted towards slightly larger values with increasing h_i . To probe this effect, we consider quenches with different prequench Hamiltonians $H(h_i)$, using initial fields $h_i = 0$ and 0.2 . In Fig. 4 we show and compare the corresponding dynamical phase diagrams. In both cases the transition from a dynamically ordered to a disordered phase is clearly established, but a shift of the dynamical transition point, if present, is concealed by numerical noise.

It would be interesting to complement the results presented in this paper by studying quenches in the opposite direction, i.e., starting from the fully x -polarized ground state of the Hamiltonian (1) in the limit $h_i \rightarrow \infty$ and quenching towards and across the quantum critical point from above. This setting is somewhat more difficult to investigate numerically, as in this case, in addition to the Hamiltonian, the initial state is also \mathbb{Z}_2 symmetric. As a consequence, the magnetization is zero for all times and cannot be used to detect a dynamical quantum phase transition. Alternatively, one could use second cumulants of the order parameter as done in Ref. [12], but such a signal is difficult to detect on the basis of limited-time data. Another possibility is to detect critical behavior on the basis of a diverging correlation length, as proposed in Ref. [33], but such an approach is tricky in long-range models, where, even away from criticality, ground-state correlations are in general not exponentially clustered and hence the correlation length is diverging (or ill defined).

VIII. CONCLUSIONS

In summary, we have studied the occurrence of a dynamical quantum phase transition after a quench of the magnetic field in a transverse-field Ising model with long-range interactions. We have provided evidence that a symmetry-broken, ferromagnetic phase can be stabilized dynamically, in the sense that it persists for intermediate times in a prethermalized regime, even in the absence of a ferromagnetically ordered equilibrium phase at finite temperature. Our iMPS variational principle allows us to clearly confirm that such a symmetry-broken phase also persists in the thermodynamic limit. Whether the transition to a symmetric phase with magnetization $\tilde{m} = 0$ is a sharp one, or a smooth crossover, cannot be established with absolute certainty on the basis of numerical data. So while our results are not fully conclusive on this aspect, the numerical data do not hint at a nonvanishing \tilde{m} for sufficiently large h_f .

We studied the dependence of the dynamical quantum phase transition on model parameters and quench parameters, in particular on the long-range exponent α and the prequench magnetic field h_i . While a specific model was chosen for the numerical study, we expect our findings to be valid more generally for long-range models, also in higher lattice dimension.

The question studied in this paper is a numerically challenging one, and our results are obtained by state-of-the-art implementations of t -DMRG for finite one-dimensional lattices and an iMPS variational principle for infinite lattices. The latter is particularly suited for the problem at hand. An experimental investigation of the phenomena described in this paper should also be feasible: one-dimensional [34,35] or two-dimensional [36] arrays of trapped ions allow for the emulation of long-range interacting Ising spins in a magnetic field and, at least in principle, long-range exponents can be tuned in the range $0 \leq \alpha \leq 3$ [37]. Preparation of fully polarized initial states as well as parameter quenches are feasible by standard experimental techniques. The required time scales, like in the numerical simulations, are an issue, but do not seem entirely out of reach.

Note added in proof. When finishing up this work we became aware of a preprint by Žunkovič *et al.* [38] that

addresses a similar question, but reaches different conclusions. In particular, the finite-size scaling extrapolations of Ref. [38] are inconsistent with our infinite-system data.

ACKNOWLEDGMENTS

The authors would like to thank P. Calabrese, L. Carr, D. Draxler, M. Eckstein, J. Haegeman, D. Jaschke, S. Kehrein, F. Piazza, and F. Verstraete for fruitful discussions. V.Z.-S. acknowledges financial support by the Austrian Science Fund (FWF), Grants No. F4104 SFB ViCoM and No. F4014 SFB FoQuS. I.P.M. acknowledges support from the Australian Research Council (ARC) Centre of Excellence for Engineered Quantum Systems, Grant No. CE110001013, and the ARC Future Fellowships scheme, FT140100625. I.d.V. acknowledges support by the Nanosystems Initiative Munich (NIM) (Project No. 862050-2). M.K. acknowledges support from the National Research Foundation of South Africa via the Incentive Funding and the Competitive Programme for Rated Researchers.

APPENDIX: FITTING PROCEDURE

When fitting numerical data like those of Fig. 2, the situation can be summarized as follows: We have data of high accuracy, limited to an interval of times up to the order of 10. The data show a decaying tendency, with fairly strong oscillations superimposed, like in the inset of Fig. 2. Our aim is to extrapolate the decay to intermediate times that are, say, an order of magnitude longer than the times t_f reached in the simulations. This time scale of extrapolation is reasonable for several reasons: (i) It is substantially longer than the time scale on which the decay to a prethermalization plateau occurs, hence we look at a time scale that is well separated from the initial dephasing dynamics. (ii) It is at least comparable to the time scales that, with some optimism, might be reached in experimental implementations. (iii) The time scale is short enough such that the error bar that propagates to the extrapolated value is manageable. (Extrapolations to times that are orders of magnitude longer than the simulated times simply become unreliable.)

The main difficulty arises from the fact that the functional form of the decay is not known. Depending on the type of model, quench, and quantity monitored, the decay could be exponential, power law, a combination of both, or something else. To account for this lack of knowledge, we decided to fit a variety of functions to the data,

$$m_1(t) = A \exp(-at), \tag{A1a}$$

$$m_2(t) = A \exp(-at) + c, \tag{A1b}$$

$$m_3(t) = At^{-a}, \tag{A1c}$$

$$m_4(t) = At^{-a} + c, \tag{A1d}$$

$$m_5(t) = A(t - t_0)^{-a}, \tag{A1e}$$

with A , a , c , and/or t_0 as real fit parameters. Using Mathematica's `NonlinearModelFit`, optimal values are returned together with standard error estimates for the fit parameters. The error bars for the fit parameters give us a first indication on which fit functions are suitable for a given data set: If, for a given fit function, one or several of the fit parameters

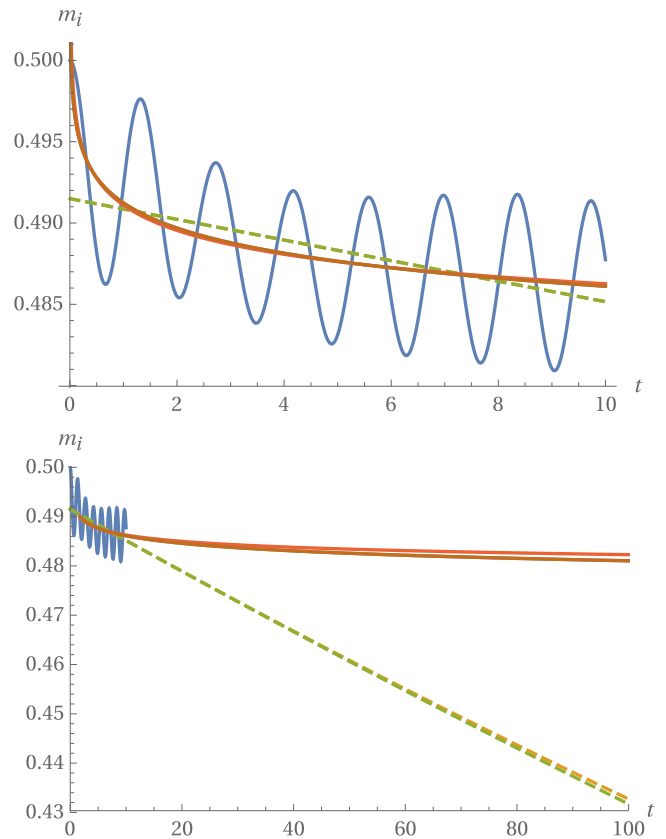


FIG. 5. Illustration of the fitting and extrapolation procedure for $\alpha = 3$, $h_i = 0$, $h_f = 0.28$. The oscillating blue line shows the iMPS data. Dashed lines (yellow and green, almost on top of each other and hardly distinguishable on the scale of the plots) show the exponential fit functions m_1 and m_2 , solid lines (orange, brown, and purple, again hardly distinguishable) show power law fits m_3 , m_4 , and m_5 . For the three-parameter fits m_2 , m_4 , and m_5 , the optimal values of the fit parameters come with large error bars, and those functions are therefore discarded. Among the two-parameter fits, m_3 (solid orange line) has a significantly smaller mean squared deviation from the simulation data than m_1 (dashed yellow), and is therefore used for determining the prethermal magnetization $\tilde{m} = m_3(10t_f)$.

are afflicted with large relative error bars, the fit function has more parameters than is justified by the data and therefore should be discarded. For the remaining fit functions the accuracy with which they fit the data is assessed on the basis of the mean-squared deviation, and the functions with larger deviations are discarded; see Fig. 5 (top) for an example.

After these two selection steps, depending on the specific data set used, one or several suitable fit functions remain, and those are extrapolated to a time $10t_f$ (Fig. 5, bottom). The arithmetic mean of the extrapolated values is used to define the prethermal magnetization,

$$\tilde{m} = \sum_i m_i(10t_f), \tag{A2}$$

where the summation is over those of the fit functions (A1a)–(A1e) that survived the above described selection procedure. The corresponding standard deviation is used as an error

estimate for \tilde{m} . It is the lack of knowledge of the functional form of the decay of $m(t)$, and the resulting variety of possible fits, that accounts for the fairly large error bars in Figs. 3 and 4. While the above described fitting and extrapolation procedure

clearly contains some arbitrariness, the rather conservative error estimation makes sure that the phase diagrams are not biased by (possibly unjustified) assumptions about the functional form of the decay of $m(t)$ or the extrapolation time.

-
- [1] M. Moeckel and S. Kehrein, Interaction Quench in the Hubbard Model, *Phys. Rev. Lett.* **100**, 175702 (2008).
- [2] M. Eckstein and M. Kollar, Nonthermal Steady States After an Interaction Quench in the Falicov-Kimball Model, *Phys. Rev. Lett.* **100**, 120404 (2008).
- [3] M. Eckstein, M. Kollar, and P. Werner, Thermalization After an Interaction Quench in the Hubbard Model, *Phys. Rev. Lett.* **103**, 056403 (2009).
- [4] M. Moeckel and S. Kehrein, Crossover from adiabatic to sudden interaction quenches in the Hubbard model: Prethermalization and non-equilibrium dynamics, *New J. Phys.* **12**, 055016 (2010).
- [5] B. Sciola and G. Biroli, Quantum Quenches and Off-Equilibrium Dynamical Transition in the Infinite-Dimensional Bose-Hubbard Model, *Phys. Rev. Lett.* **105**, 220401 (2010).
- [6] B. Sciola and G. Biroli, Dynamical transitions and quantum quenches in mean-field models, *J. Stat. Mech.* (2011) P11003.
- [7] A. Gambassi and P. Calabrese, Quantum quenches as classical critical films, *Europhys. Lett.* **95**, 66007 (2011).
- [8] N. Tsuji, M. Eckstein, and P. Werner, Nonthermal Antiferromagnetic Order and Nonequilibrium Criticality in the Hubbard Model, *Phys. Rev. Lett.* **110**, 136404 (2013).
- [9] B. Sciola and G. Biroli, Quantum quenches, dynamical transitions, and off-equilibrium quantum criticality, *Phys. Rev. B* **88**, 201110 (2013).
- [10] A. Chandran, A. Nanduri, S. S. Gubser, and S. L. Sondhi, Equilibration and coarsening in the quantum $O(N)$ model at infinite N , *Phys. Rev. B* **88**, 024306 (2013).
- [11] A. Maraga, A. Chiochetta, A. Mitra, and A. Gambassi, Aging and coarsening in isolated quantum systems after a quench: Exact results for the quantum $O(N)$ model with $N \rightarrow \infty$, *Phys. Rev. E* **92**, 042151 (2015).
- [12] P. Smacchia, M. Knap, E. Demler, and A. Silva, Exploring dynamical phase transitions and prethermalization with quantum noise of excitations, *Phys. Rev. B* **91**, 205136 (2015).
- [13] T. Langen, T. Gasenzer, and J. Schmiedmayer, Prethermalization and universal dynamics in near-integrable quantum systems, *J. Stat. Mech.* (2016) 064009.
- [14] M. Marcuzzi, J. Marino, A. Gambassi, and A. Silva, Prethermalization from a low-density Holstein-Primakoff expansion, *Phys. Rev. B* **94**, 214304 (2016).
- [15] The dynamical quantum phase transition introduced in [39], based on a formal analogy to Fisher zeros in the complex temperature plane for equilibrium transitions, leads to nonanalyticities in time, which is not what we discuss in the present paper.
- [16] F. J. Dyson, Existence of a phase-transition in a one-dimensional Ising ferromagnet, *Commun. Math. Phys.* **12**, 91 (1969).
- [17] A. Dutta and J. K. Bhattacharjee, Phase transitions in the quantum Ising and rotor models with a long-range interaction, *Phys. Rev. B* **64**, 184106 (2001).
- [18] A. Das, K. Sengupta, D. Sen, and B. K. Chakrabarti, Infinite-range Ising ferromagnet in a time-dependent transverse magnetic field: Quench and ac dynamics near the quantum critical point, *Phys. Rev. B* **74**, 144423 (2006).
- [19] B. Žunkovič, A. Silva, and M. Fabrizio, Dynamical phase transitions and Loschmidt echo in the infinite-range XY model, *Philos. Trans. R. Soc. A* **374**, 20150160 (2016).
- [20] S. R. White, Density Matrix Formulation for Quantum Renormalization Groups, *Phys. Rev. Lett.* **69**, 2863 (1992).
- [21] U. Schollwöck, The density-matrix renormalization group, *Rev. Mod. Phys.* **77**, 259 (2005).
- [22] U. Schollwöck, The density-matrix renormalization group in the age of matrix product states, *Ann. Phys. (NY)* **326**, 96 (2011).
- [23] S. R. White and A. E. Feiguin, Real-Time Evolution Using the Density Matrix Renormalization Group, *Phys. Rev. Lett.* **93**, 076401 (2004).
- [24] F. Verstraete, J. J. García-Ripoll, and J. I. Cirac, Matrix Product Density Operators: Simulation of Finite-Temperature and Dissipative Systems, *Phys. Rev. Lett.* **93**, 207204 (2004).
- [25] G. Vidal, Efficient Simulation of One-Dimensional Quantum Many-Body Systems, *Phys. Rev. Lett.* **93**, 040502 (2004).
- [26] A. J. Daley, C. Kollath, U. Schollwöck, and G. Vidal, Time-dependent density-matrix renormalization-group using adaptive effective Hilbert spaces, *J. Stat. Mech.* (2004) P04005.
- [27] D. Gobert, C. Kollath, U. Schollwöck, and G. Schütz, Real-time dynamics in spin- $\frac{1}{2}$ chains with adaptive time-dependent density matrix renormalization group, *Phys. Rev. E* **71**, 036102 (2005).
- [28] A. N. Krylov, On the numerical solution of the equation by which in technical questions frequencies of small oscillations of material systems are determined, *Izvestija AN SSSR (News of Academy of Sciences of the USSR)*, Otdel. mat. i estest. nauk **VII**, 491 (1931), in Russian.
- [29] F. Verstraete, V. Murg, and J. I. Cirac, Matrix product states, projected entangled pair states, and variational renormalization group methods for quantum spin systems, *Adv. Phys.* **57**, 143 (2008).
- [30] J. Haegeman, J. I. Cirac, T. J. Osborne, I. Pižorn, H. Verschelde, and F. Verstraete, Time-Dependent Variational Principle for Quantum Lattices, *Phys. Rev. Lett.* **107**, 070601 (2011).
- [31] J. Haegeman, C. Lubich, I. Oseledets, B. Vandereycken, and F. Verstraete, Unifying time evolution and optimization with matrix product states, *Phys. Rev. B* **94**, 165116 (2016).
- [32] J. C. Halimeh and V. Zauner-Stauber, Enriching the dynamical phase diagram of spin chains with long-range interactions, [arXiv:1610.02019](https://arxiv.org/abs/1610.02019).
- [33] E. Nicklas, M. Karl, M. Höfer, A. Johnson, W. Muessel, H. Strobel, J. Tomkovič, T. Gasenzer, and M. K. Oberthaler, Observation of Scaling in the Dynamics of a Strongly Quenched Quantum Gas, *Phys. Rev. Lett.* **115**, 245301 (2015).
- [34] P. Richerme, Z.-X. Gong, A. Lee, C. Senko, J. Smith, M. Foss-Feig, S. Michalakis, A. V. Gorshkov, and C. Monroe, Non-local propagation of correlations in quantum systems with long-range interactions, *Nature (London)* **511**, 198 (2014).

- [35] P. Jurcevic, B. P. Lanyon, P. Hauke, C. Hempel, P. Zoller, R. Blatt, and C. F. Roos, Quasiparticle engineering and entanglement propagation in a quantum many-body system, *Nature (London)* **511**, 202 (2014).
- [36] J. W. Britton, B. C. Sawyer, A. C. Keith, C.-C. J. Wang, J. K. Freericks, H. Uys, M. J. Biercuk, and J. J. Bollinger, Engineered two-dimensional Ising interactions in a trapped-ion quantum simulator with hundreds of spins, *Nature (London)* **484**, 489 (2012).
- [37] D. Porras and J. I. Cirac, Effective Quantum Spin Systems with Trapped Ions, *Phys. Rev. Lett.* **92**, 207901 (2004).
- [38] B. Žunkovič, M. Heyl, M. Knap, and A. Silva, Dynamical quantum phase transitions in spin chains with long-range interactions: Merging different concepts of non-equilibrium criticality, [arXiv:1609.08482](https://arxiv.org/abs/1609.08482).
- [39] M. Heyl, A. Polkovnikov, and S. Kehrein, Dynamical Quantum Phase Transitions in the Transverse-Field Ising Model, *Phys. Rev. Lett.* **110**, 135704 (2013).

Chapter 4

Enriching the dynamical phase diagram of spin chains with long-range interactions

In the previous chapter, we discussed the Landau-type dynamical phase transition (DPT-I), which relies on extracting a proper order parameter after the system has relaxed into a (quasi-)steady state as a function of a quench control parameter. In this chapter, we study the Loschmidt-echo return-rate dynamical phase transition (DPT-II or type-II DPT). The latter does not require a steady-state value of an order parameter, but rather manifests as nonanalytic cusps in the Loschmidt-echo return rate as a function of evolution time. We consider the LR-TFIM and find for large α behavior that is qualitatively similar to that in the NN-TFIM in that the return rate has (no) nonanalytic cusps if the quench is (not) across a certain critical value of the quench control parameter, but we additionally find that this critical value depends on the initial state of the system. More interestingly though, we find, in quenches starting from zero initial field strength, that for small values of α , i.e. when the interactions are sufficiently long-range, nonanalytic cusps arise in the return rate even when the quench is below the critical value, whereas for large α there simply are no cusps in such a case. These anomalous cusps behave quite differently to their regular counterparts in that they temporally grow apart with quench strength whereas the regular cusps show smaller temporal separation with greater quench strength. Moreover, the anomalous cusps arise later in time, preceded by analytic crests in the return rate, behavior also not seen in the case of regular cusps. We argue that the anomalous cusps constitute a new dynamical phase, thus enriching the dynamical phase diagram of long-range interacting spin chains.

- *Enriching the dynamical phase diagram of spin chains with long-range interactions*
Jad C. Halimeh and Valentin Zauner-Stauber
arXiv:1610.02019

Enriching the dynamical phase diagram of spin chains with long-range interactions

Jad C. Halimeh¹ and Valentin Zauner-Stauber²

¹*Physics Department and Arnold Sommerfeld Center for Theoretical Physics,
Ludwig-Maximilians-Universität München, D-80333 München, Germany*

²*Vienna Center for Quantum Technology, University of Vienna, Boltzmannngasse 5, 1090 Wien, Austria*

(Dated: October 7, 2016)

Using an infinite matrix product state technique (iMPS) based on the time-dependent variational principle, we study two major types of dynamical phase transition (DPT) in the transverse-field Ising model with long-range power-law ($\propto 1/r^\alpha$ with r inter-spin distance) interactions in the thermodynamic limit – *type-I*: based on order parameters in a (quasi-)steady state, and *type-II*: based on nonanalyticities (cusps) in the Loschmidt-echo return rate. We construct the corresponding rich dynamical phase diagram, whilst considering different quench initial conditions. We find a nontrivial connection between both types of DPT based on their critical lines. Moreover, we observe a new type-II dynamical phase in a certain range of interaction exponent α , characterized by what we call *anomalous cusps*, which are distinct from the regular cusps usually associated with a type-II DPT. We illustrate the transition between these two groups of cusps through the rate-function branches of the iMPS transfer matrix, which is a major strength of this method for studying the type-II DPT. Our results provide the characterization of experimentally-accessible signatures of the dynamical phases studied in this work.

I. INTRODUCTION

Phase transitions are among the most fascinating phenomena in physics whereby a small change in a control parameter of the system can drive the system between extremely different phases that are not adiabatically connected to one another, thus giving rise to nonanalyticity in the free energy even when the system itself is described by a completely analytic Hamiltonian with no singularities. Quantum and classical equilibrium phase transitions are textbook subjects that have been very well studied and established in various systems. Recently, and particularly in the context of closed quantum systems, quench dynamics¹ and post-quench system behavior has received a lot of attention. Of special interest is the concept of dynamical phase transitions (DPTs), where, for one type of such DPTs, critical behavior is inspected in a post-quench (quasi-)steady state, such as a prethermal state at intermediate times, or steady state that looks locally thermal in case of thermalization in a nonintegrable system, in some cumulant (such as e.g. the order parameter or variance thereof) as a function of some control parameter in the quenching Hamiltonian. This type-I DPT is particularly interesting in the sense that it is shown to exist in models where the corresponding finite-temperature equilibrium phase transition is absent.² Reaching a quasi-steady state is crucial in this DPT in order to extract a steady-state value of the cumulant under consideration. On the other hand, there is the type-II DPT, which, in addition to the seminal work³ defining it, has been extensively studied analytically^{4–8} and numerically^{9,10} in several models, and just recently even observed experimentally¹¹ in the dynamics of a fermionic many-body state after a quantum quench. Similar to the type-I DPT, the type-II DPT also involves a quench between an initial and a final Hamiltonian, however, unlike the type-I DPT, (pre)thermalization is not

a requirement, not least because the type-II DPT actually manifests itself as a nonanalyticity in the Loschmidt-echo return rate³ as a function of evolution time. In general, the type-II DPT occurs when an initial state at $T = 0$ undergoes a quench between two Hamiltonians such that the control parameter that effects this quench crosses the equilibrium critical point,^{3–5} and has been observed in the nearest-neighbor transverse field Ising model (TFIM) with quenches across the quantum equilibrium critical point from both phases.^{3,5} However, there have been exceptions to this general rule, where a type-II DPT does occur for quenches within the same phase and is absent in quenches across the quantum equilibrium critical point,^{12,13} and it has been shown that the type-II DPT is absent in the nearest-neighbor transverse field Ising model (NN-TFIM) at $T > 0$.¹⁴

We have shown in a related work with colleagues,² that the type-I DPT in the long-range TFIM might exist in situations even when the system under consideration does not exhibit a finite-temperature phase transition.¹⁵ For further details, we refer the reader to Ref. 2. In this paper, we shall focus on the behavior of the type-II DPT, how we detect it in the framework of infinite matrix product states (iMPS)^{16,17} in the thermodynamic limit, and characterizing its different phases. We find that it is extremely beneficial to work with iMPS here as opposed to finite-size time-dependent density matrix renormalization group (t -DMRG) methods.^{18–20} As we shall see later, and as shown in the seminal works^{3,5} in the nearest-neighbor TFIM, the type-II DPT manifests itself as nonanalyticities in the form of cusps in some analogue of the free energy. Due to finite size effects, these cusps will be smoothed out in finite systems, thus indicating no nonanalyticity (and thus no criticality) in the free energy analogue. One can in principle use finite-size scaling in order to surmise a cusp in the thermodynamic limit, but such a method might be error-prone, cumber-

some, and requires unrealistic numerical resources. In iMPS, on the other hand, we *a priori* deal with an infinite system, and one can directly see sharp cusps in the free energy analogue. Moreover, as explained in detail in Sec. A, the type-II DPT can be very straightforwardly detected from level crossings in the eigenvalues of the MPS transfer matrix.

Naturally, several questions arise in the context of these DPTs in the long-range TFIM, such as whether or not type-I and type-II DPTs are related, the particular phase diagram that can be constructed from studying the quantum quenches that give rise to these DPTs, proper characterization of the dynamical phases within, and what signatures would be experimentally feasible to detect. In this paper, it is exactly these questions that we study, and a summary of our results can be found in Fig. 1. The paper is organized as follows: In Sec. II we briefly review the theory of the type-II DPT and discuss its detection in the framework of iMPS. In Sec. III we present the main results of this study and discuss them. We conclude in Sec. V.

II. TYPE-II DPT

We consider the long-range transverse-field Ising model with power-law interactions

$$\mathcal{H} = -J \sum_{j>i=1}^L \frac{\sigma_i^z \sigma_j^z}{|i-j|^\alpha} - h \sum_i \sigma_i^x, \quad (1)$$

where $\sigma_i^{x,z}$ are Pauli matrices acting on site i , $J > 0$ is the spin-spin coupling constant, h is the magnetic field, L is the number of sites and we consider the thermodynamic limit $L \rightarrow \infty$. For quenches whose time evolution is propagated by \mathcal{H} , the motivation³ for studying nonanalyticities in the Loschmidt echo

$$G(t) = \langle \psi(0) | \psi(t) \rangle = \langle \psi(0) | e^{-i\mathcal{H}t} | \psi(0) \rangle \quad (2)$$

is to exploit the similarity between (2) and the partition function of the system in thermal equilibrium at inverse temperature β

$$\mathcal{Z}(\beta) = \text{Tr} e^{-\beta\mathcal{H}}, \quad (3)$$

and interpret (2) as a boundary partition function with boundary conditions $|\psi(0)\rangle$ and complex inverse temperature z

$$\mathcal{Z}_b(z) = \langle \psi(0) | e^{-z\mathcal{H}} | \psi(0) \rangle \quad (4)$$

along the imaginary axis $z = it$. Thus, the logarithm of the return probability $P(t) = |G(t)|^2$, i.e. the *return rate function*

$$r(t) = - \lim_{L \rightarrow \infty} \frac{1}{L} \log |G(t)|^2, \quad (5)$$

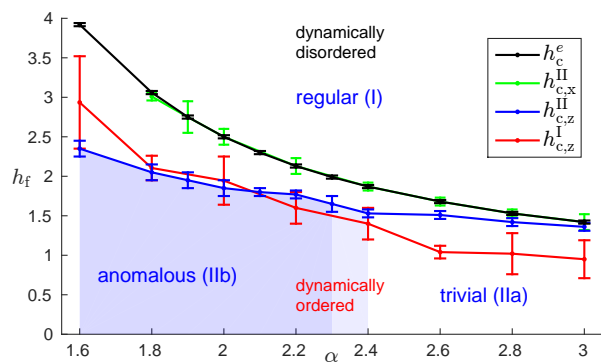


Figure 1. Enriched dynamical phase diagram of the long-range TFIM. h_c^e is the equilibrium critical line, $h_{c,z}^I$ is the type-I dynamical critical line, $h_{c,z}^{II}$ is the type-II dynamical critical line for quenches from $h_i = 0$ which signifies the onset of *regular cusps* for quenches above it, $h_{c,x}^{II}$ is the type-II dynamical critical line for quenches from $h_i \rightarrow \infty$ (there are no anomalous cusps for these quenches). Note how the critical lines $h_{c,x}^{II}$ and h_c^e overlap very well within the precision of our numerical simulations. For quenches from $h_i = 0$ to below $h_{c,z}^{II}$, the system ends up in a trivial (cusp-free) phase for $\alpha \gtrsim 2.3$ and an anomalous phase for $\alpha \lesssim 2.3$.

can be construed as an analogue of the free energy per site, in which nonanalyticities indicate the presence of a type-II DPT. Here one basically makes a connection between finite-temperature partition functions and time evolution, asking whether the latter can exhibit phase transitions as well. The type-II DPT has been studied in various systems, and in the case of the transverse-field Ising model (TFIM), it has been shown for the integrable cases of nearest-neighbor^{3,5} ($\alpha \rightarrow \infty$) and infinite-range interactions ($\alpha = 0$).⁸ In this paper, we study the type-II DPT in the one-dimensional long-range interacting ($1 < \alpha < \infty$), nonintegrable TFIM in the thermodynamic limit.

To study the type-II DPT, we calculate the return rate function per site³ (5), after performing a quantum quench, where we prepare the system in the groundstate $|\psi(0)\rangle$ of $\mathcal{H}(h_i)$ (that is $h = h_i$ in (1)), and then abruptly change the magnetic field from h_i to $h_f \neq h_i$ at time $t = 0$. As the system evolves in time as propagated by $\mathcal{H}(h_f)$, the return rate function per site (5) can then be calculated from the overlap (2) of the initial state with its time-evolved self. The return rate function can be calculated efficiently directly in the thermodynamic limit with iMPS techniques (minus) the logarithm of the dominant eigenvalue of an MPS transfer matrix at time t . Cusps in the return rate occur when there is a level crossing of the dominant eigenvalues of this transfer matrix. For details see Sec. A 3.

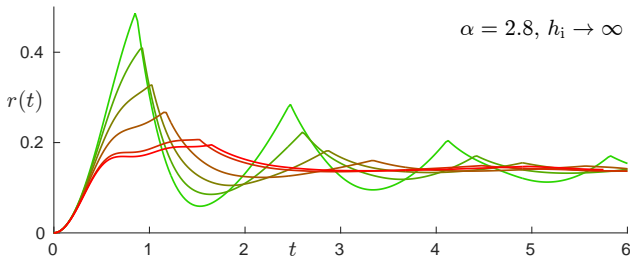


Figure 2. Return-rate function $r(t)$ for $\alpha = 2.8$, quenches from $h_i \rightarrow \infty$ to $h_f \in [0.75, 1.40]$ (from green to red).

III. RESULTS AND DISCUSSION

We shall now discuss the results of our iMPS time-evolution simulations for two types of quenches in the long-range TFIM (1) and first extract signatures of criticality for type-II DPT: (i) A quench from $h_i \rightarrow \infty$, corresponding to an initial state, which is the completely polarized state in positive x -direction (X-quench), and (ii) a quench from $h_i = 0$, where the groundstate is two-fold degenerate. We choose the completely polarized state in the positive z -direction as initial state (Z-quench).

For the X-quenches we find a critical phase, with the occurrence of conventional cusps in the return rate (5), as first observed in the nearest-neighbor transverse field Ising model (NN-TFIM).³ Henceforth, these cusps will be called *regular cusps*. We also find a trivial phase with no cusps in the return rate. These two phases exist for all studied α . For Z-quenches we again find a regular and a trivial phase, but additionally encounter an anomalous phase, replacing the trivial phase for $\alpha \lesssim 2.3$ only. The *anomalous cusps* appearing in this phase for $\alpha \lesssim 2.3$ are qualitatively different from the regular ones. Lastly, signatures of criticality for the type-I DPT, studied and characterized in Ref. 2, are also included for comparison. See Fig. 1 for the enriched phase diagram.

First, let us consider the case of X-quenches to some final value h_f of the transverse field, where we encounter the same situation as for the NN-TFIM.³ For quenches within the disordered *equilibrium* phase $h_f > h_c^e(\alpha)$, with $h_c^e(\alpha)$ the quantum equilibrium critical line,^{21–23} we observe a trivial phase with no cusps at all in the return rate. However, quenching across $h_c^e(\alpha)$ into the ordered equilibrium phase, we encounter a regular critical phase and (regular) cusps appear. Fig. 2 shows an example for $\alpha = 2.8$ and various h_f across the equilibrium critical point. It is apparent that the deeper the quench into the ordered phase, the more pronounced the cusps are, and the smaller the time intervals between the cusps become. As the quench approaches the critical point from below, these cusps appear less sharp and the intervals between them get longer. All cusps completely disappear simultaneously when crossing $h_c^e(\alpha)$ from below, i.e. when quenching within the disordered phase. The similarity to the NN-TFIM case is indicated in Fig. 1 by the

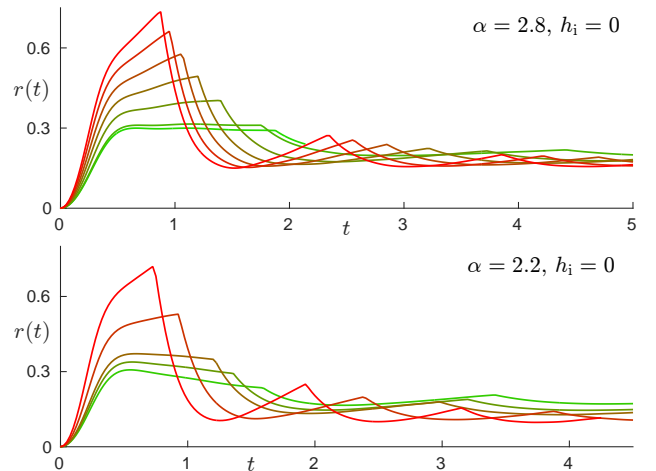


Figure 3. Return-rate function $r(t)$ for quenches from $h_i = 0$ to $h_f \in [1.50, 2.30]$ (from green to red) for $\alpha = 2.8$ (top) and $h_f \in [1.80, 2.80]$ (from green to red) for $\alpha = 2.2$ (bottom). This behavior is qualitatively the same for all α .

overlap of the type-II dynamical critical line $h_{c,x}^{\text{II}}$ for X-quenches with the quantum equilibrium critical line h_c^e within the precision of our numerical simulations.

On the other hand, for Z-quenches, we see three distinct type-II dynamical phases: (I) a *regular phase* with only regular cusps in the return rate (as for X-quenches above), that occurs when quenching across a type-II dynamical critical field value $h_{c,z}^{\text{II}}(\alpha)$, which is however lower than h_c^e (c.f. Fig. 1). For quenches below $h_{c,z}^{\text{II}}(\alpha)$ we encounter (IIa) a *trivial phase* for $\alpha \gtrsim 2.3$, that exhibits no cusps at all in the return rate, and interestingly, (IIb) an *anomalous phase* for $\alpha \lesssim 2.3$, that exhibits in the return rate anomalous cusps that are qualitatively different from the regular cusps in phase (I). The phase diagram in Fig. 1 therefore gets enriched in the regime $h_f < h_{c,z}^{\text{II}}$. The additional appearance of phase (IIb) featuring anomalous cusps and a critical field $h_{c,z}^{\text{II}}(\alpha)$ different from $h_c^e(\alpha)$ for this quench are the two major differences to such a quench in the NN-TFIM.

Let us focus on the regular phase (I) first. In Fig. 3 we show results for quenches to various $h_f > h_{c,z}^{\text{II}}$ and various α , where cusps in the rate function appear in roughly equispaced time intervals. With lowering h_f and approaching $h_{c,z}^{\text{II}}$, these time intervals *increase* and the cusps get less and less sharp until they all vanish simultaneously when crossing $h_{c,z}^{\text{II}}$. The time intervals as a function of h_f seem to be largely independent of α (see Fig. 4). These time intervals are also reflected in the oscillation period of the order parameter $m(t) = \langle \sigma^z(t) \rangle$. The times at which regular cusps appear match the zero crossings of $m(t)$ up to a temporal shift, as shown in Fig. 5. This fact has already been observed in the NN-TFIM^{3,10} and next-nearest-neighbor TFIM.¹⁰ It is worthy to note here that the periodicity of the return rate is doubled^{3,10} if one considers the return rate with respect to the degenerate

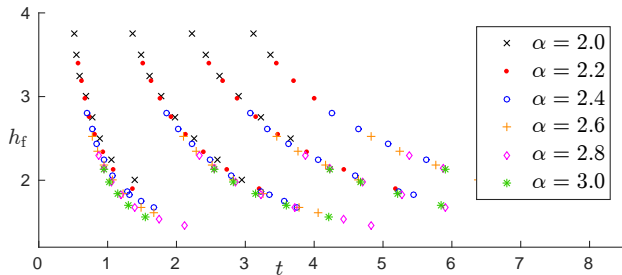


Figure 4. Times of regular cusps (c.f. Fig. 3 bottom), appearing in quenches from $h_i = 0$, for various $\alpha \in [2, 3]$ and $h_f > h_{c,z}^{\text{II}}$. It is clearly visible, that the respective times of the cusps *decrease* with increasing h_f . Moreover, the dependence of the times for each cusp seems independent of α , within an uncertainty of $\approx 5\%$.

subspace of the initial state rather than the initial state itself as we do. Thus, the only difference of this phase to conventional type-II criticality in the NN-TFIM is the critical field $h_{c,z}^{\text{II}}$.

The regular critical phase goes over into an anomalous critical phase (IIb) for quenches below $h_{c,z}^{\text{II}}$ and $\alpha \lesssim 2.3$. There, after a coexistence with the regular cusps around $h_{c,z}^{\text{II}}$, a qualitatively different type of cusps in the rate function appears (see Fig. 6). Upon further lowering h_f , the time intervals between these cusps *decreases*, contrary to the regular cusps in phase (I), and they vanish one by one as $h_f \rightarrow 0$, starting at early times, as can be seen in Fig. 7. As our evolution times for accurate simulations are limited, we can only conjecture that this type of cusps exists for any small $h_f > 0$, albeit only appearing at very large times. It is worth mentioning that some of these anomalous cusps show a “double-cusp” structure, where the location of these double cusps also seems to drift with α (for examples see Sec. B1). It also appears that these double cusps vanish sooner with lowering h_f than a preceding cusp. The nature and origin of these double cusps remains elusive. Such double cusps have previously been observed also for the transverse axial next-nearest-neighbor (ANNNI) and tilted field Ising model.¹⁰

Reiterating in comparison, upon lowering h_f the time intervals between regular cusps increases, whereas they decrease between anomalous cusps. Also, the regular cusps all vanish simultaneously when crossing $h_{c,z}^{\text{II}}$ (after a short coexistence region), whereas the anomalous cusps vanish one by one as $h_f \rightarrow 0$. Finally, the time intervals between anomalous cusps as a function of h_f shows a clear α -dependence, whereas for regular cusps the intervals seem to be largely independent of α (see Fig. 4 and Fig. 7).

For quenches below $h_{c,z}^{\text{II}}$ and $\alpha \gtrsim 2.3$, the regular phase (I) goes over into a trivial phase (IIa) with no cusps in the return rate.

We emphasize here that the two types of observed cusps are qualitatively different, as can be seen in how they arise from two qualitatively different groups of rate-

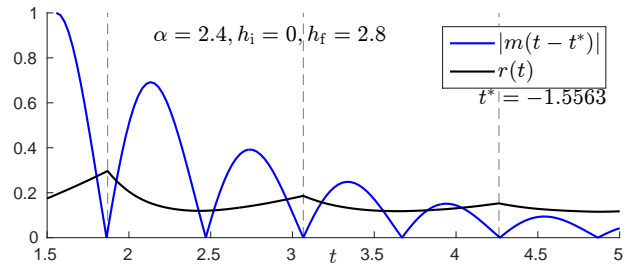


Figure 5. Return rate function $r(t)$ plotted together with (absolute value of) order parameter $|m(t)|$. The zeros of the shifted order parameter coincide with the cusps in the return rate.

function branches (A7) calculated from the MPS transfer matrix (A6), where it is always the lowest branch that corresponds to the actual return rate function. For $h_f > h_{c,z}^{\text{II}}$ the lowest rate-function branches are those developing regular cusps by crossing each other over time. Moving h_f closer and below $h_{c,z}^{\text{II}}$, this group of branches moves further up, revealing another (now lowest) group of rate-function branches developing anomalous cusps for $\alpha \lesssim 2.3$, or a group of branches without any crossings – and thus no cusps – for $\alpha \gtrsim 2.3$. These different groups of rate-function branches can in principle be distinguished by their functional form in time and the dependence of the time intervals between the crossings on h_f . For further details on the crossover between the regular phase (I) and the anomalous phase (IIb), see Sec. B2.

It would be interesting to know if the physical origin of these two different types of cusps is due to two different groups of Fisher zero lines of (4) in the complex plane,³ crossing the imaginary axis in different ways.

To summarize our findings for Z-quenches, in addition to the regular type-II critical phase (I) for $h_f > h_{c,z}^{\text{II}}$ and all α , and the trivial phase (IIa) for $h_f < h_{c,z}^{\text{II}}$ and $\alpha \gtrsim 2.3$, we also find an anomalous phase (IIb) for $h_f < h_{c,z}^{\text{II}}$ and $\alpha \lesssim 2.3$. This is surprising, as in the anomalous phase we encounter cusps without quenching across $h_{c,z}^{\text{II}}$, i.e. when quenching within the same phase. The cusps in the regular and anomalous phase differ qualitatively in their form, the time intervals between them, and how they vanish upon lowering h_f .

Finally, after characterizing the type-II DPT for X-quenches and Z-quenches and observing a new type-II phase due to anomalous cusps, we discuss the relationship of the type-I and type-II DPTs according to their critical lines in the rich phase diagram of Fig. 1. The critical line of the type-I DPT is much harder to obtain, as this kind of DPT relies on reaching a kind of a steady state at time $t \approx t^*$, from which the order parameter $\bar{m} = m(t^*)$ is extracted, and then one tries to establish the existence or absence of a nonanalyticity of this order parameter as a function of h_f , as in our case. This type-I DPT has been extensively studied in the nonintegrable long-range TFIM,² and it was estab-

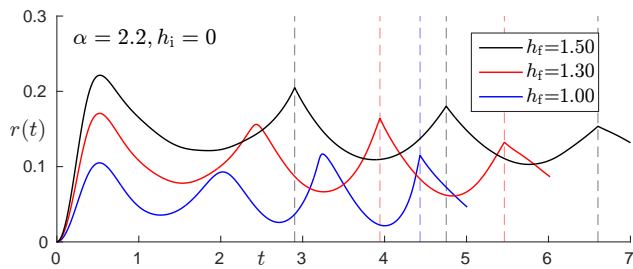


Figure 6. Examples of anomalous cusps (marked by vertical dashed lines) for $h_f < h_{c,z}^{\text{II}}$. It is clearly visible, that with increasing h_f more and more such cusps develop at smaller and smaller times, their respective locations however move to higher times (c.f. also Fig. 7). See Fig. 9 for a plot showing how these cusps arise from level crossings in the MPS transfer-matrix.

lished that pre-thermalization conspires to give rise to the type-I DPT even for $\alpha > 2$ where the long-range TFIM exhibits no thermal phase transition in one spatial dimension.¹⁵ Comparing the type-I and type-II critical lines, an unequivocal conclusion is unrealistic, given the evolution times of accurate simulations reached, or by those also done using finite-size t -DMRG.² However, from the data, it looks that the two types of DPT are nontrivially connected and at least show the same tendency in their α -dependence.

IV. CONCLUSIONS

We have carried out time-evolution simulations of pure quantum states after quantum quenches in the one-dimensional long-range TFIM in the thermodynamic limit using an iMPS technique based on the time-dependent variational principle. We considered different initial conditions for the quantum quenches and studied two corresponding types of dynamical phase transition: the type-I DPT characterized by a nonanalyticity in the magnetization of a dynamical quasi-steady state as a function of the transverse-field strength, and the type-II DPT manifested as nonanalyticities in the form of cusps in the Loschmidt-echo return rate. For the type-II DPT, quenches from the fully x -polarized state (X-quenches) lead to two dynamical phases separated by the quantum equilibrium critical line, where the return rate exhibits cusps only for quenches into the ordered equilibrium phase. These cusps resemble in their nature those already found and studied in the nearest-neighbor TFIM. On the other hand, for Z-quenches, where the initial state is fully z -polarized, when quenching into the disordered dynamical phase we observe conventional (regular) cusps for all α , where we have calculated the corresponding dynamical critical line, which differs from the equilibrium critical line. For Z-quenches below this dynamical critical line, we find two phases: the trivial cusp-free phase for $\alpha > 2.3$ similar to that found in the case of the

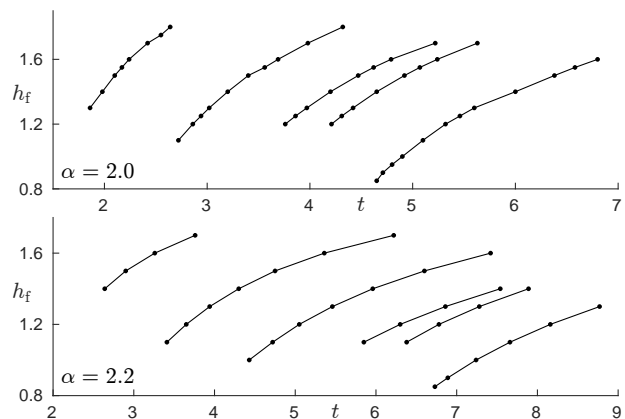


Figure 7. Times of anomalous cusps only, for $\alpha = 2$ (top) and $\alpha = 2.2$ (bottom) as a function of $h_f < h_{c,z}^{\text{II}}$. For $h_f > h_{c,z}^{\text{II}}$, the anomalous cusps vanish, as the regular cusps take over. The shown black lines would continue further to higher times (top right), but were outside our reachable simulation times.

nearest-neighbor TFIM or in the case of X-quenches in the long-range TFIM, and, quite remarkably, a third distinct anomalous phase for $\alpha \lesssim 2.3$ where the return rate shows anomalous cusps that may be the result of a different group of Fisher zero lines of the partition function in the complex plane. Finally, we also show a nontrivial connection between the type-I and type-II DPTs, albeit with the precision of our numerical simulations, this connection cannot be reasonably described as definitive.

In the final stages of writing this manuscript, we became aware of a study²⁴ that discusses some of our results in part while dealing with finite-size systems.

ACKNOWLEDGMENTS

Both authors contributed equally to this work. We thank Damian Draxler, Jutho Haegeman, Michael Kastner, Andreas Läuchli, Ian P. McCulloch, Francesco Piazza, and Frank Verstraete for inspiring and helpful discussions. V. Z.-S. gratefully acknowledges support from the Austrian Science Fund (FWF): F4104 SFB ViCoM and F4014 SFB FoQuS.

Appendix A: Infinite matrix product state technique

In this section we give a short description of the algorithm used to simulate the real-time evolution of a spin chain under a Hamiltonian with long-range interactions in the thermodynamic limit. In our case, this Hamiltonian is the long-range TFIM, but our algorithm applies to other general models.

1. Long-range interactions

We assume the Hamiltonian to contain a sum of two-body interactions of the form $h_{ij}^{(2)} = O_i O_j f(|j-i|)$, where operators O_i act on a single site i and commute when acting on different sites $[O_i, O_j] = 0$, $i \neq j$. Specifically, we consider the long-range transverse-field Ising model (1), where the distance function decays as a power law $f(n) = n^{-\alpha}$ and we assume $f(n)$ to be well approximated by a sum of K exponentials, i.e. $f(n) = \sum_{k=1}^K c_k \lambda_k^{n-1}$, with $\lambda_k < 1$ and $n > 0$. With this approximation the overall Hamiltonian is then given by

$$\mathcal{H} = -J \sum_k \sum_{j>i} c_k \lambda_k^{j-i-1} \sigma_i^z \sigma_j^z - h \sum_i \sigma_i^x. \quad (\text{A1})$$

For an infinite system we fit $f(n)$ with a suitable number of exponentials over a distance N large enough, such that $f(N) < \varepsilon_f$, where ε_f is of the order $\mathcal{O}(10^{-6})$ - $\mathcal{O}(10^{-8})$ and the largest residuals are of the order $\mathcal{O}(10^{-5})$. This usually amounts to a K in the range of 5 - 25.

2. MPS real-time evolution

To simulate the real-time evolution of a pure quantum state $|\psi\rangle$ within the variational space of Matrix Product States (MPS)^{16,17,25} with respect to (A1), we adapt the algorithm of Ref. 26 to the thermodynamic limit. The method of Ref. 26 integrates the time-dependent Schrödinger equation $\partial_t |\psi\rangle = -i\mathcal{H} |\psi\rangle$ by applying the time-dependent variational principle (TDVP) onto the subspace of MPS,²⁷ but uses a Lie-Trotter splitting scheme of the projector onto the tangent space of the variational manifold to directly integrate the effective differential equations for the MPS tensors. Due to this splitting scheme it is necessary to evolve the state in small time steps τ only. For details on notation and the algorithm we refer the reader to Refs. 26 and 27.

In the following we describe the evolution of a translation-invariant MPS in the thermodynamic limit (iMPS) by a small time step τ . We assume the state at time t to be given in terms of a translation-invariant iMPS in the mixed canonical form,²⁵ i.e. the state is approximated by an MPS given by (site-independent) MPS tensors A_L^s and A_R^s in the left and right gauge, and a bond matrix C whose singular values are the Schmidt-

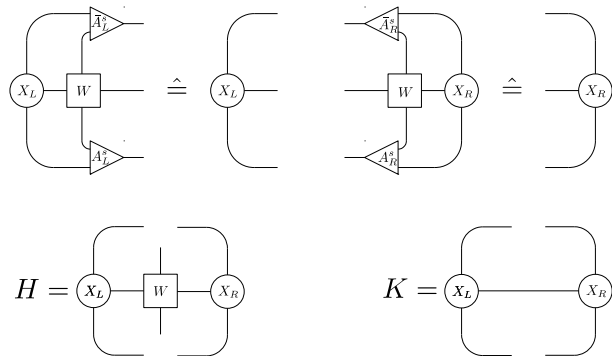


Figure 8. Fixed point relations for the left and right MPO transfer matrices (A5) and definition of the effective Hamiltonians H for A_C^s and K for C . The symbol $\hat{=}$ refers to equality up to terms contributing to the energy expectation value per site³².

values of a bipartition of the state

$$|\psi\rangle = \sum_{\mathbf{s}} (\dots A_L^{s_{n-2}} A_L^{s_{n-1}} C A_R^{s_n} A_R^{s_{n+1}} \dots) |\mathbf{s}\rangle, \quad (\text{A2})$$

where n is an arbitrary site on the chain. This also defines a center-tensor $A_C^s = A_L^s C = C A_R^s$ and the gauge conditions read

$$\sum_s A_L^{s\dagger} A_L^s = \mathbb{1} \quad \sum_s A_L^s C C^\dagger A_L^{s\dagger} = C C^\dagger \quad (\text{A3})$$

$$\sum_s A_R^s A_R^{s\dagger} = \mathbb{1} \quad \sum_s A_R^{s\dagger} C^\dagger C A_R^s = C^\dagger C. \quad (\text{A4})$$

We represent the Hamiltonian (A1) in terms of a Matrix Product Operator (MPO)²⁸⁻³¹ W with bond dimension $d_w = K + 2$. The projection of $\mathcal{H} |\psi\rangle$ onto the MPS tangent plane defines effective Hamiltonians H for A_C^s and K for C ²⁶. In order to calculate these it is necessary to determine the left and right fixed points of the MPO transfer matrices (c.f. Ref. 32 and Fig. 8)

$$\mathcal{T}_{L/R}^{ab} = \sum_{ss'} W_{s's}^{ab} \bar{A}_{L/R}^{s'} \otimes A_{L/R}^s, \quad (\text{A5})$$

where a bar denotes complex conjugation and indices $a, b \in [1, \dots, d_w]$.

The algorithm in Ref. 26 for a *finite* chain proceeds by performing the following steps sequentially for each site n of the lattice (e.g. in a left-to-right sweep)

1. Calculate $H(n)$ as a function of $\tilde{A}_L^s(m < n)$ and $A_R^s(m > n)$.
2. Evolve $\tilde{\mathbf{A}}_C(n) = \exp(-i\tau H(n)) \mathbf{A}_C(n)$ forwards in time.
3. Split $\tilde{A}_C^s(n) = \tilde{A}_L^s(n) \tilde{C}(n)$.
4. Calculate $K(n)$ as a function of $\tilde{A}_L^s(m \leq n)$ and $A_R^s(m > n)$.

5. Evolve $\mathbf{C}(n) = \exp(+i\tau K(n)) \tilde{\mathbf{C}}(n)$ backwards in time and form $A_C^s(n+1) = C(n) A_R^s(n+1)$.

Here $\tilde{A}_L^s(n)$ refers to tensors updated in previous steps and bold symbols refer to vectorizations of the tensors. Note that both H and K are calculated from *evolved* \tilde{A}_L^s and yet *unevolved* A_R^s . In the thermodynamic limit, A_L^s and A_R^s correspond to the same state and we want to evolve both of them at the same time. The following adapted algorithm achieves this

1. Calculate H and K from current A_L^s and A_R^s and form $A_C^s = A_L^s C = C A_R^s$.
2. Evolve $\tilde{\mathbf{A}}_C = \exp(-i\tau H) \mathbf{A}_C$ forwards in time.
3. Evolve $\tilde{\mathbf{C}} = \exp(-i\tau K) \mathbf{C}$ forwards in time.
4. Determine the optimal updated \tilde{A}_L^s and \tilde{A}_R^s by minimizing $\varepsilon_R = \|\sum_s \tilde{A}_C^s - \tilde{A}_L^s \tilde{\mathbf{C}}\|_2$ and $\varepsilon_L = \|\sum_s \tilde{A}_C^s - \tilde{\mathbf{C}} \tilde{A}_R^s\|_2$ under the constraints $\sum_s \tilde{A}_L^s \tilde{A}_L^{s\dagger} = \sum_s \tilde{A}_R^s \tilde{A}_R^{s\dagger} = \mathbb{1}$.

This scheme corresponds to a first-order splitting scheme³³ with an error scaling of $\mathcal{O}(\tau^2)$.²⁶ In practice we use a time step of $\tau = 0.002$. The quantities ε_L and ε_R can be used as a measure of the quality of a time step and of the constraint $A_L^s C = C A_R^s$. We regauge the state if ε_L and ε_R rise above a certain threshold.

We increase the bond dimension of the MPS whenever the smallest of the Schmidt-values (which are the singular values of C) rises above a certain threshold ε_S . For this we use a variant of a single application of the two-site integrator presented in Ref. 26, adapted to the thermodynamic limit.³⁴ In practice we use $\varepsilon_S = 10^{-9}$ and a maximum bond dimension of $D_{\max} \approx 350$, which – depending on \mathcal{H} – limits the maximum reachable simulation time t_{\max} severely due to the (at worst) linear increase of entanglement entropy^{35,36}.

3. Loschmidt echo and the return rate

The rate function of the return probability per site (5) corresponds to (minus) the logarithm of the dominant eigenvalue of the mixed MPS transfer matrix¹⁰

$$\mathcal{T}(t) = \sum_s \bar{A}^s(0) \otimes A^s(t) \quad (\text{A6})$$

between MPS tensors³⁷ at time zero and t , whose spectral radius is $\rho(\mathcal{T}(t)) \leq 1$. If $\epsilon_i(t)$ are the eigenvalues of (A6) in descending order by magnitude (i.e. $\epsilon_1(t)$ being the largest), then we define the rate-function branches

$$r_i(t) = -2 \log |\epsilon_i(t)|, \quad (\text{A7})$$

and the rate function (5) is simply $r(t) = r_1(t)$, with all other $r_{i>1} > r_1(t)$.

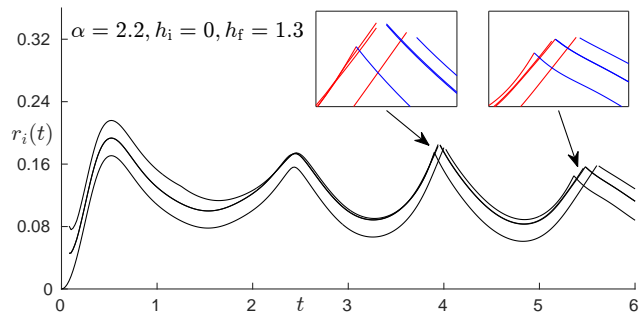


Figure 9. Example of how cusps in the return rate $r(t)$ can be detected through level crossings of the rate-function branches $r_i(t)$ (A7). Shown are the first four $r_i(t)$ for a quench from $h_i = 0$ to $h_f = 1.3$ and $\alpha = 2.2$, where the *lowest* branch represents the rate function (5). At $t \approx 2.4$ there are no level crossings, $r(t)$ is thus smooth. At times $t \approx 4$ and $t \approx 5.5$ there are level crossings in the rate-function branches, which cause cusps in $r(t)$. The example shows anomalous cusps, however also regular (or in fact any other type of) cusps show up due to this mechanism. The insets show a magnification of these cusps, where branches that are going up are colored red and branches coming down are colored blue for better visualization.

Nonanalyticities of (5) in t in the form of cusps arise due to level crossings in the eigenspectrum of (A6), which is a feature characteristic of first-order phase transitions. The occurrence of such nonanalyticities can thus nicely be anticipated by calculating and following the first few rate-function branches. Cusps arise at branch crossings, where a higher branch becomes the lowest one at some time t_c (see Fig. 9).

The mixed MPS transfer matrix (A6) represents a renormalized version of the true Quantum Transfer Matrix of a real-time path-integral formulation of (2).³⁸

4. Alternative calculation of the rate function

Trivially, (2) can also be written as

$$\begin{aligned} \langle \psi(0) | \psi(t) \rangle &= \langle \psi(0) | \exp(-i\mathcal{H}t) | \psi(0) \rangle \\ &= (\langle \psi(0) | \exp(-i\mathcal{H}t/2)) (\exp(-i\mathcal{H}t/2) | \psi(0) \rangle) \\ &= \langle \psi(-t/2) | \psi(t/2) \rangle, \end{aligned} \quad (\text{A8})$$

where in the present case the backward-evolved state $|\psi(-t/2)\rangle$ can be obtained from the forward-evolved state as $|\psi(-t/2)\rangle = \overline{|\psi(t/2)\rangle}$, i.e. by complex conjugation. We exploit this fact to evaluate the rate function at time t with the MPS at time $t/2$, i.e. we use the leading eigenvalues of

$$\tilde{\mathcal{T}}(t) = \sum_s A^s(t/2) \otimes A^s(t/2). \quad (\text{A9})$$

Thus, $r(t)$ can be calculated both from (A6) at time t and also from (A9) at time $t/2$, and the agreement of

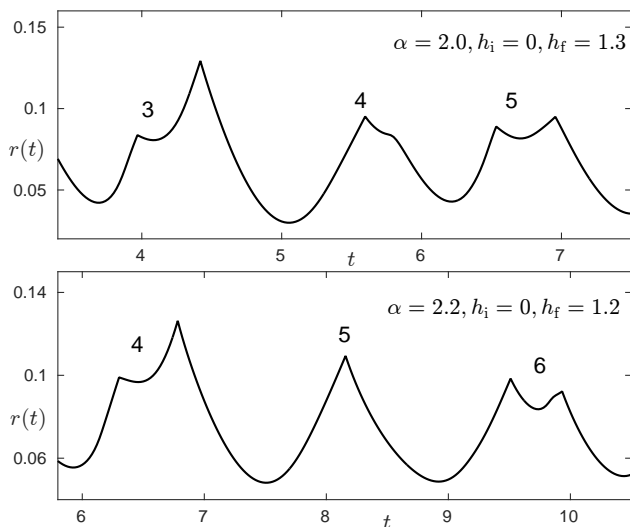


Figure 10. Examples of double cusps for quenches within the anomalous phase. Here for $\alpha = 2$, the 3rd and 5th cusp are double cusps, for $\alpha = 2.2$ the 4th and 6th cusps are double cusps.

both serves as an additional check for the validity of the numerical results.

Appendix B: Additional Rate Function Plots

1. Double Cusps

In this section we show examples of anomalous double cusps, that show up for quenches with $\alpha \lesssim 2.3$ and $h_f < h_{c,z}^{\text{II}}$. Some of the anomalous cusps develop a double cusp structure in the sense that the tip of these cusps seems to be cut off by another rate-function branch coming down at exactly that time.

2. Crossover between Regular and Anomalous Cusps

In this section we describe for quenches with $\alpha \lesssim 2.3$ and $h_i = 0$, how regular cusps overtake the anomalous cusps with h_f approaching and going over $h_{c,z}^{\text{II}}$. As mentioned in the main text, this is due to a new group of rate-

function branches $r_i(t)$ (A7) coming down with increasing h_f , which eventually become lower than the branches responsible for developing the anomalous cusps. This new group of rate-function branches then start to develop regular cusps between each other for all $h_f > h_{c,z}^{\text{II}}$. Such a crossover situation is depicted in Fig. 11 for $\alpha = 2$. Further increasing h_f will cause all anomalous cusps to be completely covered by these new branches, which develop regular cusps. The anomalous cusps could in principle still be followed and identified in the higher up rate-function branches, but they do not contribute to the actual return rate function $r(t)$ and cusps therein anymore.

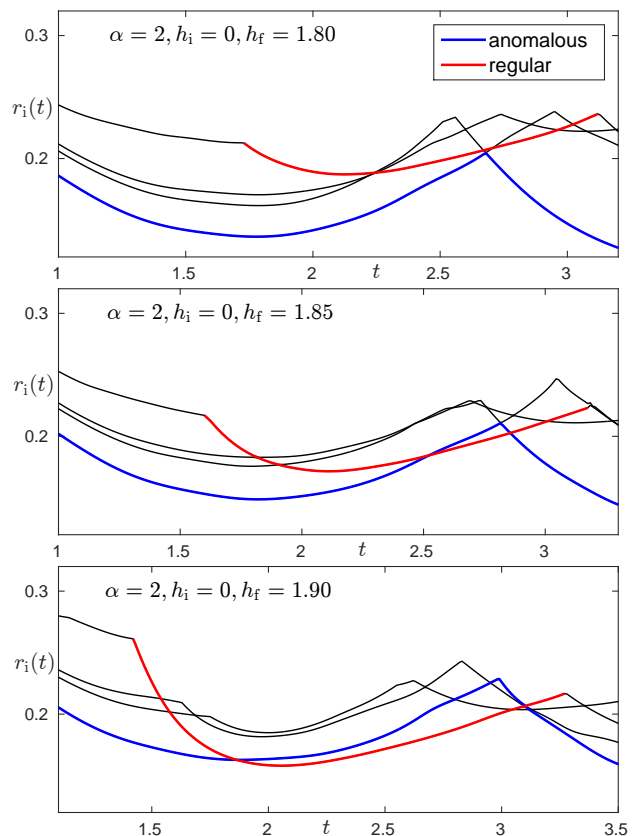


Figure 11. Example of rate-function branches $r_i(t)$ responsible for developing regular cusps (red) coming down and taking over branches responsible for developing anomalous cusps (blue) with increasing h_f (here $h_{c,z}^{\text{II}} = 1.85$).

¹ P. Calabrese, F. H. L. Essler, and M. Fagotti, Phys. Rev. Lett. **106**, 227203 (2011).

² J. C. Halimeh, V. Zauner-Stauber, I. P. McCulloch, I. de Vega, U. Schollwöck, and M. Kastner, arXiv:1610.01468 (2016).

³ M. Heyl, A. Polkovnikov, and S. Kehrein, Phys. Rev. Lett. **110**, 135704 (2013).

⁴ M. Heyl, Phys. Rev. Lett. **113**, 205701 (2014).

⁵ M. Heyl, Phys. Rev. Lett. **115**, 140602 (2015).

⁶ M. Heyl, arXiv:1608.06659.

⁷ S. Campbell, arXiv:1608.05325v1.

⁸ B. Zunkovic, A. Silva, and M. Fabrizio, Phil. Trans. R. Soc. A **374**, 20150160 (2016).

- ⁹ E. Canovi, P. Werner, and M. Eckstein, Phys. Rev. Lett. **113**, 265702 (2014).
- ¹⁰ C. Karrasch and D. Schuricht, Phys. Rev. B **87**, 195104 (2013)
- ¹¹ N. Fläschner et al., arXiv:1608.05616.
- ¹² F. Andraschko and J. Sirker, Phys. Rev. B **89**, 125120 (2014).
- ¹³ S. Vajna and B. Dóra, Phys. Rev. B **89**, 161105(R) (2014).
- ¹⁴ N. Abelung and S. Kehrein, Phys. Rev. B **93**, 104302 (2016).
- ¹⁵ A. Dutta and J. K. Bhattacharjee, Phys. Rev. B **64**, 184106 (2001).
- ¹⁶ M. Fannes, B. Nachtergaele, R. Werner, Comm. Math. Phys. **144**, 443 (1992)
- ¹⁷ F. Verstraete, V. Murg, J.I. Cirac, Adv. Phys. **57**, 143 (2008)
- ¹⁸ G. Vidal, Phys. Rev. Lett. **93**, 040502 (2004)
- ¹⁹ A. J. Daley, C. Kollath, U. Schollwöck, G. Vidal, J. Stat. Mech.: Theor. Exp. P04005 (2004)
- ²⁰ S.R. White, A.E. Feiguin, Phys. Rev. Lett. **93**, 076401 (2004)
- ²¹ The equilibrium critical line has been obtained by monitoring the order parameter $\langle \sigma^z \rangle$ as a function of h in an iMPS groundstate calculation.^{22,23}
- ²² S. R. White, Phys. Rev. Lett. **69**, 2863 (1992).
- ²³ I. P. McCulloch, arXiv:0804.2509, (2008)
- ²⁴ B. Zunkovic, M. Heyl, M. Knap, and A. Silva, arxiv:1609.08482 (2016).
- ²⁵ U. Schollwöck, Ann. Phys. (NY) **326**, 96 (2011).
- ²⁶ J. Haegeman et al., arXiv:1408.5056 (2014)
- ²⁷ J. Haegeman et al., Phys. Rev. Lett. **107**, 070601 (2011)
- ²⁸ F. Verstraete, J.J. Garcia-Ripoll, J.I. Cirac, Phys. Rev. Lett. **93**, 207204 (2004);
- ²⁹ I.P. McCulloch, J. Stat. Mech.: Theor. Exp. (2007) P10014;
- ³⁰ B. Pirvu, V. Murg, J.I. Cirac, F. Verstraete, New J. Phys. **12**, 025012 (2010)
- ³¹ G.M. Crosswhite, D. Bacon, Phys. Rev. A **78**, 012356 (2008); G.M. Crosswhite, A.C. Doherty, G. Vidal, Phys. Rev. B **78**, 035116 (2008); F. Fröwis, V. Nebendahl, W. Dür, Phys. Rev. A **81**, 062337 (2010)
- ³² L. Michel, I.P. McCulloch, arXiv:1008.4667 (2010)
- ³³ Higher order schemes can be constructed in a slightly different way, but are computationally much more unfavorable than performing a first order step several times for a smaller time step.
- ³⁴ J. Haegeman, V. Zauner-Stauber, M. Fishman, F. Verstraete, *in preparation*
- ³⁵ N. Schuch, M.M. Wolf, K.G.H. Vollbrecht, J.I. Cirac, New J. Phys. **10**, 033032 (2008).
- ³⁶ T. Prosen, M. Znidaric, Phys. Rev. E **75**, 015202 (2007)
- ³⁷ The gauge choices for $A^s(0)$ and $A^s(t)$ do not affect the eigenspectrum of $\mathcal{T}(t)$ and are therefore irrelevant.
- ³⁸ V. Zauner et al., New J. Phys. **17**, 053002 (2015)

Chapter 5

Chebyshev matrix product state approach for time evolution

The fundamental limitation to accessible evolution times in methods based on matrix product states (MPS) is linked to entanglement build-up in the wavefunction. In quenches, it is known that entanglement grows linearly with evolution time, and in MPS, the logarithm of the matrix dimension D gives the maximal entanglement between two subsystems. This means that the matrix dimension D grows exponentially in evolution time. In this work we express the time-evolution operator as an expansion in terms of Chebyshev polynomials. This leads to calculating Chebyshev vectors, which encode the time evolution of any observable, in lieu of a time-dependent wavefunction. The hope was originally that splitting the entanglement over many vectors may lead to longer evolution times.

- *Chebyshev matrix product state approach for time evolution*
Jad C. Halimeh, Fabian Kolley, and Ian P. McCulloch
Phys. Rev. B **92**, 115130 (2015)

Chebyshev matrix product state approach for time evolution

Jad C. Halimeh,¹ Fabian Kolley,¹ and Ian P. McCulloch²

¹*Physics Department and Arnold Sommerfeld Center for Theoretical Physics, Ludwig-Maximilians-Universität München, 80333 München, Germany*

²*ARC Centre for Engineered Quantum Systems, School of Mathematics and Physics, The University of Queensland, St. Lucia, Queensland 4072, Australia*

(Received 7 July 2015; published 14 September 2015)

We present and test a new algorithm for time-evolving quantum many-body systems initially proposed by Holzner *et al.* [*Phys. Rev. B* **83**, 195115 (2011)]. The approach is based on merging the matrix product state (MPS) formalism with the method of expanding the time-evolution operator in Chebyshev polynomials. We calculate time-dependent observables of a system of hardcore bosons quenched under the Bose-Hubbard Hamiltonian on a one-dimensional lattice. We compare the new algorithm to more standard methods using the MPS architecture. We find that the Chebyshev method gives numerically exact results for small times. However, the reachable times are smaller than the ones obtained with the other state-of-the-art methods. We further extend the new method using a spectral-decomposition-based projective scheme that utilizes an effective bandwidth significantly smaller than the full bandwidth, leading to longer evolution times than the nonprojective method and more efficient information storage, data compression, and less computational effort.

DOI: [10.1103/PhysRevB.92.115130](https://doi.org/10.1103/PhysRevB.92.115130)

PACS number(s): 75.10.Pq, 75.40.Mg, 21.60.Fw, 05.30.Jp

I. INTRODUCTION

Besides being of central interest in the field, achieving large accessible times in the time evolution of strongly correlated quantum many-body systems with existing numerical methods has proven to be a daunting task in any spatial dimension and particularly for global quenches. Experiments in quantum many-body physics in the last years have evolved in such a manner that local control over degrees of freedom has become more feasible [1–8] and in which quantum magnetism, spin dynamics, and relaxation dynamics have been explored. Additionally, along this experimental work a whole body of theoretical investigations has arisen that relies on various analytical and numerical methods to describe the dynamics of these experiments.

The time-dependent Schrödinger equation

$$i \frac{d}{dt} |\psi(t)\rangle = \hat{H} |\psi(t)\rangle \quad (1)$$

for a generic time-independent Hamiltonian \hat{H} and initial state $|\psi_0\rangle = |\psi(0)\rangle$ is formally solved by the time-evolution operator

$$U(t) = \exp(-i\hat{H}t), \quad (2)$$

where the reduced Planck constant \hbar is set to 1. The time-evolved quantum state for arbitrary times is then given by

$$|\psi(t)\rangle = U(t)|\psi_0\rangle = \exp(-i\hat{H}t)|\psi_0\rangle. \quad (3)$$

However, for a many-body quantum system, the dimension of the Hilbert space grows exponentially with the number of constituents in the system under consideration, making it impossible to calculate the matrix exponential in Eq. (3) exactly and, therefore, approximate methods are required.

The purpose of this work is to discuss achievable evolution times for complex quantum many-body systems such as global quenches relevant to the current experimental efforts in the field. As the errors encountered in experiments are

usually larger than those in numerical calculations, we are not interested in an increase in accuracy.

One method that has proven extremely useful is t -DMRG [9–12], which is based on the description of the quantum state in terms of matrix product states (MPS) [13–19]

$$|\psi\rangle = \sum_{\{\sigma\}} c_{\sigma} |\sigma\rangle = \sum_{\{\sigma\}} A^{\sigma_1} \dots A^{\sigma_N} |\sigma\rangle, \quad (4)$$

where $\sigma = \{\sigma_1 \dots \sigma_N\}$ is the computational basis, A^{σ_1} and A^{σ_N} are D -dimensional row and column vectors, respectively, and A^{σ_i} ($i = 2, \dots, N-1$) is a $D \times D$ matrix. Theoretically, every quantum state can be represented by an MPS if infinite matrix dimensions are allowed [20]. The practical relevance of such a state description lies in the fact that one can often very well approximate the exact quantum state by an MPS with finite matrix dimension. From this perspective, MPS presents a class of states that compress exact many-body quantum states such that the number of coefficients needed to describe the state scales linearly in the number of constituents as opposed to the exponential scaling in the exact representation. Furthermore, the approximation made in the compression step is well understood [15] and can be controlled by the matrix dimension D .

With the help of MPS, several methods have been developed to calculate the time evolution of one-dimensional many-body quantum systems [16]. The earliest methods utilize the Trotter [21,22] decomposition of the time-evolution operator. Later approaches approximate the matrix exponential in the Krylov [23] subspace. Both methods have been successfully applied to a series of different physical problems.

Nevertheless, the times reachable with current methods are still very limited making the development of new methods still a very important endeavor. The limitation of evolution times accessible with MPS-based methods is closely related to the amount of entanglement in the quantum state. The maximal entanglement between two subsystems describable by an MPS is given by the logarithm of the matrix dimension

D. On the other hand, it has been shown that the entanglement after a quantum quench grows typically linearly in time [24] leading to an exponentially growing matrix dimension, which is required in order to keep the error fixed.

In this work, we test a new method for calculating the time evolution of one-dimensional quantum many-body systems as it was proposed in Ref. [25] by Holzner *et al.* We attempt to merge MPS with the method of approximating the time-evolution operator in terms of Chebyshev polynomials. The procedure of expanding the time-evolution operator in terms of Chebyshev polynomials is general and requires in principle solely a matrix-vector multiplication. The MPS approach together with the representation of the Hamiltonian as a matrix product operator provides an efficient way to perform these operations in the quantum many-body framework. A related approach based on Chebyshev polynomials has recently been successfully applied in the frequency domain to obtain an efficient impurity solver for the dynamical mean-field theory (DMFT) algorithm [26–28] and for calculating spectral functions [29] and Green’s functions [30].

For real-time dynamics in MPS, however, the approach has not been tested so far. In this paper, we test the new method (dubbed *t*-CheMPS) for a nontrivial system of hardcore bosons which evolve in time under the Bose-Hubbard Hamiltonian in a one-dimensional lattice. We show that time-dependent observables can be calculated numerically exactly with the *t*-CheMPS method up to a certain time beyond which exponentially growing errors become dominant. The time reachable is given by the amount of entanglement in the *n*th Chebyshev vector and can be slightly increased by making use of a projection procedure onto the energy range where the initial state has finite nonzero spectral weight. We compare our results to the time-evolution methods based on the Trotter [21,22] expansion and Krylov [23] approximation of the time-evolution operator. We find that for the problem considered in this work the Trotter-based method reaches the longest times, followed by the method based on the Krylov approximation.

This paper is structured as follows: Sec. II gives a brief overview of the standard state-of-the-art methods in time evolution within the MPS context. Section III discusses the *t*-CheMPS method and its workings. Section IV presents an extension of the latter, namely, projective *t*-CheMPS based on the spectral decomposition of the initial state. Section V discusses the Bose-Hubbard-model global quench used for the simulations in this paper, the results of which are documented in Sec. VI. The paper concludes with Sec. VII.

II. STANDARD TIME-EVOLUTION METHODS IN MPS

A. Krylov time evolution

Instead of treating Schrödinger’s equation as a differential equation, one considers, for time-independent Hamiltonians, the time-evolution operator $\exp(-i\hat{H}t)$. This sets the nontrivial task of evaluating an exponential of matrices [12,31]. One of the most efficient methods is the so-called Krylov subspace approximation [12,16,23,32–35,53], where one realizes that our interest lies in $\exp(-i\hat{H}t)|\psi\rangle$ rather than $\exp(-i\hat{H}t)$. In DMRG $\hat{H}|\psi\rangle$ is available efficiently, and

this can be utilized through forming the Krylov subspace by successive Gram-Schmidt orthonormalization of the set $\{|\psi\rangle, -i\hat{H}t|\psi\rangle, (-i\hat{H}t)^2|\psi\rangle, \dots\}$, where $|\psi\rangle$ is assumed to be normalized here. Here, $-i\hat{H}t$ is approximated regarding its extreme eigenvalues by VTV^T , where V is the matrix containing the *n* Krylov vectors thus obtained from the Gram-Schmidt decomposition and T is an $n \times n$ tridiagonal matrix. This approximation is up to a very good precision even for relatively small numbers of Krylov vectors [12]. Thereafter, the exponential is given by the first column of $V \exp T$, where the latter exponential is now much easier to calculate.

B. Suzuki-Trotter time evolution

Another prominent and very efficient method for evaluating the above matrix exponential is the Suzuki-Trotter decomposition [12,16,21,22]. This method is mainly useful for Hamiltonians with nearest-neighbor interactions. In the case of a one-dimensional chain, the Hamiltonian $\hat{H} = \hat{H}_1 + \hat{H}_2$ is divided into odd- and even-bond terms, \hat{H}_1 and \hat{H}_2 , respectively, where $\hat{H}_1 = \sum_{i=1}^{N/2} \hat{h}_{2i-1}$ and $\hat{H}_2 = \sum_{i=1}^{N/2} \hat{h}_{2i}$. Here, \hat{h}_i is the local Hamiltonian linking sites *i* and *i* + 1, and *N* is the total number of sites on the lattice. $[\hat{H}_1, \hat{H}_2] \neq 0$ as neighboring local Hamiltonians do not commute in general, but all the terms in \hat{H}_1 and \hat{H}_2 commute. As such, the first-order Trotter decomposition of the infinitesimal time-evolution operator is

$$e^{-i\hat{H}\Delta t} = e^{-i\hat{H}_1\Delta t} e^{-i\hat{H}_2\Delta t} + O(\Delta t^2). \quad (5)$$

Moreover, the second-order Trotter decomposition reads

$$e^{-i\hat{H}\Delta t} = e^{-i\hat{H}_1\Delta t/2} e^{-i\hat{H}_2\Delta t} e^{-i\hat{H}_1\Delta t/2} + O(\Delta t^3). \quad (6)$$

One can go for yet higher orders and conclude that an *n*th-order Trotter decomposition will yield over a time step Δt an error of the order of $(\Delta t)^{n+1}$. As one requires $t/\Delta t$ time steps in order to reach an evolution time *t*, the error grows at worst linearly [12] in time *t*, and therefore, the resulting error is bound by an expression of the order of $(\Delta t)^n t$. For the purposes of this study, it turns out that second-order Trotter decomposition is optimal.

Time-dependent DMRG (*t*-DMRG) uses adaptive Hilbert spaces that follow the state $|\psi(t)\rangle$ being optimally approximated, and was first proposed independently in the works of Daley, Kollath, Schollwöck, and Vidal [36] and White and Feiguin [9], based on the time-evolving block-decimation (TEBD) algorithm [20,37] for the classical simulation of the time evolution of weakly entangled quantum states, and by Schmitteckert [38] who published on nonequilibrium electron transport in interacting one-dimensional spinless Fermi systems using *t*-DMRG (without basis adaptation). Shortly afterwards, Manmana *et al.* [39] discusses basis adaptation in the context of *t*-DMRG and MPS.

Additionally, it is worth mentioning other viable time-evolution methods in the context of MPS such as the time-dependent variational principle [40] (TDVP) for infinite one-dimensional lattices that has the advantage of not relying on the Trotter decomposition, thus avoiding the Trotter error, and also preserving symmetries and conservation laws. Also, matrix-product-operator-based (MPO) time evolution [41] has

been used to simulate a matrix-product state under a long-ranged Hamiltonian in systems with moderate entanglement. Although these methods are appealing in their own right, we do not include results based on them in this study as we feel it is more pertinent to restrict the comparison to more quotidian methods in the field, namely Trotter decomposition and the Krylov approximation.

III. t -CheMPS

In this section, we review a recipe for time evolution using the Chebyshev matrix product state approach, namely t -CheMPS, as it was proposed in Ref. [25] by Holzner *et al.* As such, a brief exposé on Chebyshev polynomials is in order.

Chebyshev polynomials of the first kind, $T_n(x)$; $n \in \mathbb{N}$ are given by the recursive relations

$$T_n(x) = \begin{cases} 1 & \text{for } n = 0, \\ x & \text{for } n = 1, \\ 2xT_{n-1}(x) - T_{n-2}(x) & \text{for } n > 1. \end{cases} \quad (7)$$

A useful nonrecursive expression for the Chebyshev polynomials is

$$T_n(x) = \cos(n \arccos x). \quad (8)$$

Moreover, they form an orthonormal set of polynomials on the interval $x \in [-1, 1]$ with respect to the weighted scalar product

$$\langle T_n, T_m \rangle = \int_{-1}^1 \frac{dx}{\pi \sqrt{1-x^2}} T_n(x) T_m(x), \quad (9)$$

and are divergent in the region $x \in (-\infty, -1) \cup (1, \infty)$. Chebyshev polynomials have been extensively studied in the mathematics and engineering literature [42–46].

A. Chebyshev expansion in the time domain

We consider a system in which a Hamiltonian \hat{H} acts on an initial state $|\psi_0\rangle$, thus propagating its time evolution. The full many-body bandwidth of \hat{H} is $W = E_s - E_g$, where E_g (E_s) is the ground-state (sky-state) energy of \hat{H} . In many cases, this bandwidth is far larger than the effective bandwidth $W^* = E_s^* - E_g^*$ that one can determine from the spectral function of $|\psi_0\rangle$ relative to \hat{H} . As illustrated in Fig. 1, the spectral function of $|\psi_0\rangle$ relative to \hat{H} has nonzero weight mainly over $[E_g^*, E_s^*]$. Since the Chebyshev polynomials of first kind are divergent outside of the region $x \in [-1, 1]$, and knowing that these polynomials will be functions of a Hamiltonian, this effective bandwidth is rescaled to $[-W', W']$ where $W' = 1 - \frac{\epsilon_t}{2}$ and ϵ_t is a safety factor to guarantee that the domain of the Chebyshev polynomials will remain within $\mathcal{I} = [-1, 1]$. In our numerical simulations, ϵ_t has been set to 0.025. This rescaling, when applied to the original Hamiltonian \hat{H} will lead to a rescaled Hamiltonian \hat{H}' where

$$\hat{H}' = \frac{\hat{H} - b}{a}, \quad (10)$$

with $a = W^*/(2 - \epsilon_t)$ and $b = (E_g^* + E_s^*)/2$. Now one can express the Chebyshev polynomials of the first kind in terms of this rescaled Hamiltonian.

Several constructions of Chebyshev approximations [46] can be found for a given function $f(x)|_{x \in \mathcal{I}}$, with the one most

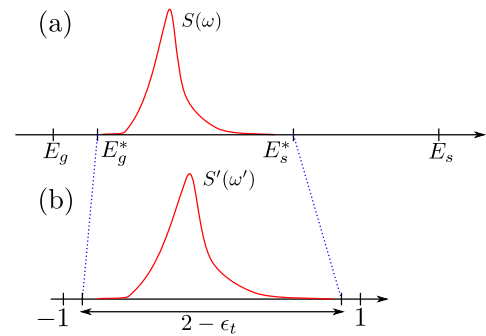


FIG. 1. (Color online) (a) The spectral decomposition $S(\omega)$ of $|\psi_0\rangle$ relative to \hat{H} has nonzero weight in the region $[E_g^*, E_s^*]$ where the effective bandwidth $W^* = E_s^* - E_g^*$ is significantly smaller than the full many-body bandwidth $W = E_s - E_g$. (b) In the Chebyshev expansion approach for time evolution, it may be advantageous to rescale \hat{H} by mapping the effective bandwidth from $[E_g^*, E_s^*]$ to $[-W', W']$ where $W' = 1 - \frac{\epsilon_t}{2}$ with $\epsilon_t = 0.025$ being a safety factor [25].

suitable for our purposes being

$$f(x) = \frac{1}{\pi \sqrt{1-x^2}} \left[\mu_0 + 2 \sum_{n=1}^{\infty} \mu_n T_n(x) \right], \quad (11)$$

where the Chebyshev moments μ_n are given by

$$\mu_n = \int_{-1}^1 f(x) T_n(x) dx. \quad (12)$$

An order of N approximation $f_N(x)$ of $f(x)$ is possible if one has access to the first N terms ($0 \leq n \leq N-1$), and thus it follows that

$$f_N(x) = \frac{1}{\pi \sqrt{1-x^2}} \left[\mu_0 + 2 \sum_{n=1}^{N-1} \mu_n T_n(x) \right]. \quad (13)$$

The time-evolution operator can be expressed as ($\hbar = 1$)

$$\hat{U}(t) = e^{-i\hat{H}t} = \int_{-1}^1 d\omega' e^{-i[a(\omega'+W')+E_g^*]t} \delta(\omega' - \hat{H}'), \quad (14)$$

and upon expressing the δ function term therein as per Eq. (13), one obtains

$$\hat{U}_N(t) = e^{-i(E_g^*+aW')t} \sum_{n=0}^{N-1} \phi_n(t) T_n(\hat{H}'), \quad (15)$$

with $\phi_0(t) = c_0(t)$ and $\phi_{n>0}(t) = 2c_n(t)$, where

$$c_n(t) = \int_{-1}^1 \frac{e^{-iat\omega'} T_n(\omega')}{\pi \sqrt{1-\omega'^2}} d\omega' = (-i)^n J_n(at), \quad (16)$$

and $J_n(at)$ is the Bessel function of the first kind of order n .

It is to be noted here that in t -CheMPS, as will be elucidated later, one does not have to calculate the actual wave function $|\psi_N(t)\rangle = \hat{U}_N(t)|\psi_0\rangle$ at a Chebyshev order N in order to determine the time evolution of some observable.

B. Recipe for time evolution of initial state $|\psi_0\rangle$

Here, we provide the steps needed to time evolve an initial state $|\psi_0\rangle$ under a Hamiltonian \hat{H} using the t -CheMPS method.

As an initialization step, we calculate the ground state $|g\rangle$ and the sky state (the moniker we shall use for the eigenstate of highest eigenenergy) $|s\rangle$ of \hat{H} , noting that the sky state of \hat{H} is nothing but the ground state of $-\hat{H}$. This allows us to determine the bandwidth W of \hat{H} , from which we can make a specific choice for W^* using the spectral-decomposition technique highlighted in the next section. Then we can determine a and b and rescale \hat{H} to \hat{H}' as per Eq. (10). The first Chebyshev vector $|t_0\rangle$ is set to the initial state $|\psi_0\rangle$, while the second Chebyshev vector is given by $|t_1\rangle = \hat{H}'|t_0\rangle$. Thereon, any Chebyshev vector $|t_{n\geq 2}\rangle$ is obtained via the recursive relation

$$|t_n\rangle = 2\hat{H}'|t_{n-1}\rangle - |t_{n-2}\rangle. \quad (17)$$

This recurrence relation can be implemented using the compression or fitting procedure [16,25]. This procedure finds an MPS representation for $|t_n\rangle$ by variationally minimizing the fitting error [25]

$$\Delta_{\text{fit}} = \|||t_n\rangle - (2\hat{H}'|t_{n-1}\rangle - |t_{n-2}\rangle)\|^2. \quad (18)$$

This procedure of recurrence fitting effects variational minimization through a sequence of sweeps back and forth along the chain that proceed until the state being optimized becomes stationary. Calling the state $|t_n\rangle$ and $|t'_n\rangle$ after and before a fitting sweep, it becomes stationary once the term

$$\Delta_c = \left| 1 - \frac{\langle t_n | t'_n \rangle}{\|||t_n\rangle\| \cdot \|||t'_n\rangle\|} \right| \quad (19)$$

drops below a specified fitting convergence threshold [25], which we have determined to suffice when set to 10^{-6} for our purposes.

C. Energy truncation

The DMRG truncation step in the recursive-fitting procedure where \hat{H}' is applied onto $|t_{n-1}\rangle$ in order to calculate $|t_n\rangle$ [see Eq. (17)] is not performed in the eigenbasis of \hat{H}' , and, as such, high-energy components can be possibly passed on to subsequent recursion steps, leading to divergences in higher-order Chebyshev vectors [25]. This is remedied via energy truncation sweeps that occur locally at each site through building the corresponding Krylov subspace, proceeding with the energy truncation at the site, and completing it before moving on to the next site. As DMRG truncation occurs in the recurrence-fitting procedure, no such further truncation is carried out here. The energy eigenbasis of \hat{H}' , where the energy truncation is to be performed, is not possible to access in full, and thus a Krylov subspace of dimension d_K is constructed at each site. Then, a method such as Arnoldi's algorithm is utilized to calculate the extreme eigenvalues of \hat{H}' that are bigger than an energy truncation error bound per time step ε in magnitude, where one can set $\varepsilon = 1.0$, and focus on the proper value of W^* based on the spectral decomposition of the initial state $|\psi_0\rangle$ with respect to \hat{H}' . This is due to the fact that whatever value of W^* one picks, the range of effective eigenenergies $[E_g^*, E_s^*]$ will be rescaled to $[-W', W']$, and in the Chebyshev context, the maximum and minimum energies must be no larger than ε in magnitude. Further details on this method can be found in Ref. [25].

D. Computing the time evolution of an observable

Consider that we wish to compute the time evolution

$$\langle \hat{O}_j \rangle(t) = \langle \psi(t) | \hat{O}_j | \psi(t) \rangle \quad (20)$$

of some observable \hat{O} at a given site j on the chain. We represent the time-evolved state $|\psi(t)\rangle$ in terms of the Chebyshev representation of order N of the time-evolution operator of Eq. (15) on the initial state $|\psi_0\rangle$:

$$|\psi(t)\rangle = e^{-i(E_g^* + aW)t} \sum_{n=0}^{N-1} T_n(\hat{H}') \phi_n(t) |\psi_0\rangle. \quad (21)$$

Noticing that $|\psi_0\rangle = |t_0\rangle$ and that $T_n(\hat{H}')|t_0\rangle = |t_n\rangle$, Eq. (21) becomes

$$|\psi(t)\rangle = e^{-i(E_g^* + aW)t} \sum_{n=0}^{N-1} \phi_n(t) |t_n\rangle. \quad (22)$$

Plugging Eq. (22) into Eq. (20), we get

$$\langle \hat{O}_j \rangle(t) = \sum_{n,m=0}^{N-1} \phi_n^*(t) \phi_m(t) \langle t_m | \hat{O}_j | t_n \rangle. \quad (23)$$

As already mentioned, in t -CheMPS one is never obligated to calculate the actual wave function $|\psi(t)\rangle$ itself in order to calculate a certain observable using Eq. (23). Furthermore, the coefficients $\phi_n(t) = (-i)^n J_n(at)$ ($n > 0$) decay rapidly with n for $n > at$. It is therefore possible to define a maximum time for a given number of Chebyshev moments N such that the neglected weight in terms of the coefficients is smaller than a certain threshold. We define t_{max} as the largest t such that

$$\sum_{n=N}^{\infty} \phi_n^*(t) \phi_n(t) < 10^{-3}, \quad (24)$$

which is justified because the moments $\langle t_m | \hat{O}_j | t_n \rangle$ decay quickly with $|n - m|$ (see Fig. 8). In practice we determine t_{max} by calculating $\sum_{n=N}^{N_{\text{max}}} \phi_n^*(t) \phi_n(t) < 10^{-3}$, with $N_{\text{max}} = 500$ for which we have $\phi_{N_{\text{max}}}(t) < 10^{-100}$ in the relevant time range or $\phi_{N_{\text{max}}}(t) = 0$ for all practical purposes.

IV. PROJECTIVE t -CheMPS

We wish to find a way to calculate the effective bandwidth of a wave function $|\psi(t)\rangle$ at a time t . The reason behind this is that in t -DMRG one uses the full bandwidth while time evolving the wave function and that leads to smaller evolution times that can be reached numerically. Using a smaller effective bandwidth may lead to larger numerically accessible evolution times.

Let the full many-body bandwidth of the model be $W = E_s - E_g$. Suppose that the initial state $|\psi_0\rangle = |\psi(t=0)\rangle$ has spectral support on a limited frequency interval $[E_g^*, E_s^*]$, of width $W^* = E_s^* - E_g^*$, where $E_s^* < E_s$ and $E_g^* > E_g$. Then, it would be possible to do the time evolution with t -CheMPS by rescaling this effective bandwidth, rather than the full bandwidth, onto the interval $[-1, 1]$. Thus, it is of interest to explore the spectral decomposition of the initial state $|\psi_0\rangle$, and of its time-evolved version, $|\psi(t)\rangle$. We now discuss how this can be done, focusing first on $|\psi_0\rangle$, and thereafter generalizing

the discussion to $|\psi(t)\rangle$ in the Appendix. For ease of notation, in this section and the Appendix, \hat{H} shall denote the rescaled Hamiltonian of our system with bandwidth $W = E_s - E_g$, and $\omega \in [-1, 1]$.

A. Spectral decomposition of initial state $|\psi_0\rangle$

The spectral decomposition of $|\psi_0\rangle$ is

$$S(\omega) = \langle \psi_0 | \delta(\omega - \hat{H}) | \psi_0 \rangle. \quad (25)$$

A Chebyshev expansion of the δ function of order N has the form:

$$\delta_N(\omega - \hat{H}) = \frac{1}{\pi \sqrt{1 - \omega^2}} \left[g_0 + 2 \sum_{n=1}^{N-1} g_n T_n(\hat{H}) T_n(\omega) \right], \quad (26)$$

where the coefficient g_n is a Jackson damping coefficient defined as

$$g_n = \frac{(N - n + 1) \cos \frac{\pi n}{N+1} + \sin \frac{\pi n}{N+1} \cot \frac{\pi}{N+1}}{N + 1}. \quad (27)$$

We introduce θ_n such that

$$\theta_n = \begin{cases} g_0 & \text{if } n = 0, \\ 2g_n & \text{if } n > 0. \end{cases} \quad (28)$$

This allows us to write Eq. (26) as

$$\delta_N(\omega - \hat{H}) = \frac{1}{\pi \sqrt{1 - \omega^2}} \sum_{n=0}^{N-1} \theta_n T_n(\hat{H}) T_n(\omega). \quad (29)$$

Now we calculate $S(\omega)$ using Eq. (29) and noting that our initial wave function $|\psi_0\rangle$ equals the first Chebyshev vector $|t_0\rangle$ and that $|t_n\rangle = T_n(\hat{H})|t_0\rangle$:

$$\begin{aligned} S(\omega) &= \langle \psi_0 | \delta_N(\omega - \hat{H}) | \psi_0 \rangle \\ &= \frac{1}{\pi \sqrt{1 - \omega^2}} \sum_{n=0}^{N-1} \theta_n T_n(\omega) \langle t_0 | t_n \rangle, \end{aligned} \quad (30)$$

Hence, all we have to do to calculate $S(\omega)$ is to calculate the moments $\mu_n = \langle t_0 | t_n \rangle$. To achieve a specified spectral resolution of, say, Δ , we have to use an expansion order of $N_\Delta = 2W/\Delta$. Moreover, we provide in the Appendix a derivation in terms of the Chebyshev moments of the spectral decomposition of the time-evolved wave function $|\psi(t > 0)\rangle$, which can be used as a numerical-fidelity check.

V. GLOBAL-QUENCH TEST MODEL

For the comparison we wish to carry out between the Suzuki-Trotter decomposition, the Krylov approximation and the t -CheMPS methods, we consider a benchmark test model: a strong global quench in the Bose-Hubbard model (BHM) on a bosonic lattice at half filling with odd-site unity filling for different values of the on-site interaction strength U . Global quenches happen when an initial state undergoes a time evolution due to a new Hamiltonian for which the initial state has an extensively different energy as for the original Hamiltonian whose ground state it was.

We consider an initial state

$$|\psi_0\rangle = |\psi(0)\rangle = \prod_{i=1}^{L/2} \hat{b}_{2i-1}^\dagger |0\rangle \quad (31)$$

that is a bosonic lattice of size $L = 32$ in which every odd site has a single boson and every even site holds zero occupancy. It can be thought of as the ground state of some suitable Hamiltonian. The system is globally quenched to the Bose-Hubbard Hamiltonian

$$\hat{H} = -J \sum_{i=1}^{L-1} (\hat{b}_i^\dagger \hat{b}_{i+1} + \text{H.c.}) + \frac{U}{2} \sum_{i=1}^L \hat{n}_i (\hat{n}_i - 1), \quad (32)$$

where J and U are the hopping and interaction terms of the Bose-Hubbard model. This global quench has already been studied using t -DMRG [47–49]. We consider different values of the on-site interaction strength, including the analytically solvable case of $U = 0$.

At $U = 0$, the Hamiltonian in Eq. (32) reduces to

$$\hat{H} = -J \sum_{i=1}^{L-1} (\hat{b}_i^\dagger \hat{b}_{i+1} + \text{H.c.}). \quad (33)$$

In the case of noninteracting bosons ($U = 0$), scattering is not the physical mechanism behind local relaxation. Instead, the time-dependent contributions to the reduced density operator of the regarded subsystem consist of quickly oscillating phases that average out under sufficient conditions leading to a relaxation of the density operator [49]. In the current case, excitations start propagating from all sites with a finite speed throughout the duration of the time evolution spreading the information about the initial conditions more and more over the entire system. The incommensurate mixing of these excitations then can lead to a state that appears to be locally perfectly relaxed. This case leads to an exact analytical solution covered in Ref. [49] by a Fourier transformation of the ladder operators involved. In the Heisenberg picture the time evolution of the ladder operators reads

$$\hat{b}_i(t) = \frac{1}{L} \sum_k \sum_{l=1}^L e^{-ik(l-i)} e^{2iJ \cos(k)} \hat{b}_l(0), \quad (34)$$

$$\hat{b}_i^\dagger(t) = \frac{1}{L} \sum_k \sum_{l=1}^L e^{ik(l-i)} e^{-2iJ \cos(k)} \hat{b}_l^\dagger(0), \quad (35)$$

where $k = \frac{2\pi}{L}l$, where $l = 1, 2, \dots, L$. As $\hat{n}_i(t) = \hat{b}_i^\dagger(t) \hat{b}_i(t)$, one obtains

$$\begin{aligned} \langle \hat{n}_i \rangle(t) &= \frac{1}{2} \left(1 + \frac{1}{L} \sum_{q=0}^{L-1} (-1)^{i+1} e^{-4iJt \cos(\frac{2\pi}{L}q)} \right) \\ &\xrightarrow{L \rightarrow \infty} \frac{1}{2} [1 + (-1)^{i+1} J_0(4Jt)]. \end{aligned} \quad (36)$$

VI. RESULTS AND DISCUSSION

A. Convergence and performance

A first quantity to gauge the convergence parameters of all three methods under consideration is provided by the

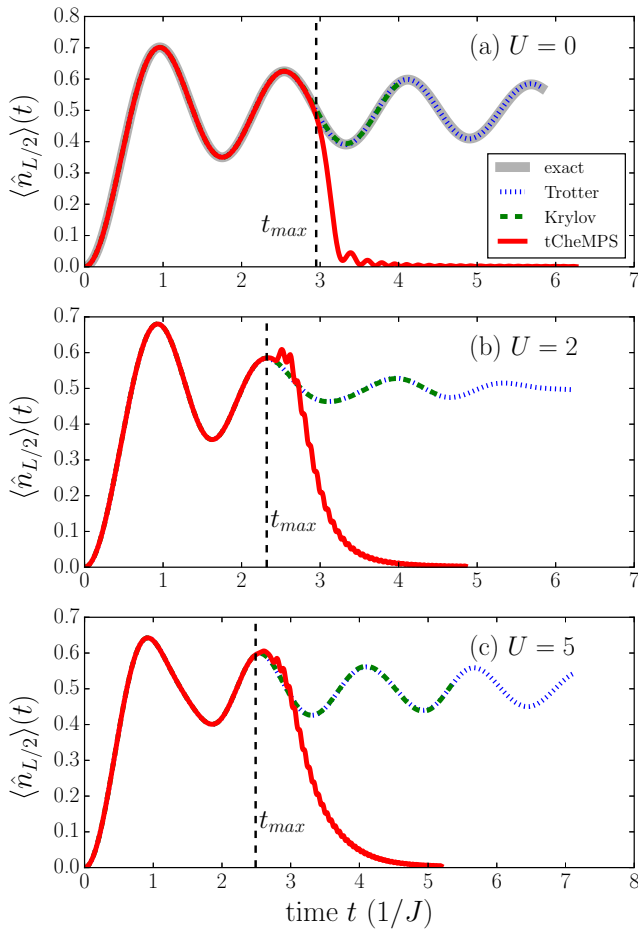


FIG. 2. (Color online) The time evolution for the particle density at site $L/2$ after a global quench with (a) $U = 0$, (b) $U = 2$, and (c) $U = 5$, each obtained with the Trotter (blue dotted), Krylov (green dashed) and t -CheMPS (red solid) methods. For $U = 0$ the exact time evolution given by Eq. (36) is shown in light gray. All the methods give numerically exact results for short times. The time reached by the t -CheMPS method is given by t_{max} [see Eq. (24)], after which the error increases quickly as discussed in Sec. III D. In all cases the Trotter decomposition method reaches the longest times followed by the Krylov approximation method.

particle density of this global quench with $U = 0$. The results shown in Fig. 2 exhibit good convergence for our purposes where the maximum on-site occupation number in t -DMRG is set to $\langle \hat{n} \rangle_{max} = 10$ in accordance with Ref. [49]. It is worth mentioning at this point that the underlying intention behind this work is not to contrive a method that surpasses standard methods, such as Trotter time evolution and Krylov time evolution in terms of accuracy, as the latter have proven to be very precise with the right set of parameters in place. However, the goal is to investigate whether an alternative method such as t -CheMPS can, at the same accuracy or that within what is acceptable from an experimentally suitable point of view, achieve larger times than those possible in Trotter time evolution or Krylov time evolution, especially as it has been demonstrated that Chebyshev polynomials can be very useful in time evolution at least outside of the context of MPS [50,51].

In this work, we use a second-order Trotter decomposition as in previous work [52] it has shown to be far more efficient than either first- or fourth-order Trotter decompositions in terms of accuracy and computational effort, respectively, while achieving approximately the same evolution times. The Krylov method we use employs an Arnoldi iteration, which is considered to be the most efficient in Krylov implementations [53]. In our calculations, we find that our Trotter calculations are convergent for a time step $\Delta t = 0.01/J$ and truncation error or fidelity threshold [10,11,54] of 10^{-8} for each time step, while Krylov and t -CheMPS calculations are convergent for a fidelity threshold of 10^{-5} for each time step. As shown in Figs. 2 and 3 for the particle density and density-density correlations, respectively, Trotter decomposition is the best method when it comes to largest accessible times. The times achieved by the Krylov method (shown in Fig. 2) match those arrived at by Flesch *et al.* in Ref. [49] for the same system. The accuracy of the t -CheMPS method is quite impressive and its results are actually quite exact for short times, but it can exceed neither the Krylov method nor the Trotter method in terms of largest evolution times reached. We do not find any significant difference in terms of computational effort between any of the methods, but the t -CheMPS vectors do require more storage space than the corresponding wave functions computed using the Krylov approximation or the Trotter decomposition methods. If we consider the storage space required by the longest-evolution-time wave function or highest-index vector calculated by any of these methods with the parameters specified above, then the t -CheMPS vector requires storage space around an order of magnitude bigger than that by the corresponding wave function computed using the Krylov approximation method, and around double the storage space occupied by the corresponding wave function obtained from the Trotter decomposition method.

B. Projective t -CheMPS results

As a further attempt at improving the results attained by the t -CheMPS method, we undertake the spectral decomposition in the cases of $U = 2$ ($\langle \hat{n} \rangle_{max} = 8$) and $U = 5$ ($\langle \hat{n} \rangle_{max} = 4$), the spectral functions of which are shown in Fig. 4. The case of $U = 0$ is not included as the bandwidth cannot be further reduced from its full size. Immediately, one notices that they both have nonzero weight mostly on the left half of the energy axis, i.e., in the lower-energy half of the bandwidth. In the calculations performed for this study, it has proven necessary to set $E_g^* = E_g$ to keep the Chebyshev approximation convergent, while $E_s^* \in [E_g + W/2, E_s)$. Here, E_s is projected according to

$$E_s^* = E_g + \alpha \cdot W, \quad (37)$$

where $\alpha \in (0, 1]$ is the projection factor, and when $\alpha = 1$, it is in fact nonprojective t -CheMPS that is being used and energy truncation is turned off in the simulations.

Reducing the full bandwidth of the system to a reduced effective bandwidth may lead to less computational effort as one now requires fewer Chebyshev vectors in order to reach a certain maximum evolution time t_{max} , which is related to the expansion order N_{max} by approximately [25] $t_{max} \approx N_{max}/a$, though, for our purposes, it is slightly smaller [see Eq. (24)] in

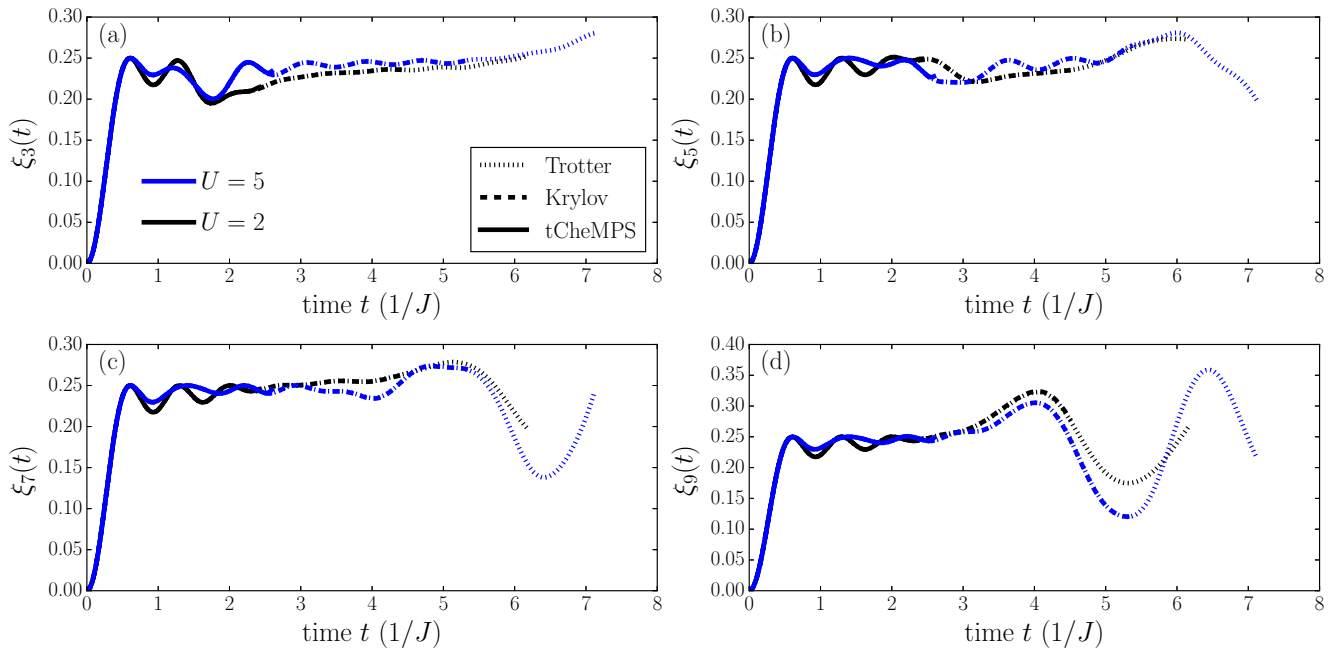


FIG. 3. (Color online) Density-density correlations $\xi_j(t) = \langle \psi(t) | \hat{n}_{L/2-j} \hat{n}_{L/2+j-1} | \psi(t) \rangle$ for $U = 2$ (black) and $U = 5$ (blue) are shown for different half distances j : (a) $j = 3$, (b) $j = 5$, (c) $j = 7$, and (d) $j = 9$. All the correlators are obtained by the Trotter (dotted), Krylov (dashed), and t -CheMPS (solid) methods. All the methods give the same results up to the corresponding reachable times.

order to achieve a desired precision (Sec. III D). Since a scales proportionally with the reduction in the full bandwidth upon projection, one need only achieve the same number of vectors in projective t -CheMPS as in nonprojective t -CheMPS to facilitate a maximum evolution time bigger by that same factor of reduction in the full bandwidth. However, in projective t -CheMPS a new function enters into the computation, namely that of energy truncation. In our numerical simulations, the projective t -CheMPS method at any factor of reduction is

unable to calculate up to the same order of expansion as the nonprojective t -CheMPS method due to the additional computational effort of energy truncation, but, nevertheless, for certain projections, evolution times bigger than those achieved in nonprojective t -CheMPS are reached as shown in Fig. 5 for both cases $U = 2$ and $U = 5$. The best result is attained for both U values at $\alpha = 0.5$, the most stringent projection factor used that did not lead to divergences, where an improvement of 20% (12%) is achieved for $U = 2$ ($U = 5$) in terms of largest accessible evolution times. The corresponding converged Trotter results are overlaid for reference. It can be seen that even though projective t -CheMPS does indeed reach greater evolution times than its nonprojective counterpart, it still does not improve over the Trotter or Krylov methods. It is also worth noting here that projective t -CheMPS, despite even sometimes significant reductions in the full bandwidth of the system, still offers exact results for short times.

Though one may be tempted to think that the projective t -CheMPS method must achieve longer times the more one projects (i.e., the smaller α is), this is not the case in reality as then more computational effort is required by the energy-truncation module that at some point it simply cannot handle all the required energy projections when $\alpha \ll 1$, and in fact this renders the maximum evolution time reachable smaller than that in the nonprojective t -CheMPS method or it may outright lead to divergences [25]. On the other extreme, if $\alpha \lesssim 1$, then $W^* \lesssim W$, and thus the computational effort is almost the same as in the nonprojective t -CheMPS method with the added cost of energy truncation, which leads to evolution times shorter than those attained by nonprojective t -CheMPS. Thus, one has to choose α in a manner where energy truncation is not pushed to its limits and while at the same time W^* is nontrivially smaller than W .

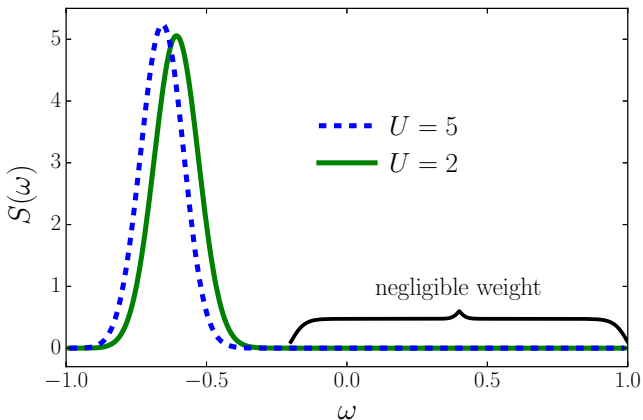


FIG. 4. (Color online) The spectral decomposition $S(\omega)$ of the initial state $|\psi_0\rangle$ as defined in Eq. (30) obtained by the procedure explained in Sec. IV. The green solid line shows the spectral decomposition of $|\psi_0\rangle$ at interaction strength $U = 2$, the dashed blue line shows the spectral decomposition at $U = 5$. In both cases the spectral weight is located at the lower end of the spectrum and is negligible at higher energies. This allows one to determine proper projections for reduced effective bandwidths and to use the projective t -CheMPS method.

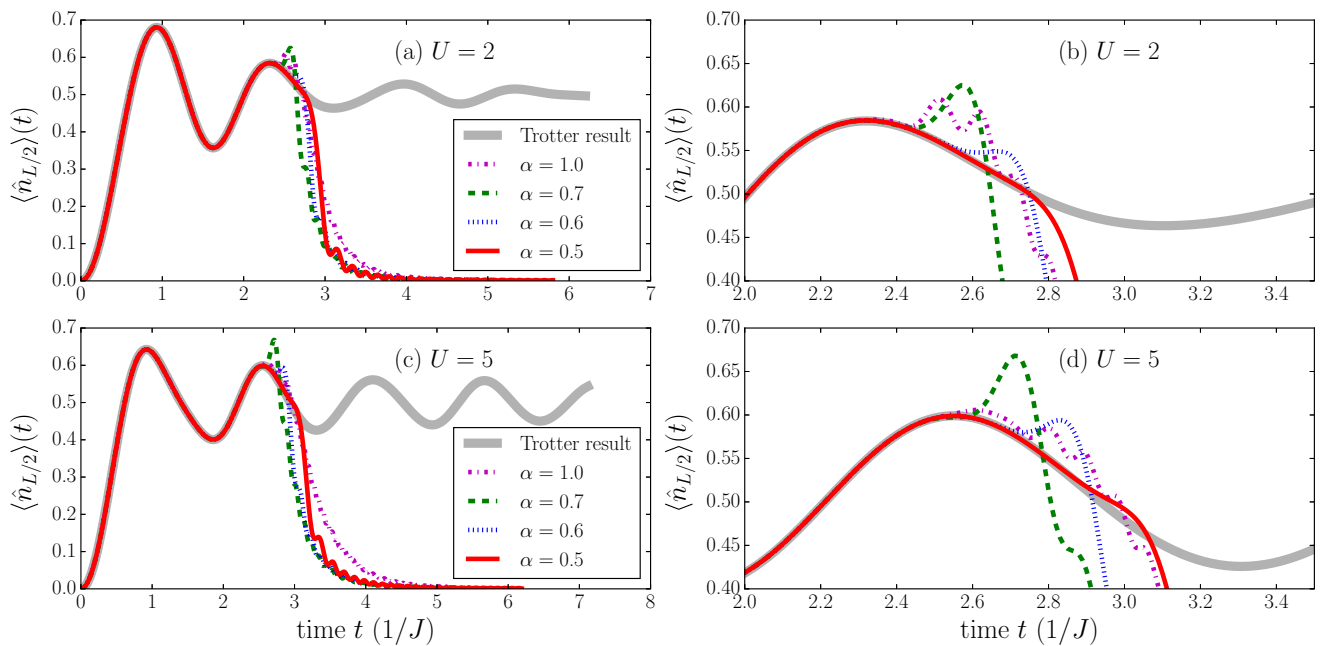


FIG. 5. (Color online) Projective t -CheMPS results for the particle density at $L/2$ of the global quench with (a) $U = 2$ and (c) $U = 5$ and different projection factors $\alpha = 0.5, 0.6, 0.7$ for an effective bandwidth $W^* = \alpha W$ as defined in Eq. (37), laid over the corresponding nonprojective ($\alpha = 1$) t -CheMPS results. (b) and (d) show the same data as (a) and (c) but zoomed in to the relevant times, where errors start to diverge. Larger evolution times can be reached with the projected effective bandwidth in addition to less computational effort in the calculations and a smaller required disk space for representation of dynamics.

C. Middle-bond dimension and vector size

To avoid any confusion, we remind the reader here that the expansion order N is the total number of Chebyshev vectors, and each of the latter is indicated by an expansion index n that goes from 0 for the first vector to $N - 1$ for the highest-index vector.

Intuitively, the projective t -CheMPS vectors are expected to comprise of higher bond dimensions at the same expansion order than their nonprojective t -CheMPS counterparts as exhibited in Figs. 6(a) and 6(b) for $U = 2$ and $U = 5$, respectively, at the middle or central bond. This can be attributed to the fact that for the same time t attained in both methods, expansion order N^* achieved by projective t -CheMPS for faithful representation of the system dynamics at this time is related to the corresponding expansion order N attained by nonprojective t -CheMPS through $N^* \approx \alpha \cdot N < N$. Hence, the vector of a certain expansion index carries more information when generated by projective rather than nonprojective t -CheMPS, because the generated N^* Chebyshev vectors in projective t -CheMPS still, assuming convergence, must carry the same information about the system as the N ($\approx N^*/\alpha > N^*$) Chebyshev vectors in nonprojective t -CheMPS do. However, it can be seen in Figs. 6(a) and 6(b) that the projective t -CheMPS vectors do not reach the maximum central-bond dimensions that occur for the nonprojective t -CheMPS vectors. In principle, one may expect that all the t -CheMPS vectors, regardless of the value of α ought to reach the same maximal matrix dimensions. This is only true, however, if the workings of these calculations are the same, but this is not the case because in projective ($\alpha < 1$)

t -CheMPS an additional computation effort is needed, that of energy truncation, which does not occur in nonprojective ($\alpha = 1$) t -CheMPS.

In addition to obtaining fewer vectors required to arrive at an evolution time t in projective t -CheMPS, one finds that these vectors are in fact smaller in size the bigger the reduction in bandwidth, i.e., the smaller α , is. In Figs. 6(a) and 6(b), each temporal isoline is constructed for a properly selected evolution time t that is appropriately matched to its corresponding expansion orders N_α for the different α values based on the criterion in Eq. (24) [one may equally well use the more relaxed criterion of $N_\alpha \approx \alpha W t / (2 - \epsilon_t)$, which our calculations show is also adequate for $U = 2$ and $U = 5$]. These temporal isolines indicate that at a time t , the corresponding projective and nonprojective t -CheMPS maximum-expansion-index vectors $|t_{N^*-1}\rangle$ and $|t_{N-1}\rangle$, respectively, are such that the latter has larger matrix dimensions than the former, and this becomes more pronounced the larger t is. It is interesting to also look at the total sum of matrix dimensions at the central bond of the Chebyshev vectors involved in arriving at a time t in t -CheMPS for different values of α . If $D_n = D(|t_n\rangle)$ indicates the matrix dimension at the central bond of $|t_n\rangle$, then $\sum_{n=0}^{N_\alpha-1} D_n$ would be a good measure of the computational effort required to reach a time t based on Eq. (24) in (non)projective t -CheMPS for some value of α . This measure not only incorporates the maximal matrix dimension attained by the highest-index Chebyshev vector required to reach an evolution time t , but it also accounts for how many vectors are required to reach t , and this number varies depending on the value of α . This measure is depicted in Figs. 6(c) and 6(d) for $U = 2$ and $U = 5$,

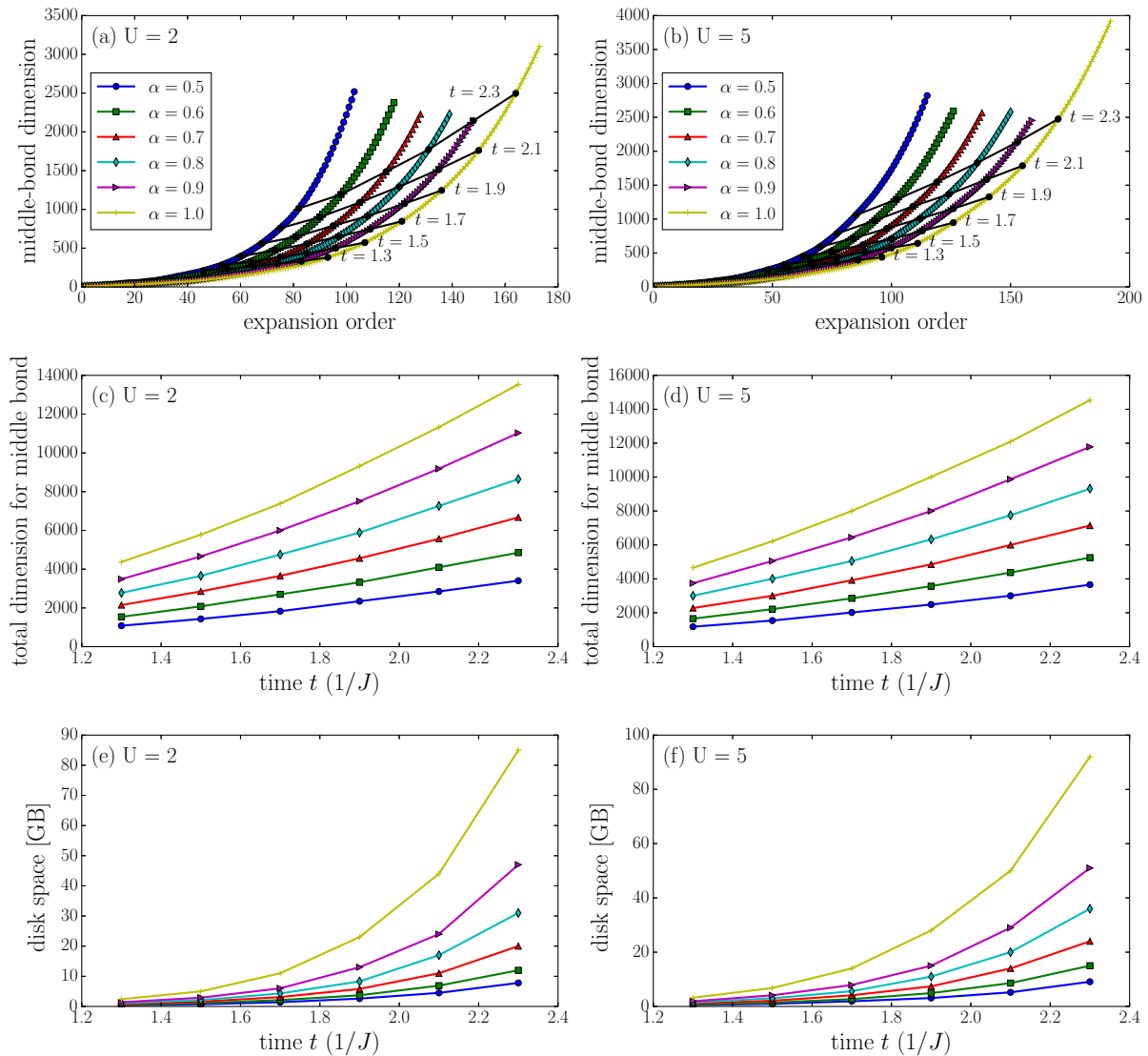


FIG. 6. (Color online) The matrix dimension at the central bond for the Chebyshev vectors due to the projective ($\alpha < 1$) and nonprojective ($\alpha = 1$) t -CheMPS methods for $U = 2$ (left column) and $U = 5$ (right column). In (a) and (b), one notices that at any expansion index n , the corresponding Chebyshev vector $|t_n\rangle$ carries a larger central-bond dimension the smaller α is (i.e., the more reduced the effective bandwidth is), as at the corresponding expansion order $n + 1$, t -CheMPS represents longer dynamics the smaller α is. However, in (c) and (d), one notices that the sum of the matrix dimensions at the central bond for the Chebyshev vectors leading up to a certain time t is far smaller the lower the value of α , indicating less computational effort upon greater reduction in the bandwidth. Note how the projective t -CheMPS vectors cannot reach the maximum matrix dimension nonprojective t -CheMPS vectors have, and this is due to the additional computational effort of energy truncation necessary in the projective t -CheMPS method but nonexistent in its nonprojective counterpart. Additionally, (e) and (f) show significant conservation of disk space in projective t -CheMPS for any evolution time t , where the smaller α is, the less disk space is required for storing the Chebyshev vectors that are necessary to represent dynamics up to t . Note that the selected times are indicated via temporal isolines in (a) and (b).

respectively, where one can conclude that the more reduced the effective bandwidth is (the smaller α is), the smaller is the computational effort required to reach a certain evolution time t . For the longest common time arrived at by all calculations ($t \approx 2.3/J$), there is a factor of roughly 4 with regards to mitigation of computational effort from $\alpha = 1$ to $\alpha = 0.5$.

Moreover, at a certain evolution time t corresponding to a set of expansion orders N_α for the different α -valued t -CheMPS calculations, one finds that the highest-index Chebyshev vector $|t_{N_\alpha-1}\rangle$ occupies less disk space the smaller

α is. If $d_n = d(|t_n\rangle)$ is the disk space occupied by Chebyshev vector $|t_n\rangle$, then $\sum_{n=0}^{N_\alpha-1} d_n$ is the total disk space needed to house those Chebyshev vectors required to arrive at the dynamics up to time t corresponding to N_α as per Eq. (24). This is presented in Figs. 6(e) and 6(f) for $U = 2$ and $U = 5$, respectively, where it can be seen that the greater the projection (or the smaller α is), the more reduction one obtains in total disk space. In fact, at $t = 2.3/J$, the reduction is more than an order of magnitude from $\alpha = 1$ to $\alpha = 0.5$. Therefore, upon projection, one obtains fewer Chebyshev vectors that as a

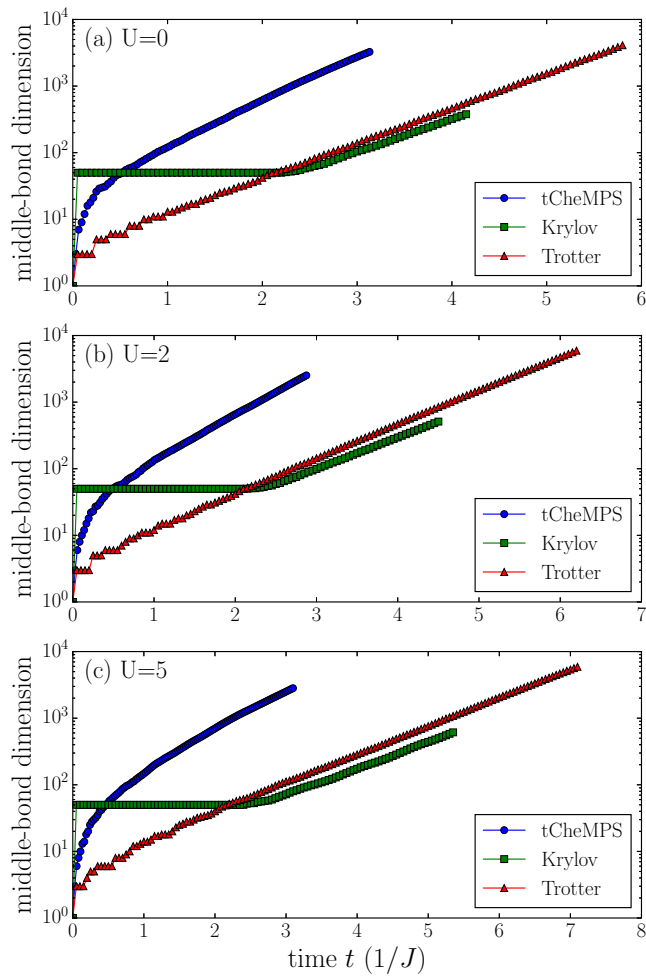


FIG. 7. (Color online) The matrix dimension at the central bond of the bosonic chain using the t -CheMPS, Krylov approximation, and Trotter decomposition methods for interaction strengths (a) $U = 0$, (b) $U = 2$, and (c) $U = 5$. The matrix dimension for t -CheMPS increases very quickly and greatly exceeds its counterparts in the Krylov approximation and Trotter decomposition methods for common evolution times irrespective of the interaction strength. This prohibits the method from achieving much longer times.

whole are also smaller in size while representing the same dynamics, which indicates data compression.

D. Comparison with other methods

It is interesting to produce a quantitative comparison of the t -CheMPS method with the Krylov approximation and Trotter decomposition methods in the time domain. One can consider the matrix dimension at the central bond required to faithfully represent the dynamics over the evolution times. One can again here represent the central-bond total matrix dimension for t -CheMPS at a time t as $\sum_{n=0}^{N_\alpha-1} D_n$, where D_n is the matrix dimension at the central bond of $|t_n\rangle$, and N_α and t are related as per Eq. (24), as is done in Fig. 6, but this representation would not be fair as it encompasses all the Chebyshev vectors required to construct the wave function $|\psi(t)\rangle$, the construction of which, unlike in the Trotter decomposition or Krylov

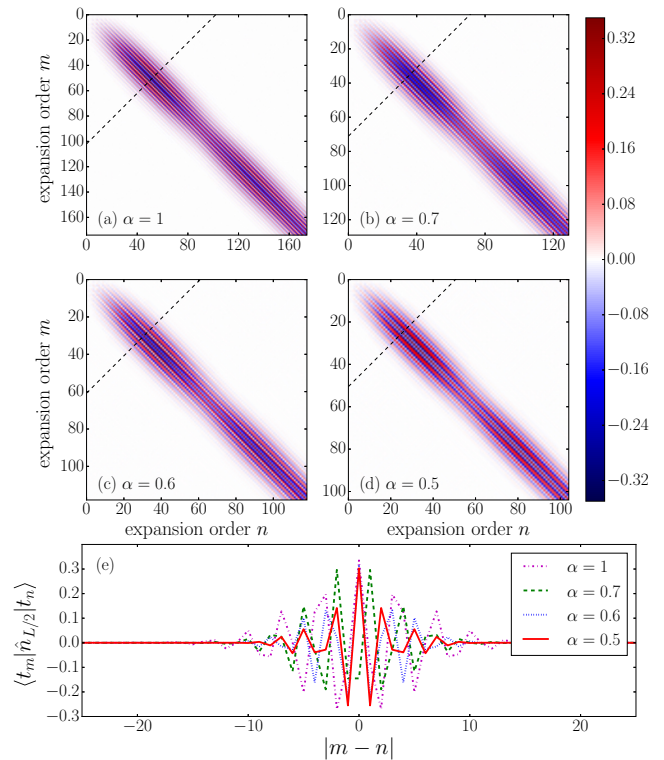


FIG. 8. (Color online) The behavior of the Chebyshev moments $\langle t_m | \hat{n}_{L/2} | t_n \rangle$ for (a) nonprojective ($\alpha = 1$) and projective t -CheMPS for (b) $\alpha = 0.7$, (c) $\alpha = 0.6$, and (d) $\alpha = 0.5$. It can be seen how the bulk of the information lies where $|m - n| < 15$ and is biggest around $m \approx n$. In (e) the cross sections of these moments along the back diagonal $\{(N_\alpha, 0), (0, N_\alpha)\}$ where $N_\alpha = 100\alpha$ are shown, displaying rapid decay around $|m - n| = 0$ for all α values.

approximation methods, is never undertaken in the t -CheMPS method (see Sec. III D). Thus, even though this representation is proper in Figs. 6(c) and 6(d) as it involves a comparison between the different bandwidth reductions in the t -CheMPS method through covering the number of Chebyshev vectors involved in reaching an evolution time t , for comparison with the results obtained from the Trotter decomposition and Krylov approximation methods, $D_{N_\alpha-1}$ is the proper quantity to look at, because $D_{N_\alpha-1}$ is the largest matrix dimension of the central bond attained by any of the Chebyshev vectors required for faithful representation of the dynamics up to evolution time t . For this comparison, the $\alpha = 0.5$ projective t -CheMPS result for $U = 2$ and $U = 5$ is chosen as it performs best compared to other t -CheMPS approaches at those interaction strengths (see Fig. 5), while the nonprojective ($\alpha = 1$) t -CheMPS result is used for $U = 0$ as there no projection is possible. The comparison is displayed in Fig. 7, where it can be noted that the central-bond matrix dimension required in the t -CheMPS method to represent the dynamics up to a common evolution time t is much greater than that in the Krylov approximation or Trotter decomposition methods regardless of what the interaction strength U is. This is in agreement with Ref. [29], particularly in the case where the rescaled Hamiltonian \hat{H}' is simply a factor of the original Hamiltonian \hat{H} , which is the case in this study when $U = 0$, depicted in Fig. 7(a). At this

interaction strength, the sky-state and ground-state energies are equal in magnitude but of opposite sign, rendering $b = 0$. This leads to $\hat{H}' = \hat{H}/a$, which is the condition proven in Ref. [29] to assert that then the Chebyshev vectors are equivalent to time-evolved wave functions for a proper time step in the Krylov approximation or Trotter decomposition methods [29].

E. Matrix moments

Finally, in Fig. 8, we take a closer look at the behavior of the Chebyshev moments $\langle t_m | \hat{n}_{L/2} | t_n \rangle$. In particular, we observe that these moments carry the greatest weight along the back diagonal (\backslash). This is to be expected as these Chebyshev moments involve two states $|t_n\rangle$ and $|t_m\rangle$ that have little overlap, since, if $m > n$, $|t_m\rangle$ is arrived at by consecutively applying \hat{H}' $m - n$ times onto $|t_n\rangle$, and as the latter is not an eigenstate of \hat{H}' , this renders the two vectors with little overlap the bigger $|m - n|$ is. Moreover, the cross sections of these moments along the dotted black lines in Figs. 8(a)–8(d), corresponding to some expansion order, say $N(\alpha) = 100\alpha$, exhibit a decaying behavior around $|m - n| = 0$ that is zero for large $|m - n|$. These cross sections for the different α values are depicted in Fig. 8(e). As mentioned previously, this validates the constraint for the maximum evolution time t_{\max} that $\sum_{n=N}^{\infty} \phi_n^*(t) \phi_n(t) < 10^{-3}$ while neglecting off-diagonal terms as indeed one can see that the Chebyshev moments in Fig. 8 carry nontrivial weight mostly for quite small values of $|m - n|$, thereby making this constraint sufficient.

VII. CONCLUSION

A new method, t -CheMPS, based on the Chebyshev expansion in the time domain in the context of MPS has been presented for calculating the time evolution of quantum many-body systems, including global quenches. Using a test system of importance in the field of quantum many-body physics, we demonstrate that t -CheMPS arrives at exact solutions of a given observable for short times, but does not exceed the largest times accessible by standard time-evolution methods such as the Trotter decomposition and the Krylov approximation. Furthermore, a projective version of the method, projective t -CheMPS, based on spectral decomposition and system-bandwidth reduction is introduced that improves on the largest evolution times accessible while significantly easing computational effort and greatly reducing disk space for the same dynamics. Moreover, we find again that Trotter expansion is still the favorable method with regards to largest accessible evolution times.

ACKNOWLEDGMENTS

The authors are grateful to Thomas Barthel (Duke University), Alex Wolf, Andreas Holzner, Andreas Weichselbaum, and Jan von Delft (all of LMU Physik) for fruitful discussions, and to Ulrich Schollwöck (LMU Physik) for a thorough reading of and subsequent valuable comments on the manuscript. J.C.H. acknowledges support through the FP7/Marie-Curie Grant No. 321918 and DFG FOR 801. I.P.M. acknowledges the support from the Australian Research Council Centre of Excellence for Engineered Quantum Systems, CE110001013, and the Future Fellowships scheme, FT100100515.

APPENDIX: SPECTRAL DECOMPOSITION OF THE TIME-EVOLVED WAVE FUNCTION $|\psi(t > 0)\rangle$

Reminding the reader that here for ease of notation, as in Sec. IV, \hat{H} is taken to be the rescaled Hamiltonian with bandwidth $W = E_s - E_g$, and $\omega \in [-1, 1]$, we proceed with first remarking that the spectral decomposition of the time-evolved state $|\psi(t)\rangle$ is equal to that of the initial state $|\psi_0\rangle$:

$$\begin{aligned} \langle \psi(t) | \delta(\omega - \hat{H}) | \psi(t) \rangle &= \langle \psi_0 | \hat{U}^\dagger(t) \delta(\omega - \hat{H}) \hat{U}(t) | \psi_0 \rangle \\ &= \langle \psi_0 | \delta(\omega - \hat{H}) | \psi_0 \rangle, \end{aligned} \quad (\text{A1})$$

where the time-evolution operator $\hat{U}(t)$ commutes with $\delta(\omega - \hat{H})$. Thus, it is a good check of the validity and convergence of the Chebyshev vectors to ascertain that the spectral decomposition is the same at any time t when calculated by the corresponding Chebyshev moments. Furthermore, this may also be employed as an alternate way to Eq. (24) to determine how many Chebyshev vectors one would need to faithfully represent the physics at an evolution time t , using the error with respect to $S(\omega)$ in Eq. (30) as a gauge. As such, we provide here a derivation that allows one to calculate the spectral decomposition of the time-evolved wave function $|\psi(t)\rangle$ from the corresponding Chebyshev moments.

In the t -CheMPS method, one can represent the wave function $|\psi(t)\rangle = \hat{U}(t) |\psi_0\rangle$ as

$$|\psi(t)\rangle = e^{-i(E_g + aW)t} \sum_{n=0}^{N-1} \phi_n(t) |t_n\rangle \quad (\text{A2})$$

as per Eq. (21). To reach a specified evolution time t , we need to use an expansion order of $N_t \approx tW/2$ or, more stringently, as specified by Eq. (24).

Now, to calculate the spectral function $S_t(\omega)$ for the wave function $|\psi(t)\rangle$, with a specified spectral resolution Δ , we can proceed as follows:

$$\begin{aligned} S_t(\omega) &= \langle \psi(t) | \delta_{N_\Delta}(\omega - \hat{H}) | \psi(t) \rangle \\ &= \sum_{n, n'=0}^{N_t-1} \phi_n^*(t) \phi_n(t) \langle t_{n'} | \delta_{N_\Delta}(\omega - \hat{H}) | t_n \rangle \\ &= \frac{1}{\pi \sqrt{1 - \omega^2}} \sum_{n, n'=0}^{N_t-1} \sum_{n''=0}^{N_\Delta-1} \phi_n^*(t) \phi_n(t) \phi_{n''} T_{n''}(\omega) \mu_{n''}^{n, n'}, \end{aligned} \quad (\text{A3})$$

where $\mu_{n''}^{n, n'} = \langle t_{n'} | T_{n''}(\hat{H}) | t_n \rangle$.

Note that we need to use different upper limits on the sums on n and n' than on the sum on n'' , in order to reach a specified time t with a specified spectral resolution Δ . To evaluate the moments arising here, we recall the following identity:

$$T_{n_1}(\hat{H}) T_{n_2}(\hat{H}) = \frac{1}{2} T_{n_1+n_2}(\hat{H}) + \frac{1}{2} T_{|n_1-n_2|}(\hat{H}). \quad (\text{A4})$$

It is advisable to use it in such a way that the order of the polynomials that arise remain as small as possible. Thus, for the case that $n < n'$, we proceed as follows (with $n_1 = n''$ and

$n_2 = n$):

$$T_{n''}(\hat{H})T_n(\hat{H}) = \frac{1}{2}T_{n''+n}(\hat{H}) + \frac{1}{2}T_{|n''-n|}(\hat{H}), \quad (\text{A5})$$

which leads to

$$\begin{aligned} \mu_{n''}^{n'n} &= \langle t_{n'}|T_{n''}(\hat{H})|t_n\rangle = \langle t_{n'}|T_{n''}(\hat{H})T_n(\hat{H})|t_0\rangle \\ &= \frac{1}{2}\langle t_{n'}|T_{n''+n}(\hat{H})|t_0\rangle + \frac{1}{2}\langle t_{n'}|T_{|n''-n|}(\hat{H})|t_0\rangle \\ &= \frac{1}{2}\langle t_{n'}|t_{n''+n}\rangle + \frac{1}{2}\langle t_{n'}|t_{|n''-n|}\rangle. \end{aligned} \quad (\text{A6})$$

For the case that $n' < n$, we proceed analogously, but with $n_1 = n'$ and $n_2 = n''$:

$$T_{n'}(\hat{H})T_{n''}(\hat{H}) = \frac{1}{2}T_{n'+n''}(\hat{H}) + \frac{1}{2}T_{|n'-n''|}(\hat{H}), \quad (\text{A7})$$

which in turn leads to

$$\begin{aligned} \mu_{n''}^{n'n} &= \langle t_{n'}|T_{n''}(\hat{H})|t_n\rangle = \langle t_0|T_{n'}(\hat{H})T_{n''}(\hat{H})|t_n\rangle \\ &= \frac{1}{2}\langle t_0|T_{n'+n''}(\hat{H})|t_n\rangle + \frac{1}{2}\langle t_0|T_{|n'-n''|}(\hat{H})|t_n\rangle \\ &= \frac{1}{2}\langle t_{n'+n''}|t_n\rangle + \frac{1}{2}\langle t_{|n'-n''|}|t_n\rangle. \end{aligned} \quad (\text{A8})$$

Thus, we conclude that in order to calculate $S_t(\omega)$ with a specified resolution of Δ up to a specified time t , we need all Chebyshev vectors up to order $N_\Delta + N_t$.

-
- [1] I. Bloch, J. Dalibard, and S. Nascimbéne, Quantum simulations with ultracold quantum gases, *Nature Phys.* **8**, 267 (2012).
- [2] M. Cheneau, P. Barmettler, D. Poletti, M. Endres, P. Schau, T. Fukuhara, C. Gross, I. Bloch, C. Kollath, and S. Kuhr, Light-cone-like spreading of correlations in a quantum many-body system, *Nature (London)* **481**, 484 (2012).
- [3] S. Trotzky, Y.-A. Chen, U. Schnorrberger, P. Cheinet, and I. Bloch, Controlling and Detecting Spin Correlations of Ultracold Atoms in Optical Lattices, *Phys. Rev. Lett.* **105**, 265303 (2010).
- [4] S. Trotzky, Y.-A. Chen, A. Flesch, I. P. McCulloch, U. Schollwöck, J. Eisert, and I. Bloch, Probing the relaxation towards equilibrium in an isolated strongly correlated one-dimensional Bose gas, *Nature Phys.* **8**, 325 (2012).
- [5] J. Simon, W. S. Bakr, R. Ma, M. E. Tai, P. M. Preiss, and M. Greiner, Quantum simulation of antiferromagnetic spin chains in an optical lattice, *Nature (London)* **472**, 307 (2011).
- [6] M. Greiner, O. Mandel, T. Esslinger, T. W. Hänsch, and I. Bloch, Quantum phase transition from a superfluid to a Mott insulator in a gas of ultracold atoms, *Nature (London)* **415**, 39 (2002).
- [7] T. Fukuhara, A. Kantian, M. Endres, M. Cheneau, P. Schau, S. Hild, D. Bellem, U. Schollwöck, T. Giamarchi, C. Gross, I. Bloch, and S. Kuhr, Quantum dynamics of a mobile spin impurity, *Nature Phys.* **9**, 235 (2013).
- [8] J. P. Ronzheimer, M. Schreiber, S. Braun, S. S. Hodgman, S. Langer, I. P. McCulloch, F. Heidrich-Meisner, I. Bloch, and U. Schneider, Expansion Dynamics of Interacting Bosons in Homogeneous Lattices in One and Two Dimensions, *Phys. Rev. Lett.* **110**, 205301 (2013).
- [9] S. R. White and A. Feiguin, Real-Time Evolution Using the Density Matrix Renormalization Group, *Phys. Rev. Lett.* **93**, 076401 (2004).
- [10] U. Schollwöck, The density-matrix renormalization group, *Rev. Mod. Phys.* **77**, 259 (2005).
- [11] S. R. White, Density Matrix Formulation for Quantum Renormalization Groups, *Phys. Rev. Lett.* **69**, 2863 (1992).
- [12] U. Schollwöck, Time-dependent density-matrix renormalization-group methods, *J. Phys. Soc. Jpn.* **74**, 246 (2005).
- [13] S. Östlund and S. Rommer, Thermodynamic Limit of Density Matrix Renormalization, *Phys. Rev. Lett.* **75**, 3537 (1995).
- [14] J. Dukelsky, M. A. Martn-Delgado, T. Nishino, and G. Sierra, Equivalence of the variational matrix product method and the density matrix renormalization group applied to spin chains, *Europhys. Lett.* **43**, 457 (1997).
- [15] F. Verstraete and J. I. Cirac, Matrix product states represent ground states faithfully, *Phys. Rev. B* **73**, 094423 (2006).
- [16] U. Schollwöck, The density-matrix renormalization group in the age of matrix product states, *Ann. Phys. (NY)* **326**, 96 (2011).
- [17] F. Verstraete, J. J. García-Ripoll, and J. I. Cirac, Matrix Product Density Operators: Simulation of Finite-Temperature and Dissipative Systems, *Phys. Rev. Lett.* **93**, 207204 (2004).
- [18] A. Feiguin and S. White, Time-step targeting methods for real-time dynamics using the density matrix renormalization group, *Phys. Rev. B* **72**, 020404 (2005).
- [19] D. Gobert, C. Kollath, U. Schollwöck, and G. Schütz, Real-time dynamics in spin-1/2 chains with adaptive time-dependent density matrix renormalization group, *Phys. Rev. E* **71**, 036102 (2005).
- [20] G. Vidal, Efficient Classical Simulation of Slightly Entangled Quantum Computations, *Phys. Rev. Lett.* **91**, 147902 (2003).
- [21] H. F. Trotter, On the product of semi-groups of operators, *Proc. Am. Math. Soc.* **10**, 545 (1959).
- [22] M. Suzuki, Relationship between d -Dimensional Quantal Spin Systems and $(d + 1)$ -Dimensional Ising Systems, *Prog. Theor. Phys.* **56**, 1454 (1976).
- [23] A. N. Krylov, On the Numerical Solution of the Equation by Which are Determined in Technical Problems the Frequencies of Small Vibrations of Material Systems, *News of Academy of Sciences of USSR*, 1931, VII, Nr. 4, 491-539 (in Russian).
- [24] P. Calabrese and J. Cardy, Evolution of entanglement entropy in one-dimensional systems, *J. Stat. Mech.* (2005) P04010.
- [25] A. Holzner, A. Weichselbaum, I. P. McCulloch, U. Schollwöck, and J. v. Delft, Chebyshev matrix product state approach for spectral functions, *Phys. Rev. B* **83**, 195115 (2011).
- [26] F. A. Wolf, I. P. McCulloch, O. Parcollet, and U. Schollwöck, Chebyshev matrix product state impurity solver for dynamical mean-field theory, *Phys. Rev. B* **90**, 115124 (2014).
- [27] Martin Ganahl, P. Thunström, F. Verstraete, K. Held, and H. G. Evertz, Chebyshev expansion for impurity models using matrix product states, *Phys. Rev. B* **90**, 045144 (2014).
- [28] A. C. Tiegel, S. R. Manmana, T. Pruschke, and A. Honecker, Matrix product state formulation of frequency-space dynamics at finite temperatures, *Phys. Rev. B* **90**, 060406(R) (2014).
- [29] F. A. Wolf, J. A. Justiniano, I. P. McCulloch, and U. Schollwöck, Spectral functions and time evolution from the Chebyshev recursion, *Phys. Rev. B* **91**, 115144 (2015).

- [30] A. Braun and P. Schmitteckert, Numerical evaluation of Green's functions based on the Chebyshev expansion, *Phys. Rev. B* **90**, 165112 (2014).
- [31] C. Moler and Ch. van Loan, Nineteen dubious ways to compute the exponential of a matrix, twenty-five years later, *SIAM Rev.* **45**, 3 (2003).
- [32] T. J. Park and J. C. Light, Unitary quantum time evolution by iterative Lanczos reduction, *J. Chem. Phys.* **85**, 5870 (1986).
- [33] R. M. Noack, S. R. Manmana, S. Wessel, and A. Muramatsu, Studying Time-Dependent Quantum Phenomena with the Density-Matrix Renormalization Group, *Springer Lecture Notes in Physics* **739**, 637 (2008).
- [34] M. Hochbruck and C. Lubich, On Krylov Subspace Approximations to the Matrix Exponential Operator, *SIAM J. Numer. Anal.* **34**, 1911 (1997).
- [35] M. L. Wall and L. D. Carr, Out-of-equilibrium dynamics with matrix product states, *New J. Phys.* **14**, 125015 (2012).
- [36] A. J. Daley, C. Kollath, U. Schollwöck, and G. Vidal, Time-dependent density-matrix renormalization-group using adaptive effective Hilbert spaces, *J. Stat. Mech.: Theory Exp.* (2004) P04005.
- [37] G. Vidal, Efficient Simulation of One-Dimensional Quantum Many-Body Systems, *Phys. Rev. Lett.* **93**, 040502 (2004).
- [38] P. Schmitteckert, Nonequilibrium electron transport using the density matrix renormalization group, *Phys. Rev. B* **70**, 121302(R) (2004).
- [39] S. R. Manmana, A. Muramatsu, and R. M. Noack, Time evolution of one-dimensional Quantum Many Body Systems, *AIP Conf. Proc.* **789**, 269 (2005).
- [40] J. Haegeman, J. I. Cirac, T. J. Osborne, I. Pizorn, H. Verschelde, and F. Verstraete, Time-Dependent Variational Principle for Quantum Lattices, *Phys. Rev. Lett.* **107**, 070601 (2011).
- [41] M. P. Zaletel, R. S. K. Mong, C. Karrasch, J. E. Moore, and F. Pollmann, Time-evolving a matrix product state with long-ranged interactions, *Phys. Rev. B* **91**, 165112 (2015).
- [42] *Handbook of Mathematical Functions with Formulas, Graphs, and Mathematical Tables*, edited by M. Abramowitz and I. A. Stegun (Dover, New York, 1970).
- [43] *Chebyshev Polynomials*, J. C. Mason and D. C. Handscomb (CRC Press, Boca Raton, 2002).
- [44] J. P. Boyd, *Chebyshev & Fourier Spectral Methods*, Lecture Notes in Engineering Vol. 49 (Springer-Verlag, Berlin, 1989).
- [45] T. J. Rivlin, *Chebyshev Polynomials: From Approximation Theory to Algebra and Number Theory, Pure and Applied Mathematics* (Wiley, New York, 1990).
- [46] A. Weiße, G. Wellein, A. Alvermann, and H. Fehske, The kernel polynomial method, *Rev. Mod. Phys.* **78**, 275 (2006).
- [47] M. Cramer, A. Flesch, I. P. McCulloch, U. Schollwöck, and J. Eisert, Exploring Local Quantum Many-Body Relaxations by Atoms in Optical Superlattices, *Phys. Rev. Lett.* **101**, 063001 (2008).
- [48] M. Cramer, C. M. Dawson, J. Eisert, and T. J. Osborne, Exact Relaxation in a Class of Nonequilibrium Quantum Lattice Systems, *Phys. Rev. Lett.* **100**, 030602 (2008).
- [49] A. Flesch, M. Cramer, I. P. McCulloch, U. Schollwöck, and J. Eisert, Probing local relaxation of cold atoms in optical superlattices, *Phys. Rev. A* **78**, 033608 (2008).
- [50] T. Dutta and S. Ramasesha, Effect of dimerization on dynamics of spin-charge separation in Pariser-Parr-Pople model: A time-dependent density matrix renormalization group study, *Phys. Rev. B* **84**, 235147 (2011).
- [51] H. Fehske, J. Schleede, G. Schubert, G. Wellein, V. S. Filinov, and A. R. Bishop, Numerical approaches to time evolution of complex quantum systems, *Phys. Lett. A* **373**, 2182 (2009).
- [52] J. Honer, J. C. Halimeh, I. McCulloch, U. Schollwöck, and H. P. Büchler, Fractional excitations in cold atomic gases, *Phys. Rev. A* **86**, 051606(R) (2012).
- [53] J. J. García-Ripoll, Time evolution of matrix product states, *New J. Phys.* **8**, 305 (2006).
- [54] S. R. White, Density-matrix algorithms for quantum renormalization groups, *Phys. Rev. B* **48**, 10345 (1993).

Chapter 6

Domain-wall melting in ultracold-boson systems with hole and spin-flip defects

Ultracold-boson experiments have become ubiquitous in quantum-optics and many-body laboratories around the world. In addition to probing fundamental physics questions, a huge part of the investigations of these laboratories is dedicated to efficient ways of preparing certain, often paradigmatic, initial quantum states to which a local or global quench is then applied. For faithful interpretation of physical reality in such experiments, it is therefore essential to understand the limitations of such preparation methods and the consequences of their potential imperfections. In this Chapter we look at the effect of defects in a domain wall on the subsequent dynamics after a global quench. The domain wall consists of two species of bosons – commonly, ^{87}Rb atoms prepared in different internal states $|F = 1, m_F = +1\rangle$ and $|F = 2, m_F = -1\rangle$ – and the defects can either be holes (the absence of an atom) or a spin flip (the presence of an atom of the wrong species on either side of the domain wall). The initial state is then quenched with the two-species Bose-Hubbard model, which maps onto the spin-1/2 XXZ model in the large-interaction limit. We show that the effect of holes is innocuous and can be accounted for with a simple linear combination of spatially-shifted observables relative to the clean case. However, a spin flip has a nontrivial effect on the melting of the domain wall as its dynamics has the same time scale as the dynamics of the domain-wall melting.

- *Domain-wall melting in ultracold-boson systems with hole and spin-flip defects*
Jad C. Halimeh, Anton Wöllert, Ian P. McCulloch, Ulrich Schollwöck, and Thomas Barthel
Phys. Rev. A **89**, 063603 (2014)

Domain-wall melting in ultracold-boson systems with hole and spin-flip defects

Jad C. Halimeh,¹ Anton Wöllert,¹ Ian McCulloch,² Ulrich Schollwöck,¹ and Thomas Barthel^{3,1}

¹*Department of Physics and Arnold Sommerfeld Center for Theoretical Physics, Ludwig-Maximilians-Universität München, Theresienstr. 37, D-80333 Munich, Germany*

²*Centre for Engineered Quantum Systems, School of Mathematics and Physics, University of Queensland, Brisbane 4072, Australia*

³*Laboratoire de Physique Théorique et Modèles Statistiques, Université Paris-Sud, CNRS, UMR8626, F-91405 Orsay, France*

(Received 25 July 2013; revised manuscript received 28 February 2014; published 4 June 2014)

Quantum magnetism is a fundamental phenomenon of nature. As of late, it has garnered a lot of interest because experiments with ultracold atomic gases in optical lattices could be used as a simulator for phenomena of magnetic systems. A paradigmatic example is the time evolution of a domain-wall state of a spin-1/2 Heisenberg chain, the so-called domain-wall melting. The model can be implemented by having two species of bosonic atoms with unity filling and strong on-site repulsion U in an optical lattice. In this paper, we study the domain-wall melting in such a setup on the basis of the time-dependent density matrix renormalization group (tDMRG). We are particularly interested in the effects of defects that originate from an imperfect preparation of the initial state. Typical defects are holes (empty sites) and flipped spins. We show that the dominating effects of holes on observables like the spatially resolved magnetization can be taken account of by a linear combination of spatially shifted observables from the clean case. For sufficiently large U , further effects due to holes become negligible. In contrast, the effects of spin flips are more severe as their dynamics occur on the same time scale as that of the domain-wall melting itself. It is hence advisable to avoid preparation schemes that are based on spin flips.

DOI: [10.1103/PhysRevA.89.063603](https://doi.org/10.1103/PhysRevA.89.063603)

PACS number(s): 03.75.Lm, 37.10.Jk, 75.10.Jm, 05.70.Ln

I. INTRODUCTION

Recent progress in ultracold-atomic-gas experiments [1,2] has allowed for greater degrees of control where now one has the tools to explore many interesting and fascinating phenomena of quantum many-body physics that previously have been restricted only to the realm of theoretical investigation. Gases of ultracold fermionic and bosonic atoms in optical lattices provide the arguably cleanest implementations of the Fermi and Bose-Hubbard models and are very well tunable. These fundamental models of condensed matter physics have by now been studied quite extensively in diverse experiments. See, for example, Refs. [3–13]. The experimental capabilities are very well developed, as exemplified by the controlled shifting between the superfluid (SF) and Mott-insulator (MI) regimes [2,3], generation of random potentials [14–16], single-atom imaging [17–20], or single-site manipulation [21,22].

In the vein of Feynman's idea to use one well-controllable quantum many-body system to simulate others [23,24], it is of particular interest to gain a thorough understanding of experimentally feasible ultracold-atomic-gas systems that can be used to faithfully implement spin models. Such setups could then be used to study the diverse phenomena of quantum magnetism.

As it turns out, the drosophila of quantum magnetism, the Heisenberg spin-1/2 XXZ model, appears quite naturally as an effective model for the subspace of unitary occupancy of the two-species Bose-Hubbard (BH) model in the limit of strong on-site interaction strengths [25–29]. The effective spin-exchange couplings are determined by the tunneling parameters and the inter- and intraspecies interaction strengths. Numerical investigations [29] have been presented and an experimental realization of this model has recently been implemented in order to study the quantum dynamics of a single spin impurity [30]. One can envisage many interesting experiments using this setup in order to observe and

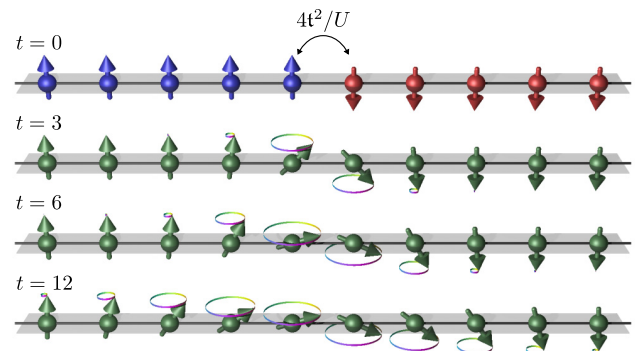


FIG. 1. (Color online) Initial *clean* domain-wall state with spin-up (spin-down) bosons on the left (right) half of the system at $t = 0$. The illustrations for times $t > 0$ are based on the actual evolution of the on-site magnetizations $\langle \hat{S}_i^z \rangle$ with hopping amplitude $t = 1$ and onsite repulsion $U = 15$. The domain wall melts and evolves into a nontrivial magnetization profile.

investigate important many-body phenomena such as quantum phase transitions, long-range order, the temporal growth of entanglement, diffusive versus ballistic transport, relaxation dynamics, or integrability, to name a few. It can also provide a testbed for ultracold-atomic-gas experimental setups where their robustness to defects can be investigated and scrutinized.

A prominent nonequilibrium process that comprises several of the aforementioned many-body phenomena is the melting of a domain wall as depicted in Fig. 1, and this naturally becomes an important phenomenon to probe in ultracold-atom experiments that aim to map onto the spin-1/2 XXZ model. Initially, the system is in a product state where the left half of the system is occupied by up-spins and the right half by down-spins. During the evolution, magnetization flows from left to right, accompanied by a growing entanglement. The dynamics has been studied analytically and numerically, for

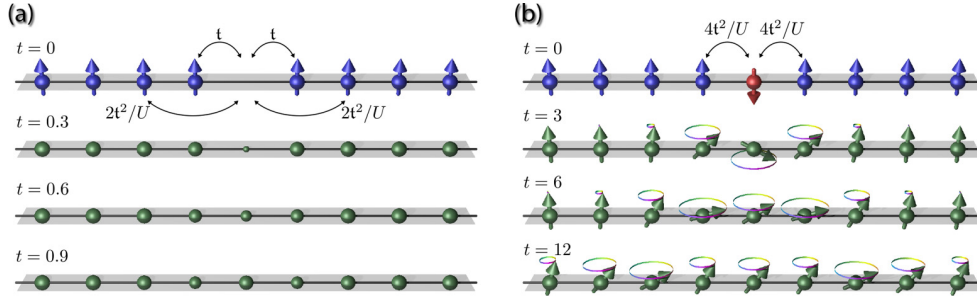


FIG. 2. (Color online) Illustration of the time evolution of a hole and a spin-flip defect in a fully polarized background. The sketches are based on the actual evolution of densities $\langle \hat{n}_{\uparrow,j} + \hat{n}_{\downarrow,j} \rangle$ and magnetizations $\langle \hat{S}_j^z \rangle$ for hopping amplitude $t = 1$ and onsite repulsion $U = 15$. (a) Holes can move by one site via direct hopping and by two sites via a second-order process that gets suppressed with increasing U . As explained in the text, the density dynamics in the effective t - J model (7) is independent of the simultaneous spin dynamics. The latter is, however, influenced by density fluctuations. (b) The Heisenberg-type spin-spin interaction is caused by a second-order exchange process where bosons hop between nearest-neighbor sites. The focus of this paper is to explore the effects of such defects on the domain-wall melting in Fig. 1.

example, in Refs. [31–40]. The transport is ballistic in the critical XY phase of the model. In the gapped phases, after some initial ballistic transport, the spin current was found to vanish for longer times. Besides this, there is an interesting nearest-neighbor beating effect in the magnetization profile (synchronized opposing oscillations of the magnetizations on neighboring sites) and small plateaus evolve at the domain-wall fronts. This can be attributed to the integrability of the model.

When one implements the domain-wall melting experimentally with ultracold bosons, defects can occur due to an imperfect preparation of the initial state. There are basically two options for the preparation. (i) In the first scheme, one prepares a Mott insulating state of spin-up bosons. Then, using a light mask, one addresses the right half of the system, bringing it into resonance with a microwave pulse that causes the spins to flip. (ii) In an alternative scheme, using light masks for the halves of the systems, one can cool the bosons in the lattice with strong chemical potential differences for the two species. In both schemes, due to an ultimately finite temperature, hole defects can occur [Fig. 2(a)]. Due to the (shallow) trapping potential, these holes correspond to the lowest excitations of the Mott insulator ground state. The first scheme allows for the preparation of a spatially tighter (less smeared) domain wall [41]. One disadvantage of this scheme is the finite spin-flip efficiency (typically around 98% in current experiments) which corresponds to the occurrence of spin-flip defects as shown in Fig. 2(b).

In this paper, numerical studies are presented for the domain-wall melting of two boson species in a one-dimensional optical lattice using various values of the on-site interaction strength U , most of which lie in the large- U limit where the model maps faithfully onto a corresponding spin-1/2 XXZ model. All corresponding model parameters offer experimental feasibility and are simulated closely following the conditions in Fukuhara *et al.* [30], and are thus very relevant to similar future experimental investigations. We focus in particular on the effects of typical experimental defects in the initial state on the melting dynamics. The quasiexact numerical treatment is performed using the time-dependent density matrix renormalization group (tDMRG) method [42–46] in the

Krylov approach [47–49] (see also [50]). The results show that the dominating effects of hole defects on observables like the spatially resolved magnetization can be taken account of by a simple averaging procedure over spatially shifted observables from the clean case. To some extent, this smoothens out the beating and plateaus in the magnetization profile of the melting domain wall. For large U , the hole dynamics is much faster than the domain-wall dynamics. Hence, effects of holes beyond the aforementioned smoothing effect become negligible. In contrast, the effects of spin flips are more severe as their dynamics occur on the same time scale as that of the domain-wall melting itself. The spatial averaging procedure employed for the holes is still useful but not as powerful in this case. For the experimental investigations, this gives a reason to favor the second preparation scheme, cooling with chemical potentials, over the first scheme that is based on inducing spin flips for one half of the system.

The paper is divided into five sections beyond the introduction: In Sec. II, the models occurring in this study and the mappings between them are discussed. After a specification of the different initial states in Sec. III, Sec. IV presents numerical simulations showing how the BH dynamics approaches the t - J model dynamics. In Sec. V, the main results are presented and explained along with a discussion of the various observables of interest that are best suited to study the domain-wall melting. The paper concludes with Sec. VI and a convergence analysis of the numerical simulations in the Appendix.

II. MODELS

A. Spin-1/2 XXZ chain

The spin-1/2 XXZ Heisenberg magnet is a classic example of a one-dimensional quantum lattice model that has been extensively studied [51–53] and that is of ideal importance to the understanding of magnetism and various phenomena in quantum many-body physics as mentioned in the introduction. Considering a one-dimensional lattice of L sites, the Hamiltonian describing this model is

$$\hat{H}_{XXZ} = J_{\perp} \sum_{j=1}^{L-1} (\hat{S}_j^x \hat{S}_{j+1}^x + \hat{S}_j^y \hat{S}_{j+1}^y) + J_z \sum_{j=1}^{L-1} \hat{S}_j^z \hat{S}_{j+1}^z, \quad (1)$$

where the spin operators obey the commutation relations $[\hat{S}_i^\alpha, \hat{S}_j^\beta] = i\delta_{ij}\epsilon_{\alpha\beta\gamma}\hat{S}_i^\gamma$ ($\hbar = 1$).

The properties of the ground state of this Hamiltonian crucially depend upon the in-plane and on-axis spin-spin interaction parameters J_\perp and J_z . In the case $J_\perp = J_z$, \hat{H}_{XXZ} becomes the isotropic Heisenberg Hamiltonian [54,55] and the interaction between the spins is rotation invariant. When $J_\perp, J_z > 0$, the Hamiltonian is antiferromagnetic, since it is energetically favorable that the spins on neighboring sites have antiparallel alignment, while when $J_\perp, J_z < 0$, parallel alignment is favorable and thus the Hamiltonian is ferromagnetic. Moreover, at the critical point $J_z/|J_\perp| = 1$, there is a Kosterlitz-Thouless-type phase transition that the system undergoes from a gapless XY regime ($J_z/|J_\perp| \leq 1$) to the gapped ($J_z/|J_\perp| > 1$) Néel phase.

Domain-wall melting in this system has been investigated analytically and numerically [31–39], and one can observe a transition from ballistic to subdiffusive dynamics when going from the gapless to the gapped regime. To be able to simulate this model with an ultracold-atomic-gas system would be a very interesting way to experimentally probe such dynamics, and such a mapping has already been proposed [25–29], where a two-species BH model in the limit of large interactions at unity filling can be approximated by the spin-1/2 XXZ model with an induced ordering field. This is discussed in the following.

B. Two-species Bose-Hubbard model and the relation to the XXZ model

A prominent example for using bosonic systems to simulate others [23,24] is that of using the *two-species Bose-Hubbard* (BH) model (ultracold bosonic atoms in optical lattices) to emulate the spin-1/2 XXZ model [25–29], where the two boson species correspond to spins up and down, respectively. This two-species BH model is described by the Hamiltonian,

$$\hat{H}_{\text{BH}} = - \sum_{\sigma, j=1}^{L-1} t_\sigma (\hat{b}_{\sigma, j}^\dagger \hat{b}_{\sigma, j+1} + \text{H.c.}) + \sum_{\sigma, j=1}^L \frac{U_\sigma}{2} \hat{n}_{\sigma, j} (\hat{n}_{\sigma, j} - 1) + V \sum_{j=1}^L \hat{n}_{\uparrow, j} \hat{n}_{\downarrow, j}, \quad (2)$$

where σ ($=\uparrow$ or \downarrow) labels the boson species, t_σ is the tunneling parameter for “ σ ” bosons, U_σ is the intraspecies on-site interaction strength for “ σ ” bosons, V is the interspecies interaction strength between “ \uparrow ” and “ \downarrow ” bosons on the same site, $\hat{b}_{\sigma, j}$ is the annihilation operator for “ σ ” bosons on site j ($[\hat{b}_{\sigma, j}, \hat{b}_{\sigma', j'}^\dagger] = \delta_{\sigma\sigma'}\delta_{jj'}$), and $\hat{n}_{\sigma, j} = \hat{b}_{\sigma, j}^\dagger \hat{b}_{\sigma, j}$ is the number operator for “ σ ” bosons on site j . The bosonic species “ \uparrow ” and “ \downarrow ” are associated with two internal states of the atomic species used in the experimental setup (such as rubidium isotope ^{87}Rb , where the two species correspond to two hyperfine states $|F = 1, m_F = +1\rangle$ and $|F = 2, m_F = -1\rangle$ of the bosonic atom). Moreover, both bosonic species can be trapped by separate standing laser-light waves *via* polarization selection [56] and the spin distribution of such a system can then be probed by single-site-resolved fluorescence imaging with a high-resolution microscope objective [17–19].

In the limit of large U_\uparrow , U_\downarrow , and V , using second-order perturbation theory or the corresponding Schrieffer-Wolff transformation [25–29], one can derive an effective Hamiltonian for the subspace of unity filling (number of particles equal to the number of lattice sites), yielding

$$\hat{H}_{XXZ} - h \sum_{j=1}^L \hat{S}_j^z, \quad (3)$$

where

$$J_z = 2 \frac{t_\uparrow^2 + t_\downarrow^2}{V} - \frac{4t_\uparrow^2}{U_\uparrow} - \frac{4t_\downarrow^2}{U_\downarrow}, \quad J_\perp = -\frac{4t_\uparrow t_\downarrow}{V}, \quad (4)$$

$$h = \frac{4t_\uparrow^2}{U_\uparrow} - \frac{4t_\downarrow^2}{U_\downarrow}. \quad (5)$$

The induced homogeneous magnetic field h can be ignored due to the conservation of the total magnetization in Eq. (1). The spin-exchange terms are due to a second-order process where bosons hop twice between neighboring sites and the energy in the intermediate states is increased due to the on-site repulsion U_σ , V .

For the experimentally most relevant situation $t_\uparrow = t_\downarrow \equiv t$, and $U_\uparrow = U_\downarrow = V \equiv U$, one arrives at the isotropic Heisenberg antiferromagnet with $J_\perp = J_z$. This regime is at the focus of this paper since, on the one hand, the main purpose of the paper is to study the effect of holes and spin flips on domain-wall melting rather than the effect of anisotropies on it and, on the other hand, significant anisotropies are very hard to achieve experimentally [30,41]. For instance, the variance in V is typically given by the parameter,

$$\Delta V = \frac{U_\uparrow + U_\downarrow}{2} - V, \quad (6)$$

and ΔV can be set experimentally [30,41] to a value in $[-0.1, 0.1] \times U_\uparrow$. Note that the available range for the effective spin couplings can be extended substantially by employing optical superlattices as discussed and demonstrated, for example, in Refs. [29,57,58].

C. The t - J model as an effective model for strong repulsion

Since we want to study the effect of hole defects which occur in the experiments, we cannot restrict the analysis to the subspace of unitary occupancy as done in the previous section. Rather, one has to take into account all states where on each site we have either one or no boson. The second-order perturbation theory for the limit of strong repulsion leads in this case to a bosonic variant of the so-called t - J Hamiltonian [60–64], containing in this case some three-site terms that are particular to the bosonic nature of the particles. For our specific two-species Bose-Hubbard model (2), we obtain a hard-core boson t - J model

$$\hat{H}_{t-J} = \hat{H}_t + \hat{H}_{XXZ} + \hat{H}_{3\text{-site}}, \quad (7)$$

where \hat{H}_{XXZ} is the XXZ Hamiltonian (1) that encodes the nearest-neighbor spin exchange and

$$\hat{H}_t = - \sum_{\sigma, j=1}^{L-1} t_\sigma (\hat{a}_{\sigma, j}^\dagger \hat{a}_{\sigma, j+1} + \text{H.c.}) \quad (8)$$

is the direct hopping. Here, $\hat{a}_{\sigma,j}$ are hard-core-bosonic annihilation operators with commutation relations $[\hat{a}_{\sigma,j}, \hat{a}_{\sigma',j'}^\dagger] = \delta_{\sigma\sigma'}\delta_{jj'} \forall j \neq j'$ and $\{\hat{a}_{\sigma,j}, \hat{a}_{\sigma',j}^\dagger\} = \delta_{\sigma\sigma'}$. In terms of the Pauli matrices $\{\hat{\sigma}^\alpha | \alpha = x, y, z\}$, the spin operators (occurring in \hat{H}_{XXZ} and $\hat{H}_{3\text{-site}}$) are given by

$$\hat{S}_j^\alpha := \frac{1}{2} \sum_{\sigma\sigma'} \hat{a}_{\sigma,j}^\dagger [\hat{\sigma}^\alpha]_{\sigma\sigma'} \hat{a}_{\sigma',j}. \quad (9)$$

The terms,

$$\begin{aligned} \hat{H}_{3\text{-site}} = & - \sum_{\sigma,j=1}^{L-2} \frac{t_\sigma^2}{V} (\hat{a}_{\sigma,j}^\dagger \hat{n}_{-\sigma,j+1} \hat{a}_{\sigma,j+2} + \text{H.c.}) \\ & - \frac{t_\uparrow t_\downarrow}{V} \sum_{\sigma,j=1}^{L-2} (\hat{a}_{-\sigma,j}^\dagger \hat{S}_{j+1}^\sigma \hat{a}_{\sigma,j+2} + \text{H.c.}) \\ & - \sum_{\sigma,j=1}^{L-2} \frac{2t_\sigma^2}{U_\sigma} (\hat{a}_{\sigma,j}^\dagger \hat{n}_{\sigma,j+1} \hat{a}_{\sigma,j+2} + \text{H.c.}), \quad (10) \end{aligned}$$

describe second-order processes, where bosons move by two sites. In the first term, a “ σ ” boson hops via a site occupied by a “ $-\sigma$ ” boson. In the second term, a “ σ ” boson hops from site $j+2$ to a neighboring site $j+1$ occupied by a “ $-\sigma$.” The latter subsequently hops to site j , causing an effective spin flip on site $j+1$. In the third term, a “ σ ” boson hops over a site occupied by the same species to a next-nearest-neighbor site. We have used the notation \hat{S}_{j+1}^σ to denote \hat{S}_{j+1}^+ (\hat{S}_{j+1}^-) when σ is “ \uparrow ” (“ \downarrow ”).

III. INITIAL STATES

In investigating the dynamics of a global quench where an initial state $|\psi_0\rangle = |\psi_0(t \leq 0)\rangle$ is time evolved for $t > 0$ with the Hamiltonian \hat{H} , which can be either \hat{H}_{BH} or \hat{H}_{t-j} for the purposes of this paper, it is particularly interesting to study the effect of *defects* in the initial domain-wall state on the melting dynamics, because defects such as holes and spin flips can occur naturally in the preparation process. For our numerical investigations of the full BH model, the *clean* domain-wall initial state $|\psi_c^{\text{BH}}\rangle$ is chosen to be the ground state of the Hamiltonian,

$$\hat{H}_{\text{prep}} := \hat{H}_{\text{BH}} - \mu \sum_{j=1}^{L/2} (\hat{n}_{\uparrow,j} + \hat{n}_{\downarrow,j+L/2}), \quad (11a)$$

$$\hat{H}_{\text{prep}} |\psi_c^{\text{BH}}\rangle = E_0 |\psi_c^{\text{BH}}\rangle, \quad (11b)$$

at unity filling with $L/2$ “ \uparrow ” bosons and $L/2$ “ \downarrow ” bosons on an L -site lattice. The species- and site-dependent chemical potential (μ), when chosen sufficiently large compared to the hopping amplitude t_σ in \hat{H}_{BH} , ensures that a domain-wall state is formed whereby the left half of the lattice ($1 \leq j \leq L/2$) is mostly occupied by “ \uparrow ” bosons and the other half ($L/2 + 1 \leq j \leq L$) is mostly occupied by “ \downarrow ” bosons. For large chemical potential and density-density interaction (U_σ, V), the state $|\psi_c^{\text{BH}}\rangle$ is in fact close to the product state,

$$|\psi_c\rangle = \prod_{j=1}^{L/2} \hat{a}_{\uparrow,j}^\dagger \hat{a}_{\downarrow,j+L/2}^\dagger |0\rangle = |\uparrow\uparrow \dots \uparrow\downarrow \dots \downarrow\rangle, \quad (12)$$

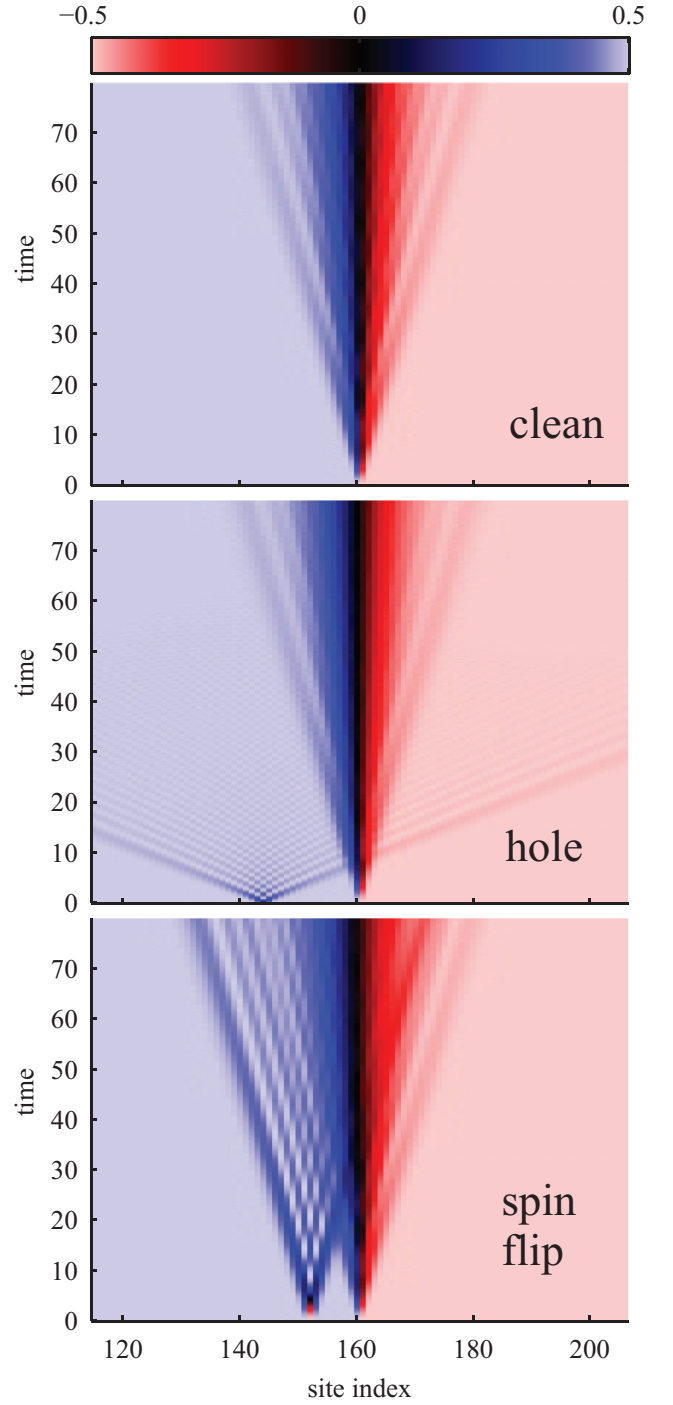


FIG. 3. (Color online) The spin-density $\langle \hat{S}_j^z(t) \rangle$ as a function of position and time for $t = 1$, $U = 15$, lattice size $L = 320$, and defect positions $j_h = L/2 - 16$, $j_f = L/2 - 8$. All three maps show times up to $80/t$ as by then the part of the hole that initially moves away from the domain wall will have been reflected off the boundary but still not interacted with the domain wall. Like the domain wall, the spin flip evolves on a time scale $(4t^2/U)^{-1}$, while the hole defect moves on the shorter time scale t^{-1} . It is interesting to note in the cases of the clean domain-wall and spin-flip initial states that along the domain wall there is a nearest-neighbor *beating* behavior (synchronized opposing oscillations on neighboring sites) that is absent in the hole case. See also Fig. 4 for slices and the Supplemental Material [59] for animations.

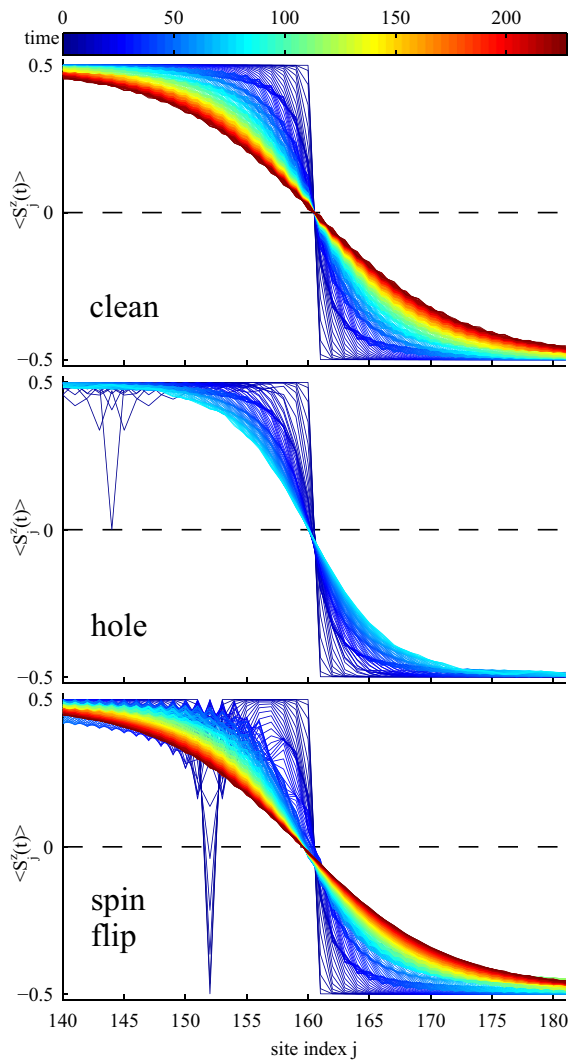


FIG. 4. (Color online) Spin-density ($\langle \hat{S}_j^z(t) \rangle$) profiles around the domain wall at various times for the clean, hole, and spin-flip initial states ($t = 1$, $U = 15$, $L = 320$, $j_h = L/2 - 16$, $j_f = L/2 - 8$). Time is indicated chromatically where blue corresponds to $t = 0$ and red to $t = 227/t$ (reached for the clean and spin-flip cases). In the case of the hole, only times up to $t = 80/t$ are shown. Also here one sees distinctive nearest-neighbor beating behavior in the clean and spin-flip cases that is considerably smoothed out in the hole case. Online, animations are provided that show the evolution of the states with defects in direct comparison to the clean domain-wall state [59].

where $|0\rangle$ is the vacuum state. The larger the interaction strengths in \hat{H}_{BH} , that is, the deeper the system is in the Mott-insulator phase, the greater the overlap of $|\psi_c^{\text{BH}}\rangle$ and $|\psi_c\rangle$.

In principle, one obtains the XXZ model or the t - J model within second-order perturbation theory as the effective model for the BH model for the sector of single-site bosonic states $\{|\uparrow\rangle, |\downarrow\rangle\}$ or $\{|0\rangle, |\uparrow\rangle, |\downarrow\rangle\}$, respectively. Formally one gets from the original to the effective model via a unitary Schrieffer-Wolff transformation $e^{i\hat{S}}$ followed by a projection to the aforementioned subspace. So the correspondence between

the spin $|\sigma\rangle$ and bosonic atom $|\sigma\rangle$ is not 1 : 1—one has corresponding perturbative corrections on top due to the unitary transformation [29]. Thus, if one wants to study the analog of the XXZ domain-wall dynamics in the BH model, one should not start from the state $|\psi_c\rangle$, but take the perturbative corrections into account. If one did not, one would have nontrivial dynamics also in the “fully polarized” regions that are not influenced by the domain wall. In a bosonic state $|\uparrow\uparrow\uparrow \dots \uparrow\rangle$, for example, the BH dynamics is not trivial: Due to the hopping, states with $n_{\uparrow,j} \neq 1$ get populated (also, the boundary acts as a distortion). This also leads to entanglement growth in this supposedly trivial state. One can take into account the perturbative corrections very easily, by choosing the initial state, as described above, to be the ground state $|\psi_c^{\text{BH}}\rangle$ of the BH model with a strong chemical potential for “ \uparrow ” bosons on the left half and for “ \downarrow ” bosons on the right half. This state is the actual counterpart of the spin domain-wall state $|\psi_c\rangle = |\uparrow\uparrow \dots \uparrow\downarrow \dots \downarrow\rangle$ in the XXZ chain and the dynamics far away from the center is trivial then as it should be. With the Schrieffer-Wolff transformation $e^{i\hat{S}}$, the correspondence between the states is

$$|\psi_c^{\text{BH}}\rangle \approx e^{-i\hat{S}}|\psi_c\rangle. \quad (13)$$

The dominant defects occurring in the different experimental preparation schemes, as described in the introduction, are holes,

$$|\psi_h^{\text{BH}}\rangle = \hat{b}_{\uparrow,j_h}|\psi_c^{\text{BH}}\rangle, \quad (14)$$

and spin flips,

$$|\psi_f^{\text{BH}}\rangle = \hat{b}_{\downarrow,j_f}^\dagger \hat{b}_{\uparrow,j_f}|\psi_c^{\text{BH}}\rangle, \quad (15)$$

where, in this paper, the defects are initially located in the left half of the system ($1 < j_h, j_f < L/2$) without loss of generality. These types of defects naturally arise in the initial-state preparation or can simply be prepared deterministically in order to investigate their effects. The evolution of magnetization profiles for the different initial states are shown in Figs. 3 and 4 and will be discussed in Sec. V.

IV. CONVERGENCE OF BH DYNAMICS TO THE t - J DYNAMICS AND DMRG SPECIFICS

For the reasons given in Sec. II A, in the following, the analysis will be restricted to the isotropic case, where $t_\uparrow = t_\downarrow \equiv t$ and $U_\uparrow = U_\downarrow = V \equiv U$. The resulting isotropic two-species BH model (2) is found to map faithfully onto the t - J model (7) for $U \gtrsim 8$ ($t = 1$). Figure 5 shows a comparison of the BH- and t - J -model results for the observable $\langle \hat{S}_{L/2+\Delta x}^z \rangle$ as well as the connected two-point correlation functions $\langle \hat{S}_i^z \hat{S}_j^z \rangle - \langle \hat{S}_i^z \rangle \langle \hat{S}_j^z \rangle$ and $\langle \hat{S}_i^x \hat{S}_j^x \rangle$ (note that $\langle \hat{S}_i^x \rangle = 0$ for all times) for an initial hole state where the hole is located at $L/2 - 4$ and $\Delta x = 1$. For all considered observables, the agreement is good for all values of $U \gtrsim 8$, and matches remarkably well for larger U , as is expected.

Although it is not an exact correspondence, we used here for the Bose-Hubbard model,

$$\frac{1}{2} \sum_{\sigma\sigma'} \hat{b}_{\sigma,j}^\dagger [\hat{\sigma}^\alpha]_{\sigma\sigma'} \hat{b}_{\sigma',j}, \quad (16)$$

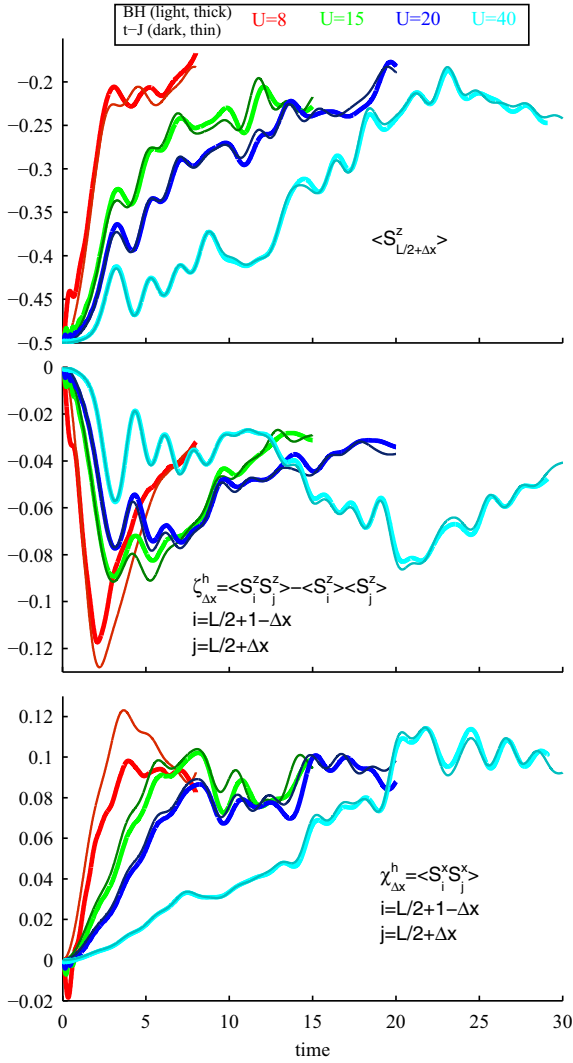


FIG. 5. (Color online) Comparison of the dynamics in the full BH model (2) (light, thick lines) and the corresponding t - J model (7) (dark, thin lines) for an initial state with a hole at $j_h = L/2 - 4$, where $L = 20$ and $t = 1$. Here, $\Delta x = 1$ for all observables. Even for the smallest U ($=8$), there is good agreement between the results of the BH and t - J models. With increasing U , the agreement improves and the time from which deviations become appreciable increases.

as the counterpart of the observable \hat{S}_j^α in the t - J model. In analogy to the relation (13) of states in the original (BH) and the effective model (t - J) which is “simulated” in the original model, the correct counterpart of an observable \hat{O} of the effective model is $e^{-i\hat{S}} \hat{O} e^{i\hat{S}}$ for the original model. Simply employing \hat{O} also in the original model, as we did in this case by using the expression (16) instead of $e^{-i\hat{S}} \hat{S}_i^\alpha e^{i\hat{S}}$ causes an error $\mathcal{O}(\hat{S}) = \mathcal{O}(t/U)$ in the expectation values. A thorough discussion concerning these issues can be found in Ref. [29].

All simulations are carried out using tDMRG [44–46] in the Krylov approach [47–49] (see also [50]), where we compute each Krylov vector as a separate matrix product state. In the DMRG framework, one can control the accuracy of the simulation using the so-called *truncation* or *fidelity*

threshold [42,43,65] which puts an upper bound on the norm distance between the exactly evolved state and the approximately evolved state of the simulation. For the results of the main text, we used a threshold of 10^{-6} for each time step and time steps of size $0.01/t$ and $0.1/t$ for the BH and the t - J model, respectively. The convergence of the numerical results with respect to the fidelity threshold is demonstrated in the Appendix.

V. DOMAIN-WALL MELTING WITH AND WITHOUT DEFECTS

As was described and numerically checked above, the two-species BH model \hat{H}_{BH} maps onto the spin-1/2 XXZ model \hat{H}_{XXZ} [25–29] or on the hard-core boson t - J model (7) for sufficiently large $U/t \gtrsim 8$. As this is the regime of experimental interest we can hence base the further analysis on simulations of the t - J model. The t - J -model parameters are set to $t = 1$ and $U = 15$ for a lattice of $L = 320$ sites. The domain wall is located between sites $L/2$ and $L/2 + 1$ and, in the following, the cases of the clean domain-wall state $|\psi_c\rangle$ [Eq. (12)], a domain wall with a hole defect at site $j_h = L/2 - 16$, $\hat{a}_{\uparrow, j_h}^- |\psi_c\rangle$, and a domain wall with a spin-flip defect at site $j_f = L/2 - 8$, $\hat{S}_{j_f}^- |\psi_c\rangle$, are investigated beginning with the magnetization profiles as shown in Fig. 3.

A. Magnetization profiles

The clean case is not surprising and exhibits the known domain-wall melting dynamics associated with the Heisenberg XXZ model [31–38]. A noteworthy feature of this domain-wall melting process in the clean case is a nearest-neighbor *beating* mechanism (synchronized opposing oscillations of the magnetizations on neighboring sites) that persists even at later times and that one can make out in Fig. 3 and clearly see in Fig. 4. Corresponding animations are available online [59]. This feature, which causes short magnetization steps, is noticeably missing in the hole case, where the beating is strongly reduced and the short steps in the magnetization are smoothed out. At long times a further notable feature consists in (short) magnetization plateaus around the fronts of the domain wall [34,38] that will also be smoothed in the presence of hole defects. The spin-flip defect does not smoothen out the beating but it does have an effect on it nevertheless, as also shown in Fig. 4. Figure 3 also shows the significant difference in the velocities of the hole ($2t = 2$) and that of the spin flip ($4t^2/U = 4/15$) which is a manifestation of the spin-charge separation [51,66,67]. In Fig. 3 it is difficult to pinpoint the influence of the defects on the domain wall, but Fig. 4 indicates, for example, that there is a resulting spatial shift of the magnetization profile. In Fig. 4 this shift is the reason why magnetization profiles of the evolved defect states at different times do not intersect the $\langle \hat{S}_j^z \rangle = 0$ line at the same point. For sufficiently large times, the magnetization profile is, in comparison to the clean domain-wall evolution, shifted by about 0.5 sites in the hole case and by 1 site in the spin-flip case.

B. Explanation for the smoothening effect and spatial shifts

The observed spatial shifts and smoothening effects can be understood as follows. If one looks at the system at some long time t , at which the right-traveling part of the defect is assumed to have passed through the domain wall, one can express the time-evolved wave function $|\psi\rangle$ as a superposition of two approximately orthogonal states:

$$|\psi\rangle = \frac{1}{\sqrt{2}}(|\psi_\ell\rangle + |\psi_r\rangle). \quad (17)$$

Here, $|\psi_\ell(t)\rangle$ describes a state with a defect traveling to the left, and thus the defect never interacts with the domain wall, and $|\psi_r(t)\rangle$ describes a state with a defect traveling to the right and that has already interacted with and passed through the wall. Now in the case of the hole defect, due to the absence of one “ \uparrow ” boson, it is expected that the domain wall in $|\psi_r(t)\rangle$ is shifted by a single site towards the left, while in the case of the spin flip, not only is one “ \uparrow ” boson missing, but in its place we have an extra “ \downarrow ” boson, and thus the shift is expected to be by two sites to the left. The states $|\psi_{\ell,r}(t)\rangle$ that contain defect wave packets traveling to the left or right, respectively, are for sufficiently long times (approximately) orthogonal. This is due to the conservation of the particle number (hole case) or magnetization (spin-flip case) in the spatial region where the left-moving wave packet is supported. With this, one obtains at some site j not too far away from the domain-wall region,

$$\begin{aligned} \langle\psi|\hat{S}_j^z|\psi\rangle &= \frac{1}{2}(\langle\psi_\ell|\hat{S}_j^z|\psi_\ell\rangle + \langle\psi_r|\hat{S}_j^z|\psi_r\rangle) \\ &\approx \frac{1}{2}(\langle\psi_c|\hat{S}_j^z|\psi_c\rangle + \langle\psi_c|\hat{S}_{j+d}^z|\psi_c\rangle), \end{aligned} \quad (18)$$

where $d = 1$ (2) in the case where the defect is a hole (spin flip) and $|\psi_c(t)\rangle$ is the evolved wave function for the clean domain-wall state. Figure 6 shows the magnetization profile for each of the hole and spin-flip states at three different points in time as compared to the corresponding magnetization profiles for the clean state $|\psi_c\rangle$ and the corresponding magnetization profiles due to the superposition as quantified in Eq. (18). In the case of the hole, there is great agreement between the magnetization profile of the hole state and Eq. (18), especially for long times at which the hole has already passed through the domain wall (Fig. 3). Moreover, this averaging of two density profiles shifted by one site from each other (18) explains well why the beating observed for the clean case in Fig. 4 is smoothened out in the case of the hole state: The beating consists of a synchronized opposing oscillation of the magnetizations on neighboring sites. Summing the magnetization profile and its one-site translate (18), the opposing oscillations basically cancel out. The remaining smaller deviations are beyond the simple “classical” shifting effect. They are due to the modification of the domain-wall dynamics caused by the passing hole. At the location of the passing hole, the spin-spin interaction is practically switched off for a short period of time. This alteration of the domain-wall evolution will reduce with increasing U , as the hole will then pass faster and faster through the domain wall (when viewed in time units of $1/J$). In the case of the spin-flip defect, the superposition picture (17) is still useful but not as powerful for explaining the deviations to the clean case. One observes that, even at longer times, the magnetization profile for the spin-flip state does not fully

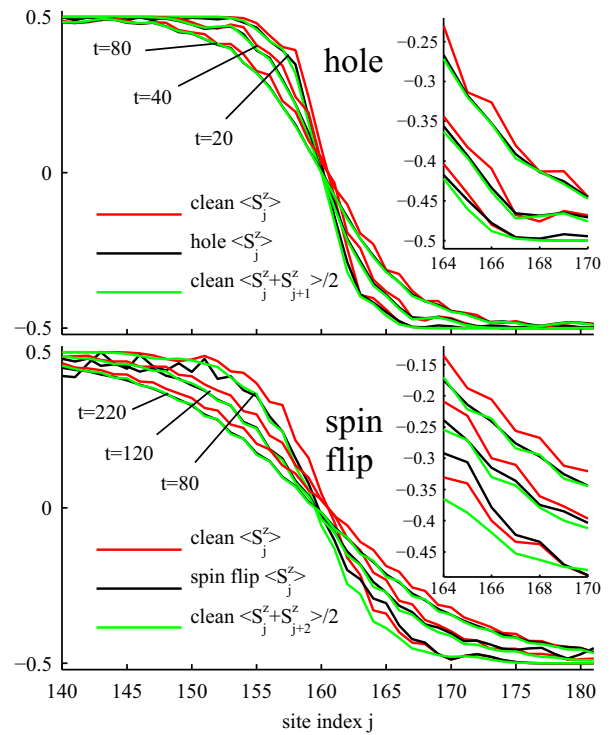


FIG. 6. (Color online) Investigation of the influence of hole and spin-flip defects on the magnetization profile ($t = 1$, $U = 15$, $L = 320$, $j_h = L/2 - 16$, $j_f = L/2 - 8$). It is observed that at long times, the magnetization profile in the hole case matches its corresponding average quantity (18) due to the superposition hypothesis (see text) very well, whereas the correspondence is not as good in the spin-flip case. This is due to the fact that the hole completely passes through the domain wall while the spin flip does not.

converge to the corresponding averaged profile of Eq. (18). This is due to the fact that the spin-flip defect dynamics occurs on the same time scale as the domain-wall dynamics and that, at least up to the maximum simulated times, the spin flip does not completely pass through the domain wall. Besides this, it is clear that the beating is not reduced by the spin-flip defect because, according to the superposition hypothesis, one has to add magnetizations of next-nearest neighbor sites [$d = 2$ in Eq. (18)] for which the beating oscillations are in sync.

C. Correlation functions

The above intuitive notion of a superposition of left- and right-moving defects works well when it comes to the magnetization profile. Additionally, one can see how it fares when considering experimentally relevant connected two-point correlators around the domain wall,

$$\zeta_{\Delta x} := \langle \hat{S}_i^z \hat{S}_j^z \rangle - \langle \hat{S}_i^z \rangle \langle \hat{S}_j^z \rangle \quad \text{and} \quad (19a)$$

$$\chi_{\Delta x} := \langle \hat{S}_i^x \hat{S}_j^x \rangle, \quad (19b)$$

where $i = L/2 + 1 - \Delta x$ and $j = L/2 + \Delta x$. For clarity, $\zeta_{\Delta x}$ and $\chi_{\Delta x}$ will refer to the clean case, while in the case of a hole or a spin flip, both two-point correlators will be augmented with the superscript “h” or “f,” respectively. Moreover, it is to be noted that, in this model, one always has $\langle \hat{S}_j^y \rangle = \langle \hat{S}_j^x \rangle = 0$,

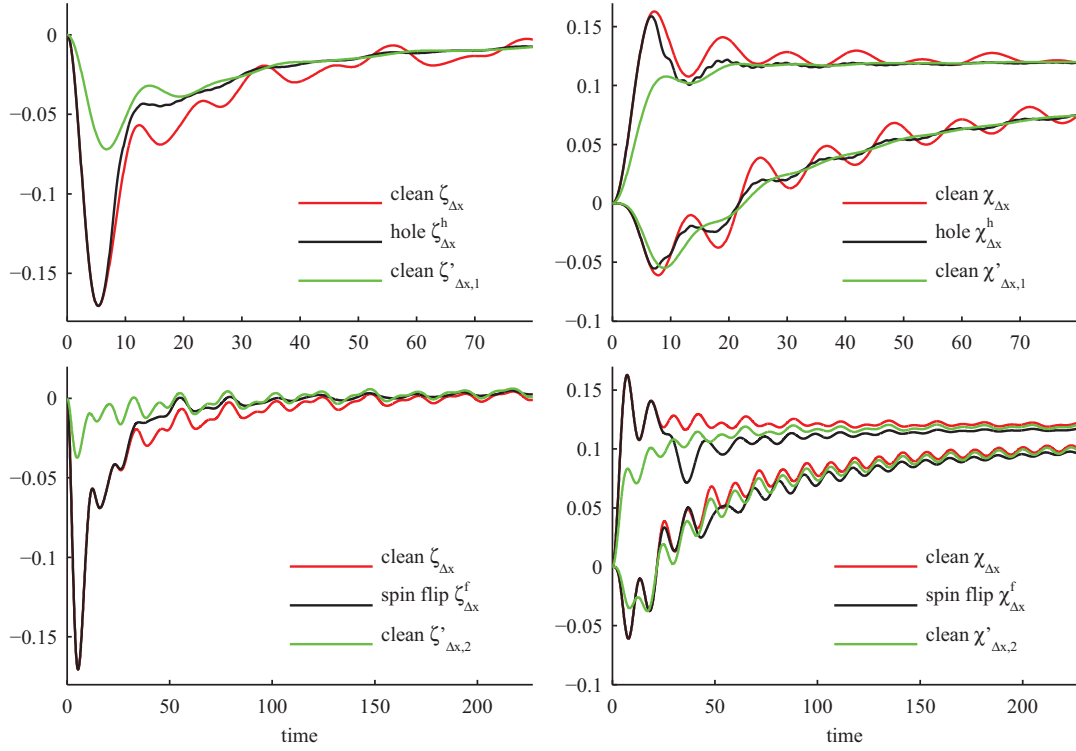


FIG. 7. (Color online) (Left) Connected S^z - S^z correlators (19) with $\Delta x = 1$ ($t = 1$, $U = 15$, $L = 320$, $j_h = L/2 - 16$, $j_f = L/2 - 8$). The results show that the correlator $\zeta_{\Delta x}^h$ for the hole case deviates quite strongly from the same correlator $\zeta_{\Delta x}$ in the clean case. But, after the point in time where the hole has passed the domain wall, $\zeta_{\Delta x}^h$ agrees very well with $\zeta'_{\Delta x,1}$ [Eq. (20)] which is computed from the clean correlator $\zeta_{\Delta x}^h$ by superimposing results for a small spatial shift. The coincidence of $\zeta_{\Delta x}^f$ and $\zeta'_{\Delta x,2}$ is not as good, indicating that holes have much less influence on the spin dynamics than spin-flip defects. (Right) The same conclusion holds for the S^x - S^x correlators. Also here, $\chi_{\Delta x}^h$ agrees very well with $\chi'_{\Delta x,1}$ [Eq. (21)], while deviations of $\chi_{\Delta x}^f$ from $\chi'_{\Delta x,2}$ are still appreciable and comparable to the deviation from $\chi_{\Delta x}$.

hence the apparent difference in the definitions of $\zeta_{\Delta x}$ and $\chi_{\Delta x}$. Based on the superposition in Eq. (17), the two-point correlators for the defect case should agree with

$$\begin{aligned} \zeta'_{\Delta x,d} := & \frac{1}{2} (\langle \psi_c | \hat{S}_i^z \hat{S}_j^z | \psi_c \rangle + \langle \psi_c | \hat{S}_{i+d}^z \hat{S}_{j+d}^z | \psi_c \rangle) \\ & + \frac{1}{4} (\langle \psi_c | \hat{S}_i^z | \psi_c \rangle + \langle \psi_c | \hat{S}_{i+d}^z | \psi_c \rangle) \\ & \times (\langle \psi_c | \hat{S}_j^z | \psi_c \rangle + \langle \psi_c | \hat{S}_{j+d}^z | \psi_c \rangle), \end{aligned} \quad (20)$$

and

$$\chi'_{\Delta x,d} := \frac{1}{2} (\langle \psi_c | \hat{S}_i^x \hat{S}_j^x | \psi_c \rangle + \langle \psi_c | \hat{S}_{i+d}^x \hat{S}_{j+d}^x | \psi_c \rangle), \quad (21)$$

respectively. As above, we have again $d = 1$ for the hole case and $d = 2$ for the spin-flip case. As shown in Fig. 7, $\zeta_{\Delta x}^h$ ($\chi_{\Delta x}^h$) agrees well with $\zeta'_{\Delta x,1}$ ($\chi'_{\Delta x,1}$) for longer times, and this behavior supports the idea that the hole indeed passes through the domain wall completely, leading to a smoothening effect as dictated by the superposition concept of Eq. (17). However, in the case of the spin flip, the explanatory power of this concept is again not as impressive.

D. Particle density is independent of spin dynamics

Next, the particle density is considered. In the case of the clean domain-wall state and the case of a domain wall with a spin-flip defect, the particle density is simply constant with exactly one particle per site for all times.

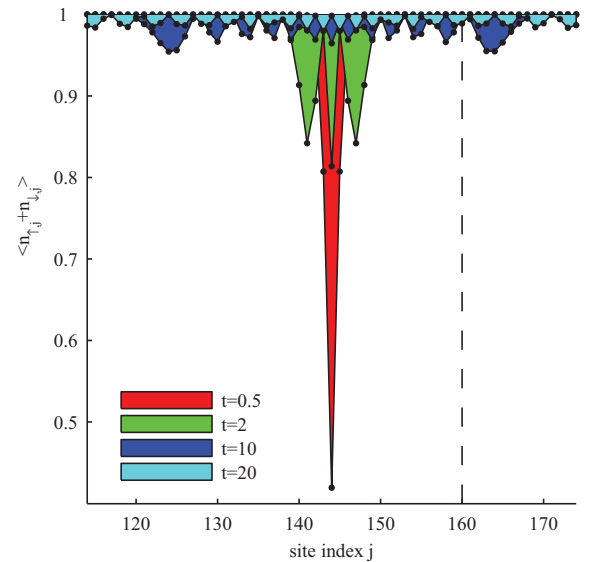


FIG. 8. (Color online) Dynamics of the particle density $\langle \hat{n}_{\uparrow,j} + \hat{n}_{\downarrow,j} \rangle$ for the domain-wall state with a hole defect ($t = 1$, $U = 15$, $L = 320$, $j_h = L/2 - 16$). The particle density is symmetric with respect to the initial position of the hole and shows now particular features at the domain wall (dashed line). As discussed in the text, the density dynamics is in fact completely independent of the spin dynamics (the converse is of course not the case).

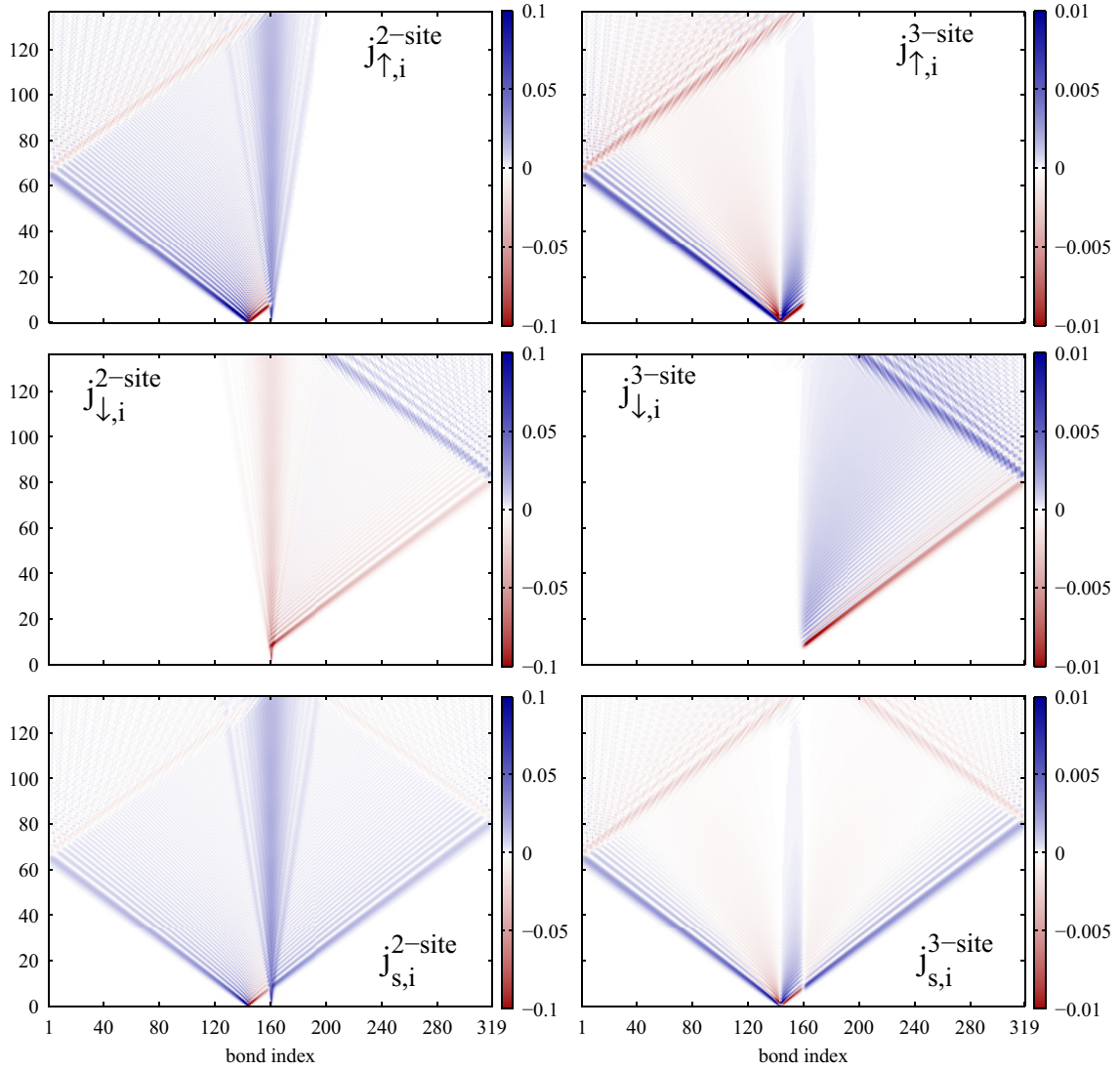


FIG. 9. (Color online) Currents (22) for a domain wall with a hole defect ($t = 1$, $U = 15$, $L = 320$, $j_h = L/2 - 16$). The figures show from top to bottom the density currents for “ \uparrow ” bosons, “ \downarrow ” bosons, and the spin current. On the left, the contributions of the dominating two-site terms (24) are shown. The contributions (25) of the three-site hopping terms [$\hat{H}_{3\text{-site}}$ in the t - J Hamiltonian (7)] are given on the right. For the given U , they are suppressed by one order of magnitude. The suppression is stronger for larger U .

For the hole defect, one might naively expect some nontrivial effects, like reflection of the hole from the domain wall, etc. However, as the Hamiltonian terms that change the particle density distribution are species independent ($t_\uparrow = t_\downarrow$), the hole dynamics is completely independent of the spin dynamics. This is visualized in Fig. 8 where the initial position of the domain wall is marked by a dashed line. Indeed, $\langle \hat{n}_{\uparrow,j} + \hat{n}_{\downarrow,j} \rangle$ is symmetric around the initial position of the hole for all times and shows no special features in the domain-wall region.

E. Quantification of higher-order effects by spin and density currents

Finally, let us consider the spin and density (“charge”) currents during the dynamics. They correspond to specific short-range correlators which are in principle accessible in experiments. Besides offering another perspective on the evolution of the domain wall and the defects, we can use it

to quantify the effect of the higher-order (three-site) hopping terms $\hat{H}_{3\text{-site}}$ in the effective model (7). The density current $\hat{j}_{\sigma,i}$ for boson species “ σ ” at a bond $(i, i + 1)$, denoted by the bond index i , is defined as the time derivative of the total particle number $\sum_{j>i} \hat{n}_{\sigma,j}$ to the right of that bond. For the t - J model (7), one obtains

$$\begin{aligned} \hat{j}_{\sigma,i} = & -it_\sigma(\hat{b}_{\sigma,i}^\dagger \hat{b}_{\sigma,i+1} - \text{H.c.}) + i \frac{J_\perp}{2} (\hat{S}_i^\sigma \hat{S}_{i+1}^{-\sigma} - \text{H.c.}) \\ & + \hat{j}_{\sigma,i}^a + \hat{j}_{\sigma,i}^b + \hat{j}_{\sigma,i}^c, \end{aligned} \quad (22)$$

where

$$\begin{aligned} \hat{j}_{\sigma,i}^a = & -\frac{it_\sigma^2}{V} (\hat{b}_{\sigma,i-1}^\dagger \hat{n}_{-\sigma,i} \hat{b}_{\sigma,i+1} + \hat{b}_{\sigma,i}^\dagger \hat{n}_{-\sigma,i+1} \hat{b}_{\sigma,i+2} - \text{H.c.}), \\ \hat{j}_{\sigma,i}^b = & -\frac{it_\uparrow t_\downarrow}{V} (\hat{b}_{-\sigma,i-1}^\dagger \hat{S}_i^\sigma \hat{b}_{\sigma,i+1} + \hat{b}_{\sigma,i}^\dagger \hat{S}_{i+1}^{-\sigma} \hat{b}_{-\sigma,i+2} - \text{H.c.}), \\ \hat{j}_{\sigma,i}^c = & -\frac{2it_\sigma^2}{U_\sigma} (\hat{b}_{\sigma,i-1}^\dagger \hat{n}_{\sigma,i} \hat{b}_{\sigma,i+1} + \hat{b}_{\sigma,i}^\dagger \hat{n}_{\sigma,i+1} \hat{b}_{\sigma,i+2} - \text{H.c.}). \end{aligned}$$

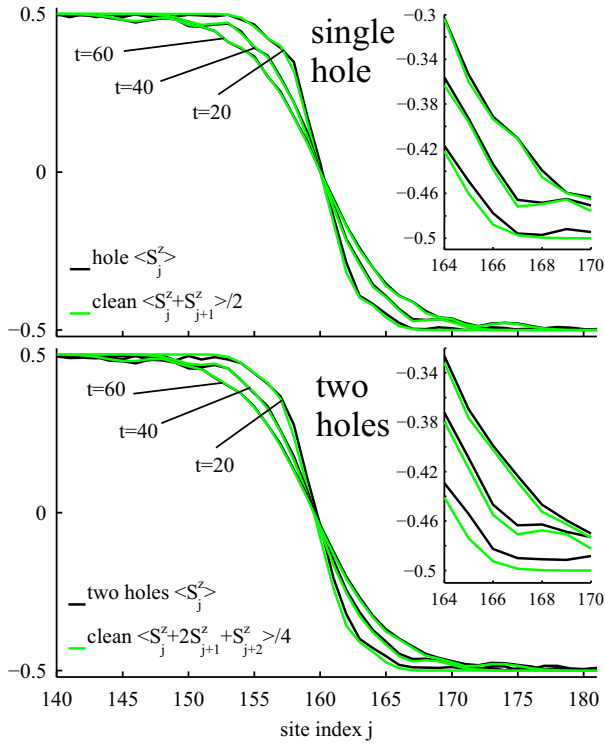


FIG. 10. (Color online) Investigating the effect of two holes with initial positions $j_{h_1} = L/2 - 16$ and $j_{h_2} = L/2 - 8$ ($t = 1, U = 15$). The magnetization profiles at long times indicate that, like in the single-hole case [(17)], the two-hole dynamics can be approximated as a superposition of orthogonal states which correspond to spatial shifts of the clean domain-wall state; see the text and Eq. (27).

The spin current is then simply

$$\hat{J}_{s,i} = \frac{1}{2}(\hat{J}_{\uparrow,i} - \hat{J}_{\downarrow,i}). \quad (23)$$

In Fig. 9 the two-site and three-site contributions to the charge and spin currents,

$$\hat{J}_{\sigma,i}^{2\text{-site}} = -it_{\sigma}(\hat{b}_{\sigma,i}^{\dagger}\hat{b}_{\sigma,i+1} - \text{H.c.}) + i\frac{J_{\perp}}{2}(\hat{S}_i^{\sigma}\hat{S}_{i+1}^{-\sigma} - \text{H.c.}), \quad (24)$$

$$\hat{J}_{\sigma,i}^{3\text{-site}} = \hat{J}_{\sigma,i}^a + \hat{J}_{\sigma,i}^b + \hat{J}_{\sigma,i}^c, \quad (25)$$

and

$$\hat{J}_{s,i}^{m\text{-site}} = \hat{J}_{\uparrow,i}^{m\text{-site}} - \hat{J}_{\downarrow,i}^{m\text{-site}}, \quad (26)$$

with $m = 2$ or 3 are shown for $t = 1$ and $U = 15$. The currents offer another deeper look at the dynamics, visualizing the flow of particles and magnetizations. For the given parameters, the contributions of the effective three-site hopping terms is one order of magnitude below that of the two-site terms. Their effect decreases further for larger U .

F. Multiple defects

Now that the effect of a single-hole defect on the domain-wall evolution is understood, one may be interested in investigating, on the one hand, the effect of two simultaneously present holes, and on the other hand, whether or not such two-hole defects interact with each other. For times when

the left- and right-moving parts of the holes are sufficiently separated, one can once again intuitively describe the system by a superposition of orthogonal states,

$$|\psi\rangle = \frac{1}{2}(|\psi_{\ell\ell}\rangle + |\psi_{\ell r}\rangle + |\psi_{r\ell}\rangle + |\psi_{rr}\rangle), \quad (27)$$

where $|\psi_{\ell\ell}\rangle$ describes two holes moving to the left, and thus they never interact with the domain wall, $|\psi_{\ell r}\rangle$ ($|\psi_{r\ell}\rangle$) is the state where the left (right) hole is moving to the left and never interacts with the wall while the right (left) hole has passed through the wall, shifting it by one site to the left, and $|\psi_{rr}\rangle$ describes the state where both holes have traveled to the right and passed through the domain wall, shifting it by two sites to the left. This leads to the following magnetization profile for the two-hole state:

$$\begin{aligned} \langle\psi|\hat{S}_j^z|\psi\rangle &= \frac{1}{4}(\langle\psi_{\ell\ell}|\hat{S}_j^z|\psi_{\ell\ell}\rangle + \langle\psi_{\ell r}|\hat{S}_j^z|\psi_{\ell r}\rangle \\ &\quad + \langle\psi_{r\ell}|\hat{S}_j^z|\psi_{r\ell}\rangle + \langle\psi_{rr}|\hat{S}_j^z|\psi_{rr}\rangle) \\ &\approx \frac{1}{4}(\langle\psi_c|\hat{S}_j^z|\psi_c\rangle + 2\langle\psi_c|\hat{S}_{j+1}^z|\psi_c\rangle \\ &\quad + \langle\psi_c|\hat{S}_{j+2}^z|\psi_c\rangle). \end{aligned} \quad (28)$$

The magnetization profiles for a single hole at site $j_h = L/2 - 16$ and two holes at sites $j_{h_1} = L/2 - 16$ and $j_{h_2} = L/2 - 8$ are shown in Fig. 10 along with the corresponding curves due to Eqs. (18) and (28) at three different points in time. One observes that, especially at longer times, the magnetization profile of the two-hole state matches remarkably well the curve due to Eq. (28). The smaller deviations beyond this effect, are roughly proportional to the number of holes and decrease when t/J is increased (larger U) as discussed in the following.

G. Reducing the effects of holes by increasing t/J

The effect of holes depends on the relative velocity of the holes with respect to the domain wall. A relatively faster hole has a smaller effect on the domain-wall dynamics, as the interaction time between the hole and the domain wall is smaller in such a case. Alternatively, a relatively slower hole will have more time to distort the dynamics of the domain wall, and thus the dynamics will deviate stronger from the superposition behavior such as that described by Eq. (18). Figure 11 shows the magnetization profiles and two-point correlators over time for the single-hole state ($j_h = L/2 - 16$) for different values of U . One sees that the smaller U is, and thus the slower the hole is relative to the domain-wall melting, the larger the deviation of the above observables from their superposition curves given in Eq. (18) for the magnetization profile and Eqs. (20) and (21) for the two-point correlators. On the other hand, for very large $U = 60$, the agreement between the magnetization profile and Eq. (18), and between $\zeta_{\Delta x}^h$ ($\chi_{\Delta x}^h$) and $\zeta'_{\Delta x,1}$ ($\chi'_{\Delta x,1}$) is excellent after a certain short time $\sim 1/t$ corresponding to the phase where the hole passes the domain-wall region.

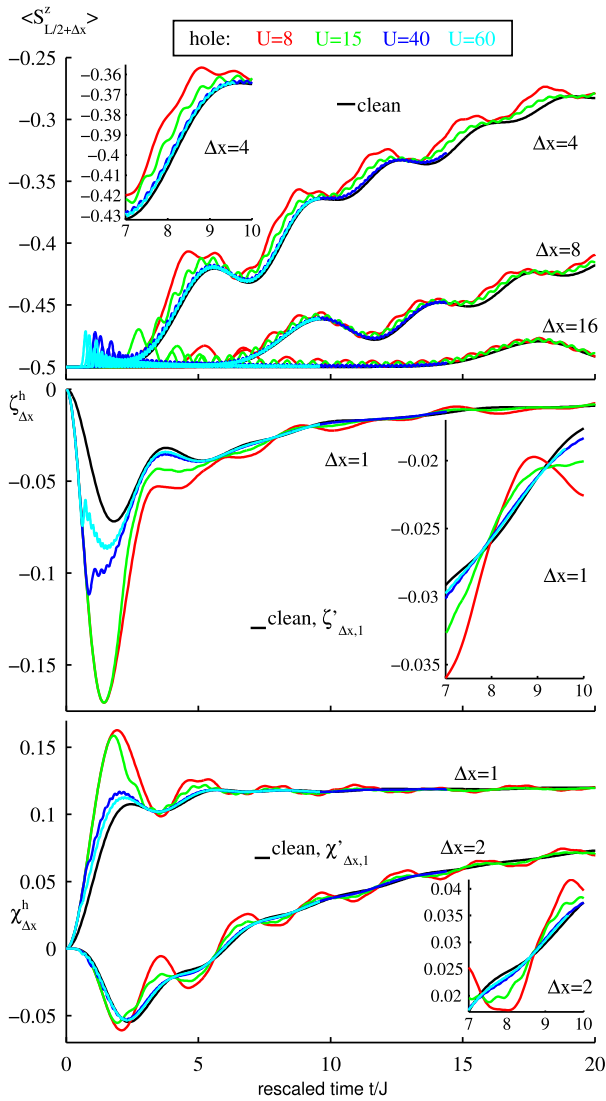


FIG. 11. (Color online) Comparison of the effect of a hole defect on two-point correlation functions in the domain-wall dynamics ($t = 1$, $L = 320$, $j_h = L/2 - 16$) at different values of the on-site repulsion U for the t - J model (7). The greater the value of U , the faster the hole propagates relative to the domain-wall front, and thus the shorter the interaction time between the hole and the domain wall, which in turn leads to greater agreement between the hole-case dynamics and the approximation due to the superposition hypothesis (27).

VI. CONCLUSION

The numerical simulations and the analysis of disturbances due to defects that we have provided in this paper give useful insights concerning future experiments using ultracold atomic gases to simulate the dynamics of quantum magnets. Specifically, we have investigated domain-wall melting in the two-species Bose-Hubbard model in the presence of hole and spin-flip defects. For large on-site repulsions, the model maps to a hard-core boson t - J model with particular effective three-site hopping terms. The study is based on tDMRG calculations using the Krylov approach. It is concluded, through measurements of magnetization profiles and two-point

correlators, that a domain wall with a single-hole defect evolves into a superposition of two (approximately) orthogonal states, where the domain-wall melting becomes equivalent to that of two domain walls, one of which is shifted towards the initial position of the hole by one site. The situation of multiple holes can be described in a similar manner. The leading effect of holes hence corresponds to a certain averaging of spatially shifted observables that can be taken account of. Further smaller deviations due to holes diminish with increasing repulsion U as the hole dynamics gets faster and faster in comparison to the domain-wall evolution. Whereas hole defects are in this sense not so problematic, the effect of spin-flip defects is more severe as they evolve on the same time scale as the domain wall itself. Although it is still useful, this limits the explanatory power of the superposition picture for spin-flip defects. For the experimental investigations this has implications on the preparation of the initial states. In particular, our results suggest that the second preparation scheme (see introduction), based on cooling with species- and position-dependent chemical potentials, should be favorable over the first scheme that is based on inducing spin flips in parts of the system.

ACKNOWLEDGMENTS

The authors are grateful to Immanuel Bloch, Marc Cheneau, Christian Gross, and Takeshi Fukuhara (all of LMU Physik and MPQ Garching) for fruitful and insightful discussions. This work has been supported through the FP7/Marie-Curie [Grant No. 321918 (J.C.H.)], the Australian Research Council [Grant No. CE110001013 (I.P.M.)], and DFG FOR 801 (US and J.C.H.).

APPENDIX: CONVERGENCE OF THE DMRG SIMULATIONS

All simulations in this paper are carried out using tDMRG [44–46] in the Krylov approach [47–49] (see also [50]) with time steps of a certain size Δt . In the tDMRG, the evolved many-body state is approximated as a so-called matrix product state at all times which is achieved by repeated truncations of small Schmidt coefficients. The accuracy of the simulation is controlled using a threshold ϵ on the fidelity loss due to truncations [42,43,65]. Let $|\psi_t\rangle$ be the state for time t . In every time step, we apply the Hamiltonian \hat{H} multiple times to $|\psi_t\rangle$, to obtain matrix product state representations of the Krylov vectors $\{|\psi_t\rangle, \hat{H}|\psi_t\rangle, \hat{H}^2|\psi_t\rangle, \dots\}$. Controlling errors due to DMRG truncations of the Krylov vectors and due to a restriction on the number of used Krylov vectors, we implement the time evolution in the Krylov subspace to obtain a new matrix product state $|\psi_{t+\Delta t}\rangle$ such that $r^2 := \|\hat{U}_{\Delta t}|\psi_t\rangle - |\psi_{t+\Delta t}\rangle\|^2 / \|\hat{U}_{\Delta t}|\psi_t\rangle + |\psi_{t+\Delta t}\rangle\|^2 < \epsilon$, where $\hat{U}_{\Delta t}$ is the (exact) time-evolution operator for a single time step. For the computation of a bound on r , we use some very conservative assumptions on the decay of the coefficients in the expansion of the evolved state in the Krylov basis.

The size of the time step was chosen such that the number of required Krylov vectors was roughly 10. In particular, we chose

$\Delta t = 0.01/t$ and $\Delta t = 0.1/t$ for the Bose-Hubbard (BH) and the t - J model, respectively. For all analyzed observables one should ensure convergence with respect to the fidelity threshold ϵ . As described in the following we determined these parameters such that the data presented in the figures is quasixact.

For the t - J model, a lattice of $L = 320$ sites was used and the results presented in the main text are based on a fidelity threshold of $\epsilon = 10^{-6}$. In order to check for convergence, several runs are carried out at different ϵ for the single-hole state where the hole is located at $L/2 - 1$ (this state is found to be the most challenging numerically among all initial states simulated) at $U = 15$ and $t = 1$. Once again, the observable

$\langle \hat{S}_{L/2+\Delta x}^z \rangle$ and the two-point correlators $\zeta_{\Delta x}^h$ and $\chi_{\Delta x}^h$ [Eq. (19)] for various Δx are taken into account, and as Fig. 12 shows, very good convergence is achieved at a fidelity threshold of 10^{-6} .

Furthermore, in order to validate the comparison in Fig. 5, one must ascertain the convergence of the corresponding BH-model results, where a fidelity threshold of 10^{-6} is also used. Figure 13 shows the observable $\langle \hat{S}_{L/2+\Delta x}^z \rangle$ and the two-point correlators $\zeta_{\Delta x}^h$ and $\chi_{\Delta x}^h$ at various Δx , and, indeed, a fidelity threshold of 10^{-6} exhibits very good convergence.

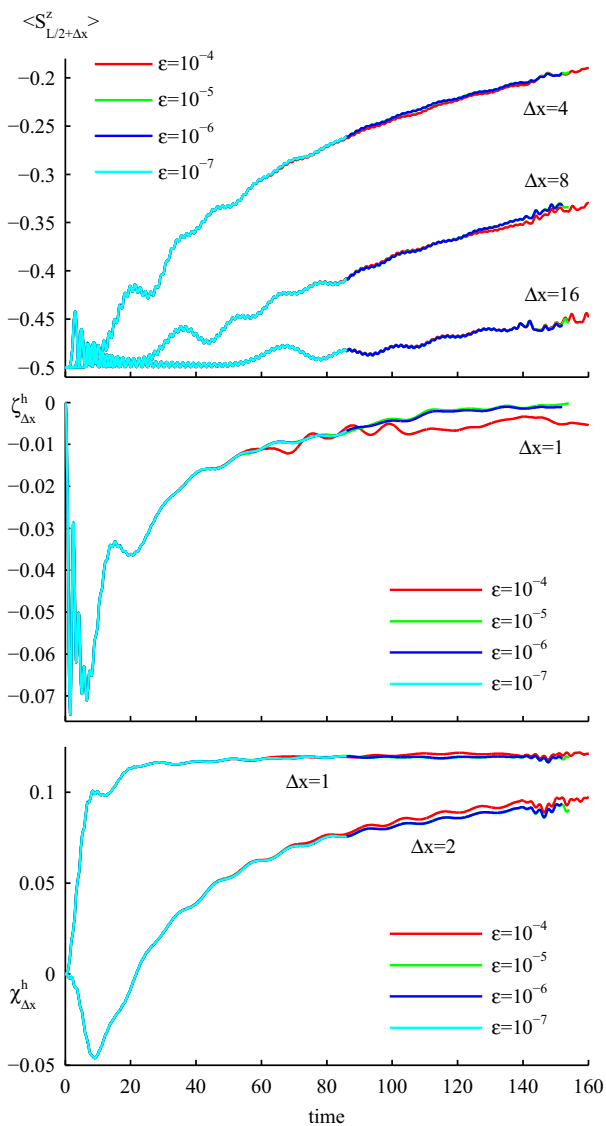


FIG. 12. (Color online) Convergence of tDMRG results with respect to the fidelity threshold ϵ , for magnetizations and two-point correlators (19) for the t - J model specified in Eq. (7) ($L = 320$, $t = 1$, $U = 15$). Here, the initial state is the domain wall with a hole defect at site $L/2 - 1$. Good convergence is achieved at a fidelity threshold of 10^{-6} .

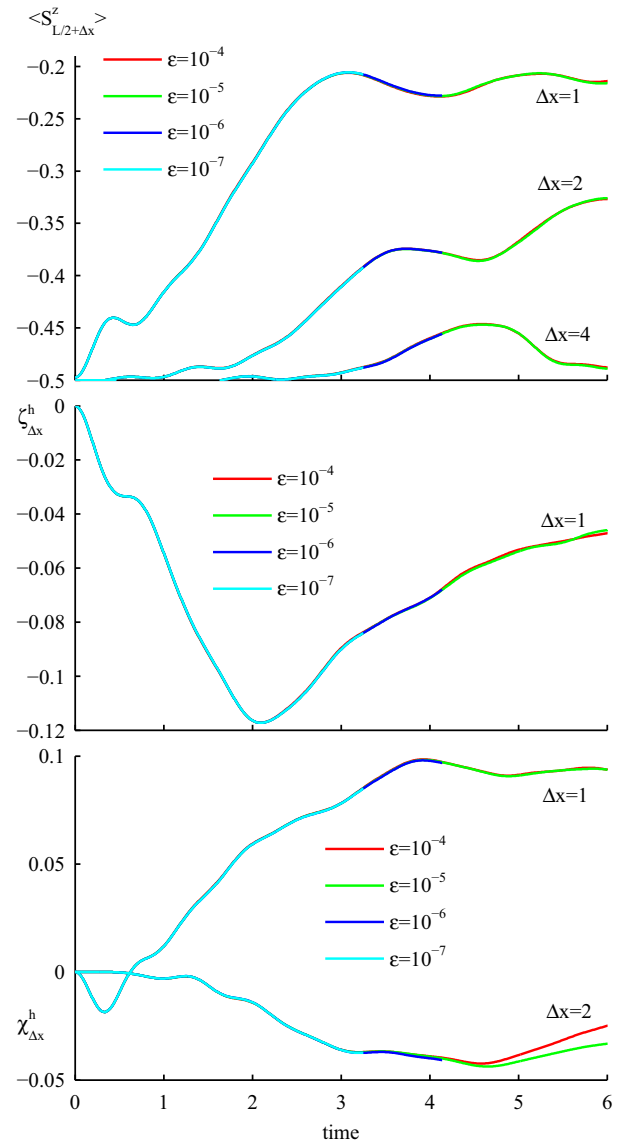


FIG. 13. (Color online) Convergence of tDMRG results with respect to the fidelity threshold ϵ , for magnetizations and two-point correlators (19) for the two-species BH model specified in Eq. (2) ($L = 20$, $t = 1$, $U = 8$). The initial state is the domain wall with a hole defect at site $L/2 - 1$ [Eq. (14)]. Good convergence is achieved at a fidelity threshold of 10^{-6} .

- [1] W. Ketterle, D. S. Durfee, and D. M. Stamper-Kurn, [arXiv:cond-mat/9904034](#).
- [2] I. Bloch, J. Dalibard, and W. Zwerger, *Rev. Mod. Phys.* **80**, 885 (2008).
- [3] M. Greiner, O. Mandel, T. Esslinger, T. W. Hänsch, and I. Bloch, *Nature (London)* **415**, 39 (2002).
- [4] G. Modugno, G. Roati, F. Riboli, F. Ferlaino, R. J. Brecha, and M. Inguscio, *Science* **297**, 2240 (2002).
- [5] T. Stöferle, H. Moritz, C. Schori, M. Köhl, and T. Esslinger, *Phys. Rev. Lett.* **92**, 130403 (2004).
- [6] R. Jördens, N. Strohmaier, K. Gunter, H. Moritz, and T. Esslinger, *Nature (London)* **455**, 204 (2008).
- [7] G. Roati, C. D’Errico, L. Fallani, M. Fattori, C. Fort, M. Zaccanti, G. Modugno, M. Modugno, and M. Inguscio, *Nature (London)* **453**, 895 (2008).
- [8] U. Schneider, L. Hackermüller, S. Will, T. Best, I. Bloch, T. A. Costi, R. W. Helmes, D. Rasch, and A. Rosch, *Science* **322**, 1520 (2008).
- [9] T. Esslinger, *Annu. Rev. Condens. Matter Phys.* **1**, 129 (2010).
- [10] F. Serwane, G. Zürn, T. Lompe, T. B. Ottenstein, A. N. Wenz, and S. Jochim, *Science* **332**, 336 (2011).
- [11] I. Bloch, J. Dalibard, and S. Nascimbène, *Nat. Phys.* **8**, 267 (2012).
- [12] U. Schneider, L. Hackermüller, J. P. Ronzheimer, S. Will, S. Braun, T. Best, I. Bloch, E. Demler, S. Mandt, D. Rasch, and A. Rosch, *Nat. Phys.* **8**, 213 (2012).
- [13] J. P. Ronzheimer, M. Schreiber, S. Braun, S. S. Hodgman, S. Langer, I. P. McCulloch, F. Heidrich-Meisner, I. Bloch, and U. Schneider, *Phys. Rev. Lett.* **110**, 205301 (2013).
- [14] L. Sanchez-Palencia, D. Clément, P. Lugan, P. Bouyer, G. V. Shlyapnikov, and A. Aspect, *Phys. Rev. Lett.* **98**, 210401 (2007).
- [15] J. Billy, V. Josse, Z. Zuo, A. Bernard, B. Hambrecht, P. Lugan, D. Clement, L. Sanchez-Palencia, P. Bouyer, and A. Aspect, *Nature (London)* **453**, 891 (2008).
- [16] S. S. Kondov, W. R. McGehee, J. J. Zirbel, and B. DeMarco, *Science* **334**, 66 (2011).
- [17] W. S. Bakr, J. I. Gillen, A. Peng, S. Fölling, and M. Greiner, *Nature (London)* **462**, 74 (2009).
- [18] W. S. Bakr, A. Peng, E. M. Tai, R. Ma, J. Simon, J. I. Gillen, S. Fölling, L. Pollet, and M. Greiner, *Science* **329**, 547 (2010).
- [19] J. F. Sherson, C. Weitenberg, M. Endres, M. Cheneau, I. Bloch, and S. Kuhr, *Nature (London)* **467**, 68 (2010).
- [20] E. W. Streed, A. Jechow, B. G. Norton, and D. Kielpinski, *Nat. Commun.* **3**, 933 (2012).
- [21] P. Würtz, T. Langen, T. Gericke, A. Koglbauer, and H. Ott, *Phys. Rev. Lett.* **103**, 080404 (2009).
- [22] C. Weitenberg, M. Endres, J. F. Sherson, M. Cheneau, P. Schauß, T. Fukuhara, I. Bloch, and S. Kuhr, *Nature (London)* **471**, 319 (2011).
- [23] R. P. Feynman, *Int. J. Theor. Phys.* **21**, 467 (1982).
- [24] I. Buluta and F. Nori, *Science* **326**, 108 (2009).
- [25] A. B. Kuklov and B. V. Svistunov, *Phys. Rev. Lett.* **90**, 100401 (2003).
- [26] L. M. Duan, E. Demler, and M. D. Lukin, *Phys. Rev. Lett.* **91**, 090402 (2003).
- [27] J. J. García-Ripoll and J. I. Cirac, *New J. Phys.* **5**, 76 (2013).
- [28] E. Altman, W. Hofstetter, E. Demler, and M. D. Lukin, *New J. Phys.* **5**, 113 (2013).
- [29] T. Barthel, C. Kasztelan, I. P. McCulloch, and U. Schollwöck, *Phys. Rev. A* **79**, 053627 (2009).
- [30] T. Fukuhara, A. Kantian, M. Endres, M. Cheneau, P. Schass, S. Hild, C. Gross, U. Schollwöck, T. Giamarchi, I. Bloch, and S. Kuhr, *Nat. Phys.* **9**, 235 (2013).
- [31] I. G. Gochev, *JETP Lett.* **26**, 127 (1977).
- [32] G. Gochev, *Sov. Phys. JETP* **58**, 115 (1983).
- [33] T. Antal, Z. Rácz, A. Rákos, and G. M. Schütz, *Phys. Rev. E* **59**, 4912 (1999).
- [34] V. Hunyadi, Z. Racz, and L. Sasvari, *Phys. Rev. E* **69**, 066103 (2004).
- [35] D. Gobert, C. Kollath, U. Schollwöck, and G. M. Schütz, *Phys. Rev. E* **71**, 036102 (2005).
- [36] J. Mossel and J.-S. Caux, *New J. Phys.* **12**, 055028 (2010).
- [37] S. Jesenko and M. Znidaric, *Phys. Rev. B* **84**, 174438 (2011).
- [38] V. Zauner, M. Ganahl, H. G. Evertz, and T. Nishino, [arXiv:1207.0862](#).
- [39] J. Lancaster and A. Mitra, *Phys. Rev. E* **81**, 061134 (2010).
- [40] Z. Cai, L. Wang, X. C. Xie, U. Schollwöck, X. R. Wang, M. DiVentra, and Y. Wang, *Phys. Rev. B* **83**, 155119 (2011).
- [41] Personal communication with the Bloch group at MPQ, Garching.
- [42] S. R. White, *Phys. Rev. Lett.* **69**, 2863 (1992).
- [43] S. R. White, *Phys. Rev. B* **48**, 10345 (1993).
- [44] G. Vidal, *Phys. Rev. Lett.* **93**, 040502 (2004).
- [45] S. R. White and A. E. Feiguin, *Phys. Rev. Lett.* **93**, 076401 (2004).
- [46] A. J. Daley, C. Kollath, U. Schollwöck, and G. Vidal, *J. Stat. Mech.* (2004) P04005.
- [47] A. E. Feiguin and S. R. White, *Phys. Rev. B* **72**, 020404(R) (2005).
- [48] J. J. García-Ripoll, *New J. Phys.* **8**, 305 (2006).
- [49] I. P. McCulloch, *J. Stat. Mech.* (2007) P10014.
- [50] P. Schmitteckert, *Phys. Rev. B* **70**, 121302 (2004).
- [51] T. Giamarchi, *Quantum Physics in One Dimension* (Oxford University Press, Oxford, 2004).
- [52] B. Sutherland, *Beautiful Models* (World Scientific, Singapore, 2004).
- [53] V. E. Korepin and N. M. Bogoliubov, *Quantum Inverse Scattering Method and Correlation Functions* (Cambridge University Press, Cambridge, 1993).
- [54] W. Heisenberg, *Zeitschrift für Physik* **49**, 619 (1928).
- [55] H. Bethe, *Zeitschrift für Physik A* **71**, 205 (1931).
- [56] O. Mandel, M. Greiner, A. Widera, T. Rom, T. W. Hänsch, and I. Bloch, *Phys. Rev. Lett.* **91**, 010407 (2003).
- [57] S. Fölling, S. Trotzky, P. Cheinet, M. Feld, R. Saers, A. Widera, T. Müller, and I. Bloch, *Nature (London)* **448**, 1029 (2007).
- [58] S. Trotzky, P. Cheinet, S. Fölling, M. Feld, U. Schnorrberger, A. M. Rey, A. Polkovnikov, E. A. Demler, M. D. Lukin, and I. Bloch, *Science* **319**, 295 (2008).
- [59] See Supplemental Material at <http://link.aps.org/supplemental/10.1103/PhysRevA.89.063603> for animations that show the evolution of the magnetization profiles $\langle \hat{S}_j^z(t) \rangle$ of states with defects in direct comparison to the clean domain-wall state ($t = 1, U = 15, L = 320, j_h = L/2 - 16, j_f = L/2 - 8$).

- [60] J. Spalek and A. M. Oleś, *Physica B* **375**, 86 (1977).
- [61] K. A. Chao, J. Spalek, and A. M. Oleś, *J. Phys. C* **10**, L271 (1977).
- [62] K. A. Chao, J. Spalek, and A. M. Oleś, *Phys. Rev. B* **18**, 3453 (1978).
- [63] P. W. Anderson, *Science* **235**, 1196 (1987).
- [64] E. Dagotto, *Rev. Mod. Phys.* **66**, 763 (1994).
- [65] U. Schollwöck, *Rev. Mod. Phys.* **77**, 259 (2005).
- [66] J. M. Luttinger, *J. Math. Phys.* **4**, 1154 (1963).
- [67] F. D. M. Haldane, *J. Phys. C: Solid State Phys.* **14**, 2585 (1981).

Chapter 7

Fractional excitations in cold atomic gases

In strongly-interacting quantum many-body systems, excitations can carry fractional quantum numbers such as the charge- $e/3$ Laughlin quasiparticle that gives rise to the fractional quantum Hall effect. One-dimensional ultracold-atomic systems have been experimentally shown to exhibit fundamental excitations in the broken-symmetry phase in the form of domain walls with an effective fractional charge. We study the tilted Bose-Hubbard model in its symmetry-broken phase where a fundamental excitation is equivalent to moving a single boson to its neighboring site, which in turn corresponds to the creation of two closely-bound domain walls. Using perturbation theory, we study the creation of fractional excitations in this setup, and provide numerical verification using t -DMRG.

- *Fractional excitations in cold atomic gases*
Jens Honer, **Jad C. Halimeh**, Ian P. McCulloch, Ulrich Schollwöck, and Hans Peter Büchler
Phys. Rev. A **86**, 051606(R) (2012)

Fractional excitations in cold atomic gases

J. Honer,¹ J. C. Halimeh,² I. McCulloch,³ U. Schollwöck,² and H. P. Büchler¹

¹*Institute for Theoretical Physics III, University of Stuttgart, Stuttgart, Germany*

²*Department of Physics and Arnold Sommerfeld Center for Theoretical Physics, Ludwig-Maximilians-Universität München, Munich, Germany*

³*Centre for Engineered Quantum Systems, School of Mathematics and Physics, University of Queensland, Brisbane 4072, Australia*

(Received 4 October 2012; published 27 November 2012)

We study the behavior of excitations in the tilted one-dimensional Bose-Hubbard model. In the phase with broken symmetry, fundamental excitations are domain walls which show fractional statistics. Using perturbation theory, we derive an analytic model for the time evolution of these fractional excitations, and demonstrate the existence of a repulsively bound state above a critical center-of-mass momentum. The validity of the perturbative analysis is confirmed by the use of time-adaptive density-matrix renormalization group simulations. These findings open the path for the experimental detection of fractional particles in cold atomic gases.

DOI: [10.1103/PhysRevA.86.051606](https://doi.org/10.1103/PhysRevA.86.051606)

PACS number(s): 67.85.-d, 66.35.+a, 75.10.Pq

Excitations carrying fractional quantum numbers are one of the most intriguing features of strongly interacting many-body systems. Arguably the most celebrated of those is the charge $e/3$ Laughlin quasiparticle responsible for the fractional quantum Hall effect. Much effort is devoted to finding novel phases with even more exotic excitations such as non-Abelian anyons and fractional statistics in three-dimensional systems. In the quest for the experimental realization of such strongly correlated phases, cold atomic gases with their clean and controllable environment are a promising candidate and testing ground [1]. A first step in this direction marks the recently observed phase transition in a one-dimensional cold atomic system [2], where the fundamental excitations in the broken-symmetry phase are domain walls carrying an effective fractional charge. In this Rapid Communication, we investigate the creation and detection of these fractional excitations in the one-dimensional tilted Bose-Hubbard model.

A variety of theoretical proposals in cold atomic gases focus on the realization of strongly correlated phases with fractional excitations, such as models supporting spin-liquid phases [3], as well as Kitaev's toric code with Abelian anyonic excitations [4–6], and systems in large effective magnetic fields [7,8] exhibiting fractional quantum Hall states [9–15]. These proposals are based on standard experimental tools presently available in the context of quantum simulation (see Ref. [16] for a review). Especially, the latest development of experiments [17,18] with single-site readout and addressability in optical lattices has opened the path for the observation of a novel quantum phase transition in tilted optical lattices [2,19–21]. The transition in this one-dimensional system takes place from a phase with one atom on each lattice site, to a broken-symmetry phase (BSP) with an alternating mean occupation (see Fig. 1).

Here, we study the behavior of excitations in the tilted one-dimensional Bose-Hubbard model (TBH) in the phase with broken symmetry, with the latter being twofold degenerate. Fundamental excitations are domain walls between the degenerate broken-symmetry phases and exhibit an effective fractional charge. In turn, the simplest excitation corresponds to moving a single atom from one site to its neighboring site. Such an excitation corresponds to the creation of two closely

bound domain walls. The important question is then whether these experimentally accessible excitations will decay into the fundamental domain-wall excitations and how to detect these fractional excitations. We derive an analytic expression for the time evolution of those excitations, and show the existence of a repulsively bound state of fractional excitations above a critical center-of-mass momentum $Q_c = 2\pi/3$. Further, we provide experimental signatures for measuring fractional excitations in a setup of cold atoms and give direct numerical calculations for the time evolution for a finite size sample.

We start with the one-dimensional tilted Bose-Hubbard model as realized in the experimental setup [17], which takes the form

$$H_{\text{TBH}} = -w \sum_i (a_i^\dagger a_{i+1} + a_i a_{i+1}^\dagger) + \frac{U}{2} \sum_i n_i(n_i - 1) - E \sum_i i n_i, \quad (1)$$

with the on-site interaction U , the hopping rate w , and the lattice tilt E per site. In addition, a_i^\dagger (a_i) is the creation (annihilation) operator for a particle on site i , and $n_i = a_i^\dagger a_i$ is the number operator on site i . We focus on the regime with an averaged density of one particle per lattice site, and assume a positive tilt $E > 0$, i.e., the lattice is tilted to the right. The system is in a metastable state, where the condition that the on-site interaction U and the lattice tilt E are much larger than the tunneling energy w prevents the relaxation into a state with more than two particles accumulating in a single site. Then, the relevant energies are the energy difference $\Delta = E - U$ and the hopping rate w .

For large negative Δ , the ground state is a Mott insulator (MI) with one particle per lattice site. Increasing $|\Delta| \sim w$, particles can tunnel to their right neighboring site, as long as the particle on that site has not tunneled. Eventually, the system undergoes a phase transition into a ground state with broken translational symmetry with two atoms on each second lattice site (see Fig. 1).

The condition $E, U \gg w, \Delta$ suppresses processes with particles hopping to the left as well as the accumulation of more than two particles in a single lattice site. These

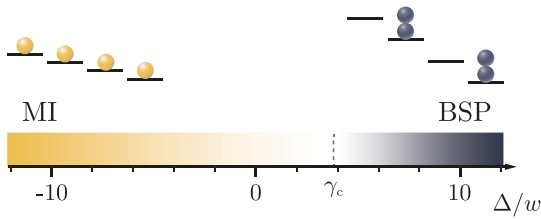


FIG. 1. (Color online) Phase diagram for the tilted Bose-Hubbard model in the regime $\Delta, w \ll U, E > 0$ and an averaged density of one particle per lattice site: The Mott insulator (MI) ground state for $\Delta/w < \gamma_c \approx 1.85$ [19], and the broken-symmetry phase (BSP) for $\Delta/w > \gamma_c$.

constraints are most conveniently incorporated by a mapping of the Bose-Hubbard model to a spin model: The spin degree of freedom resides between two lattice sites i and $i + 1$ and the spin-up state corresponds to a particle at lattice site i , while the spin-down state accounts for the situation where the particle has tunneled to the site $i + 1$. Then, the Bose-Hubbard model maps to a one-dimensional Ising model

$$H_{\text{Ising}} = -2\sqrt{2}w \sum_i S_x^i + \Delta \sum_i S_z^i + J \sum_i \left(S_z^i - \frac{1}{2} \right) \left(S_z^{i+1} - \frac{1}{2} \right), \quad (2)$$

where S_z^i (S_x^i) is the spin operator along the z (x) axis. In addition, the last term accounts for the constraint that a particle can only tunnel from site i to $i + 1$ if there is already a particle at site $i + 1$ and formally requires taking the limit $J \rightarrow \infty$. Under this mapping, the Mott-insulating state corresponds to a paramagnetic phase with all spin up, while the ordered broken-symmetry phase corresponds to an Ising antiferromagnetic ground state.

In the following, we focus on the quantum phase for $\Delta \gg w$ with two particles on every second lattice site. The experimentally accessible excitations are achieved by moving a particle from one lattice site to its neighboring site to the left, which corresponds to a single spin flip. The energy of this excitation is given by Δ . This single-particle excitation can now be decomposed into two fractional excitations via a second-order process, as indicated in Fig. 2. In the classical regime with $w = 0$, these delocalized fractional excitations have the same energy Δ as the single-spin excitations, while adding quantum fluctuations within second-order perturbation theory yields a nearest-neighbor interaction $V = 2w^2/\Delta$, as well as an effective hopping for the fractional excitations

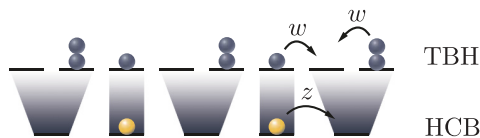


FIG. 2. (Color online) Mapping from the tilted Bose-Hubbard model (TBH) onto the effective hard-core boson model (HCB): Two neighboring lattice sites occupied by a 0,2 configuration map onto a single unoccupied site, whereas a singly occupied site maps onto an occupied site. A second-order transition with $2w^2/\Delta$ allows for an effective hopping of the fractional excitations.

with amplitude $z = 2w^2/\Delta$. Note that fractional excitations are restricted to even or odd lattice sites, depending on the local order, and hence hopping takes place from site i to site $i \pm 2$. This restriction can be uniquely fulfilled by introducing a new lattice: Each singly occupied site and the combination of a doubly occupied site next to an empty site count as a new lattice site (see Fig. 2). Consequently, the number of lattice sites between two excitations is halved, and the dynamics of fractional excitations is governed by the hard-core boson model (HCB) with nearest-neighbor hopping and interaction z and V , respectively, described by the Hamiltonian

$$H_{\text{HCB}} = -z \sum_j (b_j^\dagger b_{j+1} + b_j b_{j+1}^\dagger) + V \sum_j n_j n_{j+1}. \quad (3)$$

Here b_j^\dagger (b_j) is the creation (annihilation) operator for a fractional excitation on site j , and $n_j = b_j^\dagger b_j$ is the number operator with $\langle n_j \rangle \in [0, 1]$.

A similar Hamiltonian has previously been studied in the context of repulsively bound pairs [22,23]. Here, a bound state of domain walls means that the experimental excitation cannot decay into its fractional parts due to energy conservation, while the absence of a bound state corresponds to a situation where this experimental excitation decays into delocalized fractional excitations and allows for their experimental observation. As in the present situation, $z = V$ is the only energy scale of the model, we obtain a universal bound-state structure for the fractional excitations, which we analyze in the following.

We write the wave function for two fractional excitations in the effective model as $\psi(i, j)$, where i and j denote the positions of the fractional excitations in the effective lattice. The discrete translational invariance of the system provides conservation of the center-of-mass quasimomentum, which allows for an expansion into eigenfunctions of H_{HCB} for a fixed center-of-mass quasimomentum Q . Therefore, the two-particle wave function can be factorized as $\psi(X, x) = e^{-iQX} \psi(x)$, with the center of mass $X = (i + j)/2$ and relative coordinates $x = i - j$. We find two different regimes for the two-particle states: In the first regime for $|Q| \leq Q_c = 2\pi/3$, the two-particle eigenfunctions are given by scattering states ψ_q alone with energy $E_q = -2z_Q \cos q$, where q is the relative momentum and $z_Q = 2z \cos Q/2$ denotes the hopping rate in the center-of-mass frame. Its wave function reduces to plane waves, $\psi_q(x) = (1 - \delta_{x,0}) \cos(q|x| + \phi_{Q,q})$, with a scattering phase shift

$$\phi_{Q,q} = \arctan \frac{\cos q + 2 \cos Q/2}{\sin q}.$$

The Kronecker-delta factor $1 - \delta_{x,0}$ accounts for the hard-core constraint and enforces $\psi_q = 0$ at $x = 0$. In the second regime for $|Q| > Q_c$, an additional bound state ψ_b emerges. The repulsive interaction yields an energy $E_b = z(1 - 4 \cos^2 Q/2)$ lying above the scattering continuum. Its two-particle wave function shows an exponential decay with relative distance x , and can be written as

$$\psi_b(x) = (1 - \delta_{x,0}) \left[\frac{1 - 4 \cos^2 Q/2}{4 \cos^2 Q/2} \right]^{\frac{|x|}{2}} \left(-2 \cos \frac{Q}{2} \right)^{|x|}.$$

Note that the alternating amplitude of the wave function is a typical feature of a repulsively bound state. The general wave

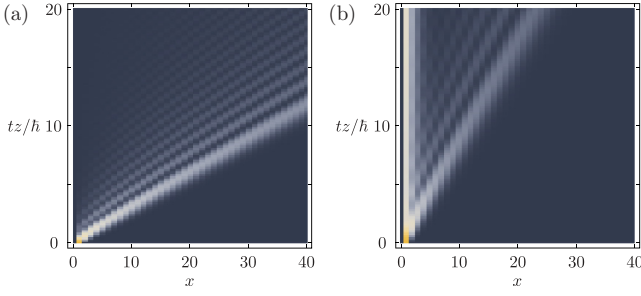


FIG. 3. (Color online) Time evolution of the relative wave function $\psi(x)$: (a) For $|Q| \leq Q_c$, the wave function is strongly localized at around a relative distance $x \sim tz_Q/\hbar$. (b) For $|Q| > Q_c$, the bound state adds an additional exponentially decaying contribution, with its maximum at $x = 1$.

function of two fractional excitations with a fixed center-of-mass momentum Q can therefore be decomposed as

$$\psi(x) = C_B \psi_B e^{-iE_B t/\hbar} + \int \frac{dq}{2\pi} C_q \psi_q e^{-iE_q t/\hbar}, \quad (4)$$

with C_B and C_q denoting the overlap of the initial wave function with the bound and scattering eigenfunctions of H_{HCB} . The experimentally accessible initial states are achieved by moving one particle to the left, which in the effective model corresponds to two adjacent occupied sites $\psi_{\text{SPE}}(x) = \delta_{x,1}$. Then the overlap is given by $C_B = \theta(|Q| - Q_c) \sqrt{1 - 4 \cos^2 Q/2}$ and $C_q = \sqrt{2} \cos(q + \phi_{Q,q})$, with $\theta(x)$ being the Heaviside step function. The integral over the relative quasimomentum q in Eq. (4) can be carried out analytically, giving rise to a formal solution in terms of an infinite sum of Bessel functions of the first kind,

$$\int \frac{dq}{2\pi} C_q \psi_q(x) e^{-iE_q t/\hbar} = \sum_n c_n(x) e^{i\frac{\pi}{2}n} J_n(2tz_Q/\hbar), \quad (5)$$

with coefficients $c_n(x)$ defined via a discrete Fourier transform $C_q \psi_q(x) = \sum_n c_n(x) e^{iqn}$.

The time evolution of the wave function is shown in Fig. 3. The superposition of the scattering states leads to a ballistic expansion of the fractional excitations with a velocity determined by the hopping energy z_Q , i.e., the two-particle wave function ψ_{SPE} is strongly localized around a linearly growing relative distance $x \sim tz_Q/\hbar$, with some additional interference fringes appearing at smaller relative distances x , but propagating at the same velocity. However, the finite overlap with the bound state ψ_B for $Q > Q_c$ creates an additional stationary peak at $x \sim 1$ [see Fig. 3(b)]. With the scattering states moving away from each other, measurement of the wave-function amplitude at $x = 1$ at times $t \gg 1/z_Q$ allows one to single out the bound-state contribution. Formally, this can be cast in terms of a correlation function $C(t) = |\psi_{\text{SPE}}(X, x = 1)|^2$ on the effective lattice. In the microscopic lattice, $C(t)$ corresponds to $\langle P_i P_{i+1} \rangle$, with $P_i = n_i(n_i - 2)$ being the projection operator on singly occupied sites. The time evolution of $C(t)$ for different center-of-mass quasimomenta is shown in Fig. 4. For $Q < Q_c$, the correlation function decays to zero with a characteristic behavior $\sim (tz_Q/\hbar)^{-3}$, and exhibits characteristic oscillations due to interference between the different scattering states. In addition, the decay

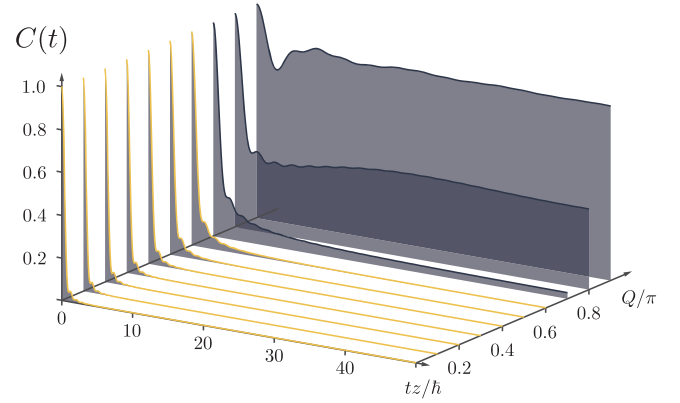


FIG. 4. (Color online) Time evolution of the correlation function $C(t)$ for different center-of-mass quasimomenta Q : Below the critical momentum $|Q| < Q_c$, the correlation function decays to zero, while for $|Q| > Q_c$ the overlap with the emerging repulsively bound state gives a finite probability for fractional excitations to stay at a finite relative distance x , resulting in a finite value of the correlation function for $tz_Q/\hbar \gg 1$.

exhibits an intermediate regime with a characteristic behavior $\sim (tz_Q/\hbar)^{-1}$. The time scale for the crossover between the long-time behavior and this intermediate regime diverges approaching the critical value Q_c . Consequently, the decay at $Q = Q_c$ is given by a critical behavior $\sim (tz_Q/\hbar)^{-1}$ for the correlation function, which follows from the analytical expression for the wave function

$$\psi_{\text{SPE}}(x) = e^{-i\frac{\pi}{2}|x|} [J_{|x|}(2zt) + iJ_{|x|-1}(2zt)].$$

Finally, the presence of a bound state is characterized by a saturation of the correlation function

$$C(t) \rightarrow \theta(|Q| - Q_c) [1 - 4 \cos^2 Q/2]^2$$

for $tz_Q/\hbar \gg 1$. The bound-state contribution grows steadily towards the edge of the Brillouin zone, and eventually ψ_{SPE} becomes an eigenstate of the Hamiltonian at $|Q| = \pi$ with a constant correlation function $C(t) = 1$. In addition, the interference between the bound state and the scattering states gives rise to a characteristic beating of the correlation function with the frequencies $\omega^\pm = E_b \pm E_{\text{sc}}(q = 0) = z(1 - 4 \cos^2 Q/2 \pm 2 \cos Q/2)$. This gives experimental access to the energy gap between bound and scattering states, and allows for the measurement of the bound-state energy.

To confirm our perturbative results and to provide further insight into an experimental realization, we provide time-adaptive density matrix renormalization group (t -DMRG) simulations [24,25] of a single-particle excitation in the original tilted Bose-Hubbard model in Eq. (1). Here, we use a realistically large lattice of $L = 30$ sites, i.e., $l = 16$ sites in the effective lattice. Time-evolution calculations are performed using second- and fourth-order Trotter decompositions. A comparison between the analytic correlation function and the t -DMRG result is shown in Fig. 5.

On the one hand, t -DMRG results show good agreement with the perturbative model. We find that the time scale of the correlation-function decay and the saturation values agree well with the analytic results.

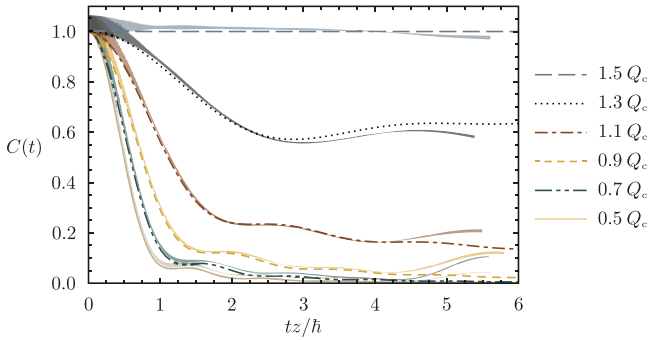


FIG. 5. (Color online) t -DMRG results (thin lines) in a finite lattice with $L = 30$ microscopic sites (i.e., $l = 16$ sites in the effective lattice) in comparison to the analytic results (thick lines) in an infinite lattice for center-of-mass momenta $Q/Q_c = 0.5$ (solid beige), 0.7 (dashed-double-dotted green), 0.9 (dashed yellow), 1.1 (dashed-dotted brown), 1.3 (dotted black), and 1.5 (long-dashed blue). Finite size effects start come into play at times $t \sim 4\hbar/z$.

On the other hand, we observe deviations due to finite system size and finite values U , E , and w , which we discuss in the following. First, the simulations are performed in a finite size system. This leads to revivals of the correlation function $C(t)$ due to scattering of fractional excitations at the system boundaries. In a microscopic lattice of $L = 30$ sites, we find deviations due to finite size at times $t \sim 4\hbar/z$. A hard-core model neglecting nearest-neighbor interaction, which allows for an analytic solution even in a finite system, agrees well with the t -DMRG result and gives an estimate for revival times. From this, we can derive a lower boundary of $L \gtrsim 26$ to observe a signature for a bound state in the correlation function. Second, the simulated correlation function shows an additional high-frequency oscillation. This can be explained as follows: Since the initial state is not an energy eigenstate of the Hamiltonian for a finite ratio w/Δ , this leads to interference between different energy contributions, and ultimately in oscillations on the order of the excitation spectrum, i.e., Δ . We find that for a ratio of $\Delta/w \gtrsim 30$ the suppression of these oscillations is strong enough to see a clear correlation-function signal (see Fig. 5).

Finally, the validity of the correlation function is based on the stability of the broken-symmetry phase. However, second-order processes in w/U and w/E allow the system to reach states with more than two particles on a single lattice site (see Ref. [19]). Our simulations show the probability for having three particles on a single lattice site at times $t = 4\hbar/z$ of the order 10^{-6} . It follows that this effect can be safely neglected

for an on-site interaction $U \gtrsim 8\Delta$ on experimentally relevant time scales. With typical lifetimes of atoms in an optical lattice being on the order of seconds, an effective hopping rate $z/\hbar \sim 1$ Hz should be sufficient for observing the saturation of the correlation function $C(t)$. Further, assuming a microscopic hopping rate of $w = 15$ Hz, suppression of high-frequency oscillations yields a single-particle excitation energy $\Delta/\hbar = 450$ Hz. Finally, an on-site interaction $U/\hbar = 3.6$ kHz results in a stable broken-symmetry phase for the duration of the experiment.

An important aspect is that, throughout this Rapid Communication, calculations used an initial state of delocalized excitations with a finite center-of-mass momentum Q in order to maximize the correlation function $C(t)$. This behavior may seem counterintuitive, as one would expect a localized excitation to yield stronger correlations. However, localization in configuration space gives rise to a flat momentum distribution; with $C(t \gg \hbar/z) \rightarrow 0$ for $|Q| \leq Q_c$, this averaging over center-of-mass momenta then results in a decrease of the correlation function by a factor ~ 0.17 . Still, the finite- Q initial state can be composed of localized excitations via superposition, i.e.,

$$|\psi_Q\rangle = \sum_{j \in 2\mathbb{N}} e^{i\frac{Q}{2}j} a_{j-1}^\dagger a_j |\text{BSP}\rangle, \quad (6)$$

with $|\text{BSP}\rangle$ denoting the broken-symmetry phase with two particles on every even lattice site. The factor of 2 in the phase then accounts for the two-site hopping of fractional excitations in the microscopic model.

In conclusion, we have presented an experimentally accessible setup for studying the creation of fractional excitations. We have found that the stability of a single-particle excitation depends on its center-of-mass momentum, giving rise to a critical center-of-mass momentum $Q_c = 2\pi/3$. Furthermore, we have provided both analytical and numerical predictions on correlation functions, which are directly accessible at single-site resolution in optical lattices demonstrated recently by several groups [17,18].

We thank J. Simon and J. von Delft for fruitful discussions. Support from the DFG (Deutsche Forschungsgemeinschaft) within SFB/TRR21 and FOR 801 is acknowledged. I.McC. acknowledges support from the Australian Research Council Centre of Excellence for Engineered Quantum Systems and the Discovery Projects funding scheme (Project No. DP1092513). This research was supported in part by the National Science Foundation under Grant No. NSF PHY11-25915.

- [1] M. Lewenstein *et al.*, *Adv. Phys.* **56**, 243 (2007).
- [2] J. Simon *et al.*, *Nature (London)* **472**, 307 (2011).
- [3] H. P. Büchler, M. Hermele, S. D. Huber, M. P. A. Fisher, and P. Zoller, *Phys. Rev. Lett.* **95**, 040402 (2005).
- [4] A. Micheli, G. K. Brennen, and P. Zoller, *Nat. Phys.* **2**, 341 (2006).
- [5] L.-M. Duan, E. Demler, and M. D. Lukin, *Phys. Rev. Lett.* **91**, 090402 (2003).

- [6] Y.-J. Han, R. Raussendorf, and L.-M. Duan, *Phys. Rev. Lett.* **98**, 150404 (2007).
- [7] J. Dalibard, F. Gerbier, G. Juzeliūnas, and P. Öhberg, *Rev. Mod. Phys.* **83**, 1523 (2011).
- [8] D. Jaksch and P. Zoller, *New J. Phys.* **5**, 56 (2003).
- [9] M. Roncaglia, M. Rizzi, and J. Dalibard, *Sci. Rep.* **1**, 43 (2011).
- [10] R. N. Palmer and D. Jaksch, *Phys. Rev. Lett.* **96**, 180407 (2006).

- [11] D. Sheng, Z.-C. Gu, K. Sun, and L. Sheng, *Nat. Commun.* **2**, 389 (2011).
- [12] B. Juliá-Díaz, T. Graß, N. Barberán, and M. Lewenstein, *New J. Phys.* **14**, 055003 (2012).
- [13] M. Popp, B. Paredes, and J. I. Cirac, *Phys. Rev. A* **70**, 053612 (2004).
- [14] A. S. Sørensen, E. Demler, and M. D. Lukin, *Phys. Rev. Lett.* **94**, 086803 (2005).
- [15] M. A. Baranov, K. Osterloh, and M. Lewenstein, *Phys. Rev. Lett.* **94**, 070404 (2005).
- [16] I. Bloch, J. Dalibard, and S. Nascimbene, *Nat. Phys.* **8**, 267 (2012).
- [17] W. S. Bakr, J. I. Gillen, A. Peng, S. Fölling, and M. Greiner, *Nature (London)* **462**, 74 (2009).
- [18] J. F. Sherson *et al.*, *Nature (London)* **467**, 68 (2010).
- [19] S. Sachdev, K. Sengupta, and S. M. Girvin, *Phys. Rev. B* **66**, 075128 (2002).
- [20] M. Kolodrubetz, B. K. Clark, and D. A. Huse, *Phys. Rev. Lett.* **109**, 015701 (2012).
- [21] S. Pielawa, T. Kitagawa, E. Berg, and S. Sachdev, *Phys. Rev. B* **83**, 205135 (2011).
- [22] K. Winkler *et al.*, *Nature (London)* **441**, 853 (2006).
- [23] Y.-M. Wang and J.-Q. Liang, *Phys. Rev. A* **81**, 045601 (2010).
- [24] A. J. Daley, C. Kollath, U. Schollwöck, and G. Vidal, *J. Stat. Mech.: Theory Exp.* (2004) P04005.
- [25] S. R. White and A. E. Feiguin, *Phys. Rev. Lett.* **93**, 076401 (2004).

Chapter 8

Conclusion

We derived and calculated the dynamical spin structure factors of chiral Schwinger-boson mean-field ansätze on the antiferromagnetic Heisenberg kagome model, where it was revealed that time-reversal symmetry is broken in that the usual six-fold rotational symmetry around the Γ point of the Brillouin zone was reduced to a three-fold rotational symmetry. Moreover, the dynamical spin structure factor revealed interesting features such as a flat onset of the spinon continuum in the *cuboc1* chiral ansatz.

The Landau-type dynamical phase transition (DPT-I) is fundamentally different from the corresponding equilibrium phase transition in the long-range transverse-field Ising model (LR-TFIM) and depends on the initial state in which the system is prepared. Prethermalization conspires to give rise to dynamical order when quenches are sufficiently small such that thermalization would not happen on any realistic time scales, and where slow relaxation leads to a quasi-stationary prethermal state from which a finite nonzero steady-state value of the order parameter can be extracted even when the equivalent finite-temperature equilibrium phase transition is absent.

The Loschmidt-echo return-rate dynamical phase transition (DPT-II) is also strongly dependent on the initial state in which the system is prepared. In addition to exhibiting the regular cusps in the return rate for quenches crossing a critical value of the quench parameter for all values of α in the LR-TFIM, we find, for quenches starting from zero field strength, anomalous nonanalytic cusps for sufficiently long-range interactions ($\alpha \lesssim 2.3$) for quenches not crossing the critical value of the quench parameter, whereas for larger values of α one would get no nonanalytic cusps in the return rate in such a case. This anomalous phase of the DPT-II is characterized by anomalous cusps that are qualitatively different from their regular counterparts in that the temporal separation between them grows with quench strength and they are additionally preceded by analytic crests, in contrast to the regular cusps.

Expansion of the time-evolution operator in terms of Chebyshev polynomials, where time evolution is carried by Chebyshev vectors in lieu of a time-evolving wavefunction, does not bring an improvement over standard t -DMRG time-evolution schemes such as the Krylov subspace approximation and the Suzuki-Trotter decomposition. A global quench in the one-dimensional Bose-Hubbard model at half filling shows that the Suzuki-Trotter

decomposition leads to the longest evolution times in this model.

We carried out t -DMRG simulations with the one-dimensional two-species Bose-Hubbard model that show that the effect of holes on domain-wall melting in ultracold-gas experiments is innocuous for all interaction strengths, and pretty much negligible for large interaction strengths. In fact, the effect of holes can be accounted for straightforwardly by a linear combination of spatially-shifted observables relative the clean case. On the other hand, spin flips make way for severe effects on the melting of the domain wall, and this is because the dynamics of each of the spin flip and the domain-wall melting share the same time scale.

Considering the one-dimensional tilted Bose-Hubbard model in its symmetry-broken phase where fundamental excitations corresponding to moving one atom to its neighboring site exhibit fractional statistics, we use perturbation theory to analytically show that a repulsively-bound state exists above a critical center-of-mass momentum, with confirmation through relevant t -DMRG simulations.

Acknowledgments

I am grateful to my PhD supervisor Ulrich Schollwöck for his support throughout my PhD tenure at LMU, for directing me in the direction of out-of-equilibrium many-body physics, and for helping further my education in condensed matter physics and statistical mechanics through teaching, projects, and many discussions. I would like to thank Erwin Frey, Roland Kersting, and Matthias Punk for serving as members of my PhD defense committee. My gratitude also extends to Ilka Brunner and Jan Lipfert for their willingness to serve as substitute members.

I would like to also thank people who have strongly influenced my education in physics, in particular Matthias Punk who instilled in me a fascination with spin liquids, and a great respect for rigor in many-body physics. Michael Kastner with his infectious passion and scrutinizing attention to detail left a great impression on how I deal with physics problems. Martin Wegener has greatly shaped my knowledge in optics. I am indebted to my collaborators who have enriched my research experience in physics, in particular Thomas Barthel, Michael Kastner, Fabian Kolley, Ian P. McCulloch, Matthias Punk, Inés de Vega, and Valentin Zauner-Stauber. I am also fortunate to have had the opportunity to engage in many interesting physics discussions with various talented physicists here at the Ludwig Maximilian University of Munich such as Carlo Cascio, Siddhant Das, Pavel Faddeev, Michael Kay, Pavel Kos, Seung-Sup Lee, Lode Pollet, Alessio Recati, Benedikt Richter, Pablo Sala Torres-Solanot, Dennis Schimmel, Andreas Weichselbaum, Oleg Yevtushenko, and others.

Moreover, my special thanks go to the other members of the group who have made the atmosphere on the fourth floor of Building A of the Arnold Sommerfeld Center for Theoretical Physics one of friendliness that is conducive to research and learning. Florian Dorfner was extremely kind with his help in the layout of this dissertation, for which I am very grateful. Leo Stenzel was kind enough to take the time to help translate the Abstract into German, which is much appreciated.

This dissertation is dedicated to my parents and Rosi.

Curriculum Vitae

Curriculum Vitae

Personal Details

Name Jad Camille Halimeh
Address Theresienstraße 37,
 80333 München
Marital Status single



Education

Ludwig-Maximilians-Universität, München, Germany

Arnold Sommerfeld Center for Theoretical Physics

- Ph.D. Degree in Physics (successfully defended on January 16, 2017)
Dissertation: Frustrated magnetism, quench dynamics, and out-of-equilibrium criticality in quantum many-body lattices
Advisor: Ulrich Schollwöck

Karlsruher Institut für Technologie (KIT), Karlsruhe, Germany

Karlsruhe School of Optics and Photonics, Institut für Angewandte Physik

- Master of Science Degree in Optics and Photonics (awarded: November 2009)
Thesis: Photorealistic Visualization of Metamaterial Optical Cloaks
Advisor: Martin Wegener

University of Arizona, Tuscon, AZ, United States of America

Department of Electrical and Computer Engineering

Department of Mathematics

- Bachelor of Science Degree in Electrical Engineering (awarded: August 2006)
- Bachelor of Science Degree in Mathematics (awarded: December 2005)

Rawdah High School, Beirut, Lebanon

Mathematics Baccalaureate (awarded: June 2000)

Publications and Preprints

1. **Jad C. Halimeh** and Valentin Zauner-Stauber, *Enriching the dynamical phase diagram of spin chains with long-range interactions*, arXiv:1610.02019.
2. **Jad C. Halimeh** and Ines de Vega, *A weak-coupling master equation for arbitrary initial conditions*, arXiv:1605.07497.
3. **Jad C. Halimeh**, Valentin Zauner-Stauber, Ian P. McCulloch, Ines de Vega, Ulrich Schollwöck, and Michael Kastner, *Prethermalization and persistent order in the absence of a thermal phase transition*, Phys. Rev. B **95**, 024302 (2017).
4. **Jad C. Halimeh** and Matthias Punk, *Spin structure factors of chiral quantum spin liquids on the kagome lattice*, Phys. Rev. B **94**, 104413 (2016).
5. **Jad C. Halimeh** and Robert T. Thompson, *Fresnel-Fizeau drag: Invisibility conditions for all inertial observers*, Phys. Rev. A **93**, 033819 (2016).
6. **Jad C. Halimeh**, Robert T. Thompson, and Martin Wegener, *Invisibility cloaks in relativistic motion*, Phys. Rev. A **93**, 013850 (2016).
7. **Jad C. Halimeh**, Fabian Kolley, Ian McCulloch, and Ulrich Schollwöck, *Chebyshev matrix product state approach for time evolution*, Phys. Rev. B **92**, 115130 (2015).
8. **Jad C. Halimeh**, Anton Wöllert, Ian McCulloch, Ulrich Schollwöck, and Thomas Barthel, *Domain-wall melting in ultracold-boson systems with hole and spin-flip defects*, Phys. Rev. A **89**, 063603 (2014).
9. **Jad C. Halimeh** and Martin Wegener, *Photorealistic ray tracing of unidirectional freespace invisibility cloaks*, Optics Express **21**(8), 9457-9472 (2013).
10. **Jad C. Halimeh** and Martin Wegener, *Photorealistic ray tracing of free-space invisibility cloaks made of uniaxial dielectrics*, Optics Express **20**(27), 28330-28340 (2012).
11. Jens Honer, **Jad C. Halimeh**, Ian McCulloch, Ulrich Schollwöck, and Hans Peter Büchler, *Fractional Excitations in Cold Atomic Gases*, Phys. Rev. A **86**, 051606(R) (2012).
12. **Jad C. Halimeh** and Martin Wegener, *Time-of-flight imaging of invisibility cloaks*, Optics Express **20**(1), 63-74 (2012).

13. **Jad C. Halimeh**, Roman Schmied, and Martin Wegener, *Three-Dimensional Newtonian Photorealistic Ray Tracing of the Conformal Grating Cloak*, Proceedings of CLEO Quantum Electronics and Laser Science Conference, paper QTuG2 (2011).
14. **Jad C. Halimeh**, Roman Schmied, and Martin Wegener, *Newtonian photorealistic ray tracing of grating cloaks and correlation-function-based cloaking-quality assessment*, Optics Express **19**(7), 6078-6092 (2011).
15. Roman Schmied, **Jad C. Halimeh**, and Martin Wegener, *Conformal carpet and grating cloaks*, Optics Express **18**(23), 24361-24367 (2010).
16. Tolga Ergin, **Jad C. Halimeh**, Nicolas Stenger, and Martin Wegener, *Optical microscopy of 3D carpet cloaks: ray-tracing calculations*, Optics Express **18**(19), 20535-20545 (2010).
17. **Jad C. Halimeh**, Tolga Ergin, Nicolas Stenger, and Martin Wegener, *Maßgeschneiderter optischer Raum. Transformationsoptik*, Physik in unserer Zeit **41**(4), 170-175 (2010).
18. **Jad C. Halimeh**, Tolga Ergin, Jonathan Mueller, Nicolas Stenger, and Martin Wegener, *Photorealistic images of carpet cloaks*, Optics Express **17**(22), 19328-19336 (2009).
19. **Jad C. Halimeh** and Martin Roser, *Raindrop Detection on Car Windshields Using Geometric-Photometric Environment Construction and Intensity-Based Correlation*, Proceedings of the IEEE Intelligent Vehicles Symposium, Xi'an, China, 2009.

Patents

1. Image restoration method in computer vision system, including method and apparatus for identifying raindrops on a windshield (Publication number: US 8797417 B2, Publication type: Grant, 05/08/2014)
Inventors: Gayko, Jens; Roser, Martin Benjamin; **Halimeh, Jad Camille**
Applicant: Honda Motor Co., Ltd.
2. Method and device for detecting an interfering object in a camera image (Publication number: US8582809 B2: Publication type: Grant, 12/11/2013)
Inventors: **Halimeh, Jad**; Simon, Stephan
Applicant: Robert Bosch GmbH

3. Method and apparatus for indentifying directional structures on a window of a vehicle (Publication number: EP2720912 A1, Publication type: Application, 23/04/2014)

Inventors: Huelsen, Michael; Frederiksen, Annette; Simon, Stephan; Schmid, Roland; Uhler, Werner; **Halimeh, Jad**

Applicant: Robert Bosch GmbH

4. Method for using a stereovision camera arrangement (Publication number: EP2293588 A1, Publication type: Application, 09/03/2011)

Inventors: **Halimeh, Jad**; Simon, Stephan

Applicant: Robert Bosch GmbH

Munich, 23.01.2017